Involvement of eIF2 in cardiomyocytes response to endoplasmic reticulum stress

Cristina Cardenal Peralta

INSTITUT POLYTECHNIQUE DE PARIS

ÉCOLE POLYTECHNIQUE

IP PARIS

NNT : 2023IPPAX067

Thèse de doctorat

Involvement of eIF2α in cardiomyocyte response to ER stress

Thèse de doctorat de l'Institut Polytechnique de Paris

préparée à l'École Polytechnique

École doctorale n°626

École Doctorale de l'Institut Polytechnique de Paris (EDIPP)

Spécialité de doctorat : Biologie

Thèse présentée et soutenue à Palaiseau, le 15 septembre, par

Cristina Cardenal Peralta

Composition du jury :

Franck MARTIN Directeur de Recherche Architecture et Réactivité de l'ARN (UPR 9002) Institut de Biologie Moléculaire et Cellulaire-Strasbourg	Président
Christophe ROMIER Directeur de Recherche Département de Biologie Structurale Intégrative Institut de Génetique et de Biologie Moléculaire et Cellulaire-Strasbourg	Rapporteur
Magali BLAUD Maîtresse de conférences Machineries Moléculaires à ARN et Pathologies Humaines CitCom-Paris	Examinatrice
Etienne DUBIEZ Chercheur post-doctoral Assemblage, Dynamique et Réactivité Institut de Biologie Structurale-Grenoble	Examinateur
Emmanuelle SCHMITT Directrice de Recherche Laboratoire de Biologie Structurale de la Cellule (UMR 7654) École Polytechnique-Palaiseau	Directrice de thèse
Jérôme FAGART Chargé de recherche Laboratoire de Biologie Structurale de la Cellule (UMR 7654) École Polytechnique-Palaiseau	Co-directeur de thèse
Mathias MERICSKAY Chargé de recherche Signalisation et physiopathologie cardiovasculaire UMR-S 1180 Université Paris Sud	Invité

Acknowledgements

I would like to express my gratitude to my supervisors Emmanuelle Schmitt and Jérôme Fagart, for granting me the invaluable opportunity to undertake this thesis under their guidance. I am equally appreciative of Yves Mechulam for his support throughout this endeavor.

I would also like to extend my sincere thanks to the members of the jury, Franck Martin, Christophe Romier, Magali Blaud, and Etienne Dubiez.

Thank you as well to Christophe Lemaire and Melanie Gressette, our collaborators, for generously supplying us with the necessary samples for this thesis project.

Thank you to all BIOC members, especially the members of the B2 Gaby, Marc, and Mimi. I would also like to extend a special mention to Titine, whose hard work and expertise made this project possible.

A special thank you to former B2 PhD student, Ramy. For the conversations, the laughs, and everything.

I would like to equally thank the other PhD and master's students that made our office livelier. Devendra, Bhumika, Mouna, Tom, and Bérénice. Thank you for all the laughter, the much-needed gossip, and your friendship (and the coffee).

Without forgetting Irène. Thank you for all the conversations, the help, the tears shed together, and the tea (the one that smells like flowers). Slightly more forgettable, but worth mentioning, Brice. Thank you for guiding me from the darkness of incomprehension to the light of understanding. And to you Aymeric, for giving me some actual sound advice and being a worthy adversary on the tatami. Thank you to Damien, for your undying optimism and your very useful tips in French (good luck on your elephant chase by the way).

A very special thank you to the Turnipers, Alexis/Gark, Noélie/Garanth, Paul/Frerrin, and Alfred/Fiddleneck. And a little bit to Ora. For many more adventures together.

Gracias a los Patos, Eleni, Pablo, Raquel, Javi, Guayente, Laura, Elena, Alba, Nerea, Marcos y Wendy. A las Chicas con Mucho Cuento, Dely, Cris, Inma, Elena y

María Paz. Mil gracias por vuestras historias. A Antonio, por buen profe y porque me da la gana.

A Manu, por las llamadas de los domingos y un maravilloso proyecto que me llevó lejos de esta galaxia cuando más lo necesitaba. A Roberto, por estar ahí, por corregir mi muy deficiente español, pero sobre todo por su pesadez, que me hace darme cuenta de lo mucho que puedo aguantar.

A Néstor, por las llamadas sin o con urgencia, para hablar de proyectos locos o de chorradas o de nada en particular. Cosas de mejores amigos, sin que importe la distancia.

A mis hermanos, Jorge, Edu, Víctor y Pablo. Por estar ahí y compartir cada pequeño avance, libros, tik toks tontos, la sele, y porque sí.

A mis padres, por no dudar nunca de mí, por apoyarme siempre en todas mis decisiones y ayudarme a tomar las correctas. Pero sobre todo por todo su amor y cariño, sin los cuales finalizar esta tesis no habría sido posible.

Thanks to Maddy and Lucy for their unconditional love and support, and for believing in me no matter the circumstances.

And finally, thanks to Will, for being my greatest support throughout these four years of thesis (which included a pandemic, Brexit, thousands of failed experiments, lots of frustration, battling a new language, a new country, and a new life). This thesis is partly yours.

Contents

List of abbreviations

- (m7G): 7-methylguanylate cap
- AADPR: O-acetyl-ADP-ribose
- AaRS: aminoacyl-tRNA synthetase
- Ab: antibody
- ADP: adenosine diphosphate
- aIFs: archaeal initiation factors
- AMC: amino methyl coumarin
- ATF4: Activating transcription factor 4
- ATF6: Activating Transcription Factor 6
- ATF6f: ATF6 fragment.
- ATP: adenosine triphosphate
- CAT: catalytic domain
- CAT: chloramphenicol acetyltransferase
- CDS: coding sequences
- CHOP: C/EBP homologous protein
- CK2: protein kinase 2
- Co-IP: co-immunoprecipitation
- CREBH: cyclic AMP-responsive element binding protein hepatocyte
- CTD: C-terminal domain
- CTR: C-terminal region
- D1: domain 1
- DBC1: Deleted in Breast Cancer 1
- DII: domain 2
- DIII: domain 3
- DNA: deoxyribonucleic acid
- dsRNA: double stranded RNA
- EF: elongation factors
- EF1A: elongation factor 1 A
- eIF: eukaryotic initiation factor
- eIF2: eukaryotic initiator factor 2
- EIF2AKS: eIF2α protein kinases

- ER: endoplasmic reticulum
- ERAD: endoplasmic reticulum associated protein degradation
- ERC: extrachromosomal rDNA circle
- ERO-1: ER oxidase 1
- ERSE: ER stress response element
- ESA: essential for sirtuin activity
- GADD34: growth arrest and DNA damage-inducible protein-34
- GAP: GTPase activating protein
- Gcn2: General control nonderepressible 2
- GCN4: General control nonderepressible 4
- GDH: glutamate dehydrogenase
- GDI: GDP dissociation inhibitor
- GEF: Guanine-nucleotide exchange factor
- GRP78: 78-kDa glucose-regulated protein
- GTP: guanosine triphosphate
- Hac1: homologous to ATF/CREB1
- HRI: heme-regulated inhibitor
- IFs: initiation factors
- ITC: isothermal calorimetry assay
- JNK: Jun N-terminal kinase
- Kcat: catalytic constant/ turnover number
- KM: Michaelis-Menten
- LSU: large ribosomal subunit
- MAD: multiple anomalous dispersion
- MbPylRS: pyrrolysyl-tRNA synthetase (M. barkeri)
- MbtRNACUA: amber STOP codon tRNA (M. barkeri)
- MEF: mouse embryonic fibroblasts
- met-tRNAimet: methionyl-tRNA
- MFC: multifactor complex
- mRNA: messenger RNA
- MS: mass spectrometry
- NAD+: nicotinamide adenine dinucleotide

- NADPH: nicotinamide adenine dinucleotide phosphate
- NAM: nicotinamide
- Nampt: NAM phosphoribosyl transferase
- NMR: nuclear magnetic resonance
- NTD: N-terminal domain
- ORF: open reading frame
- PABP1: poly-A binding protein
- PBS: phosphate buffer saline
- PIC: pre-initiation complex
- PKR: Protein kinase RNA-activated
- PP1: protein phosphatase 1
- PPP1R15A: protein phosphatase 1 regulatory subunit 15A
- PPP1R15B: protein phosphatase 1 regulatory subunit 15B
- RBS: ribosome binding site
- RF: release factors
- RNA: ribonucleic acid
- rRNA: ribosomal RNA
- S1P: site 1 protease
- S2P: site 2 protease
- Sc: saccharomyces cerevisiae
- SERCA: sarcoplasmic reticulum Ca2+ ATPase
- Sp: schizosaccharomyces pombe
- SR: sarcoplasmic reticulum
- SREBPs: sterol response element binding proteins
- SSU: small ribosomal subunit
- STAC: sirtuin activating compounds
- TC: ternary complex
- TG: thapsigargin
- TN: tunicamycin
- tRNA: transfer RNA
- TSA: Thermal Shift Assay
- uORF: upstream open reading frame

- UTR: untranslated regions
- Vi: initial velocity.
- Vmax: maximum velocity
- WB: Western blot
- WT: wild type
- XBP-1: X-box binding protein-1
- ZBD: zinc-binding domain

List of figures

.

List of tables

Introduction

Part 1. Foreword

1.1 From DNA to protein

Since the discovery of the genetic code, major milestones have been accomplished in the field of biochemistry, structural biology, and molecular biology. Some of which are of particular interest to the subject of this thesis, such as the mechanisms of translation, the ribosomal structure, and important factors found to have a major role in cell homeostasis, survival, and regulation.

The DNA (deoxyribonucleic acid) contains all the necessary information to fabricate all cellular structures. This information is transcribed into RNA (ribonucleic acid), which will travel outside the cell's nucleus and direct this information where needed. RNA can be the final product of the transcriptional process, folding into three-dimensional structures that have structural and catalytical roles in the cell, such is the case of ribonucleic particles that form the ribosome, tRNA (transfer RNA), non-coding RNAs such as micro RNAs and nuclear RNA; or it can be an intermediary molecule that will be translated into proteins, called messenger RNA (mRNA) (figure 1). In eukaryotes mRNA must undergo three major modifications to be recognized by the ribosomal complex: 5' capping, splicing, and polyadenylation. These three processes occur co-transcriptionally, meaning that they occur as the mRNA is being polymerized by the RNA polymerase. Splicing can occur co-transcriptionally or post-transcriptionally, depending on the mRNA.

5'capping consists in the addition of a 7-guanine nucleotide connected to the mRNA via an unusual 5' to 5' triphosphate linkage. The guanosine is then methylated, referring to it as a 7-methylguanylate cap (m^7G). This modification is the first one to occur, as the 5' end of the mRNA is the first one to be synthesized. The 5' cap addition is crucial in the translation initiation step.

The addition of a poly-A tail occurs at the 3' end of the mRNA. This tail protects the mRNA against degradation, and it is known to have an important role in the translation step.

The third process is splicing, which consists in the removal of introns. It was believed that introns were just part of so-called ‘junk’ DNA that needed to be cut and deleted from the final RNA translatable form, which only contained exons, the coding part of the mRNA. However, it is now widely known that introns can have a crucial role in the recognition of RNA cutting enzymes and regulation of transcription, making them indispensable pieces of this puzzle. Splicing can occur as the mRNA is being synthesized or later. Depending on the function of the intron to be removed (David L. Bentley, 2014).

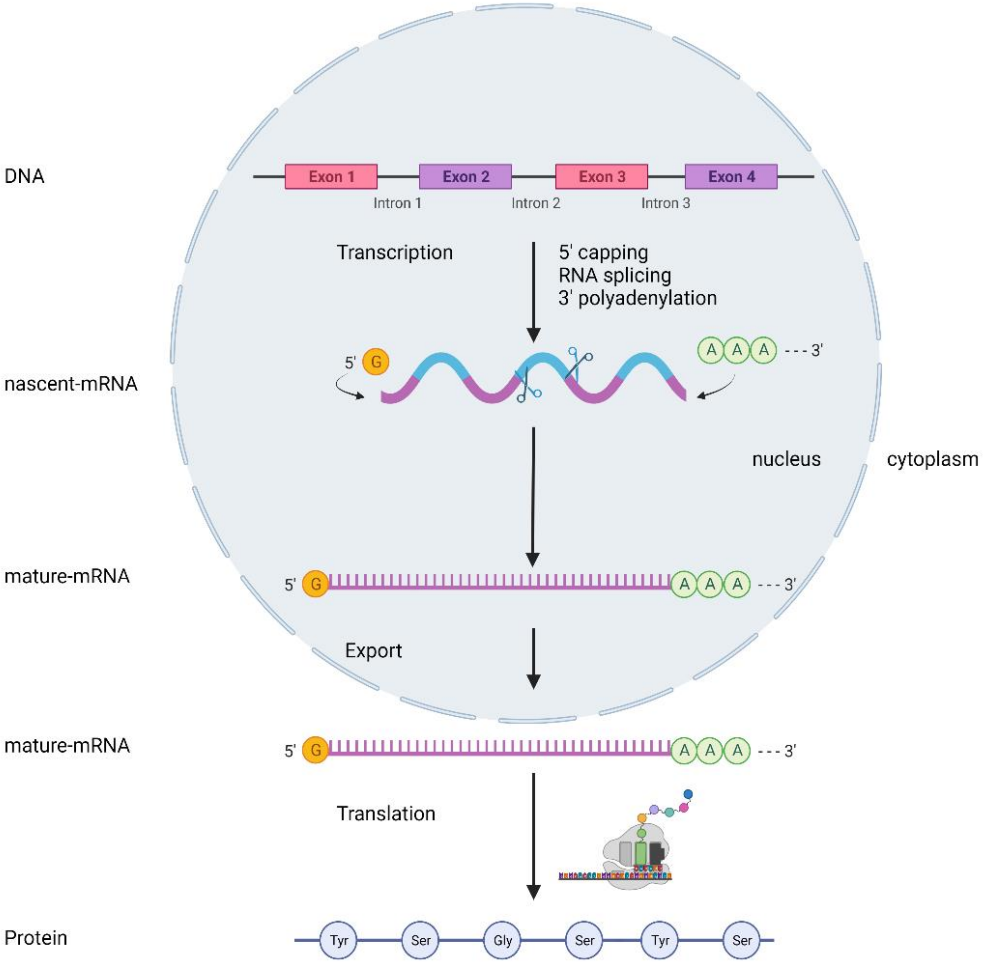

Figure 1: Schematic representation of the steps leading from gene to protein. As the DNA is transcribed, the nascent mRNA molecule is capped on its 5’ end, spliced, and polyadenylated on its 3’ end. The mature mRNA is then transported to the cytoplasm where it is translated. All figures from this manuscript have been created using Biorender.com, unless otherwise stated.

Once the mature mRNA exits the nucleus it is available to be translated by the ribosome. mRNAs can also be stored in P-bodies, nonmembranous organelles known for storing up to a third of the transcribed mRNAs in mammalian cells, specifically those encoding regulatory functions (Standart and Weil, 2018).

1.2 Translation, an overview:

Translation is the mechanism by which mRNA is scanned by the ribosome and translated into a peptide chain. Unlike transcription, the product of the translation process is chemically very different from its template. RNA and DNA are both chemically and structurally similar, DNA being a direct template for RNA production (as base pairing can occur between DNA and RNA). However, there is no way this can happen between RNA and nascent peptides. A whole proteinic-RNA platform is needed to transform the RNA message into protein. This platform is composed of many proteinic factors and the ribosome, a conglomerate of RNA particles and proteins. To transform the information contained in the mRNA into protein, the rules of the genetic code are used. By this, three bases of the mRNA correspond to one amino acid, these groups of three bases are called codons. Several codons can codify for the same amino acid, making the genetic code redundant.

The molecule that serves as a bridge between mRNA and amino acid is the tRNA molecule, another RNA that can specifically recognize the mRNA codons and carry the corresponding amino acid. The tRNA molecule can identify a specific codon because it contains a motif called anticodon, which specifically binds the three bases of the complementary codon in a canonical 5'→ 3' base pairing basis (figure 2).

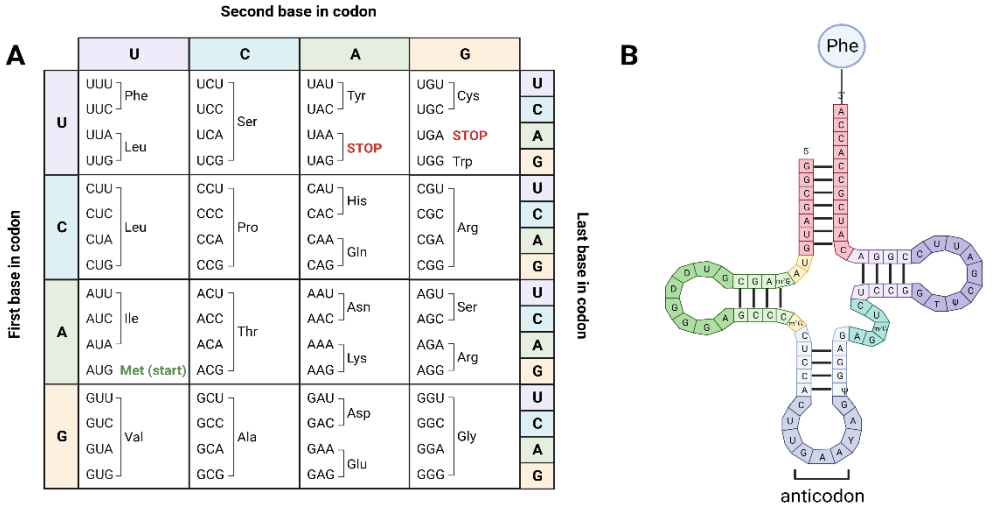

Figure 2: A) The genetic code. Each amino acid is represented in its three-letter form and associated to its corresponding codon. B) Schematic structure of a tRNA molecule. The cloverleaf structure showing the complementary base-pairing that creates the double-helical regions of the molecule (black lines). The anticodon is the sequence of three nucleotides that base-pairs with a codon in mRNA. The amino acid matching the codon/anticodon pair is esterified at the 3' end of the tRNA. tRNAs contain some unusual bases, which are added post-transcriptionally.

tRNAs are specifically aminoacylated by aminoacyl-tRNA synthetases (aaRSs). Each aaRSs esterifies a single standard amino acid to the 3' extremity of its corresponding tRNA. Since tRNAs have similar secondary and tertiary structure, the aaRSs recognizes its corresponding tRNA via specific elements on its sequence, frequently the anticodon and the acceptor stem regions; the specificity of the aminoacylation reaction is crucial to ensure appropriate mRNA translation (Pang, Poruri and Martinis, 2013).

An important feature of mRNAs is 5' leaders, also called 5' untranslated regions (5'UTRs), that span the distance between the m^7G cap and the initiation codon of the main ORF (open reading frame: a continuous stretch of codons that begins with AUG). UTRs vary in length, sequence, and structure. Usually, the AUG codon, in a correct base context, closest to the cap is recognized by the ribosome to start translation, although there are exceptions (Merrick and Pavitt, 2018).

1.2.1 Main steps of translation:

Translation is a heavily regulated process that can be divided into three steps: initiation, elongation, and termination. Translation's main effector is the ribosome. It is in this macromolecular complex where the codon-anticodon pairing occurs, and the nascent peptide is synthesized. It is composed of two subunits that vary in composition and size throughout the three domains of life: the small ribosomal subunit (SSU) and the large ribosomal subunit (LSU). Both subunits have three sites where the tRNAs will bind, called E, P, A: for exit, peptidyl-tRNA, and aminoacyl-tRNA, respectively. The SSU binds to the anticodon loop of the tRNA, whereas the LSU accommodates the acceptor stem of the tRNA (figure 3).

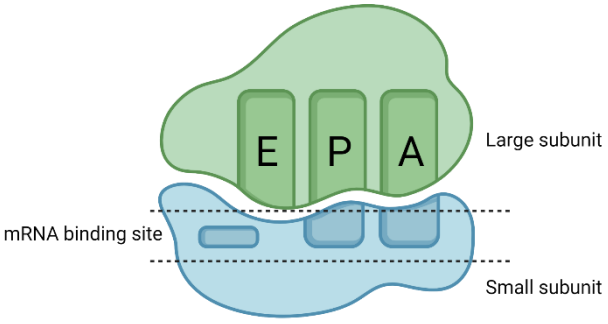

Figure 3: mRNA and tRNA binding sites in the ribosome. The E, P, and A sites span over both subunits,

The ribosome is aided throughout the three steps of translation by a wide array of protein factors: initiation factors (IF), elongation factors (EF), and termination factors (also known as release factors, RF). To initiate translation, the ribosomal complex must recognize the correct start codon on the mRNA. This generally occurs on the SSU, bound to the mRNA and in the presence of a specialized initiator methionyl tRNA.

Translation initiation starts with the coupling of mRNA to the SSU, and the recognition of the start codon by the initiator methionyl-tRNA (met-$tRNA_i^{met}$), which carries the first amino acid, canonically a methionine. The ribosome functions as a catalyzer and host of this reaction, assisted by different initiation factors. The complexity of translation initiation varies across the domains of life, but ultimately, the met-$tRNAi^{met}$ is positioned in the P site. Once the start codon has been selected, the LSU is recruited and a ribosome competent for elongation is formed.

The elongation step consists in the addition of more amino acids to the nascent polypeptide chain as the ribosome reads and matches codons to their corresponding amino acid. The elongator aminoacylated tRNAs are brought to the ribosome by elongation factors (EF-Tu in bacteria and e/aEF1A in eukaryotes and archaea). Once the elongator tRNA is brought to the ribosome, GTP hydrolysis occurs at the elongation factor, allowing it to be released from the ribosome. The elongation step can be subdivided into four different steps: tRNA-binding to the next codon in position A, peptide bond formation in which the next amino acid is added to the C-terminal of the peptide chain, followed by the translocation of the LSU, and then by the translocation of the SSU. Translocation is assisted by the elongation factor eEF2. This translocation means that the two tRNAs present in the ribosome shift to the left, placing the tRNA in P in E, and the one in A in P. The tRNA in E is released from the ribosome and the next tRNA docks in the A site. The central reaction of the protein synthesis (the formation of the peptidyl bound) is catalyzed by the peptidyl-transferase center on the LSU, thanks to a ribozyme activity of the ribosome.

Termination occurs once the ribosome reaches a stop codon: there is no tRNA that matches this triplet, instead a release factor is recruited. The exact number of RFs involved is different in the different domains of life. The mechanism of termination involves the recognition of the stop codon by the RF, the hydrolysis of the ester bond of the peptidyl-tRNA by the RF, and the dissociation of the RFs (figure 4). Translation is a highly regulated multi-step process, as well as a pivotal step in the regulation of gene expression. It's also one of the most energy consuming processes in the cell (Sivanand, 2019). It is not surprising then, that translation, specifically translation initiation, is one of the key steps in a wide variety of cellular responses to internal and external stimuli, as increasing or decreasing translational rates directly impacts gene expression and allows

cells to control energy consumption. In this thesis, we focus on initiation and one of its key factors, eukaryotic initiator factor 2 (eIF2).

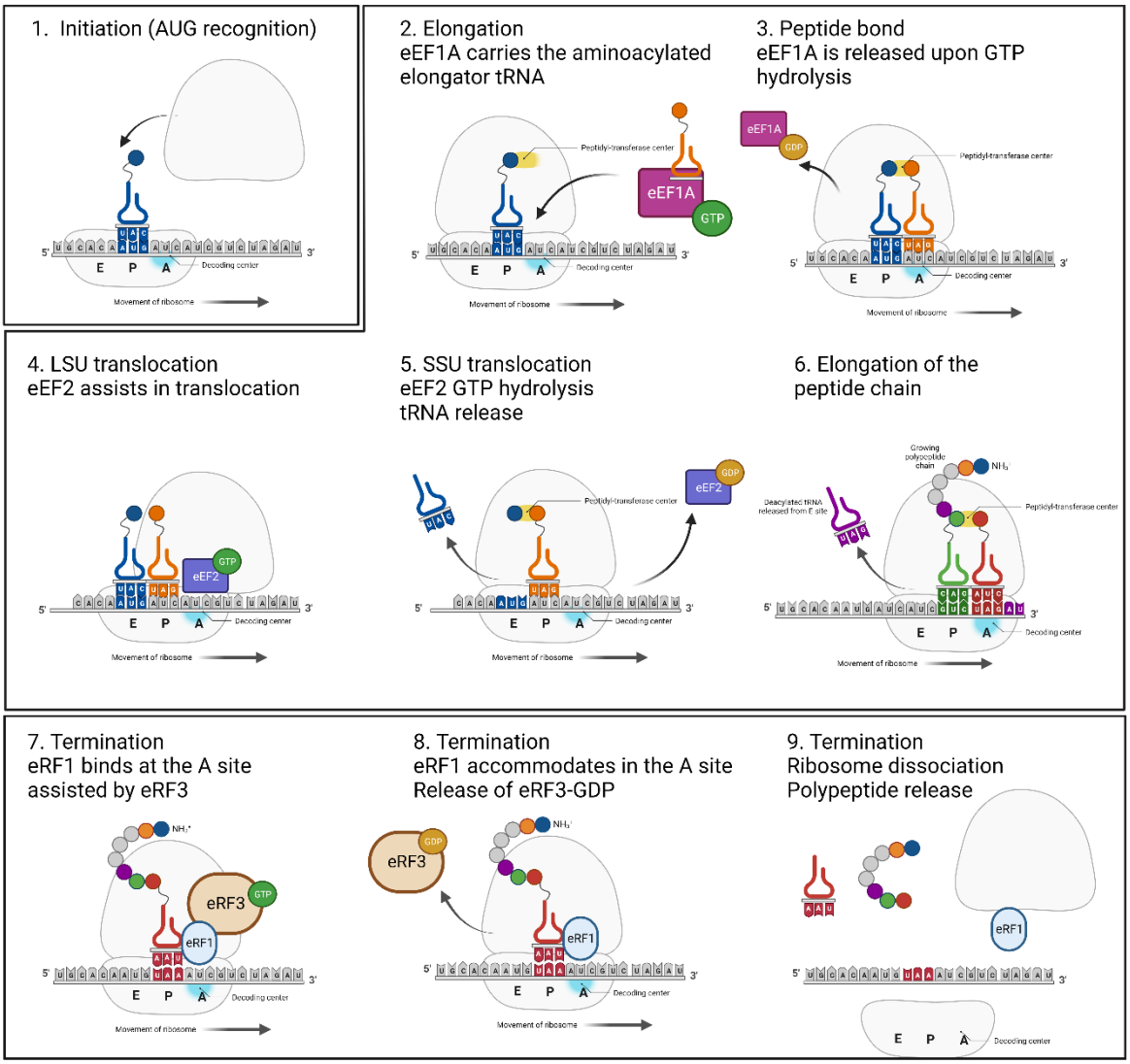

Figure 4: Translation overview. Panel: 1 recognition of the AUG codon by the SSU and the met-tRNA$_i^{met}$. The met-tRNA$_i^{met}$ is positioned in the P site. Panel 2: eEF1A carries the elongator tRNA to the A site. Panel 3: eEF1A is released after GTP hydrolysis. The peptidyl-bond is catalyzed in the peptidyl-transferase center. Panel 4: SSU translocation, aided by eEF2, shifting the tRNAs positioning from the P site to the E site, and from the A site to the P site. Panel 5: LSU shifts position. The empty tRNA on the E site exits the ribosome, so does eF2-GDP. Panels 6: elongation of the peptide chain. Panel 7: there is no tRNA that recognizes the STOP codons, instead, the release factor eRF1(eukaryotes)binds the A site, aided by eRF3. Panel 8: release of eRF3-GDP and accommodation of eRF1 in the A site. This causes the hydrolysis of the ester bond of the peptidyl-tRNA. Panel 9: Finally, the polypeptide is released from the ribosome. In another series of steps the SSU and LSU dissociate from the mRNA, as well the elongation factors.

Part 2. Translation initiation

2.1 Translation initiation in the three domains of life

Protein translation is a complex process present in all domains of life. It involves a great number of initiation factors to aid the ribosome, however, these factors and the mechanisms by which they help orchestrate protein translation vary within the three domains of life (Doolittle, 2000).

If we classify them according to complexity, the bacterial translation initiation is the simplest one, with only three initiation factors involved in the process, followed by archaeal translation initiation, in which five factors are involved, and finishing with eukaryotic translation initiation, where more than a dozen factors are involved(Kyrpides and Woese, 1998); (Schmitt *et al.*, 2020). The complexity of translation is not only given by the number of initiation factors, but also by the structural features of the mRNA, and by the ribosome itself (figure 5).

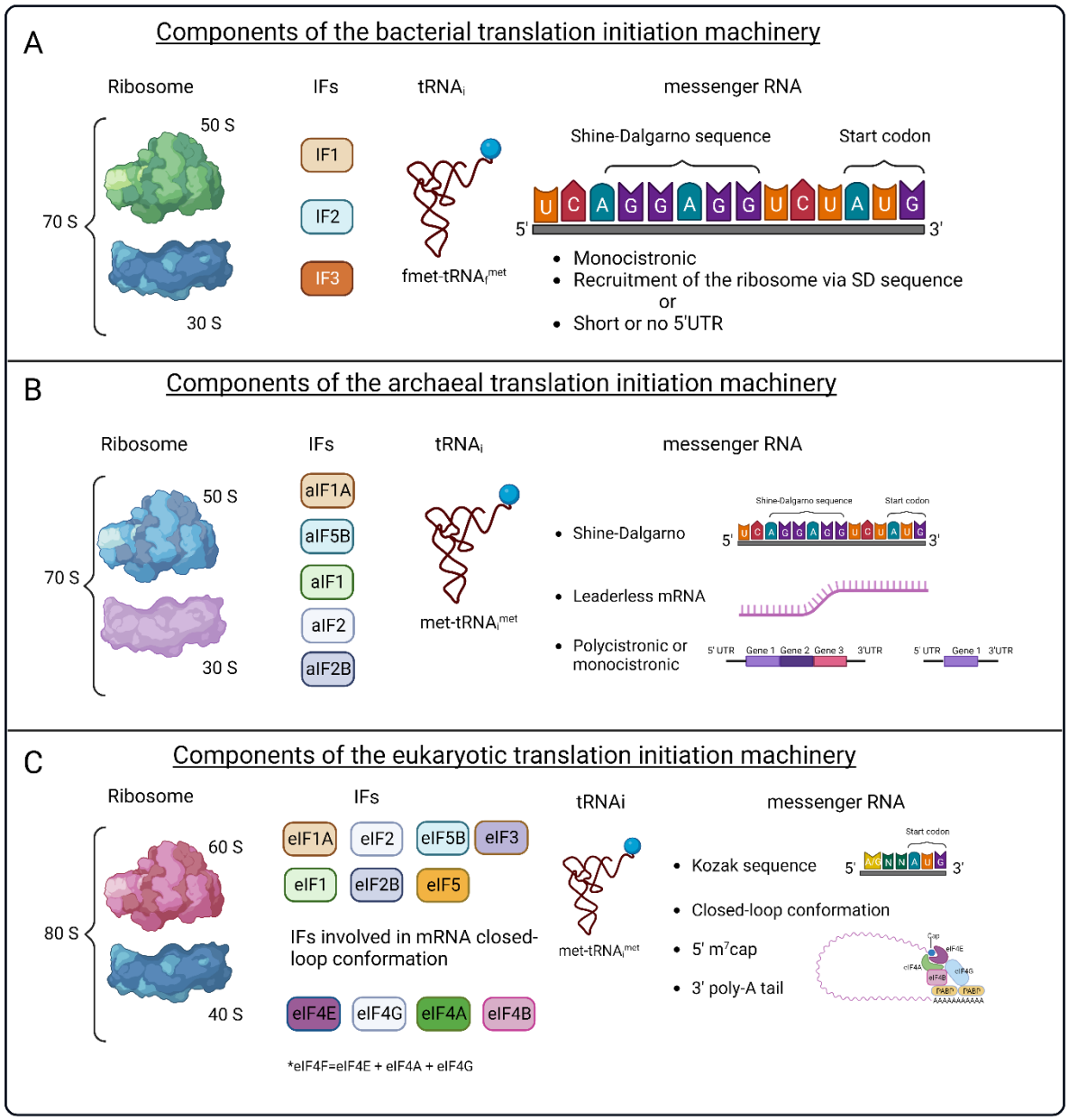

Figure 5: Overview of the different components of translation initiation in the three domains of life. Panel A shows the bacterial case, panel B shows the archaeal case, and panel C shows the eukaryotic case. In each panel there is an overview of the types of ribosomal subunits (according to their sedimentation coefficient), initiator factors, $tRNA_i$, and mRNA present in each case. The color code used for the initiation factors reflects their levels of similarity in the three domains of life. Only two factors are universal: IF1/a/eIF1A and IF2/a/eIF5B, who are structural homologues and serve a very similar function in the three domains of life. In the case of IF3 and a/eIF1, only the C-terminal domain of a/eIF1 is structurally similar to IF1 and serves a similar function. In the case of the ribosome, even though the archaeal and bacterial ribosome are similar in terms of sedimentation coefficient, the archaeal one is considered of eukaryotic type, as it is closer to the eukaryotic one in terms of rRNA and associated proteins.

2.1.1 Bacterial translation initiation

Common to any organism, translation initiation requires the positioning of the ribosome on the start AUG codon. In bacteria mRNAs do not carry a 5'cap or a 3' polyadenylated tail, they can be polycistronic, and generally carry a Shine-Dalgarno (SD) sequence , containing the GGAGG motif or RBS (ribosome binding site), complementary to the 3' end of the 16 S rRNA and located a few bases before the AUG start codon (Shine and Dalgarno, 1975).

The bacterial ribosome is divided into the SSU, also known as 30 S subunit, and the LSU, the 50 S subunit. The SSU is comprised of one ribosomal RNA (16S rRNA) and 21 proteins. The LSU is comprised of two rRNA, 23 S and 5 S, as well as 32 proteins (Goyal *et al.*, 2015); (Rodnina, 2018). Bacterial translation initiation only requires three initiation factors: IF1, IF2 and IF3.

IF1 associates with the SSU in the A site, preventing any tRNA from occupying it. IF2 interacts with the $tRNA_i$ near the P site and positions it. IF3 binds in front of the P site, favoring only the incorporation of the correct $tRNA_i$. In bacteria the $tRNA_i$ is formylated (fmet-$tRNA_f^{met}$), this formylation does not occur nor in archaea nor in the eukaryotic domains(Rodnina, 2018); (Schmitt *et al.*, 2020).

Translation in bacteria happens in the cytoplasm and it is coupled to DNA transcription. This coupling does not happen in the eukaryote domain due to compartmentalization of the two processes. Translation starts with the formation of a pre-initiation complex, comprised of the 30 S ribosomal subunit and factors IF1 and IF2, promoting the recruitment of the fmet-$tRNA_f^{met}$ and the mRNA. IF1 modulates IF2's activity, improving IF2 affinity for the fmet-$tRNA_f^{met}$, and preventing the binding of the fmet-$tRNA_f^{met}$ to the A site. The positioning of the mRNA is facilitated by the SD base pairing to the anti-Shine Dalgarno helix in the 16S rRNA of the mRNA. At this stage there is still no codon-anticodon pairing (Julián *et al.*, 2011); (Gualerzi and Pon, 2015); (Brown-Elliott *et al.*, 2006).

Following, the initiation complex 30S is activated thanks to factors IF2 and IF3. This activation consists of a conformational change that allows the codon-anticodon pairing on the P site, pairing that can only happen with fmet-$tRNA_f^{met}$, as it can displace IF3 who would otherwise prevent any other tRNA from binding to the P site. Finally, IF1 and IF3 dissociate from the 30 S, allowing the assembly of 50S subunit over the 30S

subunit. This process is favored by IF2 and coupled to GTP hydrolysis on IF2. Finally, IF2-GDP exits the ribosomal complex and translation elongation starts (Gualerzi and Pon, 2015) (figure 6).

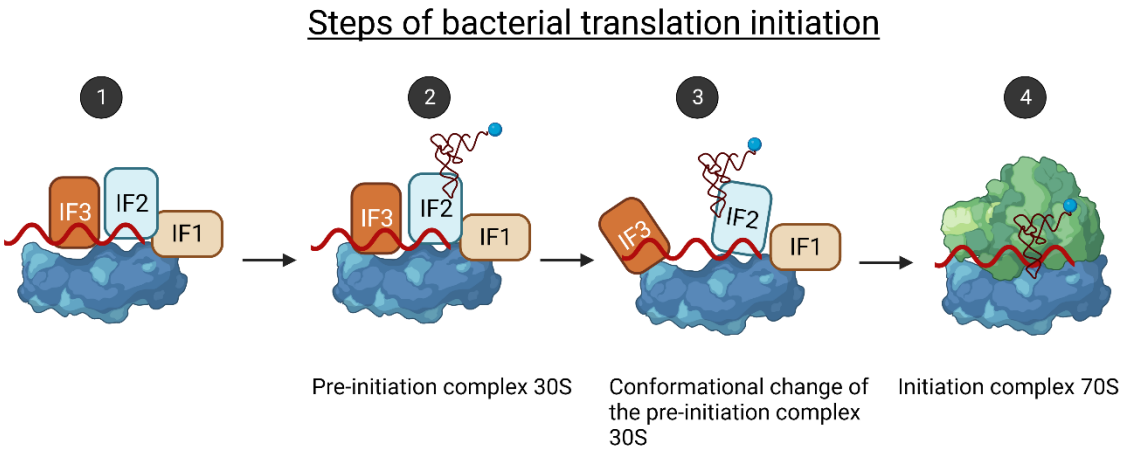

Figure 6: Translation initiation in bacteria. IF1 binds to the A site, IF3 binds in front of the P site, only being displaced by the fmet-tRNA$_f^{met}$. IF2 binds the fmet-tRNA$_f^{met}$ and promotes its correct positioning to the P site, it is also the last factor to be released after GTP hydrolysis.

2.1.2 Archaeal translation initiation

Translation is an ancestral mechanism, conserved in bacteria, archaea and eukarya. Comparison between SSU's rRNAs sequences of all organisms offered a valuable insight into their evolutionary relationships (Woese and Fox, 1977). Phylogenetic analyses based on the 16S rRNA revealed that archaea belong to a domain of their own (Woese, Kandler and Wheelis, 1990). This domain is closer to eukaryotes than to bacteria. Recent studies propose that eukaryotes could have evolved from within the archaeal phylum (Fournier and Poole, 2018).

In the matter of protein translation, archaeal machinery can be considered an intermediary step between the bacterial and eukaryotic translational apparatus. Their mRNAs are of bacterial type and the extensive processing the eukaryotic ones undergo is not observed in archaea (see section 2.2). However, the archaeal initiation factors are of eukaryotic type.

Archaeal mRNAs have bacterial characteristics: they are polycistronic, they do not have a 5' cap or a 3' polyadenylated tail, and frequently present Shine-Dalgarno sequences. Archaeal mRNAs can also be leaderless (less than five nucleotides before the

AUG codon, or totally devoid of 5' UTR). Recognition of the AUG start codon does not require mRNA scanning (which is the case in eukaryotes) (Schmitt *et al.*, 2020).

Even though their mRNAs are considered of 'bacterial' type, their ribosome presents eukaryotic features. The archaeal ribosomal subunits have the same sedimentation coefficient as the bacterial ones, however, the rRNAs sequences are closer to eukaryotic ones. Another interesting point to make in the case of a more eukaryotic-looking ribosome, is the presence of ribosomal proteins that are either universal to the three domains of life, or specific to archaeal and eukaryotic domains. There are not ribosomal proteins shared uniquely by the bacterial and archaeal domain (Woese, 1987); (Penev *et al.*, 2020); (Coureux *et al.*, 2020).

There are five archaeal translation initiation factors (aIFs). The homology between the aIFs and their eukaryotic counterparts has shed light in the study of translation initiation for both domains.

Translation initiation in archaea can be divided into two steps: start codon recognition and LSU joining. Archaeal translation initiation has been extensively studied in the lab (Schmitt *et al.*, 2020); (Kazan *et al.*, 2023); (Coureux *et al.*, 2020). The current view of the mechanism is as it follows.

The first part involves factors aIF1, aIF1A and aIF2. aIF1A binds to the A site, aIF1 binds in front of the P site, and the heterotrimeric protein aIF2 bound to GTP carries the met-tRNA$_i^{met}$ to the SSU. AUG recognition and met-tRNA$_i^{met}$ accommodation in the P site triggers the release of aIF1 because of steric hindrance. aIF1 release then triggers the departure of the P_i group coming from GTP hydrolysis on aIF2, and the final release of aIF2-GDP. aIF5B-GTP is then recruited. aIF5B in the presence of aIF1A, stabilizes the met-tRNAi^{met} in its position and facilitates the joining of the LSU. Finally, the assembly of the large ribosomal subunit triggers the release of aIF1A, GTP hydrolysis on aIF5B, and the final release of aIF5B-GDP (Kazan *et al.*, 2022) (figure 7).

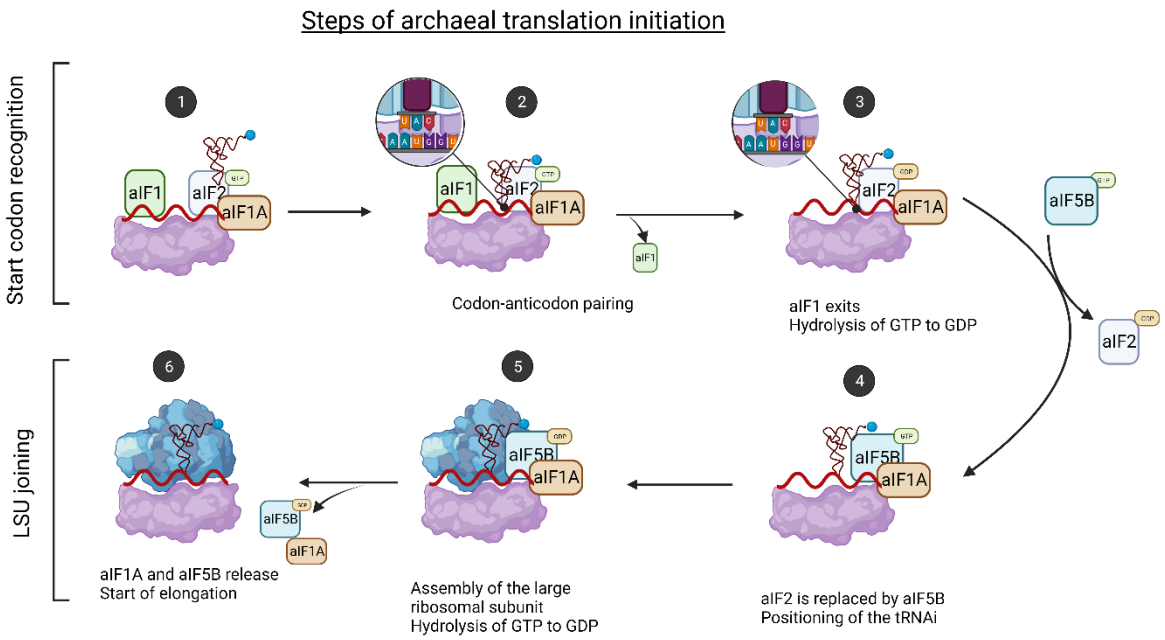

Figure 7: Steps of archaeal translation initiation. Start codon recognition and LSU joining.

2.2 Translation initiation in eukaryotes

Translation initiation is a heavily regulated step in eukaryotic organisms, involving more than a dozen initiation factors (e.g., eIF2, eIF2B), some of them being multimeric proteins of high molecular weight (e.g., eIF3). Before being able to start translation, the eukaryotic SSU, also referred to as the 40S, is primed with a series of initiation factors. This complex is called the pre-initiation complex, or PIC.

The eukaryotic translation initiation is considered the most complex among domains, not only for the abundance of initiation factors, but also for the high post-transcriptional modifications the eukaryotic mRNA undergoes, which includes its pre-activation into a closed loop conformation, stabilized by a subset of initiation factors that connect the 5' and 3' ends of the mRNA.

2.2.1 Closed-loop mRNA conformation:

Eukaryotic mRNAs undergo heavy processing before they are ready to be translated. They have a 5'(m^7G) cap and a poly-A tail on their 3' end, and they are devoid of introns due to splicing events. Eukaryotic mRNAs also present Kozak sequences (CCA/GCCAUGG). This sequence encompasses the AUG start codon. It facilitates the

identification of the start codon by the ribosomal complex, especially due to the purine on position -3 of the AUG codon (Kozak, 1986).

The closed-loop conformation of mRNA was first observed when the polysomes were discovered. By observing polysomic structures using electron microscopy, researchers described them as long hairpins closed at both ends (Christensen and Bourne, 1999). This led to the establishment of the widely accepted 'closed-loop' model of translation initiation, where the 5' cap and the 3' poly A end are bridged together by a protein scaffolding complex (Kahvejian et al., 2016). There are three initiation factors involved in the closed loop conformation of the mRNA: eIF4E, eIF4A and eIF4G (the three proteins, together, are referred to in the literature as eIF4F) and the poly-A binding protein (PABP) (figure 8).

eIF4E is a cap binding protein that can also bind to eIF4G, which is the main scaffold of this complex, as it also binds to PABP, mRNA, eIF4A, and other initiator factors described later (such as eIF1 in budding yeast and eIF3 in mammals). eIF4A is an RNA helicase that unwinds mRNA secondary structures to facilitate the recruitment of the 43S PIC (Pre-initiation complex, see below) at the m^7G cap or close to it (Kumar et al., 2016).

Other factors help in the stabilization of the complex, such as eIF4B, who bridges eIF4A and PABP. It also aids with eIF4A helicase activity, as it is a protein capable of binding single stranded RNA and preventing reannealing, thereby facilitating the helicase activity.

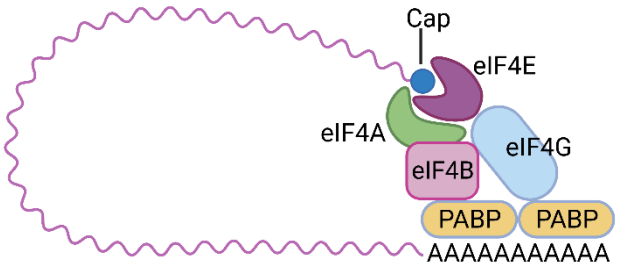

Figure 8: The closed-loop mRNA conformation. The cap binding complex is comprised of three different proteins; eIF4E, eIF4A and eIF4G. The latter binds to the poly-A binding protein (PABP), bridging both ends of the mRNA together. Also present in the complex is eIF4B, who aids eIF4A in its helicase activity.

2.2.2 Formation of the PIC:

The 43S PIC is a complex formed of several eIFs, the (40 S) SSU and an mRNA.

Five eIFs are involved in the formation of the 43S PIC. eIF1, like aIF1, is bound in front of the P site. eIF1 facilitates the binding of the met-tRNA$_i^{met}$. eIF1A, like aIF1A, binds to the A site and participates in the correct positioning of the met-tRNA$_i^{met}$. eIF2, a heterotrimeric GTPase that like its archaeal counterpart aIF2, carries the met-tRNA$_i^{met}$ to the SSU. The association of eIF2 with the met-tRNA$_i^{met}$ and GTP is called ternary complex (TC). eIF5 is a GAP protein (GTP hydrolysis activating protein), being only part of the eukaryotic domain. It aids eIF2 GTPase activity, dissociation, and recycling (explained in future sections). eIF3, found in mammals, contains 13 subunits, and it is involved in the binding to eIF4G and to the mRNA. It maintains the PIC in an open conformation, adequate for scanning.

The PIC can be assembled in two different and non-exclusive ways (figure 9):

1) The ternary complex, composed of met-tRNA$_i^{met}$ and eIF2-GTP, binds to the 40S ribosomal subunit (which has eIF1,1A, 3 and 5 attached to it already).
2) The MFC (multifactor complex) comprised of the TC, eIF1, 3 and 5, bound to the 40S subunit. The MFC was isolated first in yeast. It has also been isolated in mammalian and plant cells. The MFC helps recruiting these translation factors to the 40S subunits (Sokabe, Fraser and Hershey, 2012).

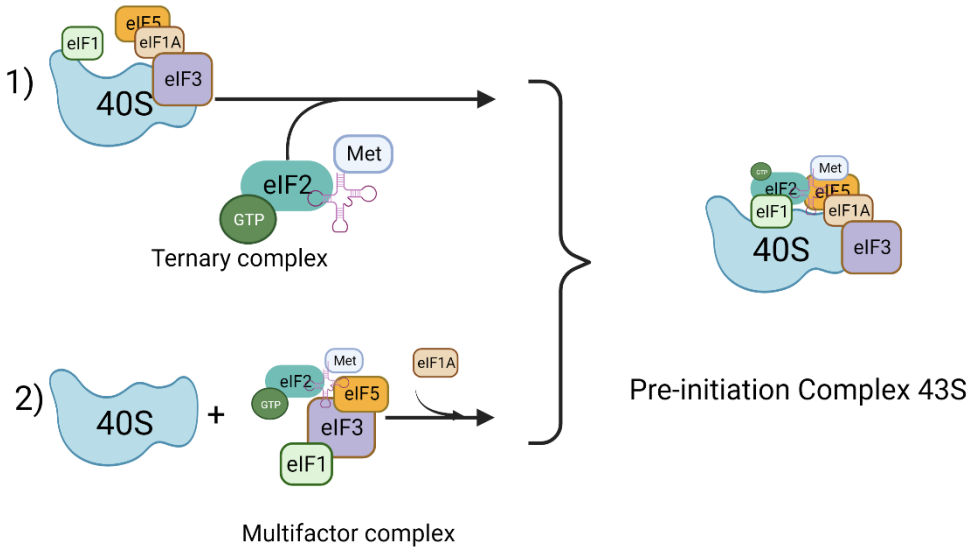

Figure 9: Formation of the 43 S pre-initiation Complex. 1) The ternary complex binds to the 40S ribosomal subunit which consequently binds factors eIF1, -1A, -3, and -5 to form the PIC. 2) The 40S binds the Multifactor Complex (MFC) which contains the ternary complex and all initiator factors necessary for the formation of the PIC.

Start codon recognition triggers a series of molecular events such as eIF1 and eIF2-GDP departure from the SSU. After start codon recognition eIF5B is recruited. This factor, with the help of eIF1A will allow the final positioning of the met-tRNA$_i^{met}$ in the P site and will favor ribosomal subunit joining, as described for archaea.

2.2.3 Steps of eukaryotic translation initiation

After the 43S PIC is formed it can bind the mRNA close to its 5' cap and start scanning nucleotide by nucleotide on a 5'→3' manner. The unwinding of the mRNA requires energy given by the hydrolysis of ATP by eIF4A. Each triplet passes through the P site until the AUG is recognized by the met-tRNA$_i^{met}$. During scanning, GTP bound to eIF2 is hydrolyzed to GDP + P_i (Hinnebusch, 2011). This reaction is activated by the N-terminal domain of eIF5, however, P_i release on eIF2 is blocked by eIF1, who maintains a close interaction with eIF5 C-terminal domain (CTD). When codon-anticodon pairing occurs eIF1 is released from the ribosome. This allows the Pi group to be released from eIF2 (figure 10). Finally, eIF2-GDP exits the ribosome, presumably bound to eIF5 (Hinnebusch, 2014); (Hinnebusch and Lorsch, 2023). eIF2-GDP recycling to eIF2-GTP is crucial to maintain translational levels constant. In eukaryotes a pentameric protein called eIF2B is in charge of eIF2-GDP recycling into eIF2-GTP (further explained in section 2.2.3.1).

After eIF2-GDP and eIF5 leave the ribosome, factor eIF5B binds the PIC. After the LSU joins, GTP bound to eIF5 is hydrolyzed, lowering the affinity of eIF5B for the fully formed 80S and eIF5B-GDP exits the ribosome.

2.2.3.1 eIF2 recycling:

eIF2 is the main met-tRNA$_i^{met}$ carrier and a key regulatory factor of translation initiation. Affinity of met-tRNA$_i^{met}$ for eIF2-GTP is 20-50-fold greater than for GDP (Jennings *et al.*, 2017). Therefore, availability of eIF2-GTP is crucial for translation initiation efficiency. The binding of eIF2 to met-tRNA$_i^{met}$ strongly depends on the methionyl moiety, as experiments done with mischarged met-tRNA$_i^{met}$ by Ile show that it poorly binds eIF2 (Kapp and Lorsch, 2004).

eIF2 exits the ribosome bound to GDP and eIF5. As stated above, eIF5 activates the hydrolysis of GTP bound to eIF2, however, its function doesn't end there. Recent

studies also show that eIF5 also prevents GDP from spontaneous disassociation from eIF2 via its GDP dissociation inhibitor (GDI) activity (Merrick and Pavitt, 2018).

Recycling of eIF2 is performed by eIF2B, a multimeric complex (comprised of five subunits α, β, γ, δ and ε) with two well-defined activities: the guanine-nucleotide exchange factor (GEF), that promotes the release of GDP from eIF2 in exchange of GTP; and the GDI factor displacement function (GDF).

eIF5 and eIF2B bind to eIF2 in a similar manner. Both factors have a highly conserved CTD (C-terminal domain) involved in the binding of eIF2, suggesting that both proteins should interact with eIF2 in a similar way (Luna *et al.*, 2012). Experiments performed by (Jennings *et al.*, 2013), show that eIF2B is able to displace eIF5 from a eIF2•GDP:eIF5 complex, confirming its GDF activity. Once eIF5 has been displaced, eIF2B is able to promote GDP/GTP exchange, releasing eIF2•GTP and allowing it to form the TC. Recycling of the TC is prevented by phosphorylation of eIF2 on its α subunit, as a response to cellular stresses. This regulatory step will be explained in the following sections (figure 10).

Control of eIF2-GTP availability is crucial to control translational rates. eIF2 has multiple partners that control its activity, such as the above-mentioned factors eIF5 and eIF2B, in control of its recycling, as well as eIF1, who controls the P_i release upon GTP hydrolysis on the SSU. Regulation of eIF2 activity is not only limited to its interaction with other initiation factors, but also with other proteins that modify eIF2 post translationally. The following sections will focus on eIF2, its structure, complex formation, and its importance on cellular stress regulation.

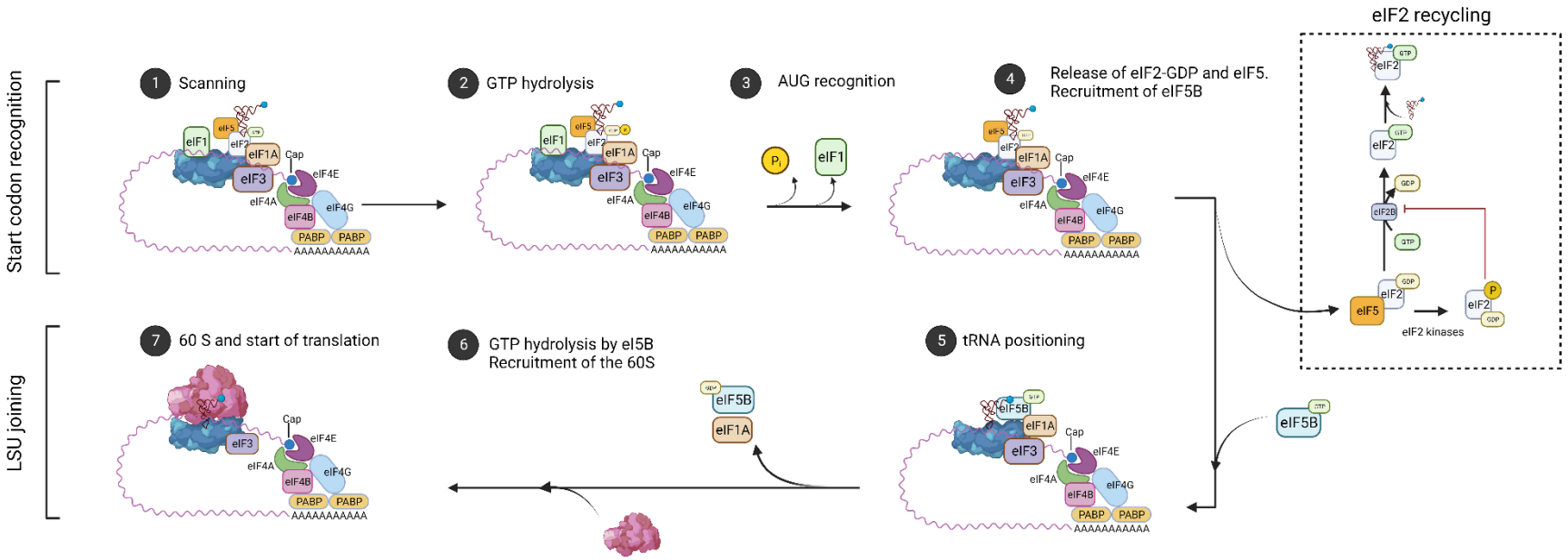

Figure 10: General view of translation initiation steps for eukaryotic organisms. Translation initiation can be divided into two steps in archaea and eukaryotes: start codon recognition and LSU joining. Additionally, eIF2 recycling by eIF2B is essential to control translational rates.

2.3 The Eukaryotic Initiation Factor 2

Eukaryotic translation initiation factor 2 (eIF2) is a heterotrimeric GTPase that has a crucial role in the recognition of the start codon upon the scanning of messenger RNA. eIF2 is part of the ternary complex, as explained in the above section, which comprises eIF2 itself, methionylated initiator tRNA and GTP. The ternary complex then binds to the small ribosomal subunit and other initiation factors, forming the PIC (Hinnebusch, 2014). Upon GTP hydrolysis and start codon recognition, eIF2-GDP is released from the ribosome accompanied by eIF5 and is later recycled by eIF2B (see section 2.2.3.1).

eIF2 is composed of subunits α, β and γ, respectively coded by SUI2, SUI3 and GCD11 in yeast (Cigan et al., 1989; (Hannig et al., 1993). The genes encoding each subunit of eIF2 were shown to be essential for yeast cell viability. Subunit γ is the central core of the heterotrimer, binding to both α and β. Study of the eukaryotic factor was hindered by the difficulty to produce each subunit using *E. coli* expression systems, although there are some studies that have successfully purified the human α subunit (Nonato, Widom and Clardy, 2002); (Ito and Wagner, 2004) and the yeast αβ subunits (Naveau *et al.*, 2013). Luckily, the high sequence similarity of its archaeal counterpart, aIF2, which is produced routinely in this lab, has provided great understanding on both the function and structure of the eukaryotic heterotrimer.

2.3.1 3D-Structure of e/aIF2:

α-subunit:

The first structural information concerning eIF2 was that of domains I and II of the human eIF2α subunit. Researchers produced the full length eIF2α, domains I, II and III, using a baculovirus system and then tried to crystallize the resulting protein. However, they only observed crystals after a six-month incubation period. In these crystals only domains I and II were observed. The 3D structure of these two domains was solved using x-ray crystallography and multiple anomalous dispersion (MAD). Using limited proteolysis techniques to shorten the full-length protein before crystallizing it, they were able to obtain crystals of domains I and II, who diffracted at a final resolution of 1.9 Å (Nonato, Widom and Clardy, 2002).

A structure containing all three domains of human eIF2α was then obtained using NMR in 2004. This protein was produced using an *E. coli* expression system and the structure was resolved using nuclear magnetic resonance (NMR) (Ito and Wagner, 2004). However, in both cases, researchers reported various difficulties when producing eIF2α, due to its lack of solubility and poor yields.

Structural studies of eIF2α, although hampered by technical difficulties, continued thanks to the archaeal protein. The structures of aIF2α determined in this lab (Yatime *et al.*, 2004), showed that the secondary structure of eIF2α and aIF2α were well conserved, allowing structural comparison.

e/aIF2α is composed of three domains. Domain I is a β-barrel, which contains a highly mobile loop between amino acids 49 and 63 in eukaryotes. This loop contains serine 51 in yeast, 52 in mammals and is subject to phosphorylation, which regulates eIF2-GDP recycling to its GTP form. This serine is not conserved in archaea. Domain II contains five α-helixes. Structural comparisons of all available 3D structures (of a/eIF2α) show that domains I and II form a rigid body linked to a mobile third domain. Domain III is composed of four antiparallel β-strands, and two α-helixes (figure 11), the eukaryotic DIII has an acidic extension, which seems to hinder its heterologous expression (Naveau *et al.*, 2013). DIII binds DII of the e/aIF2γ subunit.

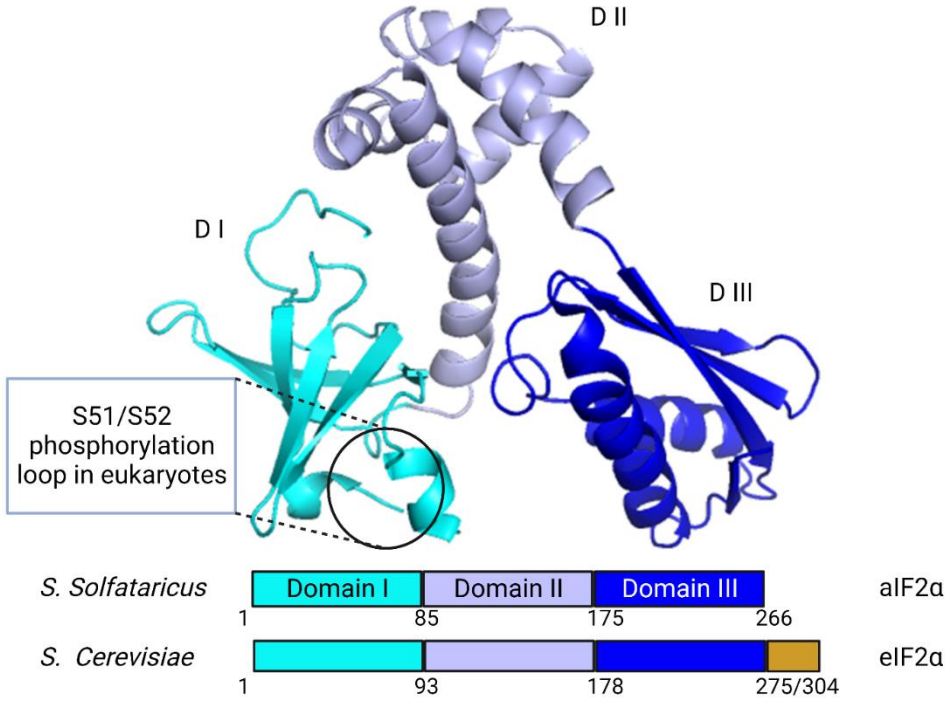

Figure 11: The α subunit from Sulfolobus Solfataricus. Each domain is colored as it follows: N-terminal domain I in cyan blue, domain II in light blue and domain III in dark blue. The loop that contains the S51/S52 phosphorylated site is indicated in domain I. The eukaryotic protein has a C-terminal acidic extension (see in yellow) PDB ID 2AHO. From Schmitt et al., 2009

β-subunit:

Like the α subunit, aIF2β has offered insights into eIF2β structure. The main difference between aIF2β and eIF2β is the presence of a supplementary N-terminal domain in the eukaryotic protein. This N-terminal domain contains three lysine-rich boxes involved in the binding of eIF5 and eIF2B. The archaeal protein contains an N-terminal α-helix, connected by a flexible linker to a central α-β domain, followed by a C-terminal Zinc-binding domain (ZBD) (figure 12). The two last domains interact with each other, forming a rigid body, whereas the N-terminal helix does not interact with the other two (Sokabe *et al.*, 2006). This N-terminal helix is responsible for the binding of a/eIF2B to a/eIF2γ.

eIF2β is also phosphorylated (Wakula *et al.*, 2006), although the role of this phosphorylation is poorly understood. The β domain interacts with many factors involved in the regulation of translation, for example, it binds protein phosphatase-1 (PP1) (Wakula *et al.*, 2006) and protein kinase 2 (CK2) (Llorens *et al.*, 2005). These two proteins perform the phosphorylation and dephosphorylation of several initiation factors. It also interacts with Nck1 (non-catalytic region of tyrosine kinase adaptor protein 1) (Kebache *et al.*, 2002), which interacts with several kinases involved in translation regulation. It is suggested then, that eIF2β has a regulatory role in translation initiation, bringing kinases and phosphatases close to the translation machinery that modify its activity.

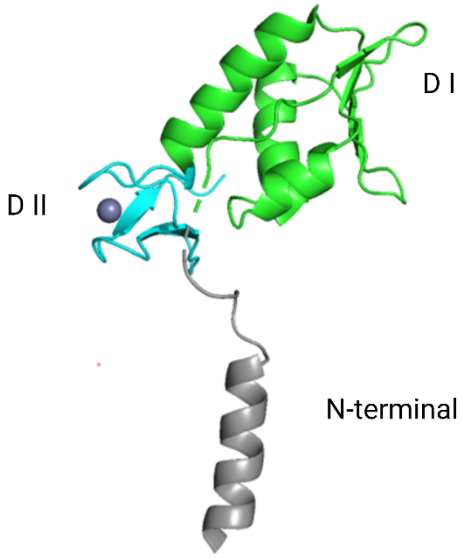

Figure 12: The β subunit from Sulfolobus Solfataricus. It contains two structural domain and a N-terminal α helix: helix 1 in pale green, domain I in green and domain II in cyan. Zn2+ is shown as a blue sphere and residues 23-27 are not visible. PDB ID 2QMU). From Yatime et al., 2006.

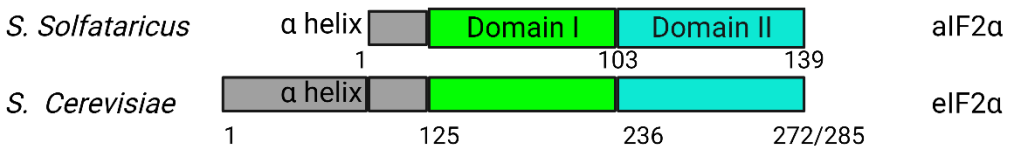

γ-subunit:

The archaeal orthologues of this subunit provided structural information before it was observed in eukaryotic organisms. The archaeal and the eukaryotic orthologues are homologous, with the exception that the eukaryotic protein also has a supplementary N-terminal domain with various lengths depending on the species.

e/aIF2γ has three domains. Domain I contains a guanine nucleotide binding pocket outlined by regions found in G-proteins, called switch regions (figure 13). Conformational changes of these regions control the active GTP-bound state of the protein (switch on) and the inactive GDP-bound form (switch off). Domains II and III are both β barrels (Schmitt, Naveau and Mechulam, 2010); (Schmitt, Blanquet and Mechulam, 2002).

From studies in yeast and in archaea, it was shown that the γ subunit binds both the α and β subunits, which do not interact with each other. In human studies, however, it has been reported a possible interaction between the α and β subunits (Suragani *et al.*, 2006).

The γ subunit is the core of the e/aIF2 heterotrimer, as it functions as a structural scaffolding (interacts with both the α and β subunits), it controls GTP/GDP exchange, and binds the initiator tRNA. Interestingly, e/aIF2γ presents a high structural homology to the elongation factor eEF1A (Schmitt, Blanquet and Mechulam, 2002). Studies on EF1A structure have given some insight on the interaction between e/aIF2γ and the met-$tRNA_i^{met}$. However, the structure of the archaeal heterotrimer bound to the met-$tRNA_i^{met}$, showed that the tRNA-binding motif of eEF1A and a/eIF2γ are radically different (Schmitt *et al.*, 2012).

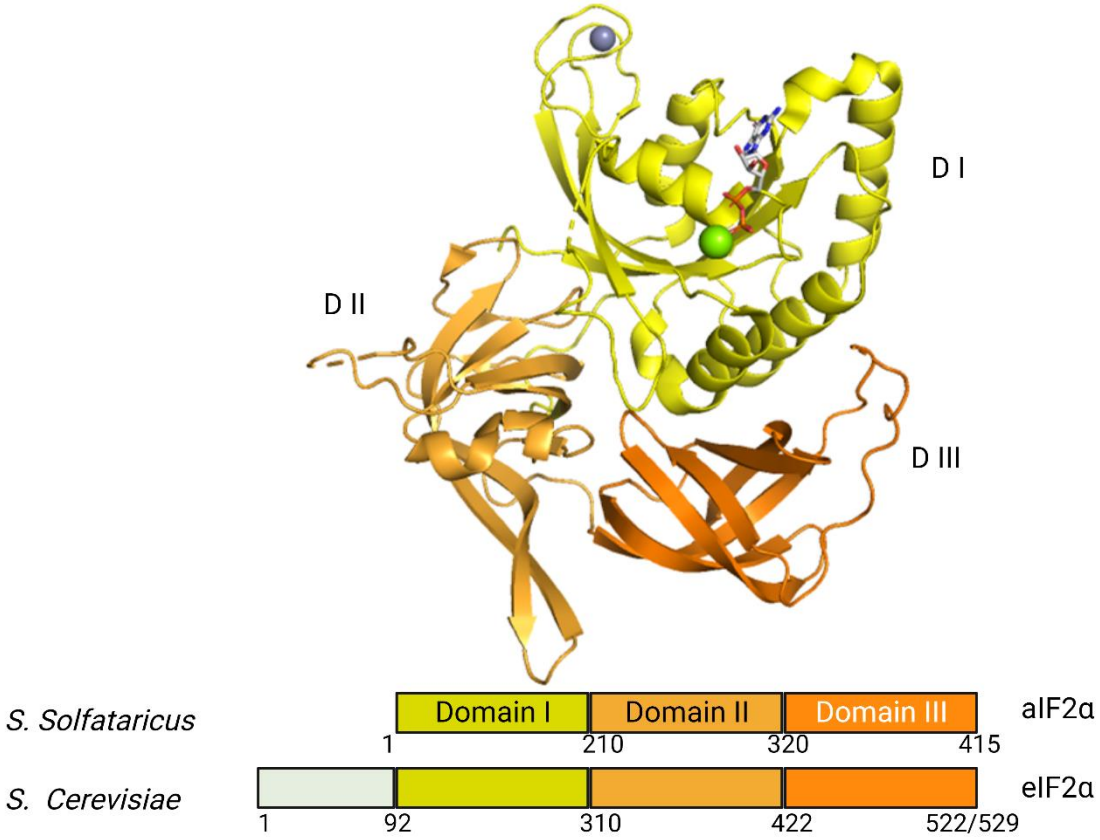

Figure 13: The γ subunit from Sulfolobus Solfataricus. Each domain is colored as it follows: domain 1 in yellow, domain 2 in pale yellow and domain 3 in orange. GDP is shown as sticks, Mg2+ as a green sphere and Zn2+ as a yellow sphere. Regions involved in nucleotide binding are highlighted. From Schmitt et al., 2009.

2.3.2 The archaeal heterotrimer aIF2

The γ subunit of e/aIF2 is considered the core of the heterodimer, as it binds both subunits α and β. Several studies aimed to understand the process by which this heterotrimer is formed, having to date two crystallographic structures of the *Sulfolobus solfactaricus* heterotrimer: one of the GDP-bound form (Yatime *et al.*, 2007), and one in its apo form (Stolboushkina *et al.*, 2008). Other studies focused on the formation of heterodimers αγ and βγ, shedding light in the structural interactions between subunits (Yatime, Mechulam and Blanquet, 2006); (Sokabe *et al.*, 2006).

aIF2γ domain II binds to domain III of aIF2α, and it binds to aIF2β N-terminal helix via its domain I (figure 14). Interestingly, aIF2β central αβ region and its zinc-binding region form a rigid body, which is quite mobile in comparison to aIF2γ (Sokabe *et al.*, 2006), capable of adopting a conformation close to the nucleotide binding site (Yatime *et al.*, 2007).

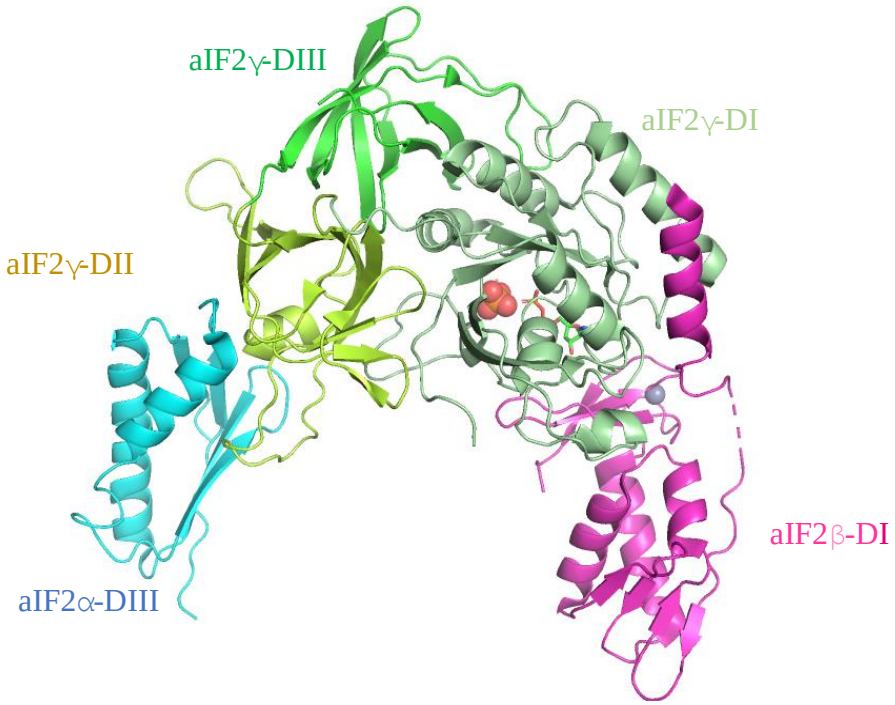

Figure 14: Structure of the aIF2 heterotrimer from Sulfolobus solfactaricus. Domain III of aIF2α is shown in blue, domain I of aIF2β is shown in pink, and aIF2γ is shown in different shades of green. PDB: 2QMU

The primary function of the e/aIF2 heterotrimer is to carry the $tRNA_i$ to the AUG start codon. Several structures of e/aIF2-$tRNA_i$ bound exist, as well as other several ones of the TC bound to the SSU (Coureux *et al.*, 2020) (figure 15). How the heterotrimer binds to the met-$tRNA_i^{met}$ was determined in this lab using *S. solfactaricus* aIF2, showing that subunits α and γ are involved in met-$tRNA_i^{met}$ binding (Schmitt *et al.*, 2012).

aIF2γ is capable of binding the met-$tRNA_i^{met}$ by itself, however, it was shown that the affinity of met-$tRNA_i^{met}$ for aIF2γ was greatly reduced when compared to the complete aIF2 (5 μM vs 120 nM) (Yatime *et al.*, 2004). Further experiments showed that upon addition of aIF2α this affinity was increased, specifically showing that aIF2α-DIII was enough to recuperate the same binding affinity as the heterotrimer (Schmitt *et al.*, 2012). Nevertheless, this doesn't seem to be the case in eukaryotes. The archaeal model offers a good insight into the structural characteristics of the heterotrimer, however, the formation of the ternary complex in eukaryotes, requires of the β subunit. Unlike in archaea, the binding of the met-$tRNA_i^{met}$ requires the β subunit as shown in yeast (Bagchi, Ghosh-dastidars and Gupta, 1982); (Flynn, Oldfield and Proud, 1993); (Mouat and Manchester, 1998) .

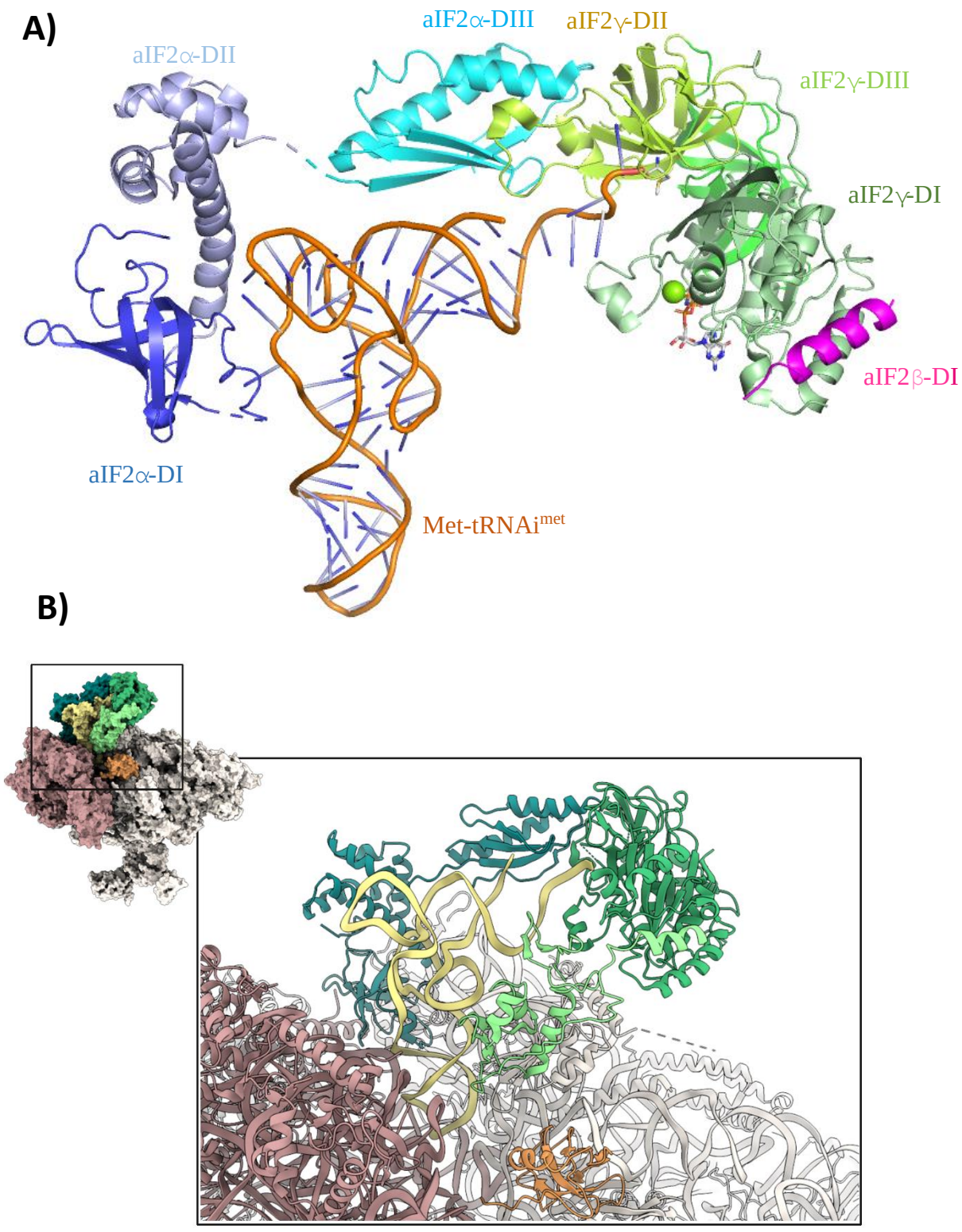

Figure 15: A) Structure of the S. solfactaricus ternary complex. Domain III of aIF2α is shown in blue, domain I of aIF2β is shown in pink, and aIF2γ is shown in different shades of green. PDB: 3V11. B) Structure of eIF2 on the 43 S PIC.

2.3.3 The eukaryotic heterotrimer eIF2: structure and assembly

The importance of eIF2 in translation initiation is evidenced by the amount of regulation this protein is subject to. For example, its GTPase activity is accelerated by eIF5, its recycling from GDP to GTP form is regulated by eIF2B, and its α subunit is subject to phosphorylation, a well-studied event that radically changes translation levels and is considered the first regulatory step to many cellular responses against stress (figure 16) (Pakos-Zebrucka *et al.*, 2016). Moreover, in 2013, researchers from the Seufert lab, added another step of control by showing that the cell division cycle 123 protein (Cdc123) is required for eIF2 assembly (Perzlmaier, Richter and Seufert, 2013).

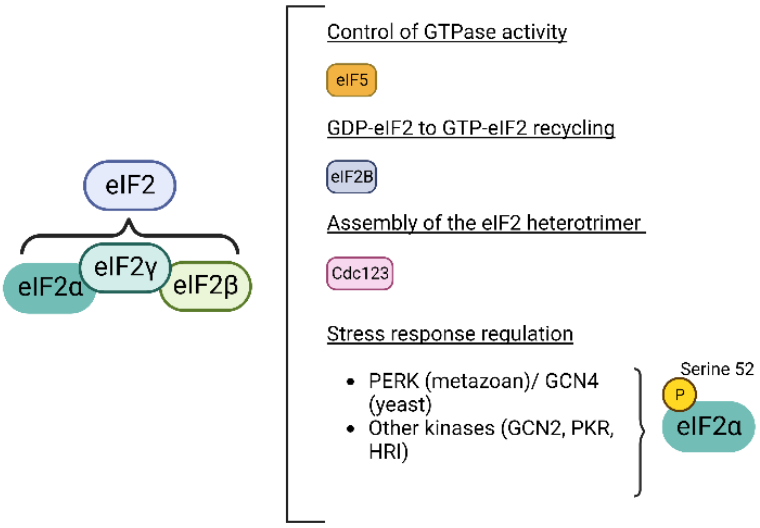

Figure 16: eIF2 known partners. As a key component of translation initiation, eIF2 activity is regulated by a number of partners that control its GTPase activity (eIF5), its recycling from a GDP inactive form to a GTP-bound active form (eIF2B), its assembly (Cdc123), and partners that modify specific residues (S52 in subunit ∝) upon specific stress-related responses.

A link of eIF2 to Cdc123 was suggested by proteomic studies that reported an interaction between eIF2γ with Cdc123 in yeast (Perzlmaier, Richter and Seufert, 2013). Cdc123 was described for the first time associated to a temperature-sensitive allele in a rat fibroblast line which blocked the G1 to S phase transition. The gene coding for human Cdc123 has been described since then as a potential oncogene in breast cancer, a risk locus in type II diabetes and lung function (Adélaïde *et al.*, 2007); (Ohno *et al.*, 1984); (Okuda and Kimura, 1996). Interestingly, mutations in Cdc123 in budding yeast reduce the formation of the eIF2 heterotrimer, reduce polysome levels, and increase GCN4 expression, a transcription factor whose expression is triggered by eIF2α phosphorylation (Perzlmaier, Richter and Seufert, 2013).

Several yeast two-hybrid experiments showed that Cdc123 specifically binds domain III of eIF2γ. Researchers isolated a clone which expressed only a small C-terminal fragment of eIF2γ. Reporter activation by the C-terminal fragment was comparable to that of full-length eIF2γ, showing for the first time that domain III of eIF2γ was sufficient for binding to Cdc123. They also performed the same experiment with a truncated version of eIF2γ that lacked the last 13 amino acids of the C-terminal domain. This mutant was unable to interact with Cdc123, as well as eIF2α and eIF2β (Perzlmaier, Richter and Seufert, 2013), further narrowing down the role of Cdc123 in the assembly of eIF2.

The structure of *Schizosaccharomyces pombe* Cdc123 (Sp-Cdc123) was elucidated in 2015 in this lab. Cdc123 is made up of two α-β domains (figure 17). Comparison of its structure to a wide database showed that Cdc123 is an atypical member of the ATP-grasp family, which was rather unexpected due to the low sequence similarity to members of this family. Consistent with this homology, it was shown in the lab that Cdc123 indeed binds ATP using ITC experiments. Moreover, ATP binding to Cdc123 was also observed in the X-ray structure. Furthermore, Cdc123 appears to have a second cavity facing the nucleotide binding pocket, suggesting a possible second ligand for Cdc123 that remains to be discovered (Panvert *et al.*, 2015)

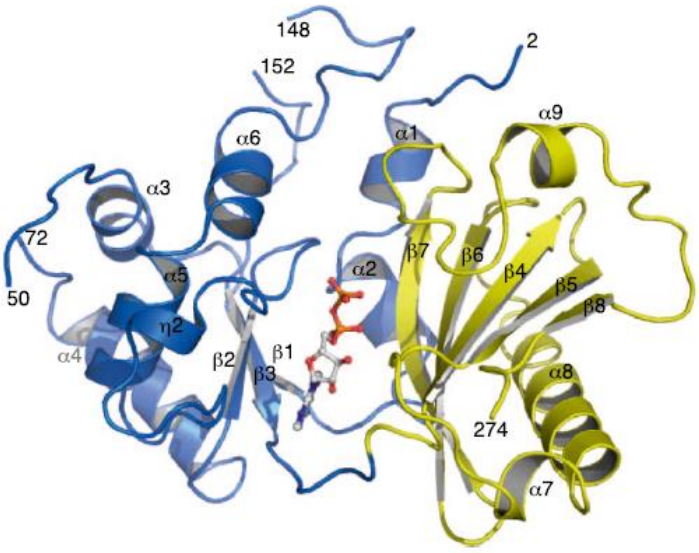

Figure 17: Structure of Sp-Cdc123, image adapted from Panvert et al. 2015. A deletion of the C-terminal tail was performed after observing in a previous structure that it was not visible in the electron density, probably because of its high mobility. The deletion of this C-terminal tail improved the quality of the structure (3.24 Å vs 2.06 Å). Cdc123 is divided into two domains, colored in blue and yellow. Panel B shows the cartoon representation of Sp-Cdc123. ADP is represented as sticks.

Binding of Sc-Cdc123 to Sc-eIF2γ-DIII did not seem to be ATP-Mg^{2+} dependent, as shown in (Panvert *et al.*, 2015). In this paper, the structure of Sp-Cdc123 and Sc- eIF2γ-DIII was obtained in the absence or presence of ATP-Mg^{2+}, showing minimal changes in the side chains of residues involved in ATP-binding. Moreover, mutations in residues D227, D239 and N241, which are involved in the binding of ATP, into alanines seemed to be deleterious to the assembly of Sc-eIF2γ to Sc-eIF2α. The obtained structures allowed the authors to propose a model for eIF2αγ assembly, mediated by Cdc123 (figure 18). This model is based on the available structures of the Sp-Cdc123: Sc- eIF2γ-DIII complex and the archaeal structure of aIF2γ (Dubiez *et al.*, 2015) and/or the archaeal aIF2αγ structure (Yatime, Mechulam and Blanquet, 2006).

According to this model, Cdc123 would bind the full γ subunit through its domain III. This would position the long L1 of domain II of eIF2γ close to the C-terminal region of Cdc123 (L1 is known to be involved in the αγ interface). Such positioning would facilitate the recruitment of the α subunit and the formation of the αγ heterodimer (figure 18).

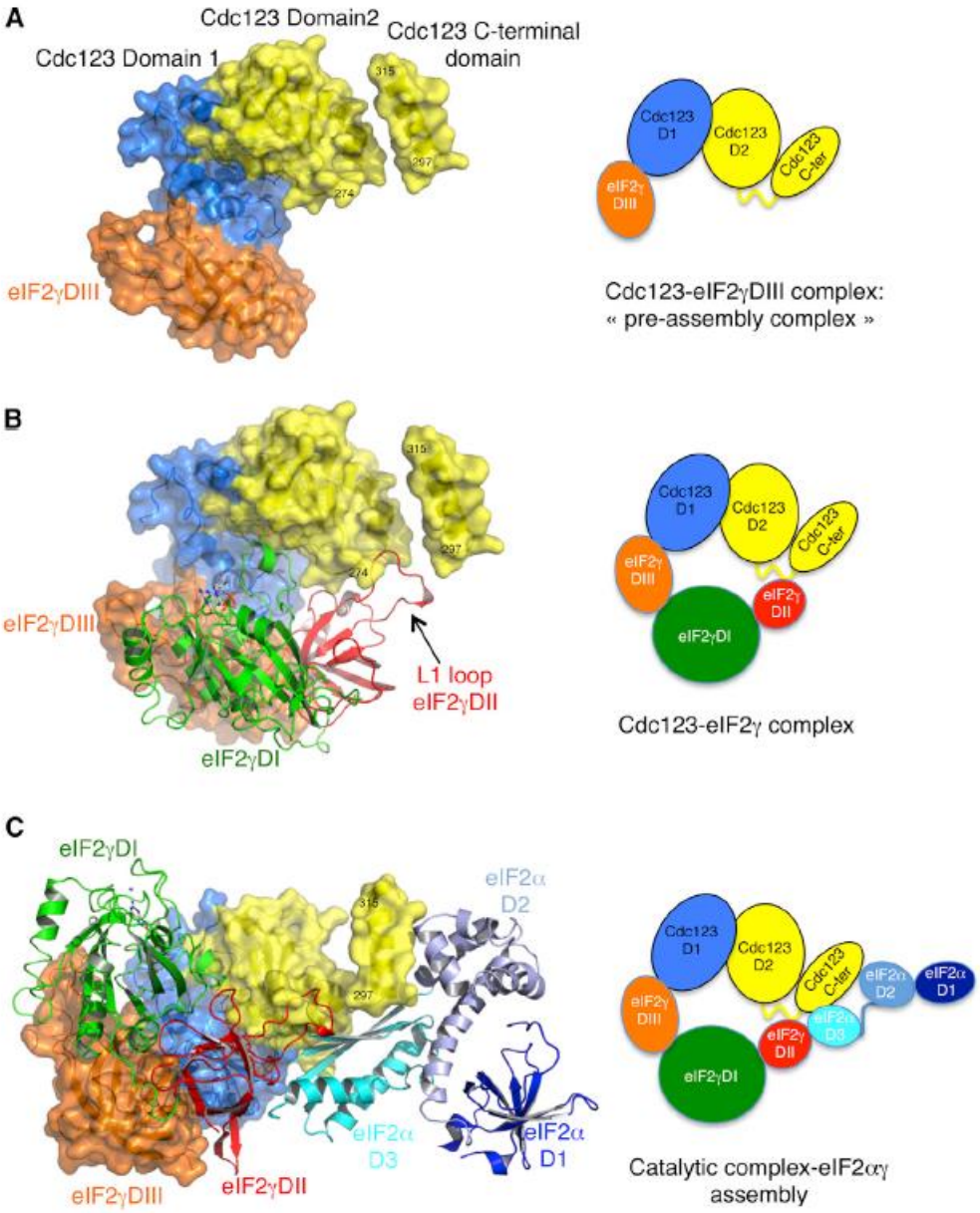

Figure 18: Model for Cdc123 binding to eIF2αγ (PDB: 2AHO). Panel A shows the surface representation of Sc-Cdc123: Sc-eIF2γ-DII. Panel B shows the docking of the archaeal aIF2γ (PDB: 4RD4) superimposed to the panel A complex. Panel C shows a docking of the archaeal αγ heterodimer onto the Sc-Cdc123: Sc-eIF2γ-DII complex.

2.4 Regulation of eIF2 activity:

eIF2's activity is regulated by a wide number of factors, see figure 19, and its availability in its GTP-bound active form is able to bind the met-tRNAimet, which directly impacts translational rates (Pakos-Zebrucka *et al.*, 2016). Phosphorylation of eIF2 in its α subunit was shown to hinder translational rates, but it was also observed as a systematic response to stress in yeast alongside with expression of stress-related genes (Dever,' *et al.*, 1992). Therefore, eIF2 not only plays an important role in translation initiation but is also a key factor in the control of stress related gene-expression programs.

Numerous genetic and environmental stresses deter the ability of cells to properly fold and post-translationally modify secretory and transmembrane proteins in the endoplasmic reticulum (ER), leading to an increase of misfolded proteins (Oakes and Papa, 2015). These proteins accumulate in the ER and cause a condition called ER stress. One of the responses to this stress by eukaryotic cells is the downregulation of protein synthesis: translation is a very energy-consuming process, lowering its rate enables the cell to redirect its energy resources to combat the stress and ensure survival. In addition, overloading the ER with more proteins would only aggravate the situation (van Anken and Braakman, 2005).

Post-translational modifications (PTMs) can modify and alter the function and structure of proteins. A well-known example is the histone code, which enables certain parts of the DNA to be read or not depending on the needs of the cell (Stillman, 2018). Responses to stress in eukaryotic cells usually conveys the modification of PTMs, altering regulatory pathways and enabling the cell to adapt quickly and efficiently to environmentally and inner stresses (Oakes and Papa, 2015a).

It has been shown that phosphorylation in Serine 52 of eIF2α lowers the ability of the ternary complex to interact with eIF2B, affecting the GTP-GDP exchange and lowering translation rates. This is because phosphorylated eIF2-GDP and eIF2B form a very stable complex lowering the available eIF2-GTP-met-tRNA$_i^{met}$ and diminishing translation rates. (Gordiyenko et al., 2019) (figure 19). Therefore, phosphorylation of the α subunit of eIF2 has an overall impact in translational rates.

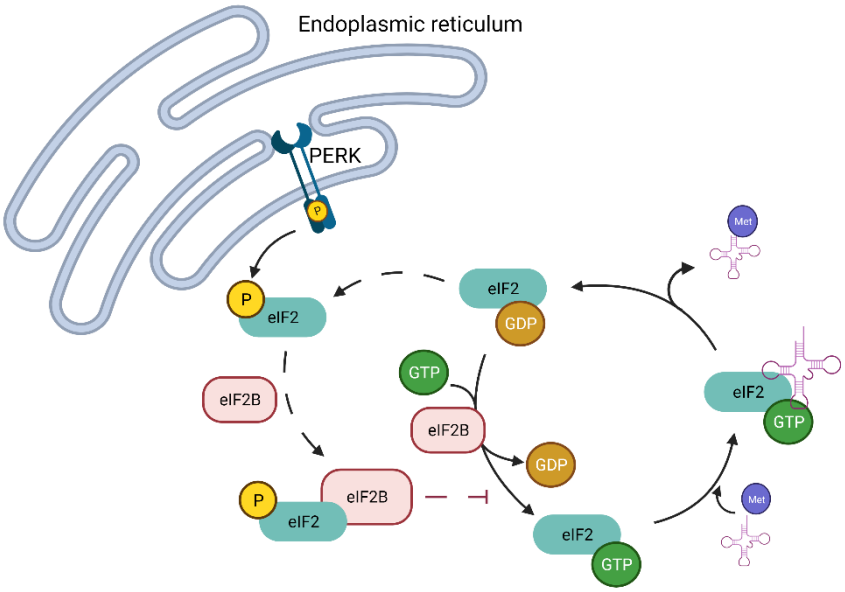

Figure 19: Phosphorylation of serine 52 in the alpha subunit of eIF2 increases the interaction between eIF2B and eIF2, impeding the GDP-GTP recycling of eIF2 and diminishing translational rates.

Our collaborator Christophe Lemaire, who works on ER stress in the cardiac context, identified two residues that are acetylated, lysines 141 and 143 (Prola et al., 2017). These two residues are likely deacetylated by a deacetylase known as sirtuin 1 (SIRT1), an NAD-dependent deacetylase that participates in modulating ER stress response in the heart. In his work, our collaborator showed that activation of SIRT1 is protective against ER stress-induced cardiac injury, by attenuating eIF2α pathway activation (Prola *et al.*, 2019); (Pires Da Silva *et al.*, 2020). Therefore, PTMs on eIF2α appear essential to regulate translational rates in response to different stresses and stimuli.

Part 3. Endoplasmic reticulum stress

3.1 The Endoplasmic Reticulum

The endoplasmic reticulum (ER) is one of the largest organelles in eukaryotic cells, occupying up to 10% of the total cell space. It consists of a continuous membrane that folds into a series of tubules and sacs throughout the cytosol, enclosing a single internal space called the ER lumen. This membrane typically constitutes about 50% of the total membrane in the average cell and mediates the selective transfer of molecules between the cytosol and the ER lumen (Oakes and Papa, 2015a).

The ER is divided into Rough Endoplasmic Reticulum (RER) and Smooth Endoplasmic Reticulum (SER). The two sub compartments have different functions: the RER plays a major role in protein synthesis, folding and post-translational modification of proteins, whereas the SER is mainly in charge of the production of lipids and steroid hormones (Anelli and Sitia, 2008); (Voeltz, Rolls and Rapoport, 2002). The RER is completely covered with ribosomes, hence its name 'rough' and it is continuous to the nuclear membrane. On the other hand, the SER faces the Golgi Apparatus, creating a vesicle transportation system (figure 20) (Schwarz and Blower, 2016). During this thesis manuscript I will discuss in further detail the functions of the RER, especially those attaining protein synthesis, post-translational modifications, and signal transduction, thus using RER and ER as synonyms from this point onwards.

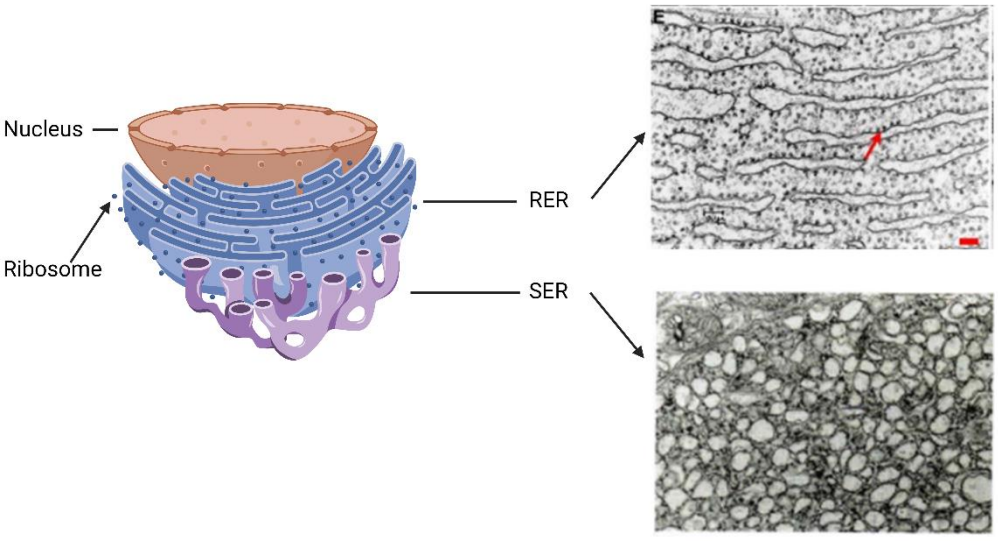

Figure 20: Rough endoplasmic reticulum and Smooth endoplasmic reticulum. The nucleus and the ER form a continuous membrane, in the illustration it is depicted in three different colors for clarity. On the top right panel, it is shown an electron microscopy picture of the RER (Schwarz & Blower, 2016), and on the bottom right one of the SER (Lodish et al, 2003).

3.1.1 Functions of the ER: protein synthesis and maturation

Proteins can be synthesized by free ribosomes in the cytosol, or by ER-bound ribosomes. Either way, all proteins need to be properly folded to ensure they are functional, whether they are structural proteins or enzymes. Some proteins need additional modifications, also known as post-translational modifications (PTMs). PTMs and protein folding both take place in the ER (Oakes and Papa, 2015b).

Proteins that are to be translocated to the ER have an N-terminal signal sequence that directs them to the ER. All these proteins are translocated via the translocon complex, and once in the lumen the N-terminal signal is removed of the polypeptide chain. Nearly all the proteins destined to the ER, membranes, Golgi, or lysosomes are translated on the ER-bound ribosomes and injected directly into the ER lumen. Once in the lumen, proteins are folded into their unique 3-D structures (Tu and Weissman, 2004). Cryo-ET studies have shown how the ribosomal population contacts the different translocon complexes in high resolution (Gemmer *et al.*, 2023) (figure 21).

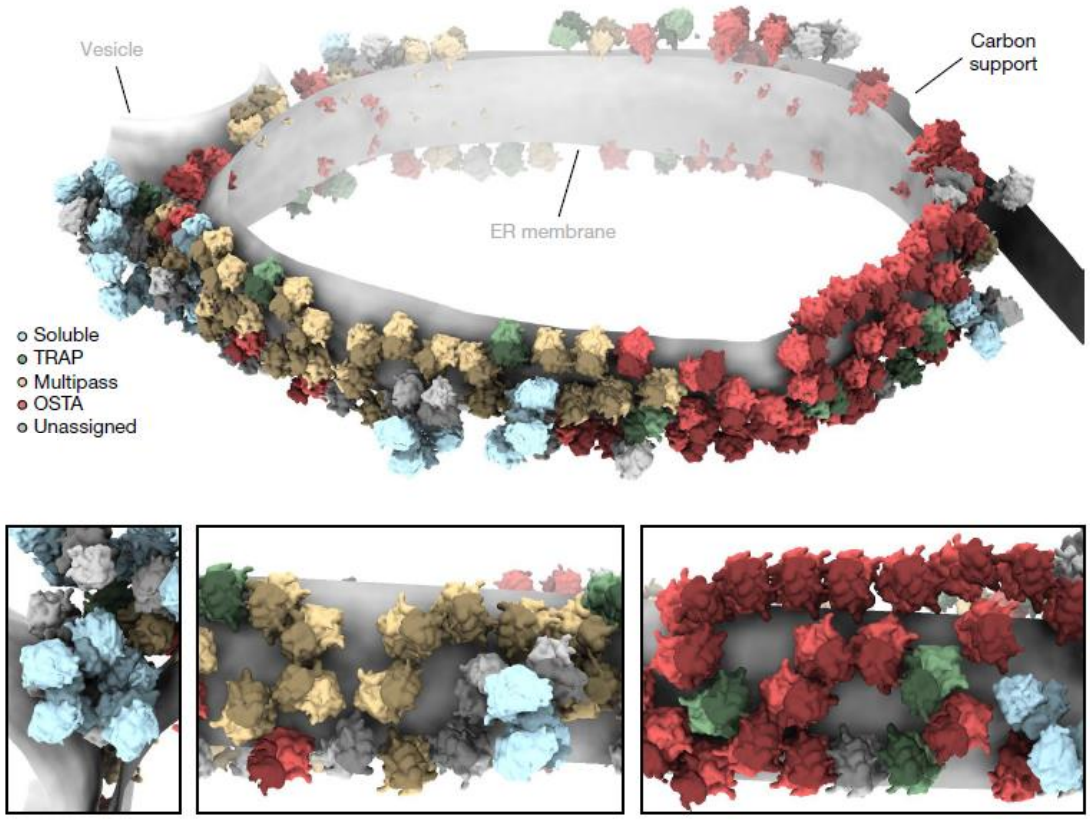

Figure 21: Cryo-ET imaging of ribosomes associated to their translocon complexes in the ER. Work by Gemmer et al., 2023. A) Segmented representation of one tomogram of an ER-derived vesicle. B) Close-up views. The color of the ribosomes corresponds to their associated translocon complex labelled on the left. In blue soluble ribosomes, in green TRAP-associated ribosomes, in yellow multipass ribosomes, in red OSTA-associates ribosomes, and in grey unassigned ribosomes.

The ER-resident proteins and enzymes include chaperones, glycosylating proteins, oxidoreductases, among others. Paired with its ionic and electronic environment, the ER is particularly suited for protein folding, as, compared to the cytosol, the ER maintains a much higher calcium concentration, which is needed by chaperones, and a more oxidizing redox potential, which favors the formation of disulphide bonds (Ma and Hendershot, 2004); (Minamino and Kitakaze, 2010).

Cells can adjust their protein-folding capacity of the ER to maintain cell homeostasis. In certain situations, such as environmental, genetic, and nutrition-related stresses, the demand for secreted and membrane proteins increases quickly. However, the ER has a limited protein folding and degradation capability, leading to the accumulation of misfolded proteins in its lumen (Bhattarai *et al.*, 2021). This is aggravated by the fact that (in normal conditions) at least a third of the proteins produced in the ER lumen undergo degradation in the cytosol, in a process known as ER-associated degradation (ERAD). An already impaired ER will fail to properly label these proteins (ubiquitination) to direct them to the proteasome in the cytosol, increasing the number of misfolded proteins in the ER lumen (Van Anken and Braakman, 2005). An overworked ER, be it because of internal or external reasons, will undergo what is known as ER stress.

3.1.2 A specialized ER: the sarcoplasmic reticulum in cardiomyocytes

Depending on their specialization, cells adapt their internal structure to suit their function. This is the case of muscle cells or myocytes, in which the specialization of the ER is such that their ER is called sarcoplasmic reticulum (SR) (Doroudgar and Glembotski, 2013). In particular, the SR is specialized in calcium storage, necessary for muscle contraction and relaxation, and protein folding (Sobie and Lederer, 2013) (figure 22). The study of ER stress in the context of muscle cells, especially in cardiomyocytes, is of particular interest since the synthesis and secretion of proteins can be impaired during cardiac pathologies like ischemia, hypertrophy and cardiac infarct (Thuerauf *et al.*, 2006).

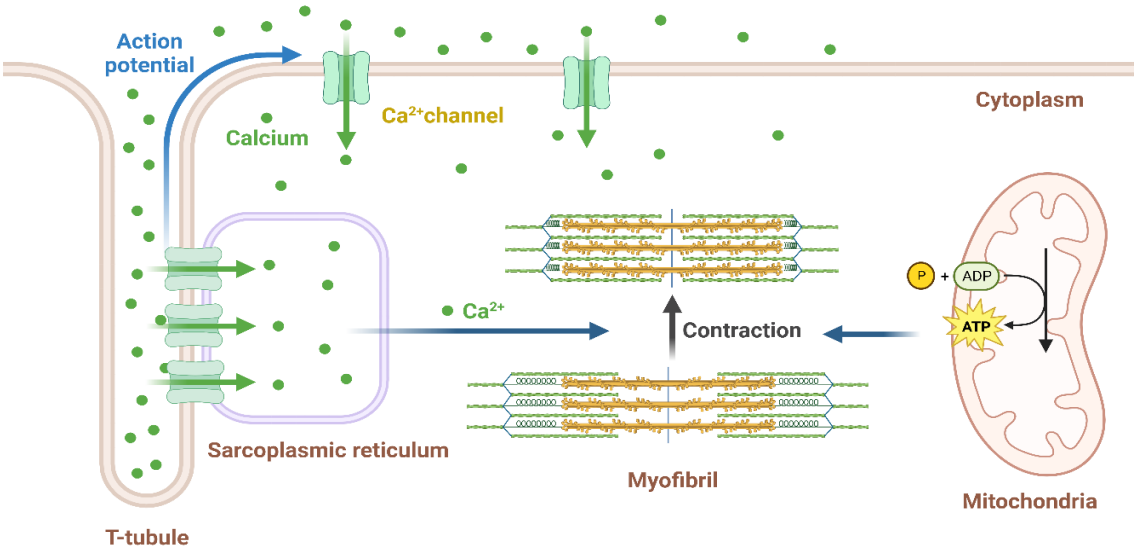

Figure 22: Structural characteristics of the cardiomyocyte. The cardiomyocyte is specialized in contraction, as such, its membrane, called sarcolemma, presents invaginations called T-tubules that aid in maintaining the action potential needed for contraction. These T-tubules are in direct contact with the ER, called sarcoplasmic reticulum in cardiomyocytes, where Ca^{2+} is pumped.

This specialized ER's protein load is especially heavy since the cardiac muscle needs constant production, folding and degradation of proteins involved in contraction, such as myosin. In the event of cardiac pathologies ER stress could be triggered, as it was demonstrated in *in vivo* experiments in mouse, and in cell cultured mouse myocytes (Thuerauf *et al.*, 2006); (Okada *et al.*, 2004); (Bousette *et al.*, 2010), disrupting the ER's normal functioning. Most importantly, as it will be discussed in the next section, researchers found that the cellular response to ER stress, also known as Unfolded protein response (UPR), leads to the restoration of homeostasis in cardiac cells. However, duration and strength of this response is crucial, as long activation of the UPR can lead to a maladaptive process instead to a survival-oriented one (Hetz, 2012); (Xu, Bailly-Maitre and Reed, 2005).

3.2 The ER stress and the Unfolded Protein Response (UPR)

Endoplasmic Reticulum Stress, or simply ER stress, is defined as the imbalance between the load of proteins that enter the ER and the capacity of the cell machinery to handle this load (Ron and Walter, 2007). Cells maintain homeostasis by activating a series of transduction pathways upon accumulation of misfolded proteins. The intracellular signaling pathway that mediates this regulation is called the Unfolded Protein Response (UPR). In the literature, UPR and ER stress response are often used interchangeably (Doroudgar and Glembotski, 2013).

The UPR is a time-dependent three-step process. First, there is a reduction of the protein load, this occurs within minutes of sensing the stress, and is a transient response. Second, there is an increased capacity to handle unfolded proteins, achieved by targeted gene expression that allows the degradation of accumulated proteins and transcription of specific UPR genes. Third, cell death will occur if it fails to recuperate homeostasis or if the stress takes place for too long, which activates cell-death related genes such as *CHOP* (Schröder and Kaufman, 2005); (Oakes and Papa, 2015).

These events are triggered by three ER stress transducers (identified so far): the inositol-requiring protein-1 (IRE1), activating transcription factor-6 (ATF6) and protein kinase RNA activated (PKR)-like ER kinase (PERK). These three transducers are ER transmembrane proteins with a lumenal part that senses misfolded protein, and a cytoplasmic part that transmits the information to the cytosol (Bernales, Papa and Walter, 2006); (Ron and Walter, 2007).

3.2.1 IRE1 branch

IRE1 was the first identified ER stress transducer. It is a transmembrane protein with two distinct domains: a lumenal domain whose function is to sense ER stress/misfolded proteins, and a cytoplasmic domain that contains a protein kinase domain. Upon recognition of misfolded proteins, IRE1 oligomerizes and trans-auto phosphorylates. The oligomerization mechanism will be discussed in a later section, as it is still a subject of debate (Zhou *et al.*, 2006); (Shamu and Walter, 1996).

Phosphorylation of IRE1 activates its dormant endonucleolytic activity, as well as it increases its affinity for nucleic acids. The substrate of this new effector activity is the *XBP1* (X-box binding protein 1) mRNA in metazoans (Calfon *et al.*, 2002), and *Hac1* (homologous to ATF/CREB1) in yeast. IRE1 cuts this mRNA twice, excising an intron. The resulting product is the *XBP1s* (s for spliced) mRNA, which codes for transcriptional factor XBP1s, an activator of UPR target genes. This factor triggers the transcription of chaperones, the transcription of ERAD proteins, and ER biogenesis. Ligation of the spliced mRNA in yeast is done by Trl1p (tRNA-ligase) (Sidrauski, Cox and Walter, 1996), however, the ligase in metazoans is still unknown. Studies in yeast indicate that this ligation is done closely to the ER membranes, due to the tight association of this mRNA to them (Ru *et al.*, 2001).

In yeast, *Hac1*, the unspliced form, cannot be translated, being the splicing of *Hac1* a key event in yeast UPR. In metazoans, however, *XBP1* and *XBP1s* are both translated and serve different functions throughout the UPR. *XBP1* translation product (XBP1u, u for unspliced) represses the activation of UPR genes, whereas XBP1s promotes the transcription of UPR genes. Moreover, *Hac1* and *XBP1* are also transcriptional targets of the UPR. In yeast, *Hac1* transcription is the main event triggered by severe protein misfolding that will in response promote the transcription UPR genes. In yeast this event is called the super-UPR (Leber, Bernales and Walter, 2004). In metazoans, levels of *XBP1* continue to rise even when the UPR is in decline, serving as a termination signal (Yoshida *et al.*, 2006) (figure 23).

IRE1 is also associated with the stress-induced Jun N-terminal kinase (JNK) and the cell death machinery, however, the importance and relevance of this pathway remains to be defined (Ron and Walter, 2007).

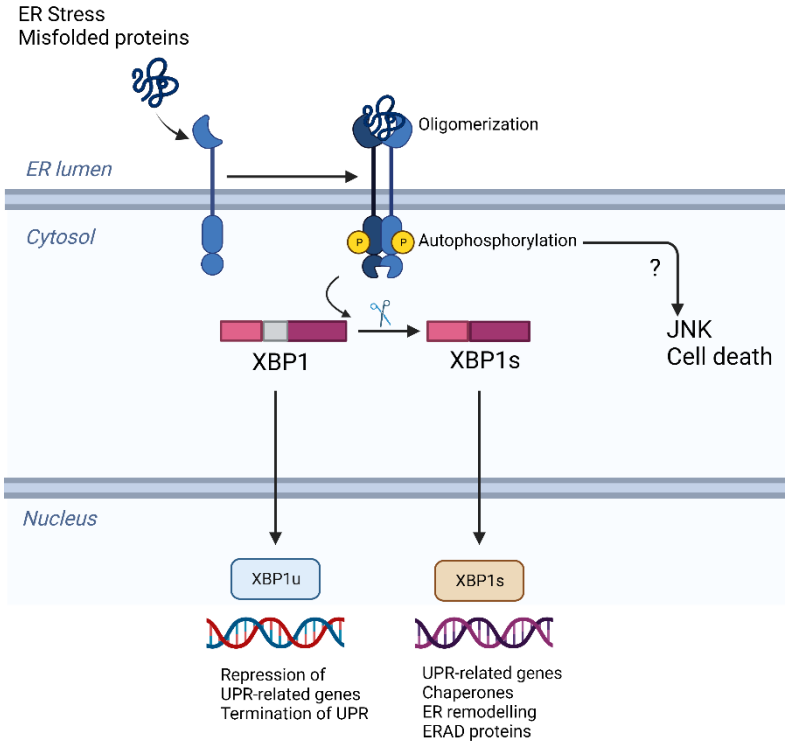

Figure 23: IRE1 signaling in ER stress. IRE1 oligomerizes upon recognition of misfolded proteins. IRE1 trans-autophosphorylates, increasing its affinity for nucleic acids, and activating its endonucleolytic activity. IRE1 will then cleave the XBP1(in metazoans, Hac1 in yeast). Cleaved XBP1, called XBP1s, is a transcription factor that activates UPR, ERAD, ER biogenesis related genes. XBP1u is the product of translation of non-spliced XBP1, and it has the function of inhibiting the UPR. This is not the case in yeast, where the non-spliced version of XBP1 homologue, Hac1, does not undergo translation. On an alternative route, phosphorylated IRE1 is associated with cell death mediated by JNK, although the complete process remains unknown.

3.2.2 ATF6 branch

Activating transcription factor 6 (ATF6) was discovered as a result of a wide-search study for metazoan ER-stress specific factors. This study focused on finding ER stress response elements (ERSE), a segment of DNA in the promoter region of genes tightly associated with the ER stress response (Yoshida *et al.*, 1998). Using yeast one hybrid screening, researchers were able to isolate ATF6, and then characterize it as a novel ER stress transducer (Haze *et al.*, 1999).

ATF6 is a transcription factor that requires processing by the same proteases as sterol response element binding proteins (SREBPs), such as CREBH (cyclic AMP-responsive element binding protein hepatocyte), which is also related to ER stress response by activating ER-stress related proteolysis (Zhang *et al.*, 2006). ATF6 is bound to the immunoglobulin binding protein (BiP), also known as GRP78 (78-kDa glucose-regulated protein). BiP is removed from ATF6 upon accumulation of misfolded proteins. This is followed by ATF6 translocation to the Golgi apparatus by an unknown mechanism. ATF6 is consecutively cleaved by S1P (site 1 protease) and S2P (site 2 protease), releasing the cytosolic DNA-binding portion of ATF6, ATF6f (ATF6 fragment) (Ye *et al.*, 2000). ATF6f acts as a transcription factor to UPR related genes, among them *XBP1*(Yoshida *et al.*, 2001) (figure 24).

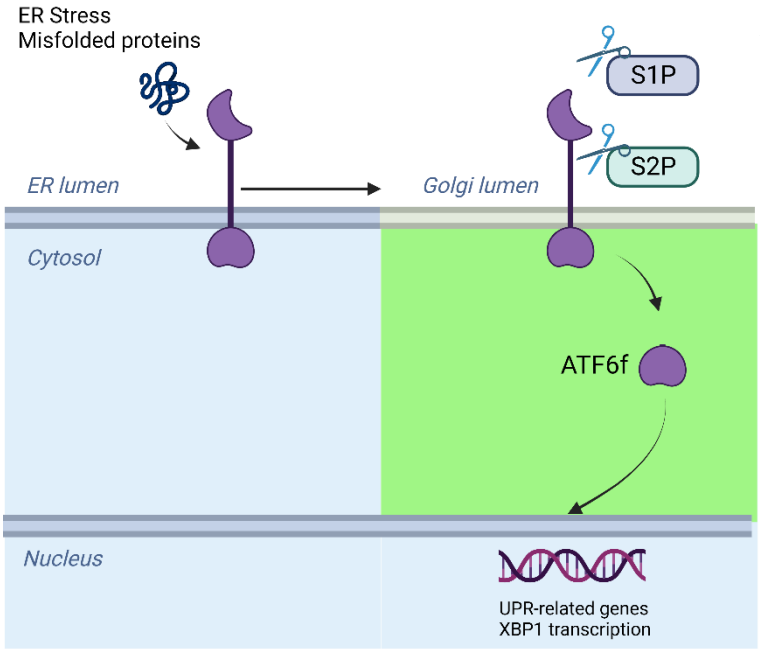

Figure 24: ATF6 signaling. ATF6 is a transcription factor that upon processing can promote the transcription of UPR-related genes. ATF6 is transported to the Golgi during ER stress conditions and processed first by S1P and then by S2P. The resulting fragment is the active form of the transcription factor, ATF6f.

3.2.3 PERK branch

This branch has the capability of regulating the ER stress both short-term and long term. PERK is structurally similar to IRE1 and also oligomerizes upon recognition of misfolded proteins and autophosphorylates. Unlike IRE1, whose sole substrate is itself, PERK phosphorylates eIF2α (figure 26) (Harding *et al.*, 1999). This has the immediate effect of lowering overall translation rates (as indicated in section 2.3.3), as eIF2α forms a very stable complex with eIF2B, its recycling factor. This reduces the immediate number of proteins that enter the already stressed ER (Hinnebusch, 2014); (Wek, Jiang and Anthony, 2006).

Reduced levels of active eIF2α-GTP will reduce overall levels of translation, however, it also allows the translation of alternative downstream ORFs. Several genes involved in the ER stress response are controlled by upstream ORFs (uORFs). These uORFs prevent the translation of UPR related factors unless the ER stress is triggered. There are several mechanisms by which uORFs prevent the translation of ER-related effectors. In this section I will focus on ATF4, a transcription factor, and the main effector of the PERK branch (Dever, Kinzy and Pavitt, 2016); (Dever,' *et al.*, 1992).

Almost 40% of mammalian genes contain uORFs. These uORFs prevent the expression of certain mRNAs unless certain conditions are met, such as the low availability of eIF2α-GTP triggered during ER stress. ATF4 has two upstream ORFs that regulate its expression, ORF1 and ORF2. ORF1 acts as a positive element that facilitates ribosome scanning and translation reinitiation at downstream regions of ATF4. When eIF2-GTP is abundant, the ribosome scanning downstream of ORF1 will be able to reinitiate translation in ORF2. ORF2 overlaps out of frame with ATF4 coding sequence (CDS), blocking ATF4 expression. During stress conditions, eIF2-GTP availability is reduced which increases the time required for the ribosome to become competent and reinitiate translation. Instead of restarting at ORF2, the ribosome restarts translation at the ATF4 coding region (figure 25) (Vattem and Wek, 2004). ATF4 allows the transcription of amino acid transporters, genes related to the antioxidant response, XBP1; which leads to the transcription of chaperone genes, and CHOP (C/EBP homologous protein) (Wek, Jiang and Anthony, 2006).

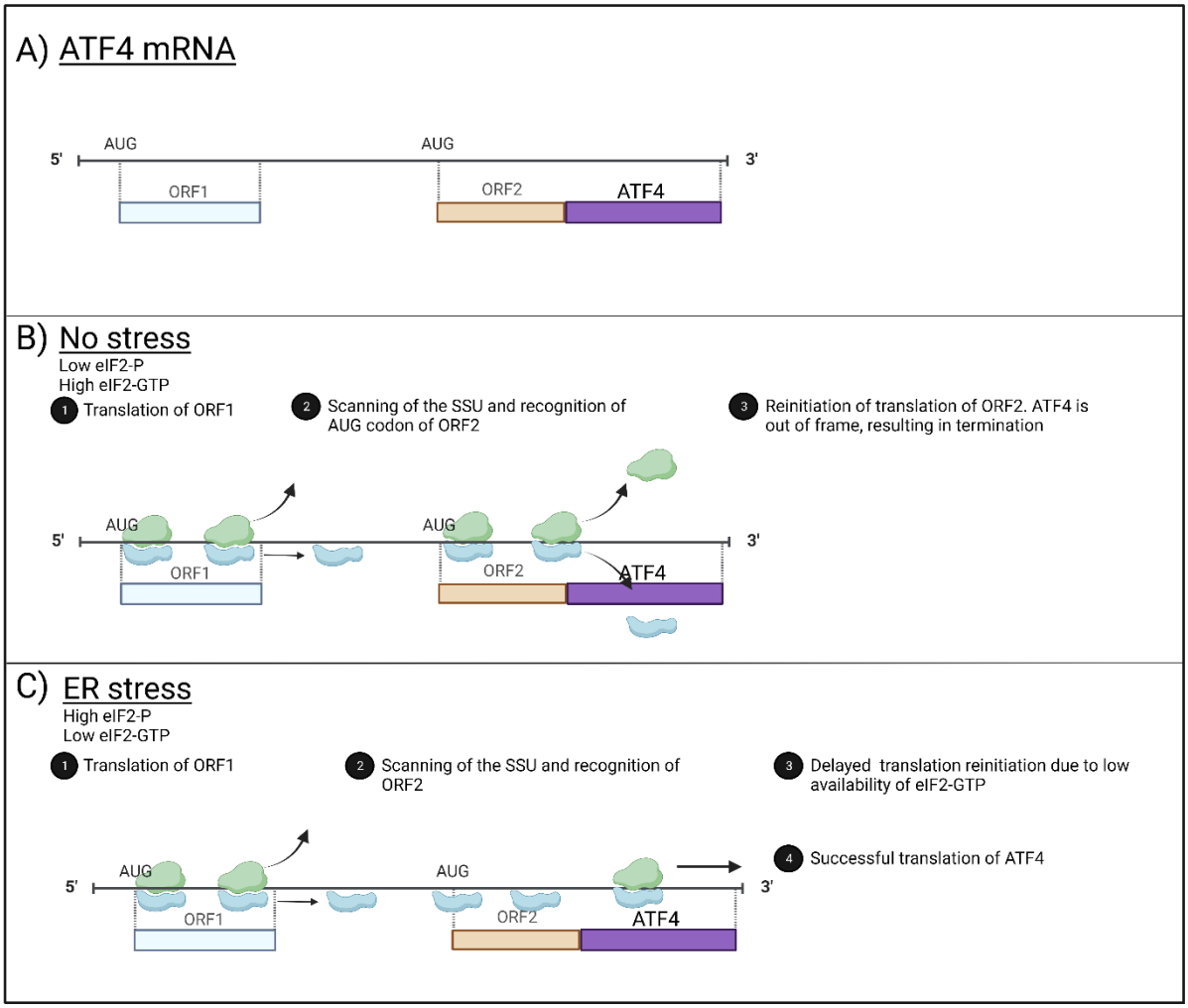

Figure 25: Control of ATF4 expression via uORFs. A) Overview of the ATF4 mRNA. ORF1 codifies for a small peptide, whereas ORF2 is continuous to ATF4 CDS. B) During non-stressful conditions, meaning eIF2-GTP is highly available, the ribosome will scan ORF1, translating this first small product, and will continue to scan until ORF2, where it will immediately restart translation by acquiring another eIF2-GTP molecule. Starting at this point is out of frame of ATF4. This leads to the ribosome terminating translation. C) Under stress conditions the ribosome will start translation of ORF1 but will continue to scan further down ORF2, as high phosphorylation levels decrease the availability of eIF2-GTP, slowing the acquisition of another eIF2-GTP molecule. This delayed restart of translation allows for the correct in frame translation of ATF4.

CHOP is a transcription factor that enables the transcription of GADD34 (growth arrest and DNA damage-inducible protein-34), which is a regulatory subunit of phosphatase complex PP1. PP1 dephosphorylates eIF2α and makes it available to the translation machinery to resume translation as usual, diminishing the translation rates of alternative ORFs and recuperating the non-stressed translational status(Wek, Jiang and Anthony, 2006); (Eva, 2022) (further explained in section 3.3.2). CHOP also promotes the transcription of *ERO-1* (ER oxidase-1), which aids in the formation of disulphide bonds.

PERK related ER stress activation is swiftly reversible, with PERK being dephosphorylated within minutes of a successful response. This negative regulation of PERK's activity is given by both dephosphorylation of PERK and eIF2α. However, prolonged signaling will result in the transcription of cell death related genes (Marciniak *et al.*, 2004).

eIF2α phosphorylation is conserved among eukaryotes, and its phosphorylation and dephosphorylation are tightly controlled. Depending on the stress, eIF2α will be phosphorylated by different kinases (Donnelly *et al.*, 2013). The array of pathways that finalize in eIF2α phosphorylation is called the intrinsic stress response (ISR) and will be discussed in coming sections.

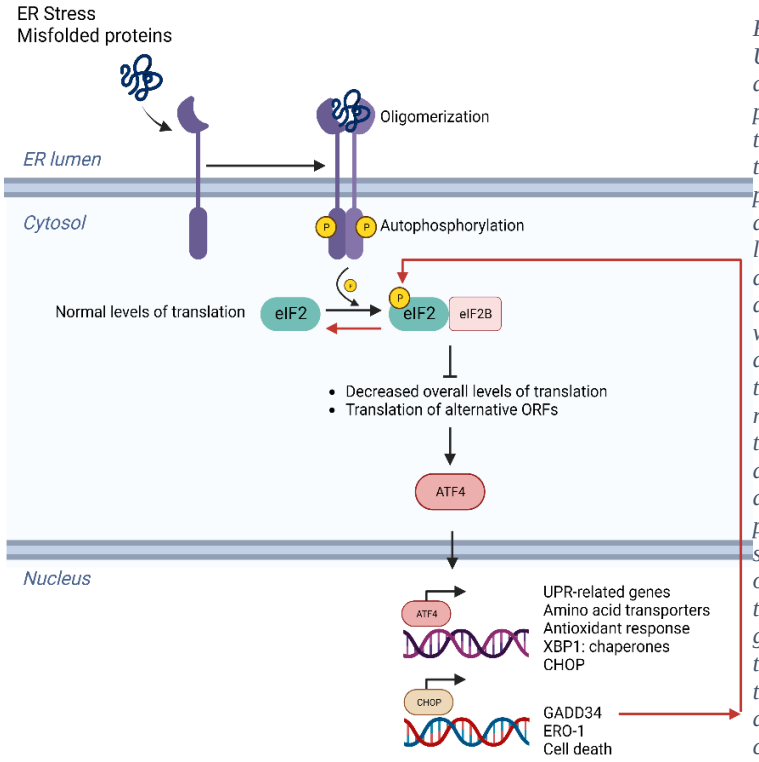

Figure 26: PERK branch of the UPR. Upon oligomerization, PERK autophosphorylates and then phosphorylates eIF2α. eIF2α is part of the eIF2 heterotrimer, crucial for translation initiation. Its phosphorylation causes an increase of affinity with its recycling factor eIF2B, locking it in place and reducing eIF2α availability to the ribosome. This causes decrease overall levels of translation, which immediately relieves the ER from a constant protein load, and promotes translation of alternative ORFs, as the ribosome keeps scanning and bypasses the initial AUG, in favor of more downstream AUGs (until it finds an active eIF2). Among the translated proteins there is ATF4, which specifically promotes the transcription of UPR-related genes, amino acid transporters, antioxidant response genes, XBP1 and CHOP. CHOP is a transcription factor that promotes the transcription of GADD34, which associates with PPIc (crating the PP1 complex) and dephosphorylates eIF2α, acting as a negative feedback effector of the response. However, if the response continues, CHOP will also continue the

3.2.4 Misfolded protein recognition in the ER stress response by IRE1 and PERK

The matter of how these two effectors recognize misfolded proteins is still being discussed to this day. There are three different proposed models for this recognition: 1) direct misfolded proteins interact with IRE1/PERK, 2) release of the immunoglobulin binding protein (BiP) that is constitutively bound to IRE1/PERK upon accumulation of misfolded proteins, 3) a hybrid model (Ron and Walter, 2007) (figure 27).

IRE1 and PERK are evolutionary related and experimentally interchangeable (Zhou *et al.*, 2006). 1) In favor of the first model, the IRE1 lumenal domain has some resemblance to the peptide-binding domains of major histocompatibility complexes (MHC), making it possible to interact with misfolded proteins. 2) The second model proposes that BiP is found associated to IRE1 and PERK. It is theorized that BiP, as a chaperone, will most likely bind to unfolded proteins, liberating both IRE1 and PERK, allowing them to oligomerize (Shamu and Walter, 1996); (Kouzarides *et al.*, 2004). 3) Finally, a recent study further explained BiP function in the recognition of misfolded proteins, putting the focus on BiP double function both as a chaperone and an ER stress signaling effector. According to the authors, BiP is sequestered by IRE1 and PERK in its ATP-bound form and it is only upon recognition of misfolded proteins by BiP that it can be released and its chaperone function triggered (Kopp *et al.*, 2020).

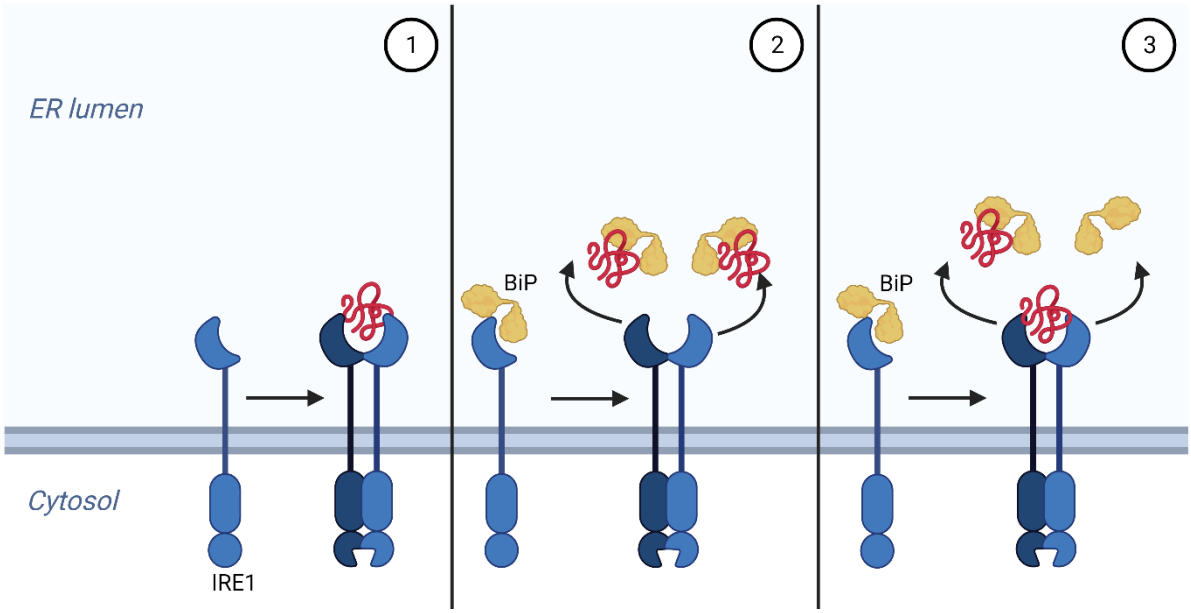

Figure 27: Misfolded protein recognition by IRE1 and PERK. There are three proposed mechanisms by which IRE1/PERK recognize ER stress. The first one proposes a direct recognition of misfolded proteins by the lumenal domain of IRE1/PERK, which triggers dimerization of the transducer. The second one proposes a recognition mediated by chaperone BiP, that will release IRE1/PERK upon misfolded protein recognition and enable its dimerization. The last one proposes a hybrid system, in which both misfolded protein recognition by IRE1/PERK is possible, as well as BiP release upon recognition of misfolded proteins.

3.2.5 ER stress termination: survival and death

Upon detection of misfolded proteins, the three branches of the UPR work simultaneously to reduce the protein load and recuperate homeostasis. The ATF6 and IRE1 branches trigger the transcription of factors that are involved in protein degradation, ER remodeling and chaperone translation. The PERK branch lowers the protein load by reducing translation rates, via eIF2α phosphorylation, and allows the translation of alternative ORFs, translating factors related to the UPR response, among them ATF4, a key transcription factor of UPR genes.

The removal of misfolded proteins in the ER is a key event to ensure homeostasis. This is achieved, among other mechanisms, by the ERAD (ER associated protein degradation), which mediates the translocation of misfolded proteins from the ER to the cytoplasm, thus lowering the transducers' activation. Translation of chaperones also aids in this endeavor, as well as remodeling of the ER architecture. The production of phospholipids is increased as part of the IRE1/XBP1 branch, increasing the ER surface and decreasing ER stress. However, this might not be enough to reduce stress levels.

Severe protein misfolding might lead to protein aggregates, which are difficult to degrade. Cells have developed a special kind of autophagy, called ER-phagy, in which ER membranes are sequestered in tightly packed autophagosomes. It was shown that sequestering oversaturated ER membranes was enough to reduce ER stress. These membranes do not need to be degraded to reduce ER stress, their isolation from the active ER seemed to be enough to reduce the overall protein load. This mechanism is the preferred survival mechanism in cell-types where apoptosis would lead to the depletion of a specific cell pool, such as cardiomyocytes, who cannot be replaced (Tabas and Ron, 2011); (Ron and Walter, 2007); (Chipurupalli, Samavedam and Robinson, 2021); (Doroudgar and Glembotski, 2013); (Mehanna *et al.*, 2022).

The ER stress response activates both pro-survival and pro-apoptotic factors. Pro-survival factors, as explained above, will aim to reduce protein accumulation, however, pro-apoptotic factors are produced at the same time, such as CHOP. When the level of pro-apoptotic factors exceeds the death threshold, cell death via apoptosis is triggered (Rutkowski *et al.*, 2006) (figure 28).

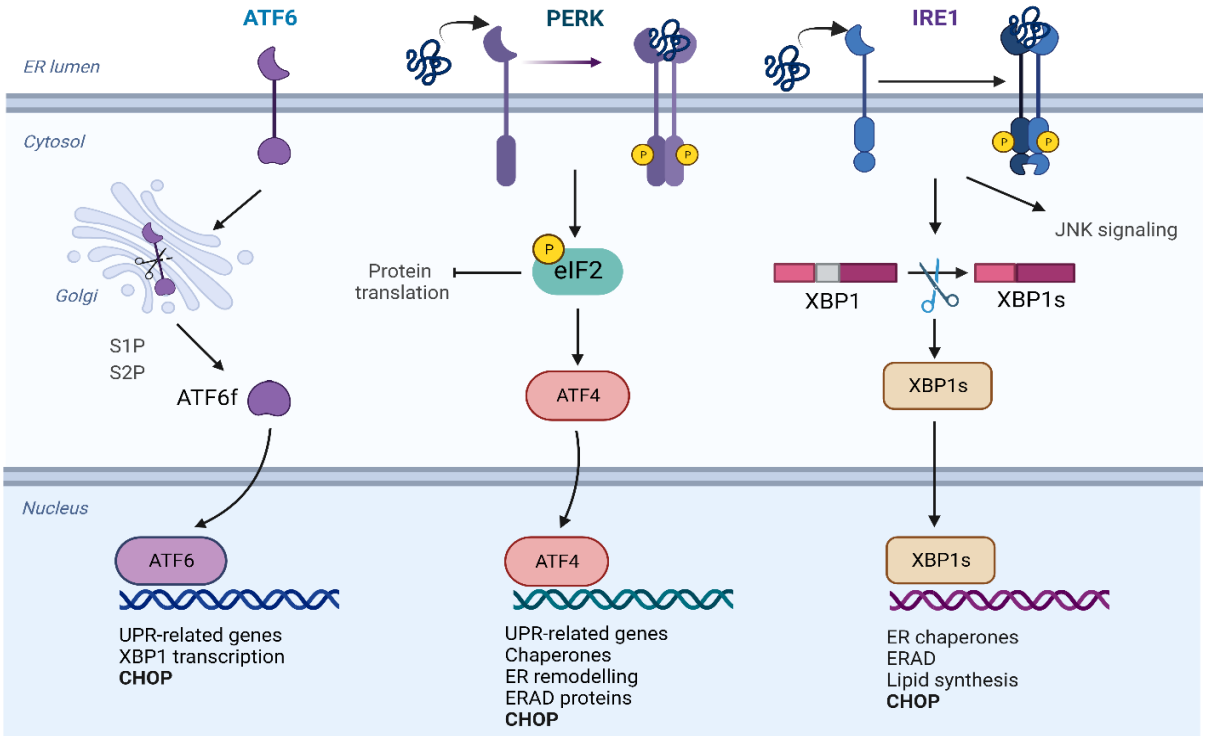

Figure 28: Schematic view of the three branches of the UPR. All of them end up with the production of CHOP when the ER stress response is prolonged.

CHOP is a leucine zipper-containing transcription factor regulated by the three UPR pathways. It promotes the transcription of UPR-related genes, as well as GADD34, which recruits PP1c and dephosphorylates eIF2α. However, prolonged activation of CHOP leads to the activation of pro-apoptotic factors such as caspase 12 (Scheuner *et al.*, 2001). Moreover, deletion of CHOP has been shown to be protective, whereas deregulated CHOP promotes cell death as it is directly linked to cell death effectors, such as BCL-2 (Cullough *et al.*, 2001).

The complex balance between pro-survival and pro-apoptotic factors is illustrated by the role of eIF2α phosphorylation. Reduced amounts of eIF2 lead to translation of alternative ORFs, specifically the translation of the ATF4 transcription factor. ATF4 will promote the transcription of pro-survival factors, but it ultimately leads to the

transcription of CHOP, triggering apoptosis if ER stress is not reduced (Wang and Kaufman, 2016) (figure 29).

Dephosphorylation of eIF2α needs to occur at an appropriate time. If active eIF2α levels are restored before the misfolded protein load is reduced, the ER stress will continue and will inevitably lead to cell apoptosis. It has been shown that pre-emptive phosphorylation of eIF2α protects against ER stress, however, other studies show that eIF2α dephosphorylation is crucial to recuperate the normal protein cell expression program (Novoa *et al.*, 2003).

The importance of eIF2α phosphorylation is not reduced to ER stress. Other environmental and cellular stimuli induce eIF2α phosphorylation, putting eIF2α in a central spot of the cellular stress regulation.

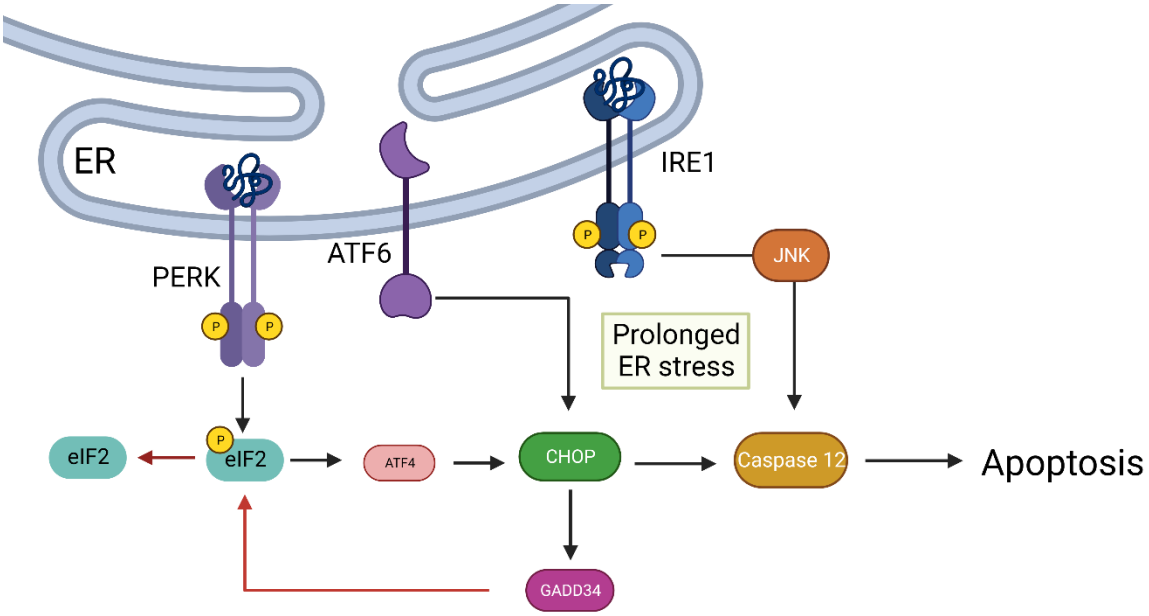

Figure 29: Apoptosis is triggered due to prolonged ER stress. The transcription factor CHOP will trigger the translation of caspases which leads to apoptosis. CHOP also induces the transcription of GADD34 that ultimately causes the dephosphorylation of eIF2α. Dephosphorylation under conditions where the ER stress has been overcome will lead to a normal resume of translation, however, if it occurs too early, resuming of normal translation will increase the protein load in the stressed ER.

3.3 The Integrated Stress Response

In response to cellular stresses and environmental stimuli, cells can activate a common restorative pathway to restore cellular homeostasis, the Integrated Stress Response (ISR). The core of this response is the phosphorylation of eIF2α, and like the ER stress response, it leads to a decrease of protein synthesis and induction of selected genes, particularly ATF4. The activation of ATF4 leads to a final cellular recovery or

apoptosis (Pakos-Zebrucka *et al.*, 2016). In a similar manner to the ER stress response, ISR is primarily a pro-survival program but exposure to severe stress can lead to programmed cell death. The ISR is triggered depending on the cellular context and the nature and intensity of stress stimuli (Meurs and Esteban, 2007).

ISR is activated by different pathological conditions, which can be external such as hypoxia, amino acid deprivation, glucose deprivation and viral infection; or internal, such as accumulation of unfolded proteins and oncogene activation (Wek, Jiang and Anthony, 2006); (Dever and Green, 2012). All these stimuli lead to the phosphorylation of eIF2α on serine 52 by four different Serine/Threonine kinases: PERK, mentioned in previous sections, GCN2 (general control nonderepressible 2, highly conserved in yeast and metazoans) (Berlanga and Santoyo, 1999), PKR (Protein kinase RNA-activated) and HRI (heme-regulated inhibitor).

One of these kinases is PERK, which has its own branch in the ER stress response. Whereas the ER stress response/UPR is a well-established cellular response to protein misfolding and accumulation, the ISR is rather a collection of pathways which all lead to the phosphorylation of eIF2α in response to different stimuli. According to this classification, the PERK branch of the ER stress response would be included in the ISR, but not the IRE1 nor the ATF6 branches.

3.3.1 eIF2α kinases:

There are four kinases that phosphorylate eIF2α depending on the environmental and physiological stimuli the cells are subject to: PERK, PKR, HRI and GCN2 (Donnelly and Gorman, 2013); (Wek, Jiang and Anthony, 2006). These four kinases belong to the eIF2α protein kinases family (EIF2AKS). Structurally they are divided into two domains: a regulatory one, that detects the stress stimuli, and the kinase domain. The kinase domains are highly similar and dimerize in a similar manner (Ramirez, Wek and Hinnebusch, 1991); (Meurs *et al.*, 1990). The kinase domain for the EIF2AKS family is composed of an N-lobe and a C-lobe as seen in figure 30. The N-lobe is responsible for monomer interaction, and the C-lobe is responsible for phosphorylation. The switch between the active and inactive form due to dimerization is conserved not only in the EIF2AKS family, but also in other families, including that of the IRE1 kinase, which lies adjacent to the EIF2AKS family (figure 31) (Lavoie *et al.*, 2014).

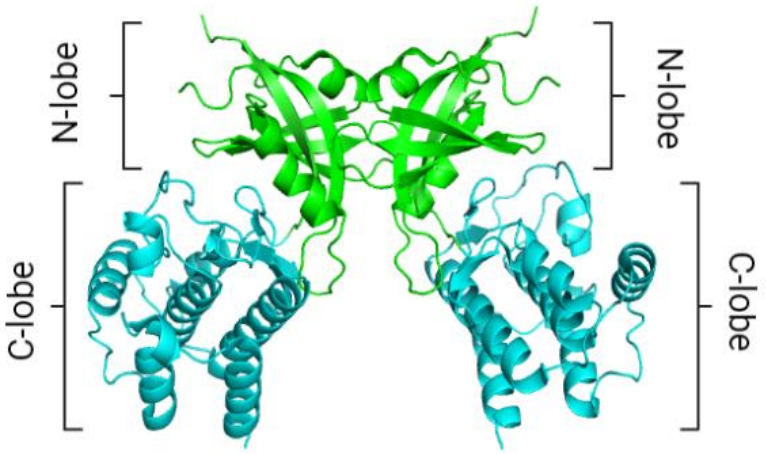

Figure 30: PKR dimer PDB (2A1A) back-to-back conformation. This conformation is common to all the EIF2AKS and IRE1. These kinases present two lobes, and N-lobe, with which the interaction occurs between monomers, and a C-lobe, where the phosphorylation of eIF2α happens in the case of the EIF2AKS. In the case of IRE1, the autophosphorylation permits the activation of the RNase domain and the cleavage of XBP1.

Upon dimerization the kinases adopt a back-to-back orientation with the active site facing outwards (Dey *et al.*, 2007). The interaction surface between monomers is conserved among the members of this family. IRE1 also presents the same back-to-back dimerization pattern, however, this dimerization rather regulates a RNase domain located just after the C-lobe (Mhatre V. Ho, Ji-Ann Lee and Dien et al., 2008) (figure 31).

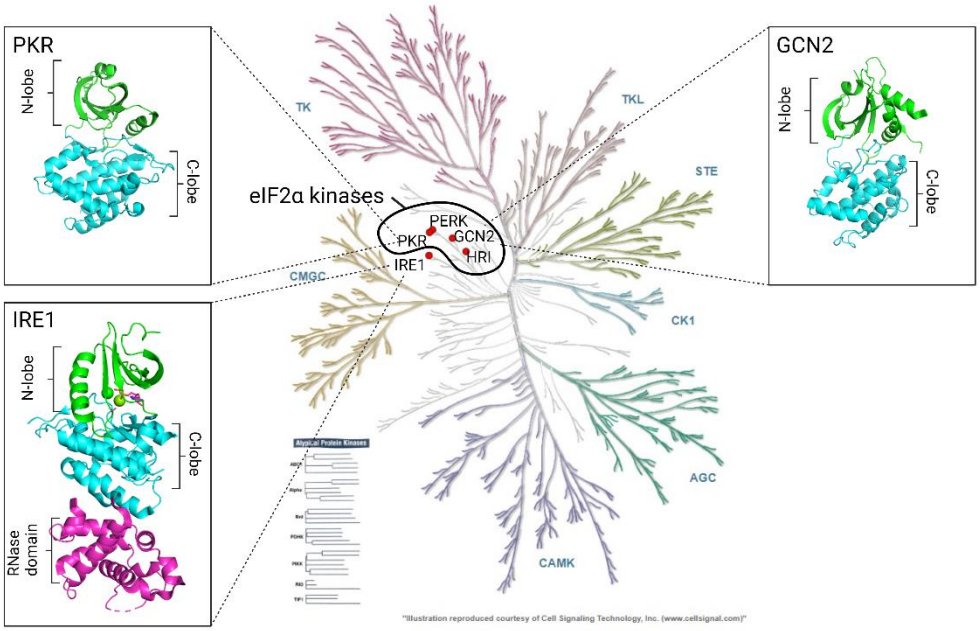

Figure 31: eIF2α kinases and IRE1 domains and positioning in the kinome tree. Many kinases regulate their function by activating its kinase domain upon dimerization. eIF2α kinases and IRE1 are such the case. Dendrogram courtesy of Cell Signaling Technology, Inc. PDB: PKR (2A1A), GCN2 (1ZYC), and IRE1 (2RIO).

3.3.1.1 GCN2: amino acid deprivation

GCN2 is highly conserved from yeast to human. It is a cytoplasmic protein and the only eIF2α kinase in yeast (Berlanga and Santoyo, 1999); (Zaborske *et al.*, 2009), and it is known to be in control of the amino acid deprivation response (Castilho *et al.*, 2014). Studies in yeast show that GCN2 binds to deacylated transfer RNAs (uncharged tRNAs) via a histidyl-tRNA synthetase-related domain, thus detecting low amino acid levels (Vazquez de Aldana *et al.*, 1994).

It has also been implicated in diseases such as cancer and Alzheimer. GCN2 is activated in response to prolonged glucose deprivation in tumor cells, probably due to the consumption of amino acids instead of glucose (Ye *et al.*, 2010). On the other hand, GCN2 function has been associated with synaptic plasticity and hippocampal memory, making it a research target of neurodegenerative disorders (Castilho *et al.*, 2014).

This kinase has also been observed to be activated by UV light in MEF cells and human keratinocytes. This model remains unclear and there are two models, one which proposes that the response is due to tRNA crosslinking with GCN2, and another which

proposes that GCN2 is activated due to the rapid consumption of arginine due to UV activation of nitric acid (Ye *et al.*, 2010).

In yeast, phosphorylation of eIF2α by GCN2 leads to the translation of GCN4 in a similar manner to that of ATF4. Phosphorylation of eIF2α and decrease of available eIF2-GTP leads to bypass of uORFs and allows translation of GCN4 (Young and Wek, 2016).

3.3.1.2 HRI: heme deficiency

HRI is found in the cytoplasm. This kinase is specific to erythroid cells and it's involved in erythrocyte differentiation during erythropoiesis (Han *et al.*, 2001). It is one of the few examples of tissue-specific translational control of gene expression. Biochemical studies suggested that post-translational control of gene expression in mammals existed, but there was lacking evidence in the matter. In a study performed in 2001 (Han *et al.*, 2001), they showed that kinase HRI, regulated the synthesis of both α and β globin precursors in red blood cells by inhibiting translation via the phosphorylation of eIF2α.

HRI couples the translation of goblin mRNAs with the availability of heme to produce hemoglobin, protecting erythroid cells against the accumulation of toxic globin aggregates in iron deficiency (Suragani *et al.*, 2012). Regulation of HRI kinase activity by heme is mediated by the two heme binding domains that are in the N-terminus and the kinase insertion domain (Rafie-Kolpin, Han and Chen, 2003).

HRI, although mostly tissue-specific and related to heme production, is activated during many different stresses, such as arsenite-induced oxidative stress, heat shock, osmotic stress among others (Ramos-Fernández *et al.*, 2016); (McEwen *et al.*, 2005).

3.3.1.3 PKR: viral infection

PKR is a central component of the innate antiviral response. It is found in the cytoplasm, nucleus, and the perinuclear region of the cytoplasm. This kinase recognizes double stranded RNA (dsRNA) (Clemens and Elia, 1997). Like the other members of the EIF2AKS, it has a regulatory domain and a kinase domain. The regulatory domain specifically recognizes dsRNA over any other ribonucleic molecule, but it does so without any sequence specificity (Bevilacqua and Cech, 1996). The kinase domain presents the typical N-lobe and C-lobe structure explained in previous sections.

It is theorized that two monomeric PKR are brought together by the binding of the same dsRNA, triggering the dimerization of its C-terminal kinase domain and the phosphorylation of several serine, threonine and tyrosine residues (Lemaire *et al.*, 2008). Studies by Lemaire et al, showed that length of this dsRNA is crucial for the appropriate activation of PKR.

Activation of PKR inhibits viral and host protein synthesis through eIF2α phosphorylation, via the mechanisms explained in previous sections. The importance of PKR in the antiviral defense is evidenced by the large number of viruses that encode PKR inhibitors (Langland *et al.*, 2006).

Interestingly, PKR is involved in sustaining ER stress-induced apoptosis (Lee *et al.*, 2007). The involvement of PKR is not directly related to the accumulation of misfolded proteins; however, it is known to be activated by the PKR activating protein (PACT).

ER stress can also be caused by redox stress, notably due to a calcium imbalance. The ER is the major calcium storage organelle in the cell, and ER stress can cause a release of Ca^{2+}. Calcium spillage to the cytoplasm causes the activation of PACT, which in return activates PKR and increases eIF2α phosphorylation and ATF4/CHOP activation (Lee *et al.*, 2007), further pushing towards an apoptotic outcome.

Calcium homeostasis in the ER is crucial to maintain not only the cell's Ca^{2+} stock, but also to ensure the appropriate redox balance in the ER, and the activation of chaperones, as a great number of them require Ca^{2+} (Schwarz and Blower, 2016). This redox imbalance and the lack of functioning chaperones will add to the number of misfolded proteins, activating the PERK pathway and causing phosphorylation of eIF2α, which will lead to ATF4/CHOP activation (Xu, Bailly-Maitre and Reed, 2005). Both pathways combined increase the chances of a final apoptotic result.

Even though these pathways are described in a linear and sequential manner, most of them are influenced by others, like explained just above. The different pathways cannot be isolated from each other, because even though they are activated in different manners, their activation directly impacts cell fate.

3.3.2 Termination of ISR:

Termination of this response is caused by dephosphorylation of eIF2α. Dephosphorylation of eIF2α leads to the restoration of protein synthesis and normal cell functioning. eIF2α dephosphorylation is mediated by protein phosphatase 1 (PP1) complex, which recruits PP1 catalytic subunit (PP1c) and one of the two regulatory subunits: GADD34 (see in section 3.2.3) and constitutive repressor of eIF2α-P (CReP). These two proteins are paralogues, also known as PPP1R15A and PPP1R15B (protein phosphatase 1 regulatory subunit 15A and B).

CReP bound to PP1c dephosphorylate eIF2α in unstressed cells, sustaining translational homeostasis by maintaining low levels of phosphorylated eIF2α (Jousse *et al.*, 2003). In contrast, GADD34-PP1 dephosphorylates eIF2α in stressed cells to restore protein synthesis once the ER stress has been resolved, aiding in cell survival (Marciniak *et al.*, 2004); (Ma and Hendershot, 2004). Both CReP and GADD34 contain a PP1c binding motif (RVxF) as well as an eIF2α binding motif (RxGx-WxxxAxDRxRFxxRI) that allows them to bind eIF2α in a PP1c-independent manner (Rojas, Vasconcelos and Dever, 2015) (figure 32).

Interestingly, dephosphorylation of eIF2α in yeast is not controlled by GADD34 or CReP, as there are no homologs of these two proteins in yeast. Dephosphorylation by the PP1c homolog in yeast, GLC7, is controlled by an N-terminal extension of yeast eIF2γ. This extension contains a PP1 binding motif (KKVAF), which enable the recruitment of GLC7 and the dephosphorylation of eIF2α (Rojas, Gingras and Dever, 2014).

ISR is also terminated upon cell death when the cells are not able to overcome the stress. Maintained phosphorylation of eIF2α facilitates the execution of cell death when cellular homeostasis cannot be restored, by allowing the synthesis of death-inducing proteins and the CHOP transcription factor that leads to the activation of pro-apoptotic routes (Novoa *et al.*, 2003); (L. Liu *et al.*, 2015).

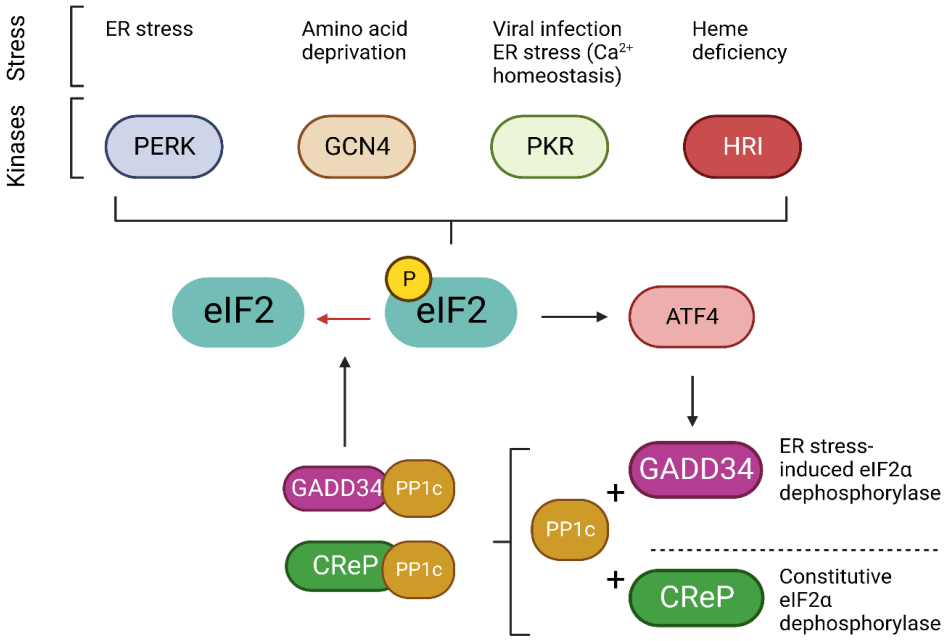

Figure 32: eIF2α kinases and dephosphorylation.

3.4 Importance of eIF2α phosphorylation in cell regulation, survival, and human pathology:

As stated above, phosphorylation of eIF2α on serine 52 is a key event in the UPR and in the ISR. These two pathways are activated in response to environmental and cellular stresses. It is no surprise that eIF2α phosphorylation regulation plays a crucial role in disease and development.

Several studies have been performed regarding phosphorylation of eIF2α and disease. For example, homozygotic mutations (S52A) at this site preventing eIF2α phosphorylation, permist normal mRNA translation even under ER stress or glucose deprivation in mice embryos (Scheuner *et al.*, 2001). These mice, however, die shortly after birth due to prolonged hypoglycemia, highlighting the importance of translation initiation regulation in glucose metabolism (Back *et al.*, 2009). The same study shows that eIF2α phosphorylation is crucial for sustaining proper physiological function of liver and pancreas after birth, as phosphorylation in eIF2α is required for the induction of gluconeogenic enzymes and insulin (Scheuner *et al.*, 2001)

Homozygotic S52A eIF2α mouse embryonic fibroblasts (MEF) are hypersensitive to ER stress and require supplementation of nonessential amino acids and reductive agents, showing that eIF2α phosphorylation protects against metabolic oxidative stress.

Cultured cells containing homozygotic S51A mutation are unable to induce autophagy upon viral infection, starvation, and ER stress (Kouroku *et al.*, 2007), increasing levels of apoptosis.

Apoptosis levels need to be controlled in specific tissues where cell renewal is not possible, such as the heart. The cardiac tissue is subject to extensive ER stress and several cardiac diseases have been linked to this stress. Tight control of the PERK/eIF2α pathway has been shown to favor ER-phagy and restoration of cell homeostasis instead of apoptosis in cardiac cells (Okada *et al.*, 2004); (Xin Wang *et al.*, 2017).

3.5 ER stress and cardiovascular diseases:

ER stress has been linked to the pathogenesis of cardiovascular diseases, such as cardiac hypertrophy, heart failure, and ischemic heart disease, among others (Xin Wang *et al.*, 2017).

In the case of cardiac hypertrophy and heart failure, it was found that affected hearts ER were overloaded by enhanced protein synthesis, oxidative stress, and hypoxia. Interestingly, the BiP chaperone levels were increased in patients with heart failure, suggesting an involvement of the UPR in the pathology (Okada *et al.*, 2004). The involvement of CHOP, the pro-apoptotic transcription factor, was extensively studied in Knock out (KO) CHOP mice and wild-type (WT) mice, finding that $CHOP^{-}$ mice were protected against apoptosis in the case of prolonged ER stress (Fu *et al.*, 2010). CHOP and IRE1 were also found to be increased in alcohol-induced heart failure (Li *et al.*, 2009).

The PERK/eIF2α pathway was demonstrated to play a cardioprotective role in heart failure. In PERK KO heart, the expression of CHOP was increased in response to stress, indicating that CHOP-induced apoptosis had a key role in heart failure (X. Liu *et al.*, 2015). Interestingly, the balance between phosphorylated and dephosphorylated eIF2α plays a critical role in heart failure in *in vivo* models, where eIF2α phosphorylated levels remained increased, but not CHOP (Li *et al.*, 2015).

Ischemia is a perfect example of the time-dependent functionality of the ER stress response. The UPR is activated in the early stages of ischemia, showing early expression of XBP-1, eIF2α and ATF6. The expression of these factors leads to a reduction in protein translation and the activation of UPR-related genes that direct the cellular program towards restoring ER homeostasis and protein folding. However, if this response takes

place for too long, apoptotic factors, such as CHOP, will shift the response towards an apoptotic program (Martindale *et al.*, 2006).

Activation of the PERK branch is an early event in ischemia. Phosphorylation levels of eIF2α immediately increase, and overexpression of PERK promotes cell survival under hypoxic conditions, whereas its knock down (KD) leads to a decrease in cell viability (Lu, Harding and Ron, 2004). However, as beneficial its early activation can be, prolonged activation of this branch leads to the transcription of CHOP and apoptosis.

It is no surprise that ER stress modulation in cardiac cells has become a new focus of study. The development of drug therapies targeting the three branches of the UPR has increased in the last decade, always aiming to reducing levels of apoptosis (Wang and Kaufman, 2016); (Minamino and Kitakaze, 2010). The heart tissue renewal is a matter of debate, as the existence of cardiac stem cells in the adult heart is still in question. However, what is known is that the heart's self-repairing capacity is minimal. Instead, cardiomyocyte apoptosis leads to the replacement of cardiac cells by fibroblasts, which create scar tissue in the heart, reducing its general pumping capacity (Mehanna *et al.*, 2022).

3.6 Modulation of the ER stress response:

A branch of compounds called sirtuin activating compounds (STACs), activate SIRT1, a NAD^+-dependent deacetylase. These compounds were shown to have a cardioprotective effect in cardiomyocytes and *in vivo* models, but it is only recently that it was shown that they do so by reducing ER stress-induced apoptosis. A study using adult-inducible SIRT1 KO mice showed that SIR1 inhibition or deficiency increases ER stress-induced injury, whereas activation of SIRT1 by activating compounds (such as STAC-3) is protective (Kouzarides *et al.*, 2004).

A possible connection between SIRT1 and the PERK pathway was made when it was discovered that SIRT1 interacted with eIF2α (Ghosh, Reizis and Robbins, 2011). In this study, researchers found out that SIRT1 was crucial for regulating eIF2α phosphorylation levels. In SIRT1-depleted cells, phosphorylation levels were maintained and elevated, which shut off protein expression and interferes with the expression of downstream stress genes such as GADD34 (Kojima *et al.*, 2003). Researchers also showed that association with eIF2α was independent of SIRT1's deacetylase activity (by using a catalytic-center mutant), leaving the question of how does SIRT1 modulate eIF2α

phosphorylation levels in the dark. By using a catalytic variant of SIRT1, researchers suggested that SIRT1 deacetylase activity was not necessary for binding eIF2α. In this study, they also showed that SIRT1 also interacts with GADD34 and CReP independently from eIF2α. Thus, the authors suggested that SIRT1 may regulate eIF2α phosphorylation levels through its binding to these two regulatory proteins.

Studies of the role of SIRT1 in the regulation of eIF2α phosphorylation levels was stalled until our collaborators showed that eIF2α is indeed acetylated in cardiac cells (Prola *et al.*, 2017). This raised the questions of whether eIF2α deacetylation by SIRT1 has any effect in ER stress levels, and since SIRT1 is an interesting pharmacological target, whether the ER stress response could be modulated using STACs.

3.6.1 eIF2α deacetylation protects against ER stress-induced apoptosis:

Finding that eIF2α is also acetylated, and that this acetylation has a role in ER stress response, was an important step forward into understanding the SIRT1—eIF2α—ER stress dynamic. Our collaborators from Christophe Lemaire's lab showed that eIF2α is acetylated in lysines 141 and 143, and that SIRT1 activation by STACs led to cardiomyocyte rescue from ER stress.

Using the H9c2 cardiomyocyte cell line they were able to prove that by activating SIRT1 with STAC-3, both phosphorylation and deacetylation levels of eIF2α were lowered. Interestingly, depletion of SIRT1 led not only to increased levels of acetylation but also to increase phosphorylation levels (Ghosh, Reizis and Robbins, 2011). To further study the correlation between acetylation and phosphorylation, our collaborators also measured phosphorylation levels using a variant eIF2α K143R, which mimics eIF2α deacetylated state. This mutation confers protection against ER stressed-induced apoptosis. They compared the effects of the K143R mutation to the S52A, which mimics dephosphorylation, finding that both conferred similar levels of protection against ER stress (levels were comparable when the mutations were performed separately and together) (figure 33). Interestingly, no protection was observed with the K141R mutant. These experiments led to the conclusion that SIRT1 protects cardiomyocytes from ER stress-induced apoptosis by attenuating PERK/eIF2α pathway activation via deacetylation of eIF2α.

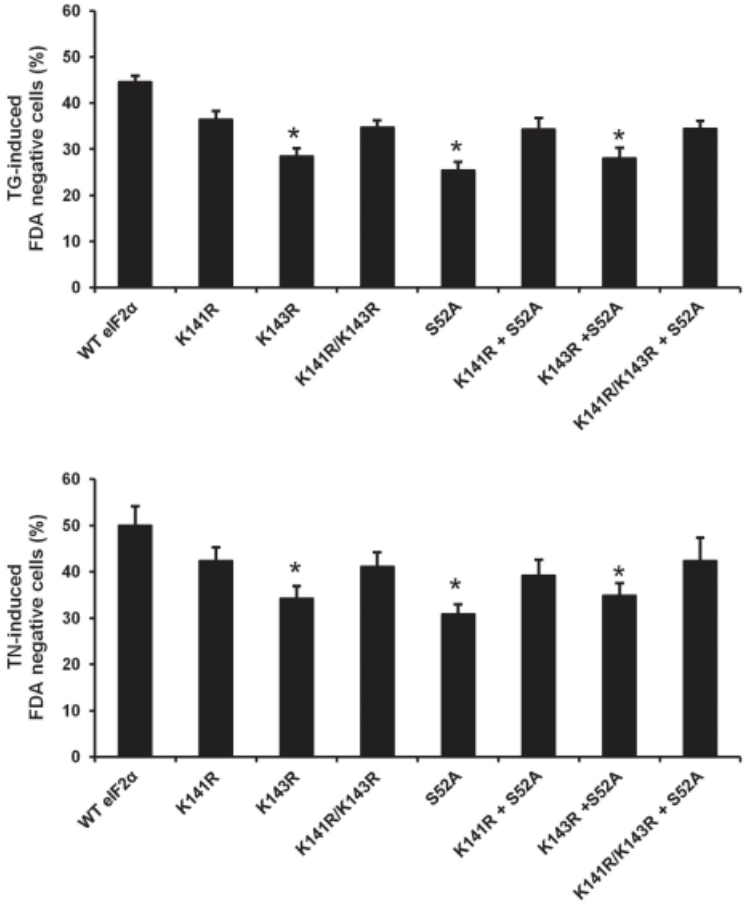

Figure 33: Effect on WT and mutant eIF2α on TG (thapsigargin)and TN (tunicamycin)-induced death, two ER stressors. A) Shows the percentage of dead cells after TG -induced cell death. Only K143R, S52A, and the double mutant K143R S52A show significant protection against cell death. B) Percentage of dead cells after TN induced cell death. Results are comparable to those obtained in panel A.

Thapsigargin is an inhibitor of sarcoplasmic reticulum Ca^{2+} ATPase (SERCA). SERCA pumps calcium ions from the cytoplasm into the lumen of the endoplasmic reticulum (ER). Its inhibition causes an increase in the cytoplasmic calcium levels while also depleting ER stores.

Tunicamycin prevents N-linked glycosylation of proteins in the ER, which causes extensive protein misfolding and activation of the unfolded protein response (UPR).

SIRT1 is activated in response to various cellular stresses (Haigis and Sinclair, 2010) and is cardioprotective in the context of aging, hypertrophy, and myocardial infarction (Alcendor *et al.*, 2007). Other studies have shown that SIRT1 is a master regulator of cellular stress and might be a therapeutic target for the prevention of cardiovascular diseases, outside of the PERK pathway (D'Onofrio *et al.*, 2015). For example, SIRT1 was reported to regulate IRE1 branch of the UPR through deacetylation of XBPs in embryonic fibroblasts and its deficiency resulted in ER stress-induced apoptosis. SIRT1 exerts deleterious effects and sensitizes these cells to ER stress-induced apoptosis via repressing XBP1s signaling (Wang, Chen and Ouyang, 2011). However, (Prola *et al.*, 2017) did not see any effect on the XBP1 pathway but in the PERK/ eIF2α, suggesting that there are cell-type specificities including differentiation state that might trigger different ER stress-induced pathways.

Some pharmacological studies have shown that resveratrol activation of SIRT1 reduced cardiomyocyte apoptosis in a diabetic cardiomyopathy model. When using compounds that provoked the inhibition of SIRT1, the PERK/ eIF2α pathway was

hyperactivated, resulting in apoptosis (Hubbard *et al.*, 2013). This suggests that by attenuating the PERK/ eIF2α pathway activation, we can reduce the initiation of apoptosis and promote cell surviving, supporting the therapeutic potential of SIRT1 activators for the treatment of cardiac pathologies associates with ER stress.

Part 4. SIRT1: a ubiquitous and multirole enzyme

SIRT1 is a NAD-dependent deacetylase that participates in many cellular processes. It is part of a large family of protein-modifying enzymes known as sirtuins conserved among bacteria, archaea, and eukaryotes. The founding member of this family is the silent information regulator 2 (*Sir2*), which was first identified in *S.cerevisiae* through genetic screening. Yeast Sir2p is necessary for silencing of the mating-type information locus, HM (Klar', Fogel and Macleod, 1979).

Later work in Sir2p showed that the sirtuin family functions primarily as a NAD+-dependent deacetylase (Tanner *et al.*, 1999); (Landry *et al.*, 2000) with specific family members reported to possess mono-ADP ribosyl transferase, demalonylase, or desuccinylase activity (Frye, 1999).

Sirtuins first started to gain the interest of the academic community because of their role in aging. This was first discovered in yeast via a model of replicative life span, measured in the number of times a yeast mother cell produces a daughter cell before senescing. A cause of yeast aging named stemming was identified, which consists of recombination at rDNA loci. This recombination leads to the formation of an extrachromosomal rDNA circle (ERC) by homologous recombination. This event leads to the amplification of ERCs in aging mother cells (Sinclair and Guarente, 1997). Remarkably, the addition of an extra copy of *Sir2* was shown to extend replicative life span by 30%, by suppressing rDNA recombination and decreasing ERC formation, while deleting *Sir2* increased ERCs and shortened lifespan.

Lifespan is also increased upon addition of multiple copies of the *Sir2* homologous gene in *C.elegans* and *Drosophila melanogaster* (Tissenbaum and Guarente, 2001)*;* (Rogina and Helfand, 2004). The fact that increasing doses of *Sir2* increased lifespan in yeast, worm, and flies, led to the search of mammalian sirtuins that could potentially increase the human lifespan and aid in the treatment of different diseases. This exciting endeavor led to the discovery of seven mammalian sirtuins (Frye, 1999); (Frye, 2000), each of them with several different roles, all related to maintaining cell homeostasis, redox balance, and aging (Sinclair, 2005).

4.1 Mammalian sirtuins:

There are seven sirtuins in mammals. They have a highly conserved central NAD+ binding and catalytic domains (Landry *et al.*, 2000). Their N and C-termini differ depending on their biological functions, due to different enzymatic activities, unique binding partners and substrates, and distinct subcellular localization (Haigis and Guarente, 2006) (table 1 and figure 34).

SIRT1, SIRT6 and SIRT7 are predominantly found in the nucleus. SIRT3, SIRT4 and SIRT5 reside in mitochondria, and SIRT2 is primarily cytoplasmic. The subcellular localization depends on cell type, stress status, and molecular interactions. For instance, SIRT1 and -2 were found to localize in both the nucleus and the cytoplasm and to interact with both nuclear and cytosolic proteins (Michan and Sinclair, 2009); (Haigis and Sinclair, 2010).

SIRT1 has a nuclear or cytosolic location depending on the environmental stresses the cell is subject to. Each sirtuin has a primary amino acid signal sequence that contributes to its intracellular localization. Nuclear localization of SIRT1, -6 and -7 is attributed to nuclear localization signals. SIRT1 has two nuclear localization signal regions and two nuclear export signals (Tanno *et al.*, 2007). Exposure of nuclear localization signals versus nuclear export signals may dictate the cytosolic versus nuclear localization of SIRT1 (Zhang *et al.*, 2009).

Sirtuin	Location	Activity	Substrate	Biology
SIRT1	Nucleus/cytosol	Deacetylase	FOXO, PGC-1α	Metabolism/Stress
SIRT2	Cytosol	Deacetylase and ADP-ribosyl-transferase	Tubulin, H4, FOXO	Cell cycle
SIRT3	Mitochondria	Deacetylase and ADP-ribosyl-transferase	GDH complex	Thermogenesis, ATP production
SIRT4	Mitochondria	ADP-ribosyl-transferase	GDH, IDE, ANT	Insulin secretion
SIRT5	Mitochondria	Deacetylase	CPS1	Urea cycle
SIRT6	Nucleus	ADP-ribosyl-transferase	Histone H3, NF-κB	Base excision repair, metabolism
SIRT7	Nucleus/Nucleolus	Deacetylase	Pol I, UBF, H3	rDNA transcription

Table 1: Summary of mammalian sirtuins, localization, main known substrates and biological process associated.

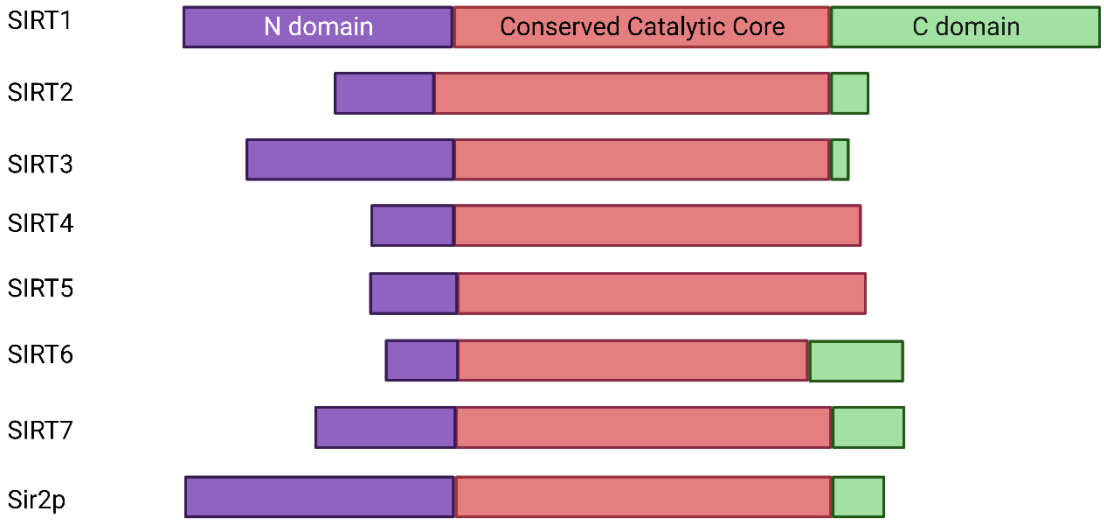

Figure 34: Comparison between the different mammalian sirtuins and their differences in N-terminal and C-terminal domains.

4.2 General sirtuin deacetylation reaction

The first reaction identified by a sirtuin was a ribosyl transfer reaction catalyzed by *Sir2* bacterial homolog CobB, which converts 5,6-dimethyl-benzimidazole to α-ribose-5,6-benzimidazole (Escalante-Semerena, 1997). CobB also presents deacetylase activity, being the main deacetylase in bacteria (Abouelfetouh *et al.*, 2015). This first study in CobB led to the discovery that sirtuins are NAD^+-dependent deacetylase and ADP-ribosyltransferase, however, most sirtuins catalyze NAD^+-dependent deacetylation (North *et al.*, 2003) (table 1).

The sirtuin deacetylation reaction is conserved among organisms. This reaction is performed via a unique mechanism that requires NAD^+ cleavage with each reaction cycle, meaning that sirtuin activity is tied to the metabolic state of the cell (Tanner *et al.*, 1999).

In this reaction, the substrate acetyl group is transferred onto the ribose moiety of NAD+, generating nicotinamide and 2-O-acetyl-adenosine disphosphoribose. The proposed mechanism suggests that the deacetylation is performed through an adenosine-diphosphoribose (ADPR)-peptidyl-imidate intermediate, which is consistent with available biochemical data (Avalos, Boeke and Wolberger, 2004); (Hoff *et al.*, 2006).

Steps (figure 35):

i) The reaction starts with a nucleophilic attack of the acyl-oxygen to the 1'-carbon of the nicotinamide ribose, which results in the C1'-alkylamidate intermediate and the release of nicotinamide. ii) histidine 133 (catalytic residue in SIRT6, being 363 in SIRT1), as a base, facilitates the intramolecular nucleophilic attack of the nicotinamide ribose 2'-hydroxyl on the O-alkylamidate carbon, resulting in the 1',2'-cyclic intermediate. iii) This intermediate is hydrolyzed, which results in the tetrahedral intermediate. iv) The catalytic histidine, positively charged, loses a proton to the imino group of this intermediate, breaking the C-N bond and yielding the final products. v) AADPR and deacetylated lysine products are released from the sirtuin (Klein and Denu, 2020).

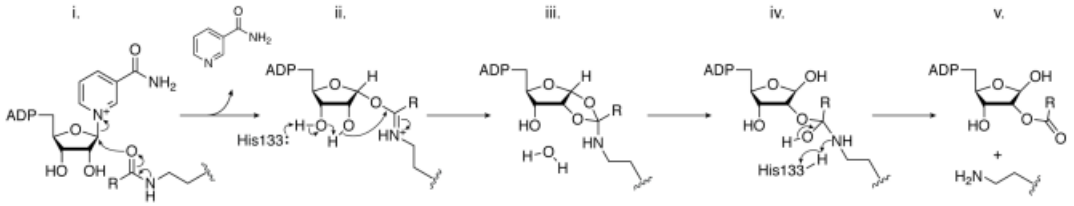

Figure 35: Steps of sirtuin deacetylation as described in the text. Klein and Denu 2020.

In addition to this proposed mechanism, three crystallographic structures of sirtuins bound to acetylated substrates have brought insight on the sirtuin de-acetylation mechanism and the positioning of the substrate in SIRT1 catalytic pocket. 1) An archaeal situin with an acetyl-peptide as a substrate derived from the C-terminal of the regulatory part of the p53 protein (Avalos et al., 2002) , 2) the yeast sirtuin HST2 (Zhao, Chai and Marmorstein, 2003), and 3) bacterial CobB, with a model peptide derived from H4 tail as substrate (Zhao, Chai and Marmorstein, 2004).

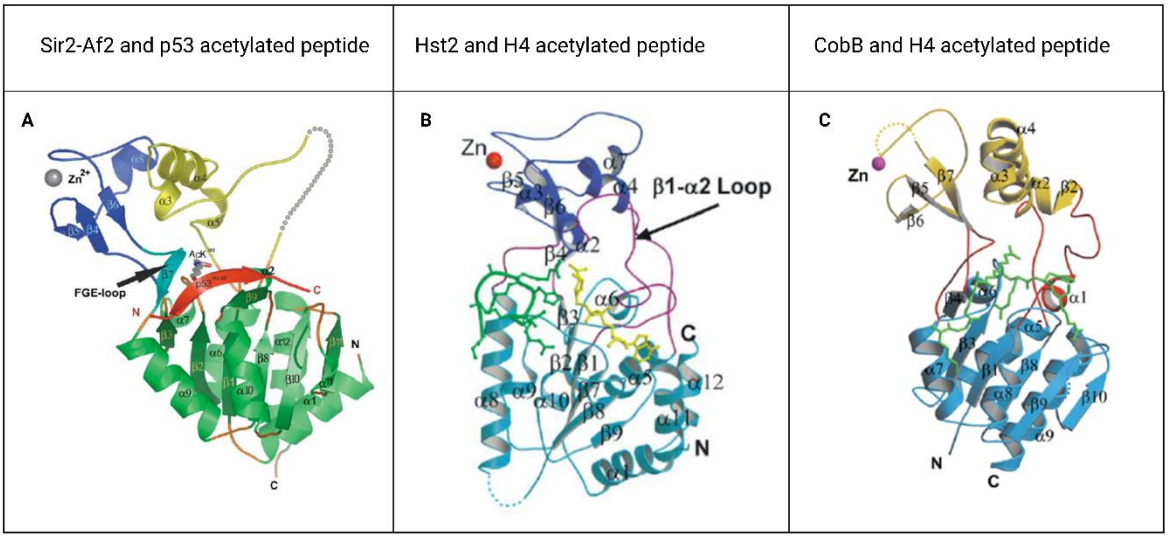

Figure 36: Sirtuin homologues. A) Sir2-Af bound to the p53 C-terminal acetylated peptide. B) Hst2 yeast Sir2 homologue bound to H4 acetylated peptide. C) Bacterial sirtuin CobB bound to H4 acetylated peptide.

Peptide binding is dominated by the insertion of the acetyl lysine into a highly conserved hydrophobic channel (figure 37). Residues F297, R274, and F414 are part of this channel, which surrounds the peptide upon binding. H363, the catalytic residue, is positioned opposite F414, stabilizing the binding of the acetylated substrate.

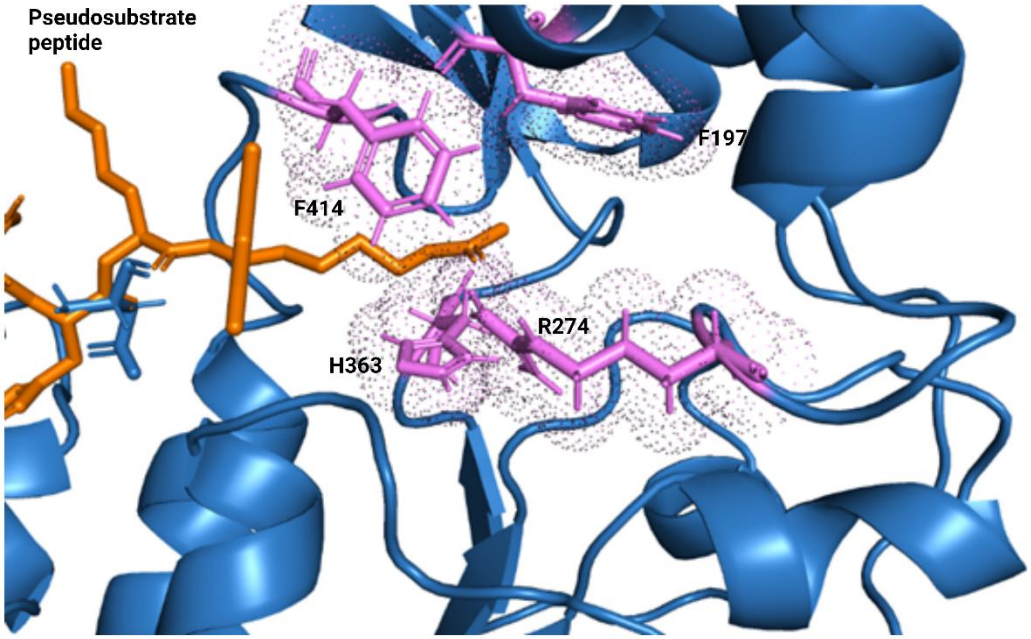

Figure 37: Residues of SIRT1 catalytic center. Histidine 363 (H118 in yeast) is the main catalytic residue of the catalytic center. The other residues R274, F297 and F414 create a hydrophobic channel where the pseudo peptide (orange) can insert itself. PDB: 5BTR

However, some steady-state kinetic analyses show varying catalytic efficiencies depending on the substrate. This suggests that sirtuins can indeed differentiate between substrates (Borra *et al.*, 2004). In favor of this idea, mutations of three residues located at the surface of *Archaeoglobus fulgidus* Sir2 results in an increase of the affinity of this enzyme for a p53 derived peptide. This shows that it is possible to modulate sirtuin specificity (Avalos, Boeke and Wolberger, 2004).

4.2.1 Sirtuin modulation by NAD+, NAM and AADPR

Biosynthetic pathways that generate NAD+ are also critical for the regulation of sirtuins in various subcellular compartments. Sirtuins are inhibited by NAM in a non-competitive manner, meaning that NAM binds to a different site of Sir2/SIRT1, specifically to a highly conserved C-pocket adjacent to the NAD^+- binding site. NAM reacts with the peptide-imidate intermediate of the reaction regenerating NAD^+ (Bitterman *et al.*, 2002); (Kouzarides *et al.*, 2004); (Sauve and Schramm, 2003). NAM cleavage is reversible, reforming into NAD^+ (Gavin *et al.*, 2006).

In mammals NAD^+ is recycled in two steps: 1) A NAM phosphoribosyl transferase (Nampt) converts NAM to nicotinamide mononucleotide (NMN). 2) Next, NMM is utilized by the isoenzymes Nmmat 1, 2 and 3 to regenerate NAD^+ in the nucleus, Golgi and mitochondria, respectively (Revollo, Grimm and Imai, 2004); (Berger *et al.*, 2005).

Nampt is one of the main regulators of SIRT1 activity. It is thought that this enzyme either hands off NAD^+ to SIRT1 or that there are pools of NAD^+ that influence SIRT1 activity (Zhang *et al.*, 2009). Furthermore, SIRT1 and Nampt are part of the mammalian circadian clock feedback cycle. Nampt is under transcriptional regulator of a *clock-BMAL-SIRT1* pathway, which increases the conversion of NAM into NAD^+. Consequently, SIRT1 is reactivated, reactivating Nampt expression, all this occurring in a 12-hour cycle (Nakahata *et al.*, 2009).

AADPR is a product of the sirtuins NAD^+-dependent reaction (as stated in previous sections). This is a novel metabolite which might have a strong physiological importance. Examples in yeast show that AADPR promotes the assembly of the Sir complex across chromatin (Liou *et al.*, 2005). In mammals AADPR is metabolized to acetate by an unidentified enzyme. There is still plenty to investigate about the cleavage products derived from sirtuin-mediated-deacetylation, as it is thought that these products

may mediate biologically relevant functions in aging, metabolism, and others (Haigis and Sinclair, 2010).

4.3 SIRT1

The direct homologue of Sir2p in humans is SIRT1. SIRT1 is the most studied mammalian sirtuin to date. Human SIRT1 distinguishes itself from others by having sizable N domain and C domains compared to the other six mammalian sirtuins (figure 35) (Frye, 2000). SIRT1 participates in a wide range of cellular processes, including energy metabolism and cell survival; and deacetylates a wide variety of substrates, including κB, FOXO transcription factors, and transcriptional coactivator PGC-1α. The importance of SIRT1 in regulation is manifested in SIRT1 knock-outs, that confer a phenotype with developmental defects and lethal in some backgrounds (Haigis and Sinclair, 2010).

A well-known SIRT1 substrate are histone tails. SIRT1 plays a crucial role in the maintenance of the histone code as it is capable of de-acetylating H3 and H4 tails, directly regulating DNA expression. Another well-known substrate is p53 factor, which is involved in apoptosis and cell death regulation (Zhao *et al.*, 2013).

In the past decade, the interest on SIRT1 and its role in the pathology of cardiovascular diseases has risen. Increased levels of SIRT1 activity led to the survival of cardiomyocytes under stress conditions (Alcendor *et al.*, 2007); (Planavila *et al.*, 2011). As mentioned previously, eIF2α is likely a newly discovered SIRT1 substrate.

4.3.1 Structure of human SIRT1

All sirtuins have a rather conserved catalytic core. The main structural differences between sirtuins are the varying lengths of their N and C domains (figure 35). Multiple different sirtuin structures, including mammalian SIRT3, SIRT5 and SIRT6, yeast Sir2p, and archaeal Sir2-Af have been obtained either by crystallographic or Cryo-EM methods (Kouzarides *et al.*, 2004); (Cosgrove *et al.*, 2006); (Min, Landry and Sternglanz, 2001); (Jin *et al.*, 2009); (Chio *et al.*, 2023). The study of the different types of sirtuins have shed some insight into both the structure and action mechanism of this whole family (Cosgrove *et al.*, 2006); (Dai *et al.*, 2015), including SIRT. To facilitate the structural study of SIRT1, researchers designed a minimal version of SIRT1 containing the catalytic (CAT) and the C-terminal domains (CTR) of SIRT1 (figure 38).

This shortened version of SIRT1 was able to deacetylate acetylated substrates and could be crystallized (Davenport, Huber and Hoelz, 2014). As shown in figure 38, SIRT1 presents two different conformations; an apo/open form, when no substrate is bound, and a closed form when a substrate is present.

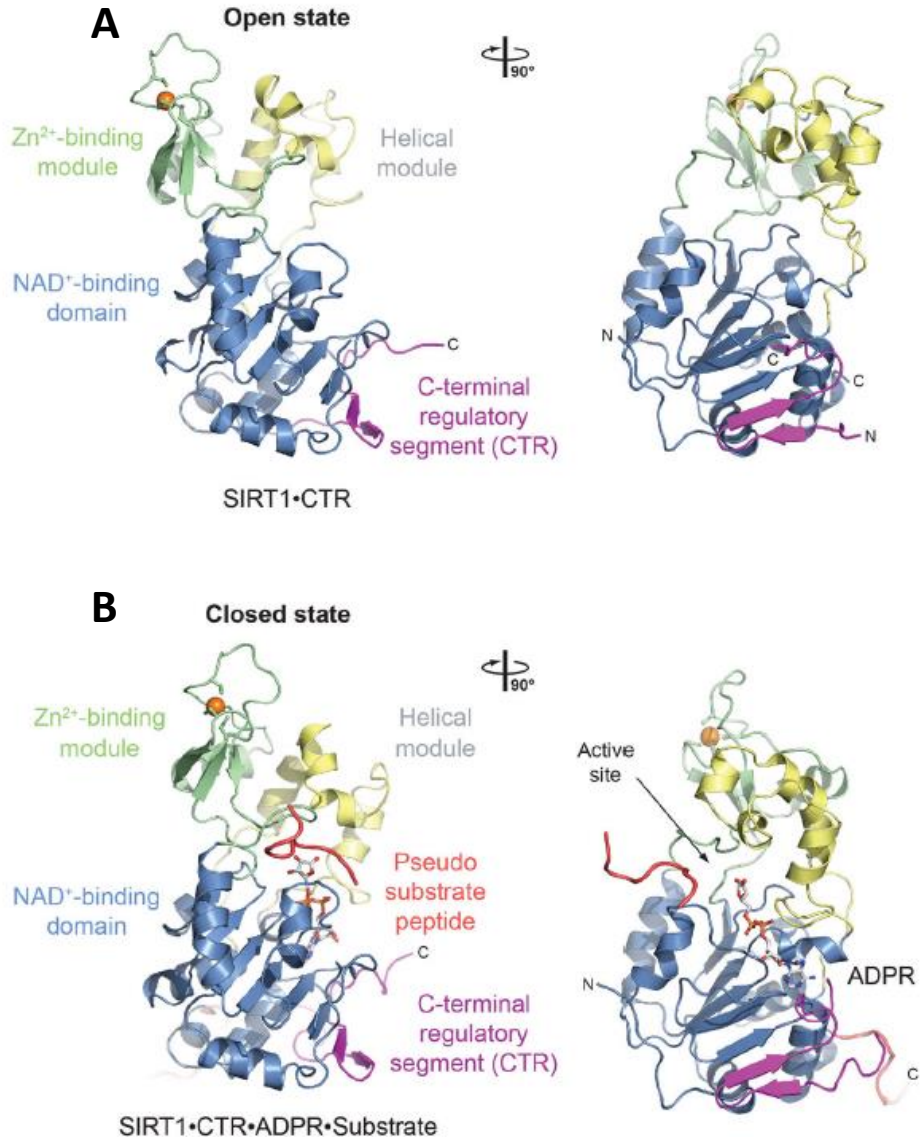

Figure 38: SIRT1 structure, image from Davenport et al 2013. A) Structure of the open apo form. Depicted in green is the ZN-binding module, in blue the NAD+-binding domain and in yellow the helical module. The pseudo-substrate peptide comes from the C-terminal extension of a neighboring SIRT1 molecule in the crystal. This pseudo-peptide perfectly accommodates in the catalytic channel. PDB: 4KXQ (closed state) and 4IF6 (open state). B) Structure of the quaternary SIRT1CAT•CTR•ADPR•Substrate complex in ribbon representation.

Structure of the catalytic domain (CAT):

The CAT contains 277 residues and is divided into two subdomains: a large NAD+ binding domain, containing a Rossmann fold, and a small domain.

The NAD+ binding domain is composed of a central six-stranded parallel β-sheet and eight α-helices that pack against the β-sheet core of the domain (Davenport, Huber and Hoelz, 2014).

The small domain contains a helical module, with four α-helixes, and a Zn binding subdomain, made up of 3 β-strands and a α-helix. An extensive hydrophobic interface holds the helical and Zn-binding molecules together, generating the tightly associated small subdomain of the catalytic core (Avalos, Boeke and Wolberger, 2004) (figure 34). The relative orientation and the interaction between the large and small domains are dramatically different in the open and closed states (figure 38) (Davenport, Huber and Hoelz, 2014).

Interaction between the catalytic domain of SIRT1 and the CTR:

The CTR (C-terminal region, residues 641-653) forms a β-hairpin that binds to the lower edge of the NAD+-binding domain of CAT, complementing the central six-stranded parallel β-sheet of the Rossmann fold with two additional β-strands. This hairpin covers an essentially hydrophobic patch. The CTR-binding site on the Rossmann fold is located close to the binding site of the adenine ring of the NAD+ (called A pocket). The CTR directly interacts with R466 of the Rossmann fold, which forms extensive van der Waals contacts with one face of the adenine ring.

The CTR domain of SIRT1 is also known as ESA (essential for sirtuin activity) (Kang *et al.*, 2012). Without this domain, the CAT is completely inactive. This domain is crucial for SIRT1 regulation in vivo, as it can be displaced by DBC-1 (Deleted in Breast Cancer-1), resulting in the inactivation of SIRT1 (Kim, Chen and Lou, 2008) (figure 39).

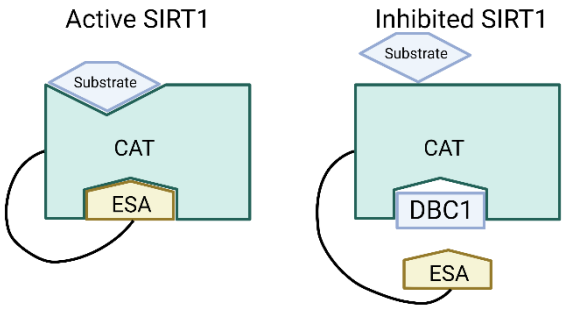

Figure 39: Simplified view of SIRT1 inhibition by DBC1. On the left: the ESA (the CTR of SIRT1), is necessary to ensure SIRT1 catalytic activity and substrate recognition. On the right: DBC1 displaces the ESA, reducing substrate recognition by SIRT1 and inhibiting its enzymatic activity. Figure modified from Kang et al., 2011.

4.3.2 Regulation of SIRT1 activity through its N-terminal domain

SIRT1 has important roles in metabolism, neurodegeneration, inflammation, and, more recently discovered, in cardiovascular diseases. SIRT1 can be modulated by sirtuin activating compounds, STACs, which specifically bind to its N domain (Cao *et al.*, 2015).

As mentioned in previous sections, STACs are small molecules that can modify SIRT1 activity and are, therefore, of great interest in the treatment of diseases (Milne *et al.*, 2007); (Dai *et al.*, 2015). However, structural studies with the full-length protein are hindered by the predicted unstructured nature of its large N domain. Using a similar approach as that described in Davenport, Huber and Hoelz, 2014, where they used only the CAT and CTR of the protein, researchers decided to identify the minimum amount of N domain necessary to study the STACs influence on SIRT1 structure and activity, in order to understand their mechanism (Cao *et al.*, 2015); (Dai *et al.*, 2015). Specifically, there are certain STACs that have been shown to protect cardiomyocytes from stress in vitro, hence the importance to have a fully functional SIRT1 (Monceaux *et al.*, 2022).

This inspired researchers to engineer another shortened version of the SIRT1 protein which conserved its catalytic capabilities and contains part of its N domain. This protein was called miniSIRT1 (Cao *et al.*, 2015); (Dai *et al.*, 2015) (figure 40).

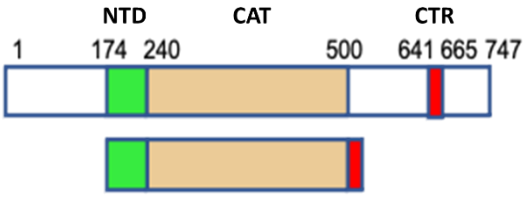

Figure 40: schematic diagram showing functional domains in full-length human SIRT1 and below of the truncated variant mini-SIRT1.

4.3.1.1 miniSIRT1 design:

Dai et al., 2015 identified the key functional regions of SIRT1 using hydrogen-deuterium (H-D) exchange mass spectrometry (HDX-MS). The exchange rate of H-D is dependent on the dynamic properties of the protein, with slower exchange occurring in more rigid or structure regions. They identified three major structure regions: the catalytic core (residues 229-516), the N-terminal region immediately preceding the CAT (183-229), and a section of the C-terminal domain (the CTR or ESA region, 641-665) (figure 41). This experiment was performed in the absence or presence of a STAC compound. The presence of the STAC slowed down the H-D exchange on the N-terminal region, confirming its role in STAC binding. This way, researchers were able to recreate a functional mini-SIRT1 that still retained its ability to bind STACs, with comparable K_M and k_{cat} values to full length SIRT1 (noted just as SIRT1 from here onwards) (Dai *et al.*, 2015).

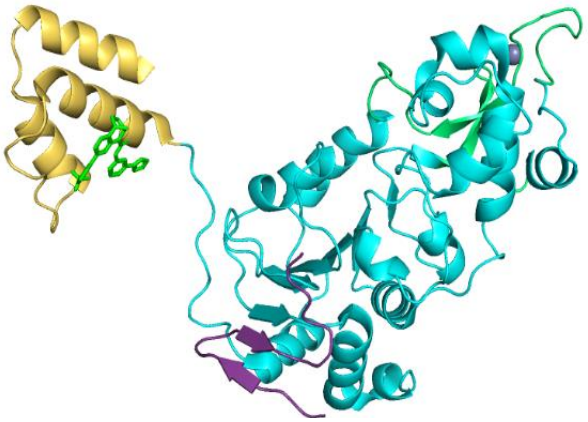

Figure 41: Structure of mini-SIRT1 by Dai et al., 2015. In yellow the N-terminal domain bound to STAC 1(in bright green). CAT is depicted in cyan (with the Zn-binding module in green), and the CTR is depicted in purple. PDB: 4ZZH.

4.4 STACs and SIRT1

STACs are known for modifying SIRT1s activity by lowering the Michaelis-Menten constant (K_M) of an acetylated peptide substrate. Thus STACs may improve the binding affinity of the acetylated substrate for SIRT1 (Howitz and Sinclair, 2003). The most studied STAC of this family is resveratrol (figure 42) which is found in grapes, berries, peanuts, and wines. It is part of a family of polyphenolic compounds known as stilbenes (Moraes *et al.*, 2020). In recent years, thousands of compounds have been tested in order to find any clinically relevant STACs (Curry *et al.*, 2021), however, their mechanism of action is still up to debate, as well as their clinical relevance.

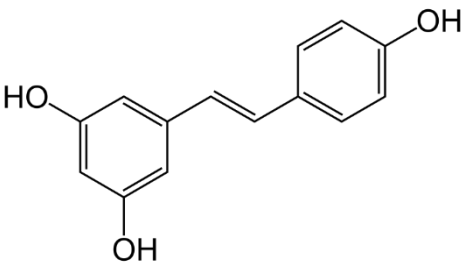

Figure 42: Resveratrol molecule.

In vitro studies that aim to understand the STAC activation mechanism use either SIRT1 or some version of the above explained mini-SIRT1. In both cases, the STAC activation event is evidenced, however, these studies do not converge in one single conclusion on how this activation is achieved (Dai *et al.*, 2010); (Pacholec *et al.*, 2010).

The main issue in the study of SIRT1 activation by STACs is the choice of substrate. Sirtuins are slow enzymes with a rather low affinity for their substrate (range of K_M is always on the μM level and higher than 10 μM in most cases (Kaeberlein *et al.*, 2005)), which in most studies are peptides derived from their original substrates, such as p53 and Histone 4 (Milne *et al.*, 2007).

To facilitate studies of the catalytic mechanism, synthetic peptides used at the beginning of SIRT1 studies carried a fluorescent AMC (7-amino-4-methylcoumarin) moiety at the C-terminal extremity (Pacholec *et al.*, 2010). Using these fluorescently labelled peptides was highly debated. There was an important doubt on whether SIRT1 was directly activated by STACs (such as resveratrol) or whether the activation effect was due to the AMC group (figure 43).

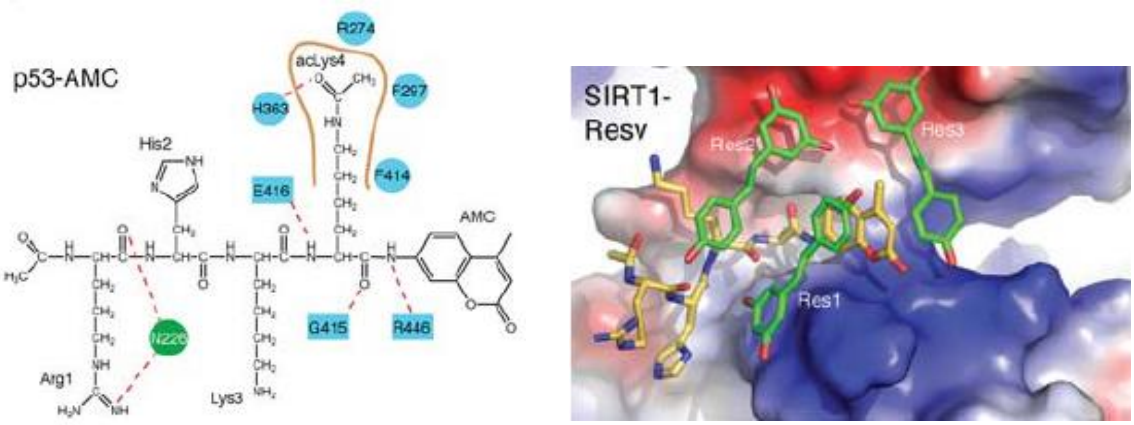

Figure 43: Modified figures from Cao et al 2020. A) Figure A shows the positioning of the acetyl group of a mimic AMC-peptide in SIRT1s hydrophobic channel. B) Positioning of an AMC-peptide substrate bound to resveratrol. Note that resveratrol directly binds to the AMC group (yellow), casting serious concern on the use of AMC peptides.

Researchers were able to show the differences in K_M and k_{cat} (Cao *et al.*, 2015) when the enzyme activity was studies in the presence of the STAC resveratrol. However, their results show that the most dramatic difference in mini-SIRT1 catalytic parameters was obtained with an AMC-peptide, putting these results in doubt.

However, Dai and collaborators from the Sinclair lab, who had been working with AMC-modified peptides, responded to this claim by showing that fluorophore moieties are dispensable if replaced with naturally occurring hydrophobic amino acids (Dai *et al.*, 2010). The Sinclair lab proposed that the activation mechanism was rather allosteric and had nothing to do to the addition of the AMC-ring (Hubbard and Sinclair, 2013). The AMC moiety only mediated activation when it was directly adjacent to Ac-Lys 9 of H3K9 at the +1 position. This discovery led to the proposal of two consensus sequences that sirtuins are most likely to recognize (figure 44).

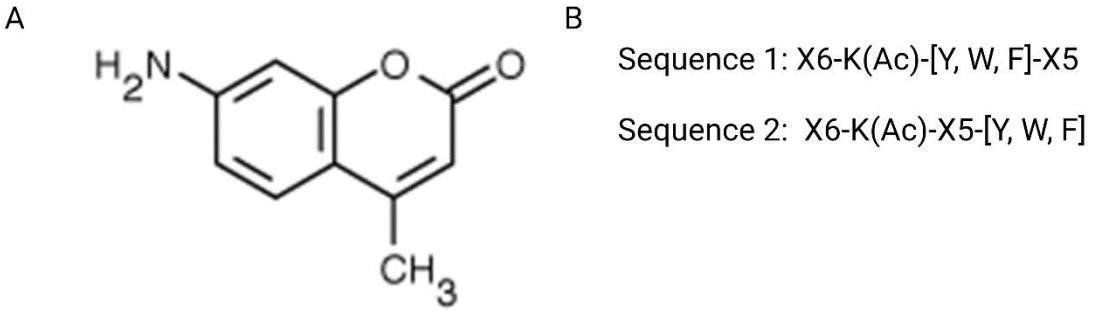

Figure 44: A) AMC ring structure. B) Consensus sequences that sirtuins are most likely to recognize

Hubbard et al, 2013, also pin pointed residue Glu230 in the sirtuin N-terminal region. This residue alone was necessary for STAC recognition, tilting the conclusion towards a STAC allosteric mechanism of activation. Finally, these studies encouraged researchers to leave behind the AMC-modified peptides in favour of peptides that resembled more the two sequences above (some of these peptides include a W in their sequence to increase sirtuin affinity) (Huynh *et al.*, 2022). The same controversy exists for experiments performed with TAMRA (5-carboxytetramethylrhodnine) peptides, which are peptides labelled with the TAMRA fluorescent tag (figure 45), which has been proven to bind to STACs (Dai *et al.*, 2010).

The specificity of STACs seems, therefore, dependent on substrate and cell-type, as not all cell types will express the same sirtuin targets. Because sirtuins are slow enzymes, their effect in longevity and disease is likely to be rooted in processes that need a balanced activation rather than an immediate one (Watroba and Szukiewicz, 2021). However, the catalytic rates and affinity for its substrate are widely varied depending on the SIRT1 construction used and type of substrate used (figure 47). Taking Huyhn et al., 2022 and Dai et al., 2015, as an example. Both studies used SIRT1 and a similar Ac-p53(W) peptide. If we compare them their K_M values are in the same order of magnitude, however, the k_{cat} is ten times higher in the case of Dai et al., 2015 studies. Cao et al., 2015 study compared catalytic rates in the presence of STACs using peptides that were tagged with AMC and others that were not. In table 2, it shown that only the peptide with the AMC moiety has a significant difference in K_M.

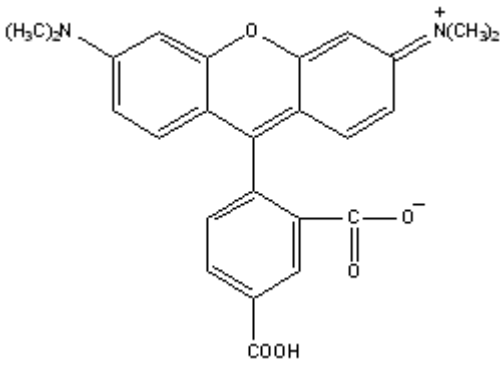

Figure 45: TAMRA fluorescent label used to tag acetylated peptides.

Sirtuin	Substrate	STAC	K_M (μM)	k_{cat} (s^{-1})	Reference
SIRT1	Ac-Histone 3 peptide	NO	109 ± 9	0.060 ± 0.003	(Smith, Hallows and Denu, 2009)
Mini-SIRT1 (143-511 U 641-655)	AMC-RHKK peptide (p53)	NO	211.1 ± 28.6	0.154 ± 0.007	(Cao et al., 2015)
Mini-SIRT1 (143-511 U 641-655)	AMC-RHKK peptide (p53)	Resveratrol 200 μM	25.8 ± 9.6	0.185 ± 0.014	Cao et al., 2015)
Mini-SIRT1 (143-511 U 641-655)	PGC-1α peptide	NO	120.9 ± 12.6	0.077 ± 0.003	(Cao et al., 2015)
Mini-SIRT1 (143-511 U 641-655)	PGC-1α peptide	Resveratrol 200 μM	103.6 ± 8.6	0.058 ± 0.001	Cao et al., 2015)
SIRT1	Ac-p53 (W) peptide	No	13 ± 1.8	0.06 ± 0.003	(Huynh et al., 2022)
SIRT1	Ac-p53 (W) peptide	Resveratrol 200 μM	6 ± 0.9	0.056 ± 0.002	(Huynh et al., 2022)
SIRT1	Ac-p53 (W) peptide	No	3.7 ± 0.8	0.37 ± 0.01	(Dai et al., 2015)
Mini-SIRT1 (186-511 U 641-655)	Ac-p53 (W) peptide	No	16 ± 2.2	0.44 ± 0.02	(Dai et al., 2015)

Table 2: Catalytic rates of the different SIRT1 variants. Rates coming from the same study are highlighted in the same color. The first study in red, set the experimental procedure used by the rest of studies, a 3-step enzymatic step in which the SIRT1 deaceetylation reaction is the limiting step. In yellow, a study by Cao et al., 2015, the different rates with and without STACs are shown for different substrates. However, the main difference in K_M is only seen with the AMC peptide when the reaction is done in the presence of STACs in green, a small study done by Huynh et al 2022 shows the differences between an enzymatic reaction performed with and without resveratrol. However, what is interesting about this study is the great difference in K_M when compared with Dai et al., 2015 study in blue. As both studies use the same enzyme and substrate but show a 10-fold difference in their obtained k_{cat}.

The catalytic parameters of SIRT1 and its variants vary from study to study. It is important to remark that most studies use peptides derived from p53 or H4, most of which are modified with the AMC-moiety or with a W added to their sequence to improve substrate affinity.

As explained in previous sections, SIRT1's relevance in cardiovascular diseases was put in evidence by our collaborator Christophe Lemaire. More importantly, the ability of certain STACs to increase SIRT1 deacetylation activity could potentially lead to future pharmacological treatments (Prola *et al.*, 2017). Even though sirtuins are known to participate in a multitude of processes, little is known about their actual substrates, apart from a handful of them (such as histones).

In the case of Christophe Lemaire's work, the target of SIRT1 was eIF2α. Most importantly, addition of STACs increased SIRT1 activity, which led to eIF2α deacetylation and dephosphorylation, linking these two post-translational modifications in a manner it is yet to be understood.

Objectives

ER stress is caused by a dysregulation of protein folding. As an immediate response (ER stress response), translation is downregulated via phosphorylation of eIF2α. Regulation of this phosphorylation is key to restore homeostasis. More recently, ER stress has been implicated in cardiovascular diseases including myocardial infarction, ischemia, dilated cardiomyopathy, and heart failure. Moderate induction of the ER stress response can be protective, whereas long response times result in apoptosis.

Importantly, our collaborator Christophe Lemaire recently studied the role of SIRT1, in the modulation of the cardiac ER stress response. Using adult inducible SIRT1 knock out mice and cell culture models of ER stress (the H9c2 cell line from *Rattus Norveticus*), they showed that SIRT1 inhibition increases ER-stress induced cardiac injury, whereas SIRT1 activation was protective. They reported that SIRT1 protects cardiomyocytes against ER stress induced apoptosis by modulating the PERK/eIF2α pathway of the UPR through eIF2α deacetylation on lysine residues 141 and 143. These results indicate that eIF2α deacetylation by SIRT1 may favor eIF2α dephosphorylation, thus triggering the end of the ER stress response and the restoration of cell homeostasis. The study of the influence of eIF2α deacetylation on eIF2α dephosphorylation is important, as SIRT1 could become a pharmacological target to modulate ER stress.

My thesis work aims to complement the results obtained in vivo by the group of C. Lemaire with in vitro approaches that will prove and characterize the activity of SIRT1 on acetylated heIF2α. Our lab's expertise in biochemical and structural studies makes us particularly well-suited to describe the catalytic activity of SIRT1 on acetylated heIF2α and acetylated derivatives. To do so, the first important goal of my thesis work was to produce an acetylated version of heIF2α using orthogonal translation systems, as well as SIRT1 derivatives.

There is no information on the effect of acetylation on heIF2α structure, so we also aim to obtain structural information on acetylated heIF2α.

Another goal of my PhD work is to study the interplay between heIF2α phosphorylation and acetylation. Indeed, the group of C. Lemaire showed that SIRT1 inhibition during ER stress-induced cardiac injury led to increased levels of acetylation and phosphorylation. This strongly suggests that deacetylation favors dephosphorylation.

To study the interplay between these two PTMs, we first wanted to produce heIF2α phosphorylation mimics (S52D) and determine SIRT1 catalytic activity to characterize the effect of phosphorylation mimics on deacetylation.

Finally, acetylation is a novel PTM for heIF2α, therefore we also aim to identify a possible network of interactions using acetylated heIF2α as bait. This result aims to widen the known interactant network of heIF2α that is dependent on its PTM state.

Results

Part 1. Production of heIF2α and acetylation of heIF2α

1.1 State of the art on e/aIF2α production

The interest in studying human eIF2α (heIF2α) is rooted in its importance in translation initiation regulation and stress regulation. However, because of technical difficulties purifying the human protein most of the structural information about heIF2α came from studies with the archaeal or yeast protein (figure 46).

Archaeal and yeast e/aIF2α are easily produced using *E. coli* expression systems. These systems are preferred because they allow the production of large quantities of protein, necessary for structural studies. Structural studies with the archaeal protein elucidated the 3D structure of this factor (Schmitt, Naveau and Mechulam, 2010). However, the archaeal protein lacks serine 51 and its consequent phosphorylation. To further study this motif, the yeast protein was also used (Dhaliwal and Hoffman, 2003).

The human protein was first produced in 2002 using a baculovirus system in Sf9 insect cells (Nonato, Widom and Clardy, 2002). A crystallographic structure of domains I and II of heIF2α was obtained, which showed structural similarity with the archaeal and yeast proteins. The insect cell system is usually more efficient to produce eukaryotic proteins, as these cells contain chaperones that aid in protein folding and add PTMs to the desired protein, facilitating their study. However, the PTMs added, especially glycosylation patterns, are different to those observed in mammals.

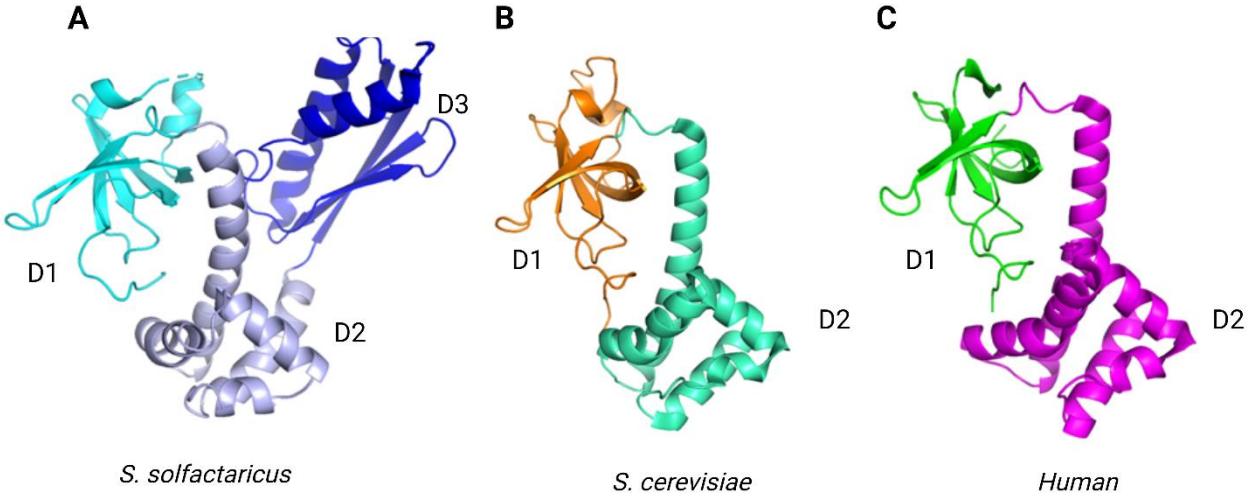

Figure 46: Comparison between the different e/aIF2α crystallographic structures. A) S. solfactaricus aIF2α, all three domains are depicted in this structure (2AHO). B) S. cerevisiae eIF2α domains 1 and 2 (PDB: 1Q46). C) Domains 1 and 2 of human eIF2α (PDB: 1KL9).

By using codon optimization, a chaperone system, and rationalized mutagenesis, researchers were finally able to produce heIF2α in *E. coli* systems (Ito and Wagner, 2004). First, researchers used a codon-optimized gene, which increased expression levels by a factor of two. Secondly, they co-expressed heIF2α with a set of bacterial chaperones (GroEL-GroES and TF), to reduce the amount of aggregated protein. Finally, they used rational mutagenesis guided by sequence alignments of heIF2α homologues.

1.2 Strategy used to produce heIF2α

First, we ordered a plasmid containing the optimized heIF2α gene for expression in *E. coli*. The gene was recloned into a pET-15b Amp^R plasmid to produce an N-terminally tagged (His-6x) version of the protein. Previous studies in the lab showed that all eukaryotic eIF2α have a C-terminal acidic tail that does not participate in eIF2 assembly, but that could potentially affect the solubility of the protein (Naveau *et al.*, 2013). Therefore, we decided to remove this tail by introducing a STOP codon at position 303 of the gene coding for heIF2α. The corresponding protein is named heIF2α-303.

Moreover, previous structural studies (figure 46) showed that domains 1 and 2 form a stable unit, separate from domain 3 (Schmitt *et al.*, 2020). Both units can move independently from each other. This mobility can hinder crystallization of the full-length protein. To facilitate our studies, we also decided to produce a protein that lacked the entire domain 3. The protein was produced after introduction of a STOP codon at position 188 of the gene encoding heIF2α. It is hereafter named heIF2-188 (figure 47).

To improve expression of heIF2α, we also co-expressed bacterial chaperones GroEL-GroES and TF as Ito and Wagner., 2004. Using this expression system, we were able to produce a large amount of heIF2α-303 and heIF2α-188.

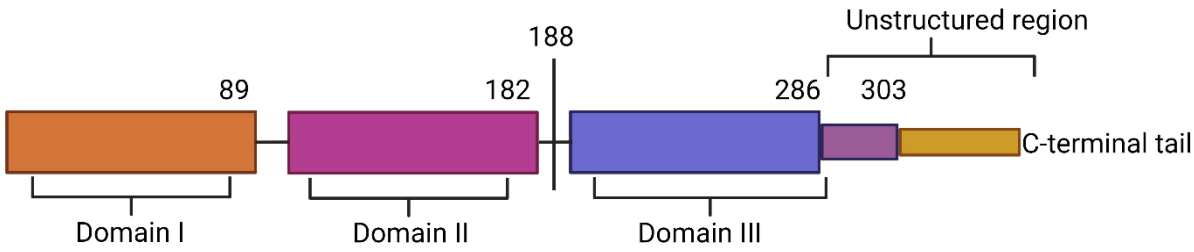

Figure 47: Schematic of heIF2α C-terminal tail and domains. Domains of heIF2α with positions 188 and 303 indicated.

A three-step protocol was used to purify heIF2α-303: a metal affinity chromatography (in a buffer containing 500 mM NaCl), an anion exchange chromatography (using an NaCl gradient from 100 mM to 1 M, heIF2α-303 pI=5.45), and a size exclusion chromatography (150 mM NaCl, 10 mM HEPES pH 7.5) (see materials and methods section). heIF2α-303 was easily concentrated in the buffer used for size exclusion chromatography. About 5 mg of protein per liter of culture were obtained (figure 48).

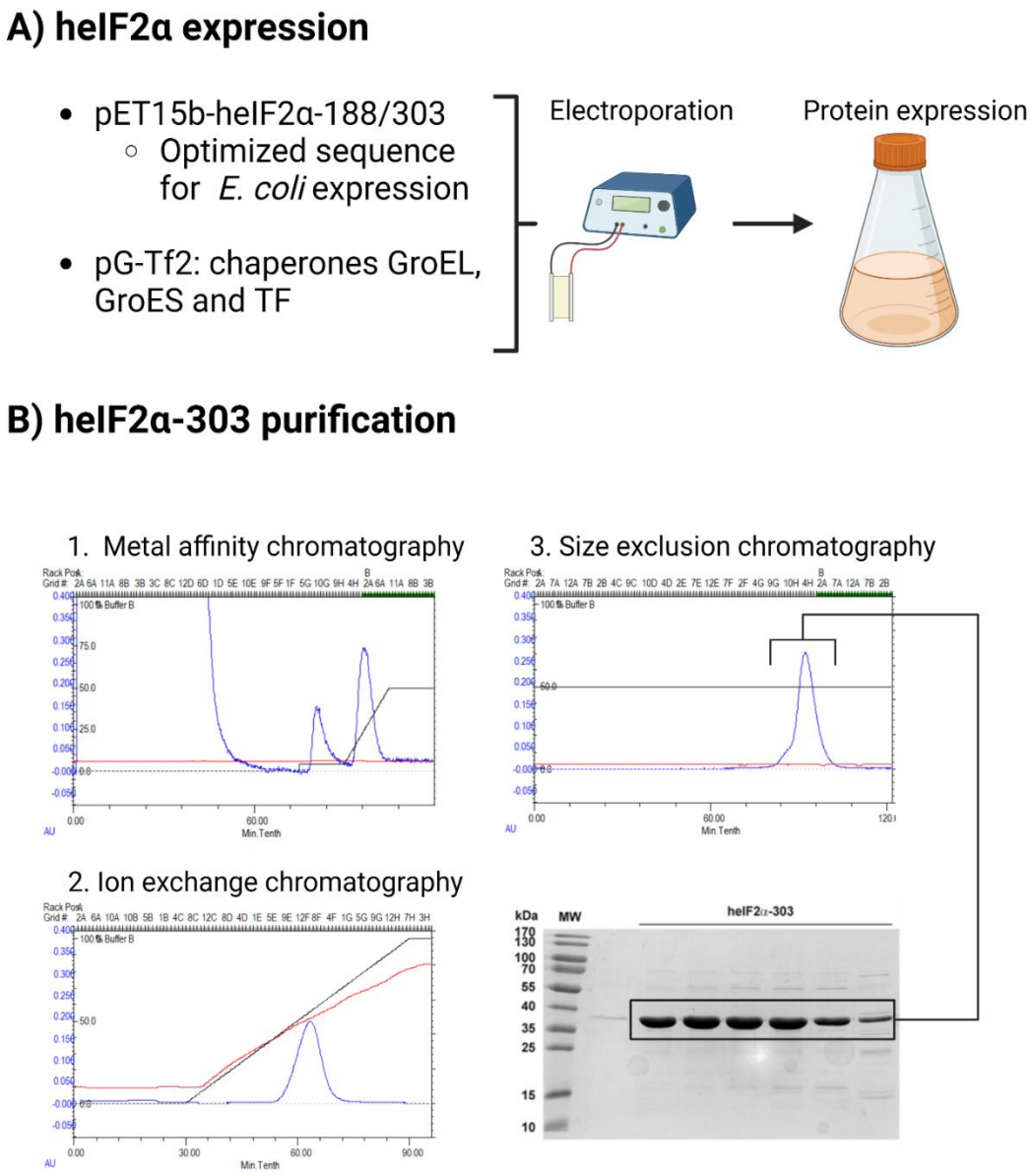

Figure 48: A) Expression of heIF2α variants. The pET15b-heIF2α-188/303 plasmid contains an optimized eIF2α gene for bacterial expression. The pG-Tf2 contains chaperones GroEL, GroeES and TF. Both plasmids are transformed into BL21-DE3 bacteria. B) Purification of heIF2α-303 1) Metal affinity chromatography, 2) ion exchange, and 3) size exclusion chromatography. SDS-PAGE analysis shows eIF2α-303 purified after size-exclusion chromatography.

heIF2α-188 was purified following a two-step purification protocol: a metal affinity chromatography (in a buffer containing 500 mM NaCl) and a cation exchange chromatography (using an NaCl gradient from 100 mM to 1 M, heIF2α-188 pI=7.8) (figure 49) (see materials and methods).

heIF2α-188 was produced in greater quantities than heIF2α-303. We estimated that around 20-25 mg of heIF2α-188 were purified after the first purification step, and about 10 mg of heIF2α-303. However, part of heIF2α-188 was lost during purification as it tended to precipitate when exposed to low NaCl concentrations. This renders the purification and storage of the protein very difficult. By maintaining the protein at a 500 mM NaCl concentration, we were able to concentrate the protein up to 1-1.5 mg/mL. In comparison heIF2α-303 could be concentrated up to 20 mg/mL in a buffer containing only 150 mM NaCl.

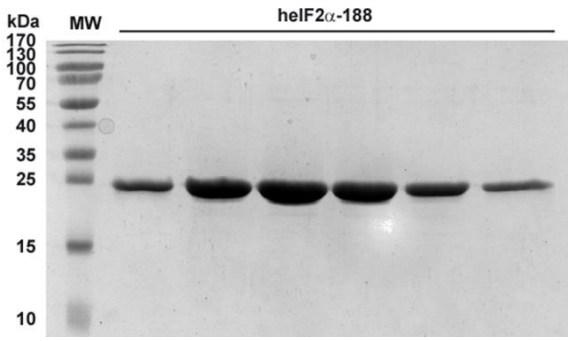

Figure 49: SDS-PAGE analysis of heIF2α-188 purification. The figure shows heIF2α-188 after the second step of purification.

1.2.1 Optimization of heIF2α-188 buffer conditions

To find better buffer conditions to store and concentrate heIF2α-188, we performed a Thermal Shift Assay (TSA) (figure 50) in which we varied salt concentration and pH. We also tested a glycerol range concentration in these trials, as it is a molecule often used to stabilize proteins in solution. The pI value of heIF2α-188 is 7.78, and therefore adjusting buffer conditions during its purification could help increase the solubility of the protein and facilitate its binding onto the S-sepharose beads (cation-exchange chromatography).

We observed two peaks during the TSA experiment but only the first peak was used to deduce the melting temperature (Tm). Interestingly, we observed an increase in the Tm when NaCl increased to 500 mM, which was consistent with our observations. No significant effect due to the pH was visible.

A)

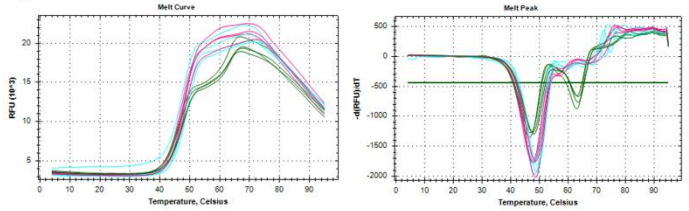

NaCl	100	250	500
MOPS 6.8	47.5	48.5	49
HEPES 7.5	47.5	48	48.5
TRIS 8	47	48	47.5
TRIS 8.5	48	48.5	49.5

B)

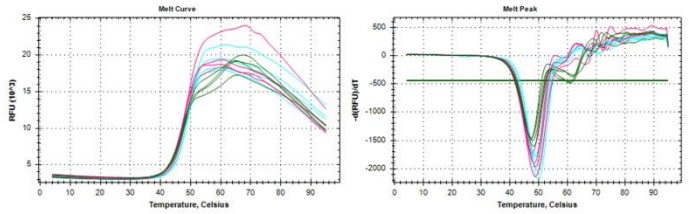

5 % glycerol

NaCl	100	250	500
MOPS 6.8	48	49	50
HEPES 7.5	48	49	49.5
TRIS 8	47.5	48.5	49
TRIS 8.5	47	47.5	49

C)

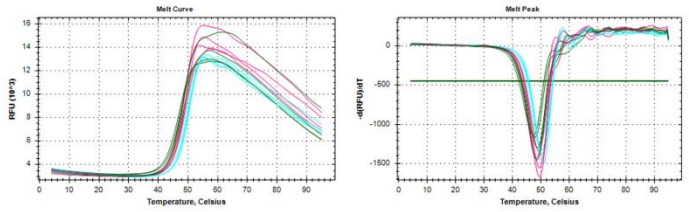

10 % glycerol

NaCl	100	250	500
MOPS 6.8	48.5	49.5	51
HEPES 7.5	49	49.5	50.5
TRIS 8	48	49.5	50.5
TRIS 8.5	47.5	48.5	49.5

Figure 50: Thermal Shift Assay results varying NaCl concentration, pH, and glycerol concentration. On the left side the Thermal Shift Assays curves in different colors: green for 100 mM NaCl, pink for 250 mM NaCl and bluee for 500 mM NaCl. On the right side the tables corresponding to the Tm's in Celsius. The top table showcases Tm's corresponding to no additional glycerol added, the second table corresponds to 5% of added glycerol, and the third to 10% of added glycerol. In blue the salt concentrations in mM and in yellow the different pH's tested.

We also generated the electrostatic surface of the protein, using the structure obtained by Nonato et al., 2002, to try to understand the origin of its solubility problems. As shown in figure 51-A, heIF2α's electrostatic surface presents several basic and acidic patches that could explain protein aggregation. In this figure 51-B, we can also observe that in the structure of Nonato, four Zn^{2+} ions are visible. Therefore, we decided to add divalent ions to our buffer, to increase heIF2α-188 solubility.

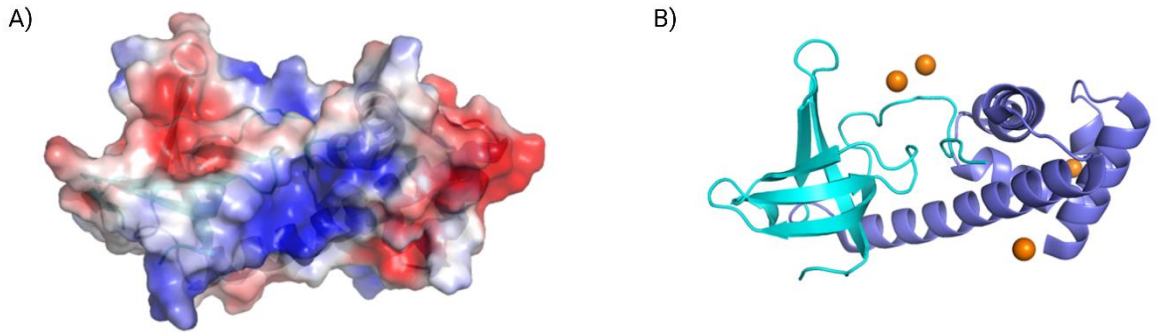

Figure 51: Electrostatic surface potential of domains 1 and 2 heIF2α (equivalent to heIF2α-188) using PDB: 1KL9. Nonato et al., 2004. A) The electrostatic surface shows the presence of acidic and basic patches (in red and blue) that can contribute to protein aggregation. B) Tridimensional structure of domains 1 (cyan) and 2 (dark blue) of heIF2α. Zn^{2+} ions are shown in orange.

Finally, we defined the new storage buffer as 500 mM NaCl, 10 mM $MgCl_2$, 2% glycerol and 10 mM HEPES 7.5. Using this buffer, we were able to concentrate heIF2α-188 to 2-3 mg/mL. This buffer was however, still not ideal as precipitation problems remained.

1.3 Introduction of the unnatural amino acid acetyl-lysine into a polypeptide chain using the archaeal pyrrolysine system, developed by the Chin lab:

The study of PTMs is of great interest for the scientific community as they have important roles in regulation of protein activity, cell fate, gene expression and many others. For many years, phosphorylation has been at the center of the PTM study, being examples of its importance the phosphorylation of PERK and eIF2α, which controls translational rates, or the JNK phosphorylation, which controls apoptosis.

Other PTMs quickly gained the interest of researchers. An important example is methylation and acetylation of histones, which are well-known to regulate gene expression. Acetylation is known to have a role in protein-protein interaction, protein stability, and subcellular targeting (Ding *et al.*, 2014); (Ree, Varland and Arnesen, 2018).

The introduction of PTMs for in vitro studies was done historically by chemical or enzymatic means. However, these methods present several problems, such as an incomplete acetylation of the final product, and unspecific acetylation. These methods do not ensure a homogeneous acetylation of the protein and require additional purification steps to isolate the acetylated final product.

In some archaea, such as *Methanosarcina barkeri*, amber codons are translated as a 22nd amino acid, pyrrolysine, encoded by an amber STOP codon UAG. This translation occurs thanks to a pyrrolysyl-tRNA synthetase (MbPylRS) and its corresponding tRNA, $MbtRNA_{CUA}$ aminoacylated with a pyrrolysine.

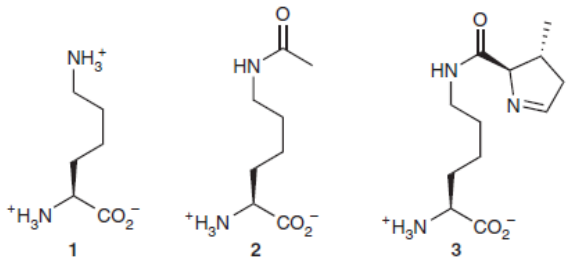

Figure 52: 1) Structure of lysine, 2) Ne-acetyl-lysine and 3) pyrrolysine. Image modified from Neumman, Peak-Chew and Chin, 2008.

Because the pyrrolysyl-tRNA synthetase and its corresponding tRNA are only found in some archaea, it offers the opportunity to use it to expand the genetic code, in *E. coli* for example, by assigning a new amino acid to an amber STOP codon (TAG). Because acetyl-lysine is very similar to pyrrolysine (figure 52), researchers evolved the MbPylRS/$MbtRNA_{CUA}$ pair to incorporate Nε-acetyl-lysine encoded by an amber codon. Using this system, the incorporation of acetyl-lysine is homogeneous allowing the production of fully acetylated target protein. To do so, researchers had to ensure the orthogonality of the system. In an orthogonal system the $tRNA_{CUA}$ is only recognized by PylRS and not any other aaRS, and PylRS only recognizes the amino acid and tRNA of interest and not any other in the *E. coli* cytoplasm.

First studies in *E. coli* showed that this MbPylRS/$MbtRNA_{CUA}$ pair was used successfully to introduce a pyrrolysine in the sperm whale myoglobin. But most importantly, it showed that the $MbtRNA_{CUA}$ is not a substrate for endogenous aminoacyl-tRNA synthetases (Srinivasan, James and Krzycki, 2002).

The experiment above showed that the unmodified $tRNA_{CUA}$ could be used in *E. coli* systems to introduce pyrrolysine. Since the objective is to incorporate acetyl-lysine, researchers needed an evolved version of PylRS able to recognize acetyl-lysine instead of pyrrolysine.

The Chin Laboratory led the development of this orthogonal system, and the evolution of the archaeal PylRS to recognize acetyl-lysine (Neumann, Peak-Chew and Chin, 2008). First, they identified the amino acids involved in the catalytic center of PylRS (Leu266, Leu270, Tyr271, Leu274, Cys313 and Trp383) (figure 53). Then, they

created a library where these six residues were randomized using PCR (Neumann, Peak-Chew and Chin, 2008). By doing three rounds of selection, positive, negative and positive, they were able to isolate a PylRS mutant that paired with $MbtRNA_{CUA}$ enabled the production of an acetylated protein.

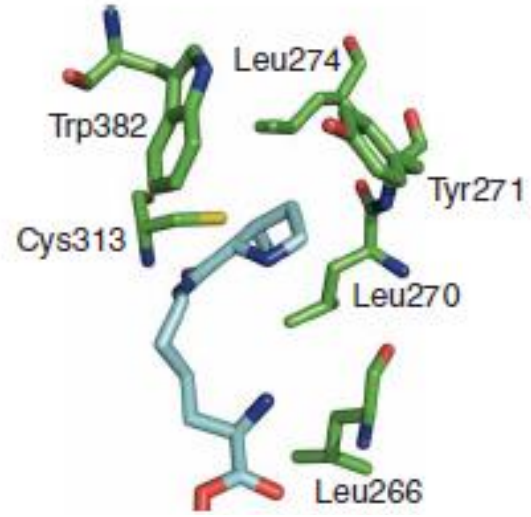

Figure 53: Catalytic center of MbPylRS.

These selection steps ensured that the resulting PylRS only incorporated acetyl-lysine to the $tRNA_{CUA}$:

1. The randomized PylRS was cloned into a pBK plasmid, originating hundreds of different variants of pBK-PylRS. This plasmid was transformed into bacteria containing a pREP-PylT plasmid, which contains the green fluorescent protein (GFP), a chloramphenicol resistance gene (coding for chloramphenicol acetyltransferase, CAT), (both with an amber STOP codon in their sequences) and the $tRNA_{CUA}$. Bacteria were then plated onto LB petri dishes with acetyl-lysine and chloramphenicol. The surviving fluorescent bacteria are those who decode the STOP codon introduced in both the chloramphenicol and the GFP genes, meaning that their synthetase can recognize acetyl-lysine and catalyze the aminoacylation of the $tRNA_{CUA}$ with acetyl-lysine. These clones were pooled and the plasmid coding for the modified PylRS gene extracted. However, at this step, the specificity to acetyl-lysine is not ensured, as the mutant PylRS could recognize other natural amino acids and enable the synthesis of GFP and of CAT.
2. The second selection is a negative one that eliminates any PylRS capable of incorporating a natural amino acid in response to the amber codon. The selected plasmids from the first step were transformed into bacteria containing a pBAR-PylT, which contains a toxic barnase gene with amber codons at positions Q2 and D44. These bacteria were cultured without any acetyl-lysine, so all the clones expressing the barnase gene, thanks to the incorporation of a natural amino acid would be eliminated.
3. Finally, the third step was performed in the same way as the first, but instead of harvesting the pool of plasmids encoding PylRS variants they picked individual

colonies. Researchers selected those bacteria that showed a strong acetyl-lysine dependent chloramphenicol resistance.

In the end, researchers obtained two different sequences, designated AcKRS-1 and AcKRS-2. The first one had six mutations in the amino acids of the catalytic center (L266V, L270I, Y271F, L274A, C313F) and a spontaneous D76G mutation. The second sequence only had four mutations (L270I, Y271L, L274A, C313F) (figure 53).

In order to obtain an acetylated version of heIF2α we used the system developed by the Chin lab. They kindly provided us with two plasmids, one containing the evolved AcKRS-1 (pBK-AcKRS-1-pylT), and another containing $tRNA_{CUA}$ (pCF-$tRNA^{CUA}$-pyIT).

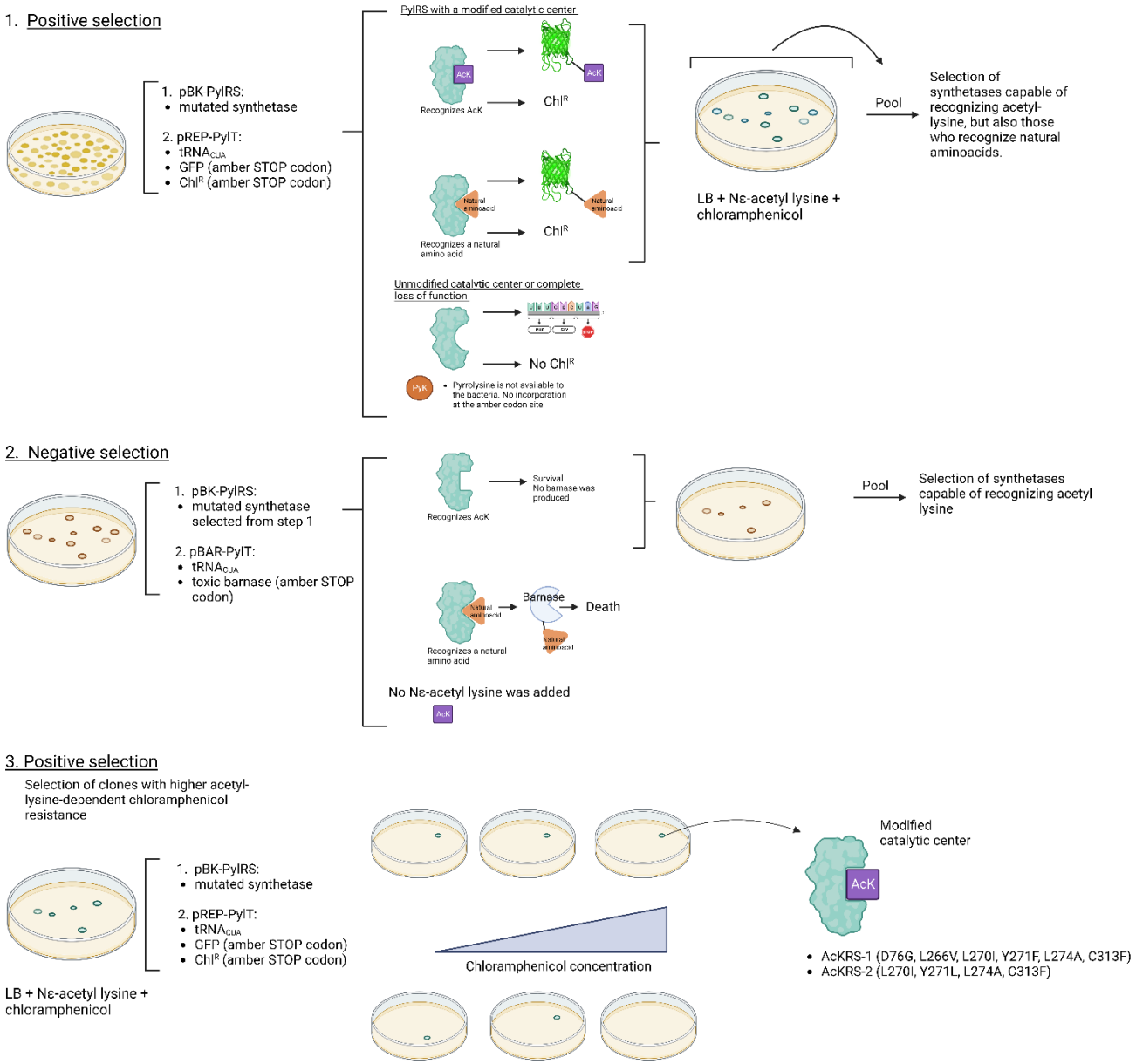

Figure 54: Positive-negative-positive selection used by the Chin lab to select Nε-acetyl lysine specific pylRS. 1) Positive selection of synthetases capable of recognizing acetyl-lysine, but also those that recognize natural amino acids. 2) Selection of synthetases capable of recognizing acetyl-lysine, other synthetases are eliminated by negative selection. 3) Positive selection of synthetases, dependent on their chloramphenicol resistance. In the end, two synthetases were selected, which bared different mutations: AcKRS-1 (D76G (unexpected), L266V, L270I, Y271F, L274A, C313F) and AcKRS-2 (L270I, Y271L, L274A, C313F).

1.3.1 Experimental design to produce acetylated heIF2α

First, we introduced amber STOP codons in the genes encoding for heIF2α-188/303 in place of lysine codon 141 and/or 143 using site-directed mutagenesis.

Previous studies in the lab of C. Lemaire indicated that only deacetylation of K143 conferred protection against ER-stress induced apoptosis. This suggests that position K143 is more important than K141 (figure 33 in section 3.6.1). Based on this result, we focused our efforts in producing the variants acetylated in position 143 first. According to the experiments in (Neumann, Peak-Chew and Chin, 2008) work, the yield of acetylated product is low, therefore, we started our purification trials with the heIF2α-188 variant, which was expected to give the highest yield of protein expression as it is the case with wild-type heIF2α-188 and heIF2α-303.

In our first trials we transformed BL21-DE3 bacteria with pCF-tRNA^{CUA}-pyIT (spectinomycin resistance), pBK-AcKRS-1-pylT (kanamycin resistance) and a third pET-15b plasmid (Amp^{R}) containing heIF2α with the amber STOP codon in position 143, pET-15b-heIF2α-143AcK-188. Then, we co-expressed our modified protein with the evolved Mb-PylRS and the Mb-tRNA$_{CUA}$. The expression of the acetylated heIF2α-188 was visible on SDS-PAGE analysis, however, protein expression was very low, and required extensive optimization.

Optimization of the production of acetylated heIF2α:

First, we optimized the amount of bacteria used to inoculate the culture media (OD_{600}=0.1). Then, we optimized the addition time of Nε-acetyl-lysine and nicotinamide during bacterial growth (OD_{600}=0.3). Finally, we also tested different conditions for IPTG induction of expression (OD_{600}=1.2).

To improve protein yields even further, we decided to minimize the number of plasmids used. To do that, we cloned the gene coding for heIF2α-143AcK-188 into the pCF-tRNA^{CUA}-pyIT, originating pCF-tRNA^{CUA}-pyIT-heIF2α-143AcK-188. Plasmid quantity was also optimized, as initial transformations with 100 ng of each plasmid didn't result in any colonies. We had to increase the plasmid concentrations up to 1 µg each to obtain enough bacteria (2 petri dishes were necessary to inoculate 1L of 2xYT media at 0.1 OD). All versions of heIF2α (188/303, TAG143/141) were eventually cloned into the pCF-tRNA^{CUA}-pyIT plasmid to reduce the number of plasmids and antibiotics. Our efforts to purify a double acetylated version of the protein were unsuccessful, probably

because of the proximity of the two STOP amber codons that render protein expression more difficult.

First trials were done in 100 mL of 2xYT media to confirm and optimize the production of the acetylated variants, and once confirmed we proceeded with large scale purifications (figure 55).

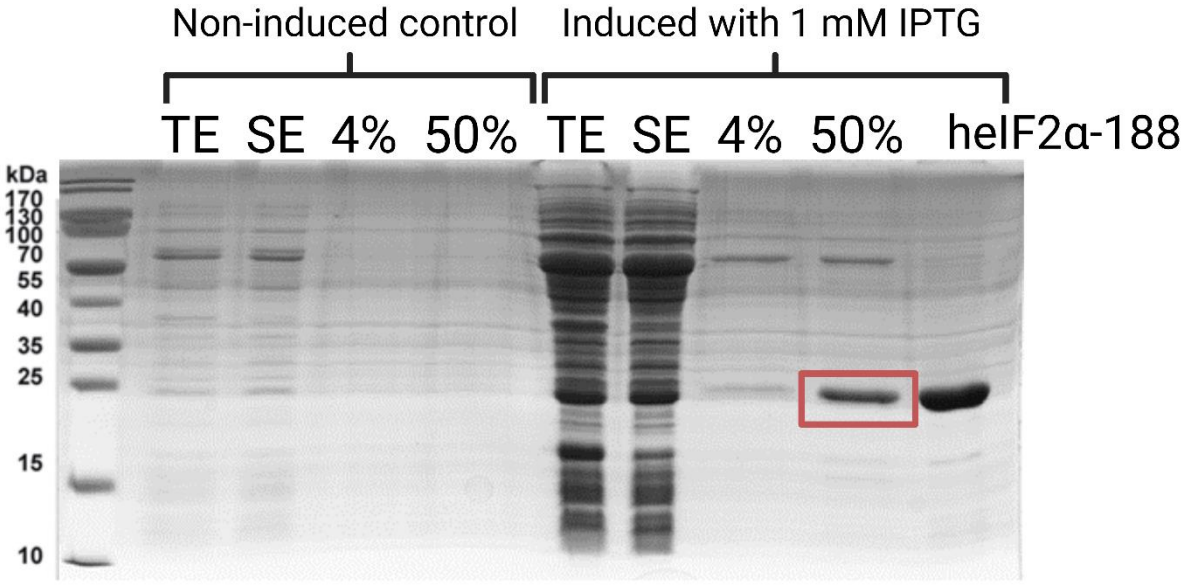

Figure 55: Small-scale purification of heIF2α-143AcK-188. Bacteria were transformed with pCF-tRNA^{CUA}-pyIT- heIF2α-143AcK-188 and pBK-AcKRS-1-pylT. Then, they were cultured in a small volume (100 mL) which was then separated in two different 50 mL erlenmeyers. Both flasks were added 10 mM N ε-acetyl-lysine and 20 mM Nicotinamide, but only one of them was induced O/N with 1 mM IPTG. The next day cells were resuspended, sonicated and their supernatants recovered and applied onto a small quantity of metal affinity beads in a 1.5 mL eppendorf tube. The protein was eluted only in the induced bacteria case, showing a band corresponding to heIF2α-188 (acetylated protein surrounded in red, with the control on its right).

We then used one- or two-liter culture to produce large quantities. The BL21-DE3 bacteria were transformed with pCF-tRNA^{CUA}-pyIT-heIF2α-143AcK-188 and pG-Tf2 (containing the GroEL, GroEs and TF chaperones). The purification steps (large scale) were like those explained for the wild-type heIF2α-188 and heIF2α-303 proteins. Notably, in the first step of purification (metal affinity chromatography) two peaks are observed: one peak corresponds to the chaperone and the second peak corresponds to heIF2α-143AcK-188 (figure 56). The presence of the acetyl group on the purified protein was then checked by Mass Spectrometry at the Pasteur Institute. Using full-length proteins, the presence of the acetyl group was confirmed (figure 56). Moreover, using protein digestion followed by peptide fragmentation methods (LC-MS/MS) the position of the acetyl group in the sequence was demonstrated (figure 56).

1. Metal affinity chromatography

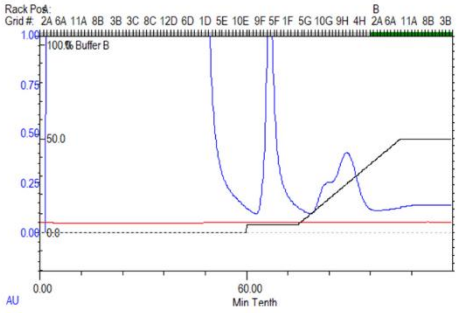

2. Ion exchange chromatography

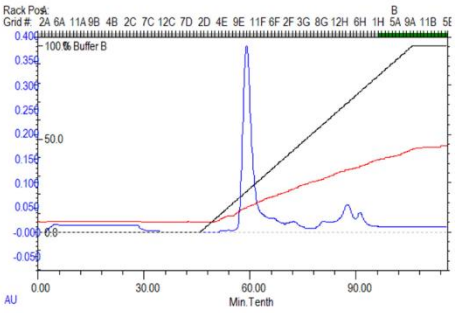

3. SDS-PAGE analysis after anion exchange chromatography

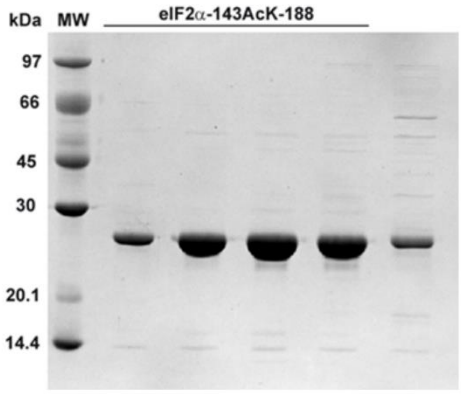

4. Verification via mass spectrometry analysis: Electrospray ionization MS

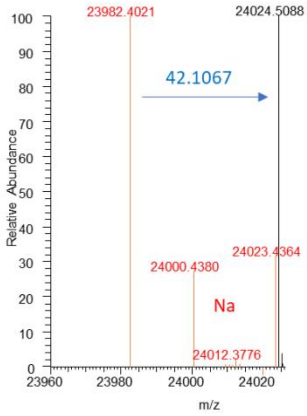

5. Verification via mass spectrometry analysis: MS/MS fragmentation

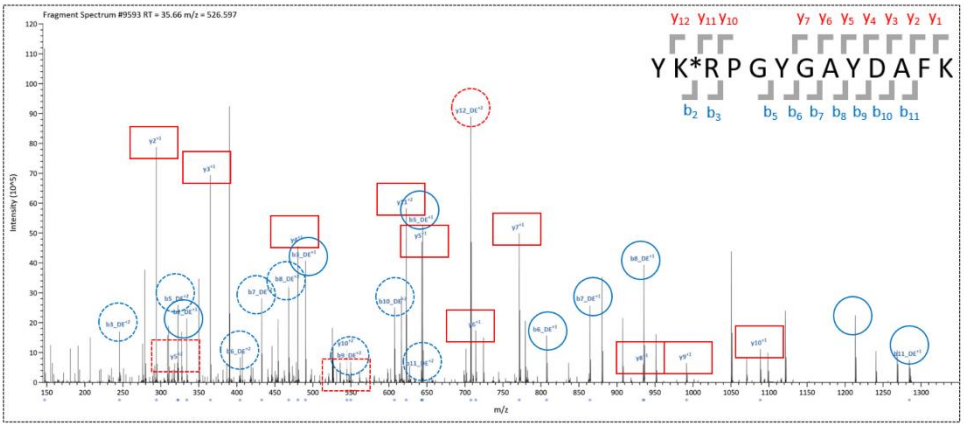

Figure 56: Purification steps and MS analysis of heIF2α-143Ack-188. 1) Metal affinity chromatography. The first peak represents the non-specific binding to the resin released by 10 mM of imidazole. During the gradient two peaks are observed: the first peak, which corresponds to the chaperones GroEL-GroES, and the second peak which corresponds to the acetylated heIF2α-188. 2) Ion exchange chromatography. 3) SDS-PAGE analysis after ion exchange chromatography. 4) Electrospray ionization mass spectrometry demonstrates that heIF2a is homogeneously acetylated. MS analysis of native eIF2a-188 revealed a mass of 23982.4 Daltons (calculated 23981.3) whereas eIF2a-Ack143-188 revealed a mass of 24024.5 Daltons. The smaller peaks to the right of the main peak of native eIF2a-188 correspond to Na-adducts. The mass difference observed (42.1 daltons) corresponds to the expected mass difference for an acetyl group. 5) MS/MS Collision induced dissociation of heIF2a-Ack143-STOP188. The sequence of a tryptic peptide corresponding to residues Y142 to K154 is shown (top). K is acetyl-lysine. Red squares are for y ions not carrying the acetyl-lysine whereas the red circle is for the y ion carrying the acetyl-lysine. Solid lines correspond to monocharged ions and the dotted lines to dicharged ions.Blue circles are for the b ions carrying the acetyl-lysine. Solid lines correspond to monocharged ions and the dotted lines to dicharged ions. The y12 ion contains the acetyl-lysine, while the following ions are devoid of acetylation. All detected b-ions (b2-b11) also contain an acetyl-lysine.*

In a similar manner to WT heIF2α, the acetylated form was more soluble in the presence of high NaCl concentrations (>500 mM NaCl).

We were also able to produce heIF2α-143AcK-303. As predicted, it was produced in much lower quantities, but as heIF2α-303 it could withstand lower NaCl concentrations (around 150 mM). The final yield was around 3-4 mg/L for heIF2α-143AcK-188 and 0.5-1 mg/L for heIF2α-143AcK-303 per liter of culture.

Plasmids produced during this thesis work	**Source plasmid**	**Product description**
pET15b-heIF2α-188	pET15b-lpa-Amp^{R} (This lab)	Human eIF2α domains 1 and 2, TAA at position 188
pET15b-heIF2α-303	pET15b-lpa-Amp^{R} (This lab)	Human eIF2α domains 1, 2 and 3 UGA at position 303
pCDF-tRNA^{CUA}-pylT-heIF2α-141AcK-188	pCDF-tRNACUA-pylT-Sm^{R} (Chin lab)	1) Human eIF2α domains 1 and 2, TAG at position 141. TAA at position 188. 2) Mb-tRNA^{CUA}
pCDF-tRNA^{CUA}-pylT-heIF2α-143AcK-188	pCDF-tRNACUA-pylT-Sm^{R} (Chin lab)	1) Human eIF2α domains 1 and 2, TAG at position 143. TAA at position 188. 2) Mb-tRNA^{CUA}
pCDF-tRNA^{CUA}-pylT-heIF2α-141AcK-303	pCDF-tRNACUA-pylT-Sm^{R} (Chin lab)	1) Human eIF2α domains 1 and 2, TAG at position 141. UGA at position 303. 2) Mb-tRNA^{CUA}
pCDF-tRNA^{CUA}-pylT-heIF2α-143AcK-303	pCDF-tRNACUA-pylT-Sm^{R} (Chin lab)	1) Human eIF2α domains 1 and 2, TAG at position 143. UGA at position 303. 2) Mb-tRNA^{CUA}
pCDF-tRNA^{CUA}-pylT-heIF2α-141/143AcK-188	pCDF-tRNACUA-pylT-Sm^{R} (Chin lab)	1) Human eIF2α domains 1 and 2, TAG at position 141 and 143. UGA at position 303. 2) Mb-tRNA^{CUA}

Table 3: List of plasmids used and designed to produce the different acetylated versions of heIF2α.

1.4 Design of heIF2α variants mimicking acetylation

The use of acetylated substrates is expected to provide valuable information about the function of the acetyl group. However, the yields obtained with orthogonal systems such as the one used in this thesis work, are often very low. Therefore, amino acid substitutions have been extensively used to mimic the PTM state of a protein. These mimics offer an advantage in terms of yield and cost, as these mimics use canonical amino acids and do not require special orthogonal systems to be produced. Indeed, the production of acetylated heIF2α requires extensive optimization and use of expensive

resources (acetyl-lysine and NAM to inhibit the bacterial deacetylase in the culture media).

Mimics have been used extensively throughout the literature, a great example is the deciphering of the histone code thanks to methylation, acetylation and phosphorylation mimics (White, Keberlein and Jackson, 2012). The principle of mimic use is to choose an amino acid that resembles the desired PTM in charge, size, and structure (figure 57).

We designed two variants of heIF2α with a glutamine in place of the lysine to mimic acetyl-lysine (K141Q and K143Q). These variants, either heIF2α-188 or heIF2α-303, followed the same purification protocol as the wild-type protein, obtaining a similar protein yield.

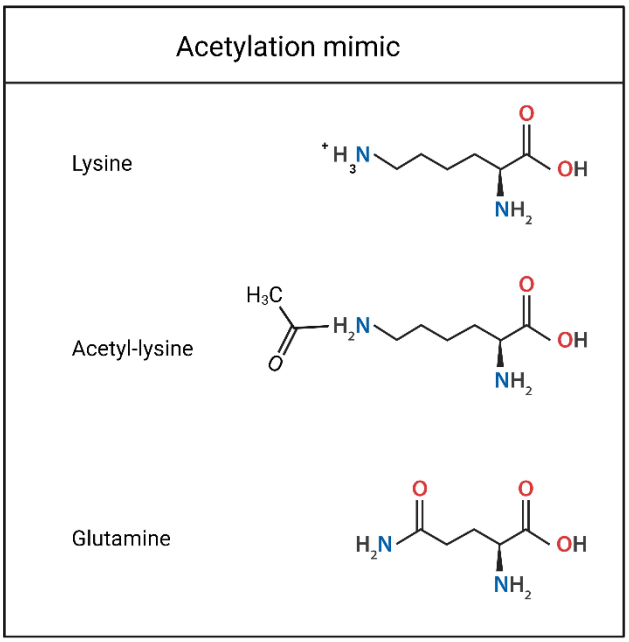

Figure 57: Use of glutamine as an acetylation mimic.

Plasmids produced during this thesis work	Source plasmid	Product description
pET15b-heIF2α-K141Q-188	pET15b-heIF2α-188	Human eIF2α domains 1 and 2, K141Q and TAA at position 188
pET15b-heIF2α-K143Q-188	pET15b-heIF2α-188	Human eIF2α domains 1 and 2, K143Q and TAA at position 188
pET15b-heIF2α-K141Q-303	pET15b-heIF2α-303	Human eIF2α domains 1, 2 and 3, K141Q and TAA at position 303
pET15b-heIF2α-K143Q-303	pET15b-heIF2α-303	Human eIF2α domains 1, 2 and 3, K143Q and TAA at position 303

Table 4: Plasmids corresponding to heIF2α-188 and heIF2α-303 acetylation mimics.

1.4.1 Optimization of heIF2α-K143Q-188 buffer conditions:

As observed for heIF2α-188, heIF2α-K143Q-188 precipitated when exposed to low salt concentrations. To increase its solubility, we always store it in a buffer containing 500 mM NaCl. The maximum concentration we could reach before precipitation is 2 mg/mL.

As for the WT protein we performed a Thermal Shift Assay with a range of NaCl concentration and different pHs (figure 58). Because of heIF2α-K143Q-188 pI value (7.16) we chose to study higher pHs. The results showed that higher pHs didn't significantly change the Tm values, but that again, high salt concentrations were required.

The optimal buffer was defined as 500 mM NaCl, 2% glycerol, 10 mM $MgCl_2$, and pH 8.5. Using this buffer, we could concentrate the protein up to 5-10 mg/mL.

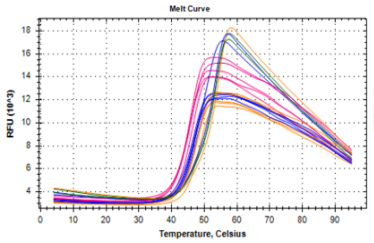

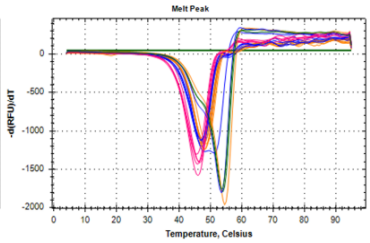

	1	2	3	4
NaCl	0	100	250	500
HEPES 8	46	47	47	53.5
HEPES 8.5	46	47	48	53.5
TRIS 8	46.5	47	48	54.5
TRIS 8.5	45.5	47	48	54
Phosphate 8	45	48	48	51

Figure 58: Thermal shift assays for heIF2α-K143Q-188 buffer optimization. On the left, the curves in pink, blue, orange, and green correspond to 0, 100 mM, 250 mM, and 500 mM, respectively. On the right, the Tm values obtained for the TSA.

1.4.2 Phosphorylation mutants

The interplay between acetylation and phosphorylation of heIF2α is still not understood. There are different ways to phosphorylate heIF2α: enzymatic methods using one of the kinases described in the introduction, or the use of orthogonal systems that allow the introduction of phosphoserine to the genetic code. The chin lab has developed a system, akin to the one described in previous sections, to introduce phosphoserine into a protein sequence (Rogerson *et al.*, 2015). However, this system also relies on the use of the amber codon to introduce phosphoserine, so it is not compatible with the orthogonal system we used to introduce acetylation.

To study the influence of this phosphorylation, we decided to produce variants of heIF2α carrying a phosphorylation mimic in place of S52. A good phosphoserine mimic is aspartic acid, as it is also negatively charged and has a similar structure to phosphoserine, although less bulky (figure 59).

Since we wanted to study the interplay between acetylation and phosphorylation, we introduced the S52D mutation onto the acetyl-mimic heIF2α-K141/143Q-188/303 and onto heIF2α-143AcK-188/303. The production of heIF2α-S52D-143Ack-188/303 allows us to test the influence of the phosphomimic on the deacetylation rate by SIRT1.

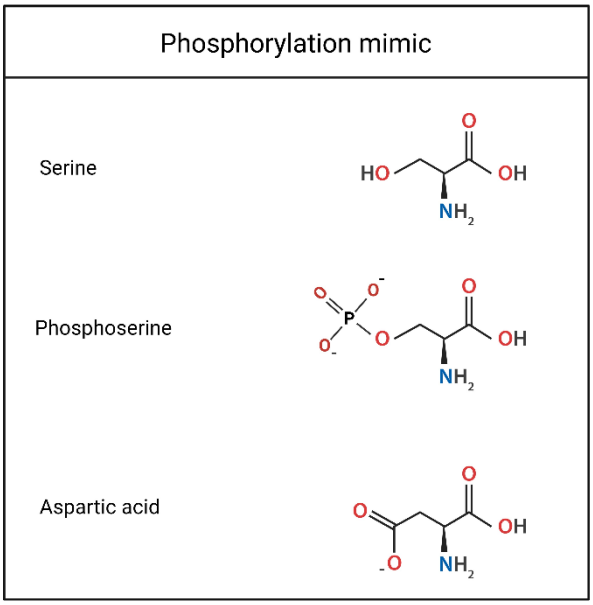

Figure 59: Phosphorylation mimic example. Depiction of serine, phosphoserine, and the amino acid of choice, aspartic acid, to mimic phosphorylation.

Plasmids produced during this thesis work	Source plasmid	Product description
pET15b-heIF2α-S52D-188	pET15b-heIF2α-188	Human eIF2α domains 1 and 2, S52D and TAA at position 188
pET15b-heIF2α-S52D-303	pET15b-heIF2α-303	Human eIF2α domains 1, 2, and 3. S52D and TAA at position 303
pET15b-heIF2α-S52D-K141Q-188	pET15b-heIF2α-188	Human eIF2α domains 1 and 2, S52D, K141Q, and TAA at position 188
pET15b-heIF2α-S52D-K143Q-188	pET15b-heIF2α-188	Human eIF2α domains 1 and 2, S52D, K143Q, and TAA at position 188
pET15b-heIF2α-S52D-K141Q-303	pET15b-heIF2α-303	Human eIF2α domains 1, 2, and 3. S52D, K141Q, and TAA at position 303
pET15b-heIF2α-S52D-K143Q-303	pET15b-heIF2α-303	Human eIF2α domains 1, 2, and 3. S52D, K143Q, and TAA at position 303
pCDF-tRNACUA-pylT-heIF2α-S52D-141AcK-188	pET15b-heIF2α-188	1) Human eIF2α domains 1 and 2. S52D, TAG at position 141, and TAA at position 303 2) Mb-tRNA^{CUA}
pCDF-tRNACUA-pylT-heIF2α-S52D-143AcK-188	pET15b-heIF2α-188	1) Human eIF2α domains 1 and 2, S52D, TAG at position 143, and TAA at position 188 2) Mb-tRNA^{CUA}
pCDF-tRNACUA-pylT-heIF2α-S52D-143AcK-303	pET15b-heIF2α-303	1) Human eIF2α domains 1, 2, and 3. S52D, TAG at position 143, and TAA at position 303 2) Mb-tRNA^{CUA}

Table 5: List of plasmids used and designed to produce the different acetylated versions of heIF2α carrying the S52D phosphorylation mimic mutation.

1.5 Conclusion

Most of the catalytic data obtained for SIRT1's activity comes from the study of mimic peptide substrates. The number of studies with native substrates of SIRT1 is very small, and most studies using peptides are with substrates derived from p53, histone H4, or FOXO. heIF2α is a newly identified substrate of SIRT1 of which there is no catalytic information to date, therefore there is a great interest in obtaining information on the interaction between these two proteins.

The use of orthogonal systems to introduce a PTM offers a great advantage as 100 % of the product is acetylated. A study by Pacholec et al., 2010, estimated the enzymatic parameters of SIRT1 on an acetylated full length p53, however, this product was only 30-70% acetylated. By using an orthogonal system to produce a consistently acetylated product we can expect to accurately measure the catalytic activity of SIRT1 on heIF2α deacetylation.

On the other hand, mimics are useful not only for optimization that requires great amounts of protein, but they can also be useful to obtain preliminary data on the structure and behavior of the acetylated counterpart, or the phosphorylated one in the case of the S52D mutants.

Part 2: Production and characterization of hSIRT1

2.1 Production of SIRT1 variants: hSIRT1, miniSIRT1, ΔN-miniSIRT1

To improve crystallization trials and structural studies, a miniSIRT1 was developed by Dai et al., 2015. This construct was able to deacetylate a substrate-derived acetylated peptide with comparable rates to SIRT1. In addition, this enzyme could be co-crystallized with its substrate (Dai *et al.*, 2015). Since then, other miniSIRT1 have been produced. The main difference between these sirtuins is the length of their N-terminal domain.

For this thesis, we produced different variants of hSIRT1.

- hSIRT1: the wild-type full-length protein (747 amino acids). The gene coding for hSIRT1 was subcloned onto a pET15-b Amp^R plasmid.
- miniSIRT1: a protein construct with the minimal domains to facilitate crystallization. Also used to determine catalytic parameters in most enzymatic studies. This enzyme contains the same domains as Cao et al., 2015. N-terminal: 143-240. CAT: 241-511 and CTR: 641-665 (391 amino acids). The gene coding for miniSIRT1 was subcloned onto a pET15-b Amp^R plasmid. Additionally, two variants were derived from this construct: miniSIRT1-H363A and miniSIRT1-H363L, two catalytic mutants of the native miniSIRT1.
- ΔNminiSIRT1: this construct was used both for crystallization and determination of catalytic parameters. It does not contain the N-terminal domain, just the CAT and the CTR. CAT: 241-511and CTR: 641-665 (294 amino acids). This variant was obtained by PCR-mediated deletion of the N-terminal domain sequence in the gene coding for miniSIRT1.

Notably, in Dai et al., 2015, the researchers substituted four cysteins for serines in miniSIRT1 to improve the solubility of the protein. Our two miniSIRT1 constructs have C→A substitutions instead of the serine ones.

Purification of hSIRT1 and miniSIRT1 is performed in three chromatographic steps (metal affinity, anion exchange and gel filtration, see materials and methods) and purification of ΔNminiSIRT1 in two steps (metal affinity and anion exchange). The figures below show SDS-PAGE analysis after the last step of purification of the three SIRT1 forms (figure 60).

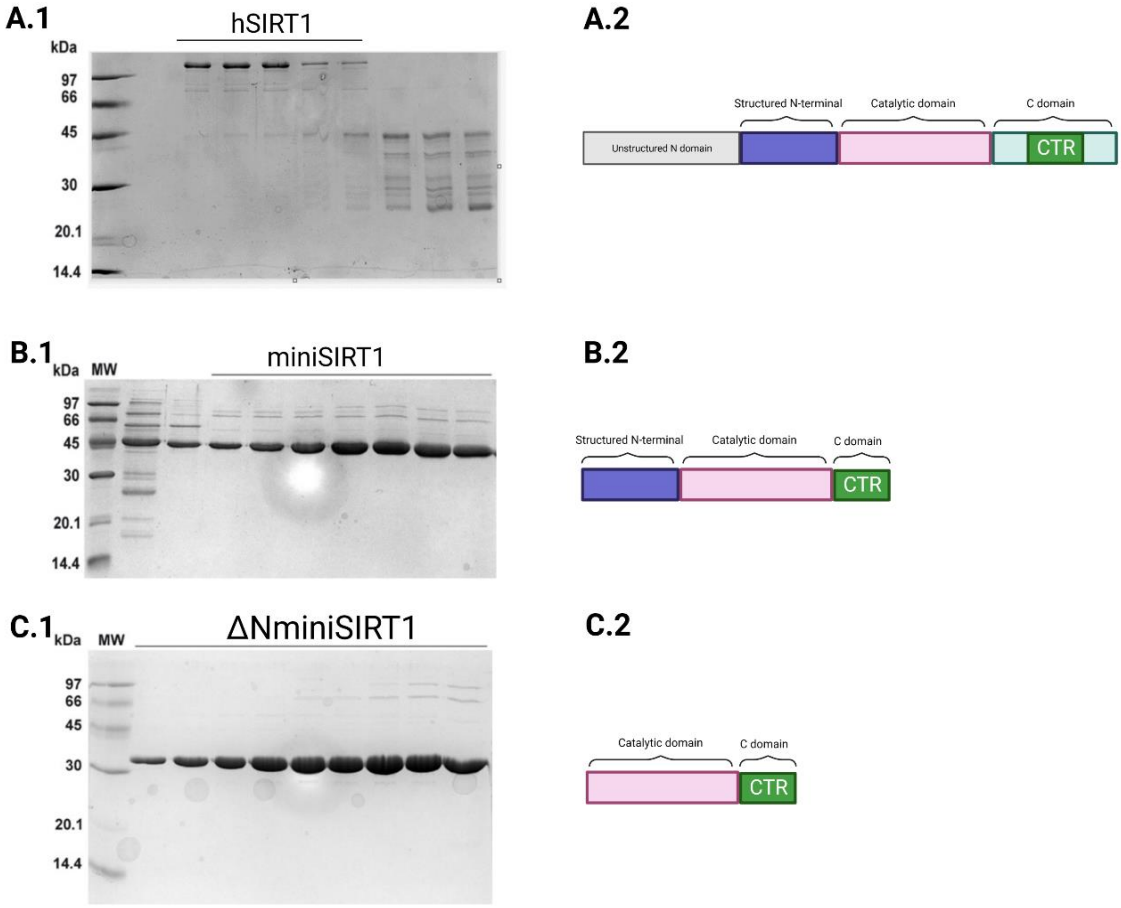

Figure 60: Purification of the different SIRT1 variants. A1) SDS-PAGE analysis after the final step of purification. hSIRT1 yield is lower than that of the miniSIRT1 version. A2) Schematic depiction of hSIRT1 structural domains. B.1) miniSIRT1 SDS-PAGE analysis after the last step of purification. B.2) Schematic depiction of miniSIRT1 structural domains. C.1) SDS-PAGE analysis after the final step of purification of ΔNminiSIRT1. C.2) Schematic depiction of ΔNminiSIRT1 structural domains.

2.2 Characterization of SIRT1's enzymatic activity

To characterize SIRT1 catalytic activity, we designed an enzymatic test based on a sirtuin enzymatic test developed by Smith et al., 2008. This is a three-step coupled assay in which the deacetylation reaction by the sirtuin is the limiting step, followed by two fast reactions by the nicotinamidase and the glutamate dehydrogenase enzymes. The reaction is followed by the consumption of NADPH, a substrate of the last step.

The reaction works as follows: SIRT1, in the presence of NAD^+ and the acetyl group from the substrate, catalyzes the deacetylation reaction, producing the AADPR intermediate, the deacetylated product, and nicotinamide. This last product, nicotinamide, is the substrate of the next enzyme, nicotinamidase. Nicotinamide is cleaved into nicotinic

acid and ammonia. This ammonia is consumed by the third enzyme, glutamate dehydrogenase (GDH) in the presence of α-ketoglutarate and NADPH, producing $NADP^+$ and glutamate (figure 61). NADPH absorbs at 340 nm, but not the product of the GDH reaction $NADP^+$. Therefore, NADPH consumption can be followed by measuring the decrease of A340nm absorbance and a rate can be deduced. Provided that the deacetylation rate is the limiting step, the rate corresponds to that of SIRT1. This will be assessed by using two different SIRT1 concentrations and checking linearity.

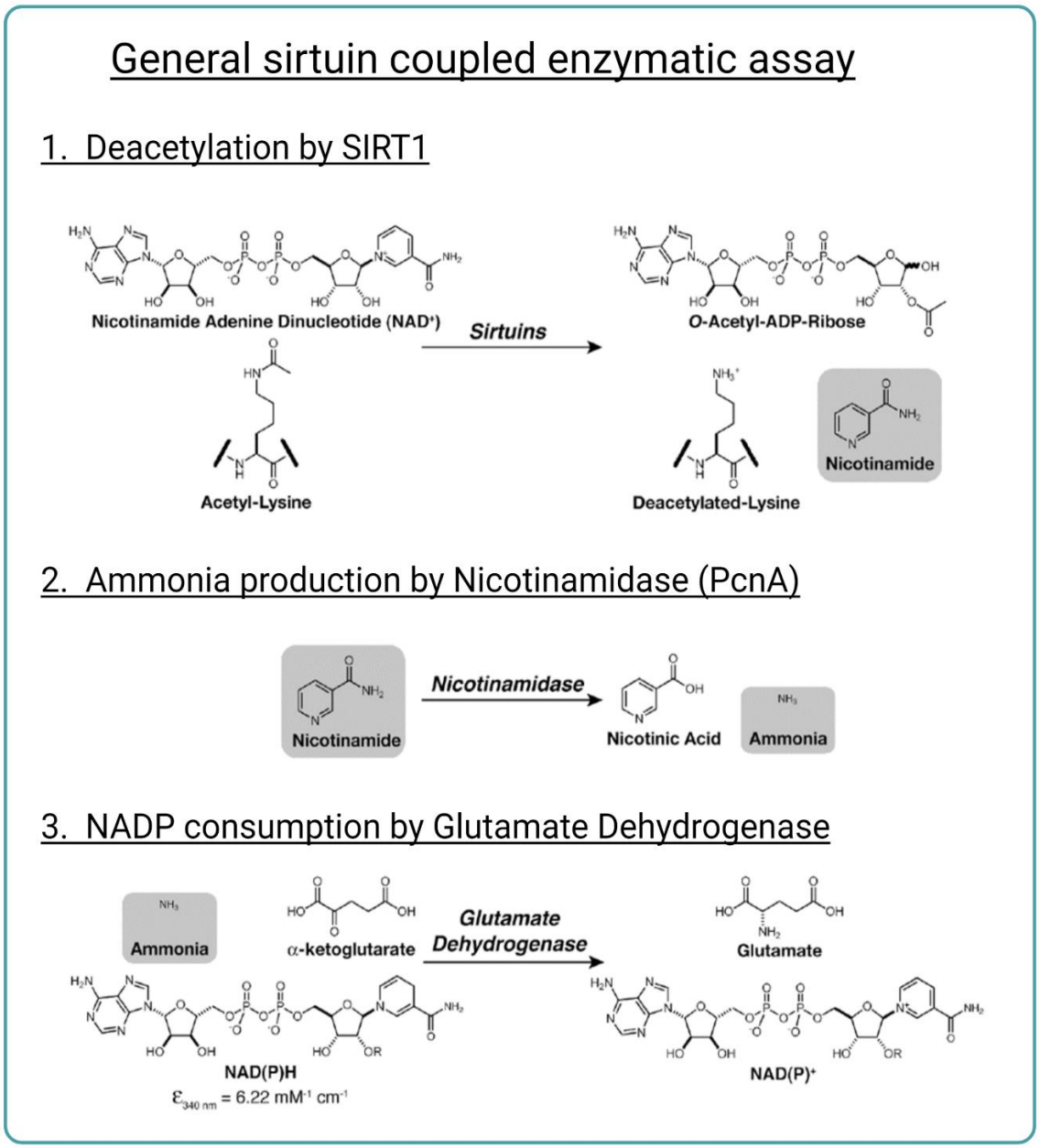

Figure 61: Outline of the three-step coupled assay used for calculating miniSIRT1's enzymatic parameters. 1) The first step is the limiting step, as sirtuins are considerably slower than the nicotinamidase or the GDH enzymes. SIRT1 requires an acetylated group/substrate and NAD+ for this first reaction, rendering the AADPR intermediate, the deacetylated product and nicotinamide. 2) Nicotinamide is the only substrate for the next reaction catalyzed by nicotinamidase, producing nicotinic acid and ammonia. 3) The resulting ammonia is then used by the GDH, alongside α-ketoglutarate and NADPH, as substrates. NADPH absorbance can be tracked at 340 nm, diminishing when it is transformed into NADP. Image modified from Smith et al 2008.

This experiment was performed with a range of acetylated substrate, in the case described below, the acetylated mimic peptide, up to saturating concentrations.

Three conditions are tested per concentration of substrate: one without any enzyme, one with 0.25 µM SIRT1, and the third with 0.5 µM SIRT1. In the beginning the three conditions are prepared adding NADPH, the acetylated substrate at 2X the

desired concentration, a master mix containing NAD^+, nicotinamidase, GDH, and α-keto glutarate. No enzyme is added at this stage (Figure 62-1).

The three conditions, three cuvettes, are placed in the spectrophotometer and the absorbance is controlled until it stabilizes, which occurs between the one and the six-minute mark (60-400s). At this time, we added SIRT1, and the buffer in the case of the blank, triggering the reaction. Between SIRT1 addition and the start of the kinetic, data collection was stopped. From this point onwards the absorption line diminishes in the experiments where the enzyme has been added, but the blank remains stable (figure 62-2). The initial velocities for each point are calculated at the linear part of the curve. The slopes for these curves represent the v_i (figure 62-3). Each v_i is plotted against SIRT1 concentration (figure 62-4) to deduce the $v_i/[E_T]$ parameter. Finally, experimental $v_i/[E_T]$ were fitted with a simple Michaelis-Menten curves using Graph-Pad (Figure 62-5).

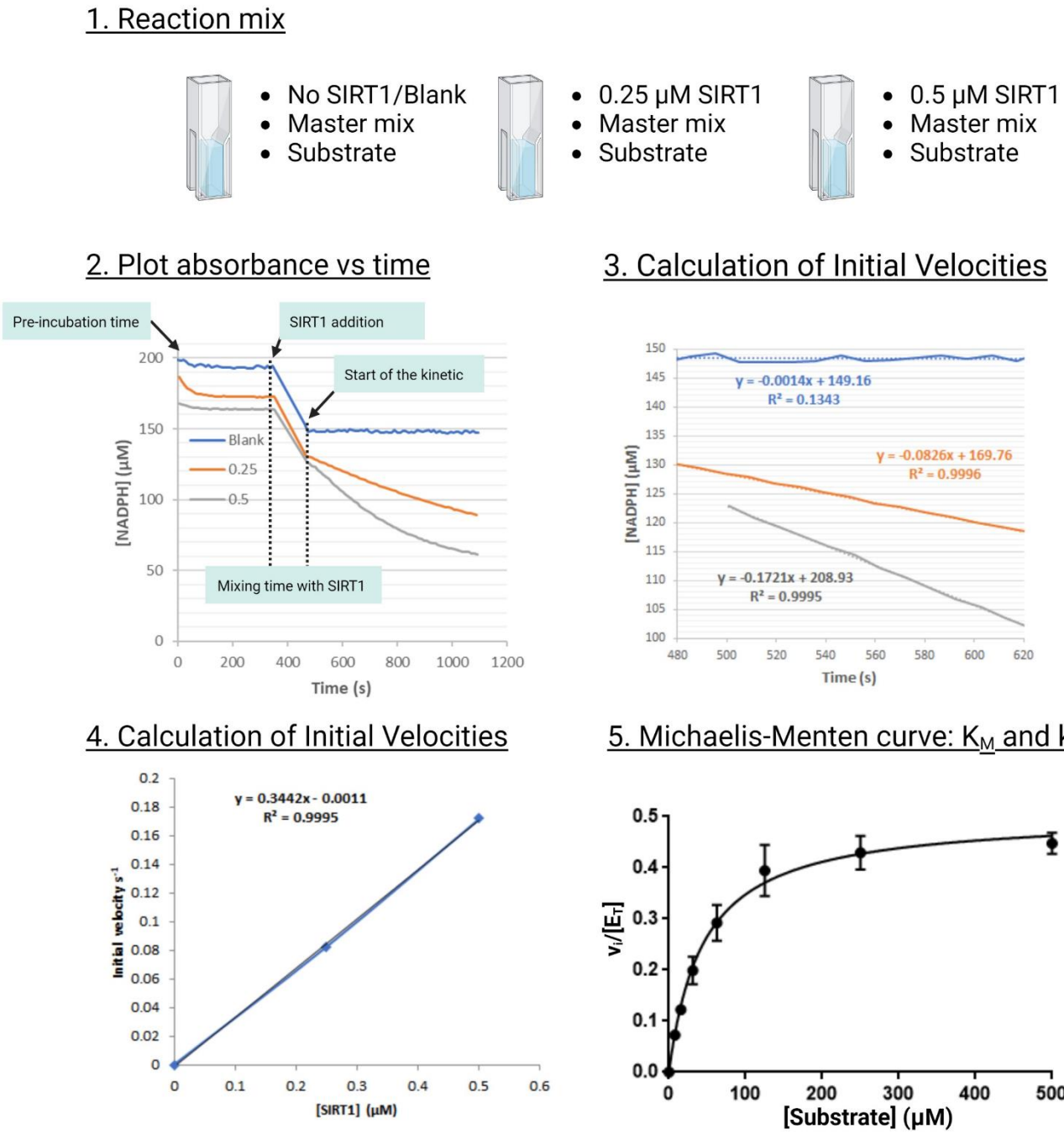

Figure 62: Experimental design of the SIRT1 deacetylation enzymatic test. 1) Three experimental conditions are prepared per concentration of substrate peptide. All reactants but SIRT1 are added. 2) SIRT1 is added, or buffer in the case of the control. During SIRT1 mixing time no data is collected, hence the decrease in absorbance obtained between SIRT1 addition and the start of the kinetic. 3) The slope of the experimental curves obtained determine the vi. 4) Plotting the v_i per condition results in a straight line. The slope of this line is the $v_i/[E_T]$ corresponding to a specific substrate concentration. 5) Plotting of the $v_i/[E_T]$ against their corresponding substrate concentration renders a Michaelis-Menten type curve, with which catalytic parameters can be determined.

2.2.1 Calculation of catalytic parameters using the Michaelis-Menten approach:

The Michaelis-Menten equation allows the determination of enzyme parameters of simple systems. In our conditions in the coupled assay, the limiting step of the reaction only depends on SIRT1 activity. We have determined that this is the case for vi up to 0.22 µM of oxidized NADPH per second. Moreover, we used saturating concentrations of NAD^+ (10 times above the published K_M values, around 90 µM (Nakamura *et al.*, 2021)) in order that SIRT1 v_i only depends on acetylated substrate concentrations.

Using the Michaelis-Menten equation, $\frac{v_i}{[E_T]} = \frac{k_{cat}\,[S]}{K_M + [S]}$, we are able to determine two different parameters: K_M, the Michaelis-Menten constant, which is defined as the substrate concentration (acetylated peptide) at which the rate of the reaction is half the maximum rate; and k_{cat}, known as the catalytic constant or turnover number, which is the number of times each enzyme site converts substrate to product per unit of time.

2.2.2 Catalytic parameters with mimic acetylated peptides

Some pioneering studies of SIRT1's catalytic activity on acetylated peptides gave an insight into SIRT1's enzymatic activity, especially the experiments that show the effect of STACs on SIRT1's activity (Dai *et al.*, 2010). However, these studies use peptides bound to fluorophores, like the AMC or TAMRA fluorophores, that put in question the validity of these results. This is because, as explained in previous sections, some researchers claimed that the STAC effect on SIRT1's activity was due to the binding of the STAC to the fluorophore and had nothing to do with the 'real' substrates (Pacholec *et al.*, 2010). Considering these concerns, model acetylated peptides used in further SIRT1 studies contained a tryptophan (W) in their sequence in replacement of the fluorescent group, as the aromatic moiety of this amino acid favors the affinity of the peptide for SIRT1.

In our study, we designed acetylated peptides corresponding to lysines 141 or 143 of the original region of heIF2α surrounding these lysines (this is the native sequence, except for the acetylation introduced in place of lysine). To study the importance of the length of the peptide in SIRT1 activity, we designed two different peptides containing either 7 amino acids or 15 (table 6). These peptides, as well as the coupled enzymatic assay will allow us to deduce information on SIRT1 activity not biased by the use of non-natural peptides.

Name	Sequence	Mimicking
TG-15	TAWVFDDKYKRPGYG	Original sequence with no changes
TG-15 (141)	TAWVFDD(AcK)YKRPGYG	Acetylation on lysine 141
TG-15 (143)	TAWVFDDKY(AcK)RPGYG	Acetylation on lysine 143
FR-7 (141)	FDD (AcK)YKR	Acetylation on lysine 141
DG-7 (143)	DKY(AcK)RPG	Acetylation on lysine 143
TG-15 (141A, 143AcK)	TAWVFDDAY(AcK)RPGYG	Acetylation on lysine 143, K141A

Table 6: Acetylated peptides used for SIRT1 enzymatic tests.

We performed a first set of experiments using the TG-15 (143) peptide and the three SIRT1 variants miniSIRT1, ΔNminiSIRT1, and SIRT1. With miniSIRT1 we measured a k_{cat} value of 0.32 ± 0.01 s^{-1} with a K_M of 8.6 ± 1.3 µM (table 7). This value is in reasonable agreement with the values measured with miniSIRT1 in previous studies with other peptide substrates, see section 4.4 of the introduction (Dai *et al.*, 2015); (Smith, Hallows and Denu, 2009); (Cao *et al.*, 2015). Moreover, the catalytic parameters of miniSIRT1 are similar to those measured with the native SIRT1 enzyme. A small drop in the k_{cat} is observed (0.17 compared to 0.32), however, considering the low purity of SIRT1, the rate value is likely underestimated. This result confirms that miniSIRT1 is a good model enzyme to study catalytic parameters with model substrates.

Finally, we compared miniSIRT1 with ΔNminiSIRT1. The K_M value as well as the k_{cat} are slightly increased, suggesting that the N-domain participates in the binding of TG-15 (143).

	miniSIRT1	ΔNminiSIRT1	SIRT1
K_M (µM)	8.6 ± 1.3	14.1 ± 1.6	5.3 ± 1.3
k_{cat} (s^{-1})	0.32 ± 0.01	0.47 ± 0.01	0.17 ± 0.01 *

Table 7: Enzymatic parameters obtained with the three different SIRT1 variants and TG-15 (143) peptide. The k_{cat} value estimated for SIRT1 is underestimated due to low purity levels.

In a second set of experiments, we varied the length, the sequence, and the position of the acetyl group in the peptide substrates. First, using miniSIRT1, we compared the catalytic parameters with TG-15 (143) and TG-15 (141) peptide. As shown in table 8, whereas the k_{cat} value for TG-15 (141) and TG-15 (143) are close (0.21 s^{-1} as compared to 0.33 s^{-1}). The K_M value of TG-15 (141) is 10 times higher than that of TG-15 (143) (89 ± 4 µM as compared to 8.6 ± 1.3 µM). This shows that the sequence of TG-15 (143) is more favorable for the binding of the acetylated group to miniSIRT1.

With a shorter peptide DG-7 (143) the K_M value is increased by a factor of 5.2 and the k_{cat} by a factor of 1.6 as compared to the longer peptide TG-15 (143). This shows that the length of the peptide impacts its binding to miniSIRT1. This is also true for the

catalytic parameters of miniSIRT1 determined for TG-15(141) and FR-7 (141). Notably with DG-7 (143), the k_{cat} and K_M values are very similar for miniSIRT1 and ΔNminiSIRT1. This indicates that the presence of the N-domain has no influence in the binding of the short peptide.

To better understand the specificity of TG-15 (143) binding to miniSIRT1, we designed a TG-15 peptide acetylated in position 143 with an alanine in position 141 (TG-15 141A, 143AcK). We observed a slight increase in the K_M and k_{cat} values as compared to TG-15 (143). These results suggest that K141 contributes to TG-15 (143) binding affinity (table 8).

Length	Peptide	N	k_{cat} (s^{-1})	K_M (µM)	SIRT1 variant
Short	FR-7 (141)	3	0.29 ± 0.02	340 ± 60	miniSIRT1
	DG-7 (143)	2	0.50 ± 0.02	45 ± 7	miniSIRT1
		3	0.52 ± 0.03	52 ± 8	ΔNminiSIRT1
Long	TG-15 (141)	3	0.21 ± 0.003	89 ± 4	miniSIRT1
	TG-15 (143)	2	0.32 ± 0.01	8.6 ± 1.3	miniSIRT1
	TG-15 (143)	2	0.47 ± 0.01	14.1 ± 1.6	ΔNminiSIRT1
	TG-15 (143)	2	0.17 ± 0.01 *	5.3 ± 1.3	SIRT1
	TG-15 (141A, 143AcK)	1	0.50	21.5	miniSIRT1

Table 8: Enzymatic parameters obtained for different SIRT1 variants and different acetylated peptides using the classic Michaelis-Menten model.

Interestingly, in the case of the TG-15 peptides independently of the SIRT1 variant, a descent on v_i was observed at high substrate levels, suggesting a possible inhibition by substrate (figure 63). We recalculated the Michaelis-Menten parameters for these peptides according to the substrate inhibition model (table 9). In this model, the k_{cat} is increased in all cases.

	Classic Michaelis-Menten		Substrate inhibition			
Peptide	k_{cat} (s^{-1})	K_M (µM)	k_{cat} (s^{-1})	K_M (µM)	Ki	SIRT1 variant
TG-15 (143)	0.32 ± 0.01	8.6 ± 1.3	0.37 ± 0.02	11.7 ± 2.0	1400 ± 600	miniSIRT1
TG-15 (141A, 143AcK)	0.50	21.5	1.06	76.4	300	miniSIRT1
TG-15 (143)	0.47 ± 0.01	14.1 ± 1.6	0.61 ± 0.02	17.9 ± 1.8	1400 ± 300	ΔNminiSIRT1
TG-15 (143)	0.17 ± 0.01 *	5.3 ± 1.3	0.21 ± 0.01	8.2 ± 1.9	1000 ± 500	SIRT1

Table 9: Enzymatic parameters obtained for different SIRT1 variants and different acetylated peptides using the substrate inhibition model.

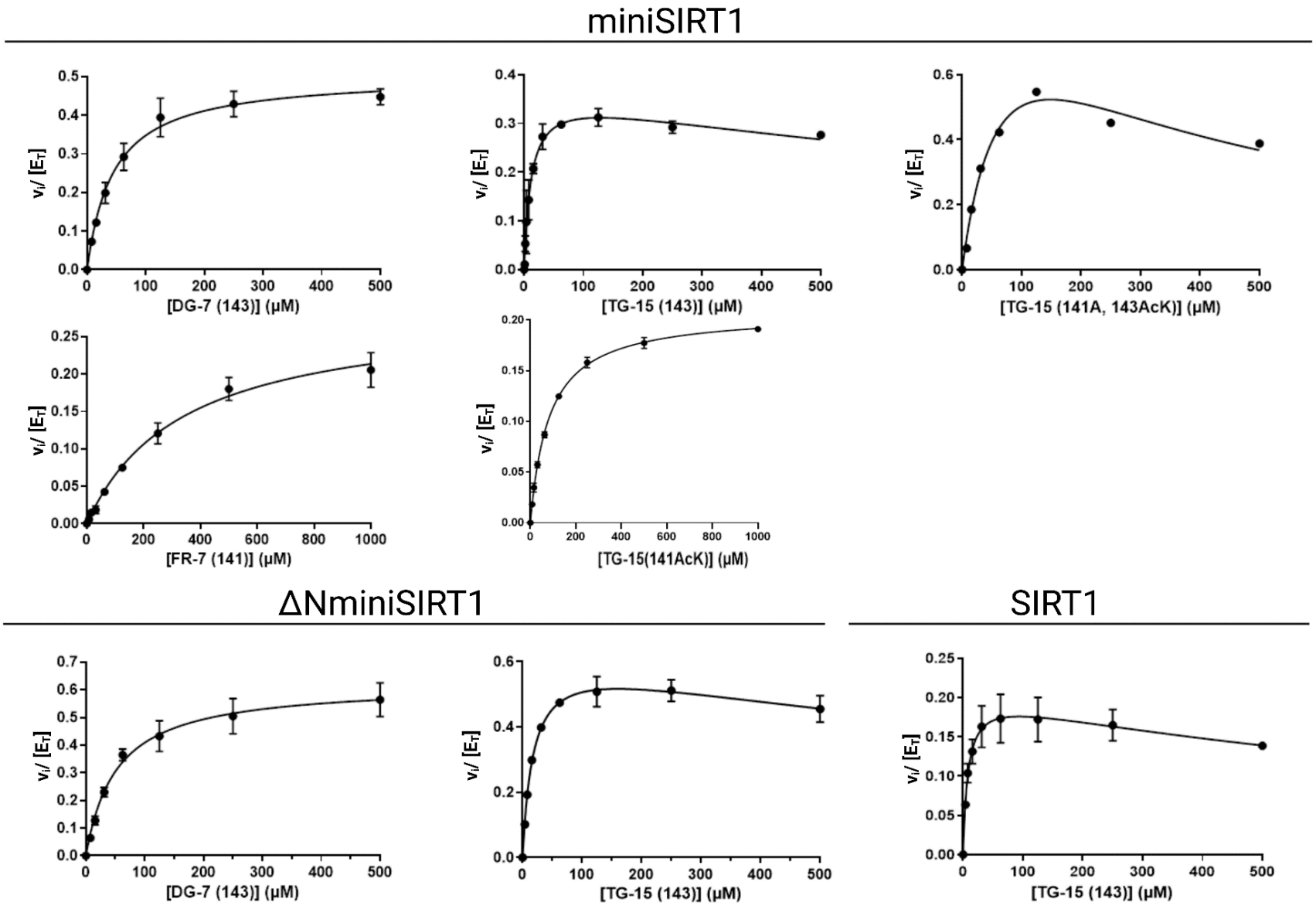

Figure 63:Michaelis-Menten curves for the different SIRT1 variants and their corresponding substrate peptides.

2.2.3 Influence of STACs on miniSIRT1 catalytic activity

STACs are molecules that modify a substrate's binding affinity for SIRT1 (Michan and Sinclair, 2009). This is evidenced by comparison of K_M values measured with and without STACs. To test the effect of STACs on a mimic peptide substrate K_M value, TG-15 (143), we performed the above-mentioned coupled enzymatic test, and added different STACs at 20 µM final concentration. These STACs are: ferulic acid (FrA), pterostilbene (Pts), an tyrosol (Tyr), the same used by our collaborator in their study (Monceaux *et al.*, 2022), as well as resveratrol and STAC-3. In cells studies these STACs were shown to protect cardiomyocytes from ER stress-induced apoptosis by regulating the PERK pathway through SIRT1-mediated deacetylation of eIF2α. However, as shown in the figure below, we did not observe any significant improvements in the K_M values for TG-15 (143) due to the addition of these STACs in our experiments performed with miniSIRT1 and TG-15 (143) (table 10; figure 64).

STAC	k_{cat} (s^{-1})	K_M (µM)
Resveratrol (RSV)	0.34	10.3
Ferulic Acid (FrA)	0.3	7.4
STAC-3	0.33	10.3
Tyrosol (Tyr)	0.3	15.5
Pterostilbene (Pts)	0.33	14.9
Reference TG-15 (143)	0.32	8.6 ± 1.3

Table 10: Catalytic parameters calculated per STAC compound with miniSIRT1 and TG-15 (143).

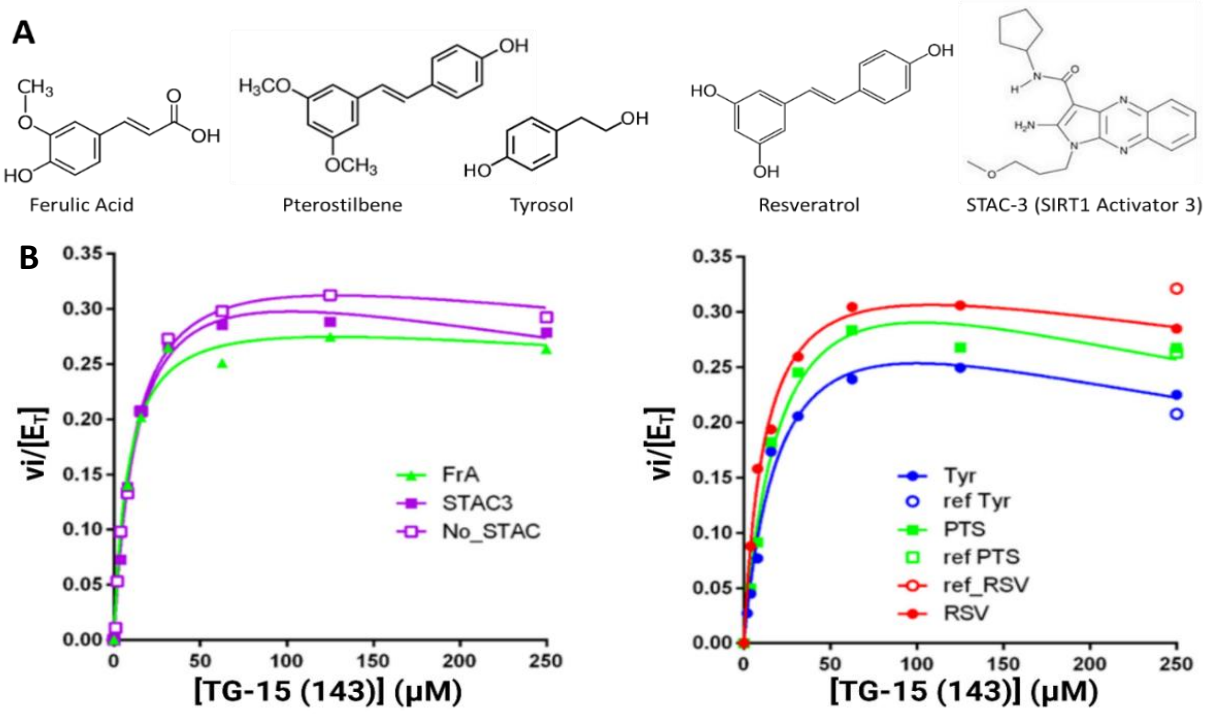

Figure 64: A) STACs used during this test and their formulas. B) Enzymatic curves obtained per STAC compound. Per experiment a control was performed at the highest peptide concentration, this control is depicted in the same color outline but without fill.

2.3 Measurement of the dissociation constant (K_D):

The K_D is a direct measurement of the binding affinity of a ligand to a protein. The lower the K_D the higher the affinity (figure 65). To measure the dissociation constant (K_D) of miniSIRT1: acetylated complexes, we used Thermal Shift Assays (TSA) and isothermal titration calorimetry (ITC).

$$E + L \underset{k_{-1}}{\overset{k_1}{\rightleftharpoons}} EL \qquad\qquad Kd = \frac{k_{-1}}{k_1}$$

Figure 65: Definition of K_D. E stands for enzyme and L for ligand. Because of the way it is defined, the lower the K_D the higher the affinity.

TSA was performed with TG-15 (143) and miniSIRT1, in the presence or absence of nicotinamide. The determination of the K_D value was performed as described in the article presented at the end of this manuscript. The obtained K_D values are 17 µM and 26 µM (figure 66), seeing no obvious positive effect of the presence of nicotinamide on the binding of the peptide.

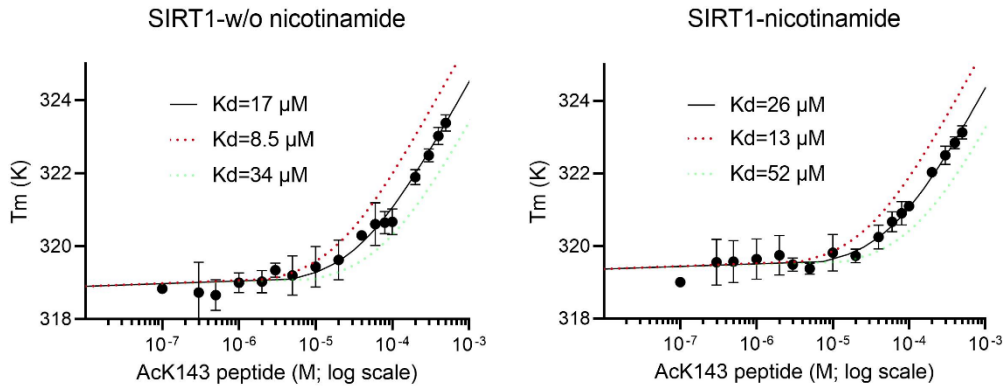

Figure 66: Estimation of K_D values. Each panel plots the measured Tm value (mean ± sd from at least two experiments) as a function of acetylated peptide in log scale. The best fit to a curve calculated as described in Materials and Methods (Pantoliano et al, 2001; Matulis et al, 2005; Cimmperman et al, 2008; Zubriené et al, 2009; Redhead et al; 2015) is drawn with a solid line. The corresponding K_D value is shown on the panel. Curves obtained with a K_D value two-fold higher (green) or lower (red) are also drawn for comparison. On the left TG-15(143) binding to miniSIRT1 and on the right TG-15(143) binding to miniSIRT1 in the presence of nicotinamide (500 µM).

The thermodynamic model for TSA data processing and K_D measurements assumes a two state-reversible unfolding behavior. Therefore, we also used the more direct ITC method, although this method uses large enzyme and peptide concentrations and requires high solubility of both components.

We first defined buffer conditions of miniSIRT1 using Thermal Shift Assays. As a result of these assays all experiments were performed in phosphate buffer 20mM, pH 8 (see Materials and Methods).

Peptide 143 (TG-15 (143)) has the lowest K_M. It was therefore chosen to start ITC trials and find optimal miniSIRT1 and peptide concentrations. The chosen concentrations were 150 µM of miniSIRT1 and 1.5 mM of peptide. With these conditions we determined a K_D value of 30 µM, which is close to the value measured using TSA (17 µM).

We then performed ITC experiments with peptides TG-15 and TG-15 (141). Interestingly, the heat changes were too small to allow an accurate K_D determination under our experimental conditions (K_D> 1000 µM) (table11; figure 67).

Substrate	K_D (µM)
TG-15 (143)	30 ± 2
TG-15 (141)	> 1000
TG-15	> 1000
TG-15 (141A, 143AcK)	29.4 ± 0.3
DG-7 (141A, 143Q)	NA
DG-7 (143)	133

Table 11: K_D obtained using miniSIRT1 and different acetylated mimic peptides/mimic acetylation peptide.

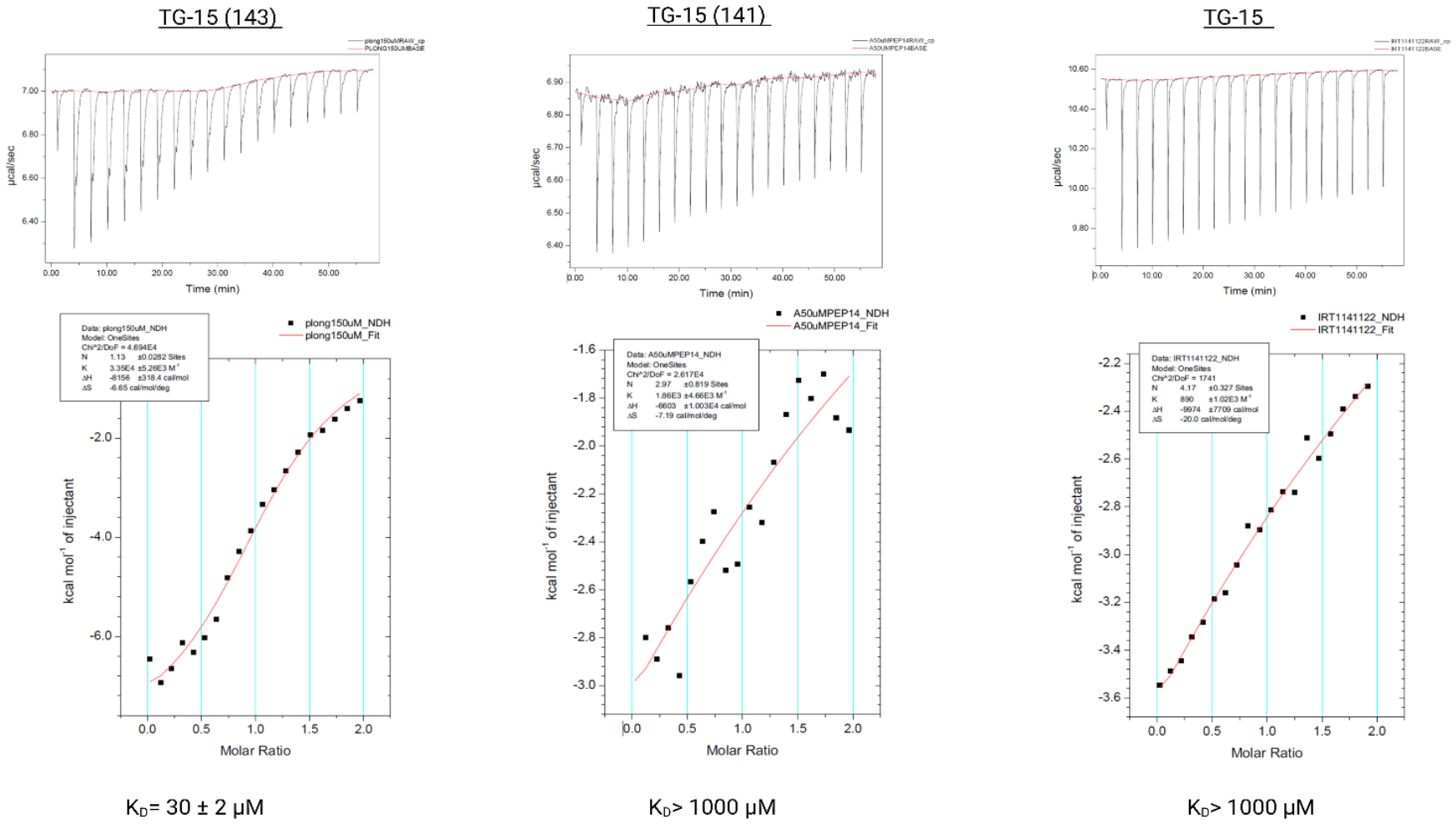

Figure 67: ITC curves for miniSIRT1 with three different peptides: TG-15(143), TG-15 (141), and TG-15. The top panel represents the raw data, and the bottom panels show the binding isotherms created by plotting the integrated heat peaks against the molar ratio. The K_D determined for TG-15 (143) is 30 ±2 µM, (n=3) whereas only weak signal was observed with the other two peptides using this method (K_D> 1000 µM).

In sight of these results, we used the TG-15 (141A, 143AcK) peptide to test the importance of K141. The results depicted below show that the K_D remains mostly unchanged in the case of TG-15 (141A, 143AcK) (table 11, figure 68).

We then measured the binding affinity of DG-7 (143). As shown in figure 68, the K_D is increased by a factor of at least 4.5 as compared to the TG-15 (143). This result confirms the K_M measurements and shows that the length of the peptide strongly influences its binding affinity. Finally, we designed a DG-7 (141A, 143Q) peptide. This peptide was also designed in hopes to use it in crystallization trials using miniSIRT1: NAD^+ and the mimic peptide. However, the K_D for DG-7 (141A, 143Q) could not be determined using ITC, as there was no heat variation. This strongly suggests that glutamine in position 143 impairs binding of the peptide to miniSIRT1 and that glutamine is not a perfect mimic of acetylation in this case.

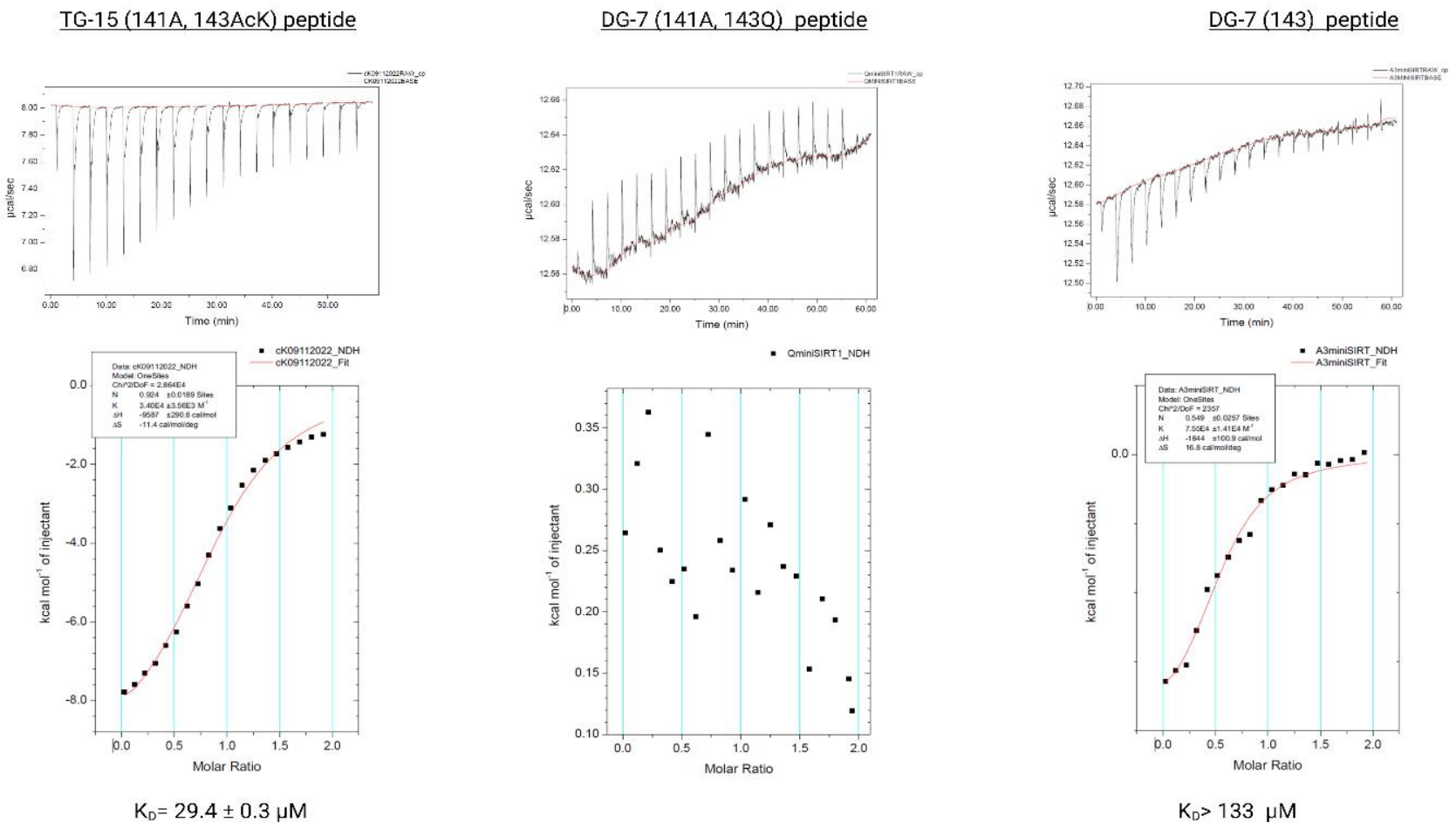

Figure 68: ITC curves for miniSIRT1 with three different peptides: TG-15(141A, 143AcK), DG-7 (141A, 143Q), and DG-7 (143). The top panel represents the raw data, and the bottom panels show the binding isotherms created by plotting the integrated heat peaks against the molar ratio. The K_D determined for TG-15(141A, 143AcK) is around 29.4 μM, whereas no significant heat changes are observed with DG-7 (141A, 143Q) using this method. A K_D of 133 μM was measure for the DG-7 (143) peptide.

As described at the beginning of this section we designed two catalytic miniSIRT1 mutants: H363A and H363L.

These mutants were designed with the idea of using them in crystallization assays, with both NAD^+ and the acetylated peptide. To ensure these variants were catalytically inactive we performed an enzymatic test as shown in section 2.2.2 with miniSIRT1-H363A and miniSIRT1-H363L, and the DG-7 (143) peptide as substrate. As shown in figure 69, no catalytic activity was measured for H363L, whereas some very small activity remained for H363A. Then, we studied these two mutants for their ability to bind acetylated peptides.

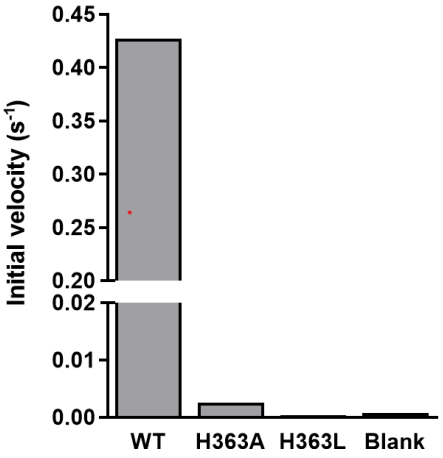

Figure 69: Measurement of initial velocities of miniSIRT1 catalytic variants performed with DG-7 (143). A minimal residual activity is observed for both variants.

To do so, we performed several ITC assays with both catalytic variants and the TG-15 (143) peptide. Interestingly, the peptide only retained some affinity to the H363L mutant, although the K_D value was higher than that obtained with WT miniSIRT1 (K_D= 100 µM for H363L as compared to 30 µM for miniSIRT1). In the presence of 500 µM NAD^+ the K_D was reduced to 60 µM, showing some coupling between the peptide binding site and the NAD^+ binding site. This result is consistent with crystallographic studies that showed that the side chain of H363 is stacked onto the acetyl peptidic moiety of the substrate (as seen in figure 37 of the introduction). As seen in figure 70, H363L has retained some ability to stabilize the binding of the acetylated peptide, which is not the case of the H363A mutant.

Since the acetylated peptide was able to bind H363L miniSIRT1 variant with a measurable affinity and that by adding NAD^+ the K_D decreased, this variant was used in crystallization assays.

miniSIRT1-H363A and TG-15 (143)

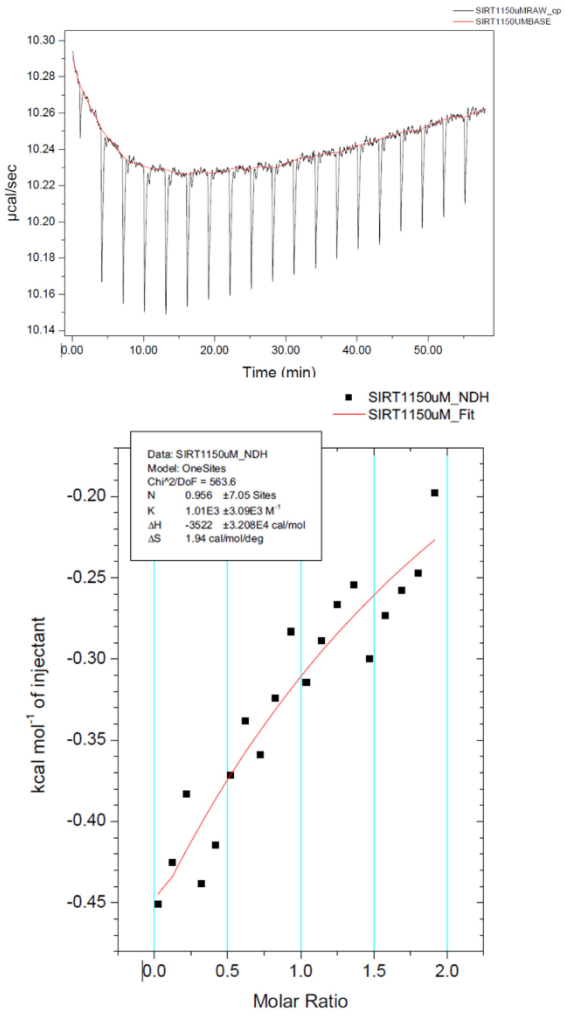

miniSIRT1-H363L and TG-15 (143)

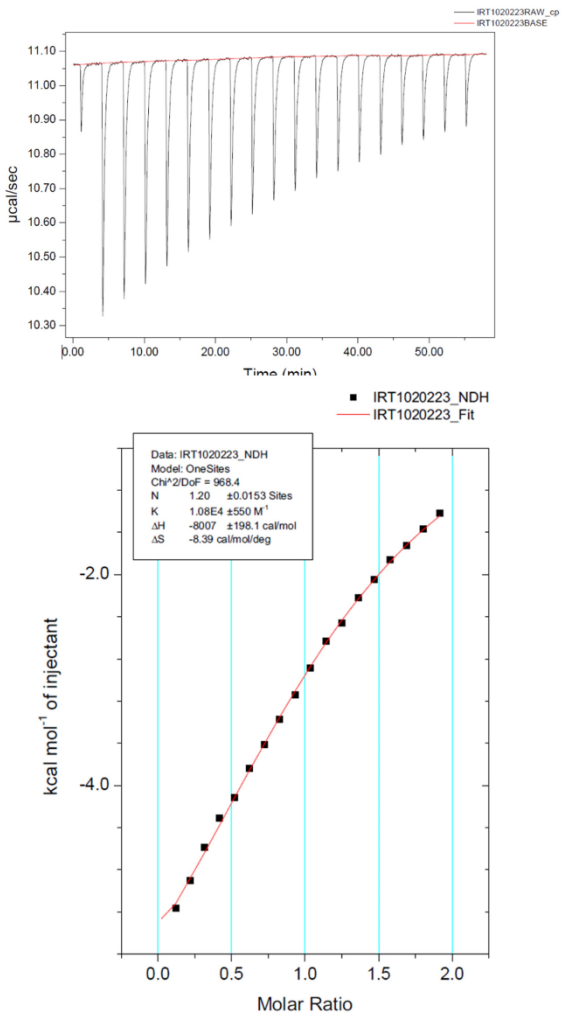

K_D= 100 ± 5 µM

miniSIRT1-H363L, TG-15 (143) and NAD$^+$

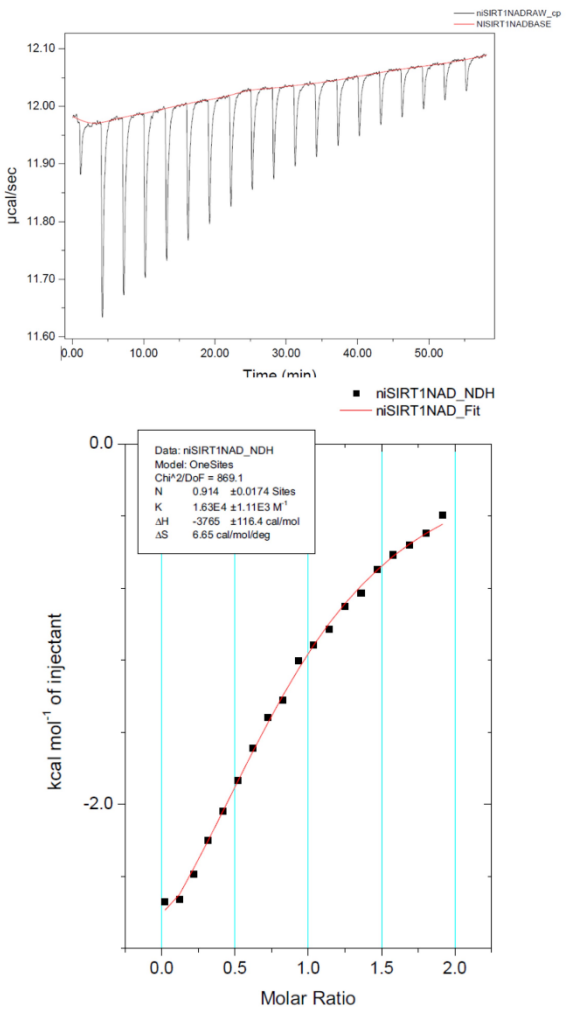

K_D= 61 ± 4 µM

Figure 70: ITC curves for miniSIRT1catalytic variants H363A and H363L and TG-15(143). The top panel represents the raw data, and the bottom panels show the binding isotherms created by plotting the integrated heat peaks against the molar ratio. No K_D could be determined in the case of the H363A variant, as no binding was observed. In the case of the H363L variant the K_D was around 100 µM, and around 61 µM when NAD$^+$ is added.

2.4 Conclusion

As observed in section 2.2.2 miniSIRT1 is a good model enzyme to study SIRT1 catalytic parameters using mimic peptides. Results show that the best substrate is TG-15 (143). When K141 was substituted for an A in TG-15 (143) a slight increase in the K_M value of the peptide is observed, showing that K141 does indeed participate in the binding of the peptide. Interestingly, longer peptides have a higher binding affinity for miniSIRT1. This suggests that interaction of SIRT1 with the peptidic part of the substrate occurs and contributes to the binding of the acetyl group in the catalytic pocket. Such interaction can confer some specificity in the binding of the substrates to miniSIRT1. Notably, high concentrations of substrate have an inhibitory effect on the catalysis. This suggests that an unspecific binding site of TG-15 on miniSIRT1 exists and interferes with its specific interaction.

In the same view, our results also show that a model peptide acetylated at position 143 is a better substrate and has a better affinity than a model peptide acetylated at position 141. Moreover, a model peptide with the glutamine mimic at position 143 does not bind miniSIRT1 (K_D not measurable with ITC). This strongly suggests that the presence of the acetyl group is essential for the binding of the peptide to miniSIRT1 and that the sequence surrounding the acetyl group influences binding affinity.

On the other hand, we did not see a major effect on the K_M due to any of the STAC compounds tested. The chosen concentrations for these experiments were consistent with the STAC concentrations used by our collaborators (Monceaux *et al.*, 2022) and also correspond to the concentration usually used in drug screening experiments (Hughes *et al.*, 2011). SIRT1 activation via STACs depends on the substrate and the STAC used, meaning that a STAC could have a lowering effect on the K_M when presented with the correct substrate. At this point, and using miniSIRT1, we cannot conclude that the tested STACs influence the peptide's binding to miniSIRT1.

Part 3: Crystallization

3.1 Crystallization of heIF2α-K143Q-188

Crystallization of the different His-tagged heIF2α variants was achieved using a NeXtal PEG II Suite crystallization kit. Crystals were easily obtained in various PEG conditions. However, these crystals diffracted to low resolution (around 3.5 Å) and we therefore had to improve their quality. We decided to use a non-tagged version of heIF2α-K143Q-188 and for that we produced a new plasmid in which the tag coding sequence had been removed. The resulting protein was slightly more soluble than the His-tagged versions, being able to concentrate it up to 10 mg/mL. With this protein we were able to obtain better quality crystals (figure 71) and to collect a dataset to 2.2 Å resolution on the PX2 beamline at the SOLEIL synchrotron. Data were processed using XDS (Kabsch, 2010) (table 12) and analyzed with CCP4 programs (Winn *et al.*, 2011).

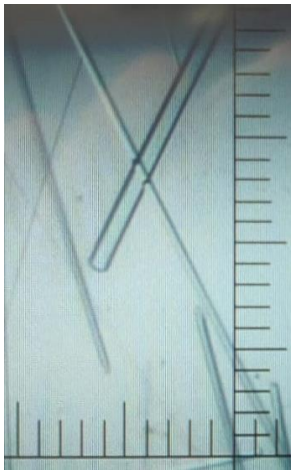

Figure 71: heIF2α-K143Q-188 crystals.

The structure was solved using the molecular replacement method and the PHASER program (McCoy *et al.*, 2007). The structure of human eIF2α (PDB: 1KL9, (Nonato, Widom and Clardy, 2002)) was used as a starting model. Statistics of data collection and refinement are given in table 12.

Data collection			
Wavelength		0.98	
Resolution range		47.98 - 2.2 (2.279 - 2.2)	
Space group		P 1	
Unit cell		53.64 57.45 58.16 112.74 110.22 103.19	
Total reflections		97477 (9695)	
Unique reflections		27128 (2694)	
Multiplicity		3.6 (3.6)	
Completeness (%)		97.75 (96.90)	
Mean I/sigma(I)		5.35 (1.00)	
Wilson B-factor		36.36	
R-meas		0.2255 (1.715)	
CC1/2		0.987 (0.454)	
Reflections used in refinement		27100 (2690)	
Refinement			
R-work	R-free	0.2394 (0.3284)	0.2846 (0.3405)
Number of non-hydrogen atoms		4605	
macromolecules		4489	
solvent		116	
Protein residues		545	
RMS (bonds)		0.002	
RMS (angles)		0.45	
Ramachandran favored (%)		97.56	
Ramachandran allowed (%)		2.44	
Ramachandran outliers (%)		0	
Clashscore		6.01	
Average B-factor		50.11	
macromolecules		50.21	
solvent		46.25	

Table 12: Data collection and refinement statistics. Statistics for the highest-resolution shell are shown in parentheses. R free was calculated with 5% of the reflexions.

Three independent molecules were found in the asymmetric unit, as shown in figure (72-A). The packing is different for each molecule, which results in stabilization of the S52 loop of molecule B, as seen in figure 72-B. The three molecules were refined to 2.2 Å resolution. The structure of molecule B was compared to the previously determined structure of human domains 1 and 2 of eIF2α (PDB: 1KL9). The two molecules were superimposed with a rmsd of 0.41 Å for 1047 atoms compared. As previously observed, domains 1 and 2 form a rigid structural unit. Only a very small difference in the orientation of domain 1 with respect to domain 2 is observed between the two structures (2.8º rotation and 3.3 Å translation). This difference is likely due to packing interactions.

Figure 72: Structure of the heIF2∝-K143Q-188 protein. A) The three molecules in the asymmetric unit A (green), B (cyan), C (pink) are shown. B) Stabilization of the S52 loop in molecule B. C) Comparison with the model structure 1KL9. Domain 2 of the two structures were superimposed (RMSD= 0.346)

To conclude, we observed that the presence of the K143Q mutation did not change the overall conformation of the protein. Notably, Q143 (K143 in the wild-type version) is positioned at the end of an α helix, whereas K141 is positioned inside the α helix (figure 73). Both side chains point towards the solvent side.

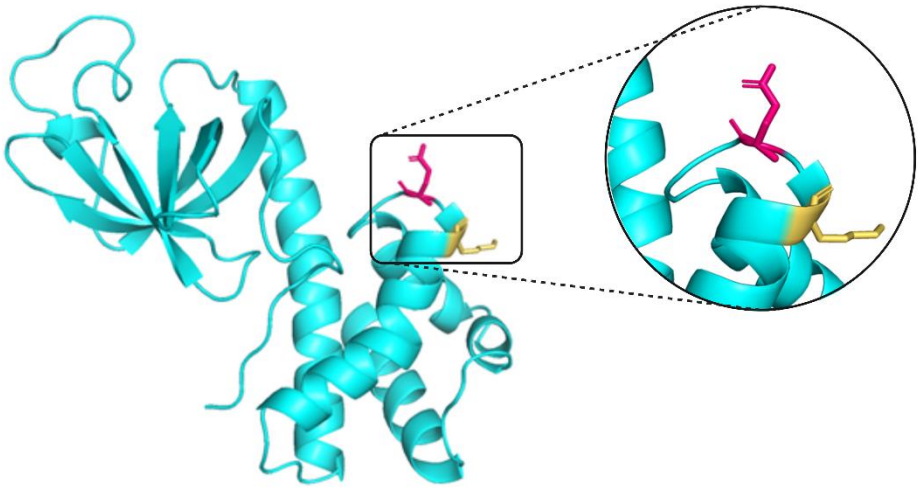

Figure 73: Depiction of Q143 and K141 in the obtained heIF2α-K143Q-188 structure.

3.2 Alpha-fold representation of miniSIRT1 and peptide variants

Several crystallization attempts with miniSIRT1 and various peptides were performed, including miniSIRT1 H363L variant, that allowed us to use NAD^+. Some attempts produced crystals with ΔNminiSIRT1, but diffracting only to low resolution around 4 Å.

To gain some insight into the structure of the heIF2α/peptide:miniSIRT1 we also performed many trials using AlphaFold v2.0 (AlphaFold2021, (Ronneberger *et al.*, 2021)).

Despite many efforts, we could not obtain crystals of miniSIRT1 in the presence of an acetylated peptide, or even better in the presence of acetylated heIF2α. These efforts will be continued. In particular, crystallization attempts with miniSIRT1-H363L in the presence of NAD^+ and TG-15 (143).

3.3 Conclusion

Crystallization of an acetylation mimic heIF2α-188 variants was a first step towards understanding the effect of acetylation on heIF2α-188 structure. No significant difference due to the presence of glutamine instead of K143 was observed, which suggests that acetylation will probably not impact the structure of heIF2α-188.

The crystallization conditions set for heIF2α-188 allowed us to also obtain small crystals of heIF2α-143AcK-188. However, these crystals were too small and did not diffract. These attempts will be continued, using an untagged version of the acetylated protein.

Efforts will also continue to try to crystallize miniSIRT1 and substrate peptides, especially with miniSIRT1-H363L which allows the addition of NAD^+ without risking peptide deacetylation.

Alpha fold modelling of a complex between miniSIRT1/SIRT1 and heIF2α did not offer any satisfactory models. The structures obtained did not position the peptide substrate adequately.

Part 4: Characterization of heIF2α: miniSIRT1 interaction

4.1 Interaction between acetylated heIF2α and miniSIRT1 via pull-down:

To evidence an interaction between acetylated heIF2α and miniSIRT1 we performed several pull-down assays in which acetylated His-tagged heIF2α acted as bait. The His-tag on miniSIRT1 was removed via thrombin digestion. This way His-tagged heIF2α would trap any interacting miniSIRT1 and the interacting complex can be observed on SDS-PAGE analysis.

As seen in the figure below, no obvious difference is observed with acetylated or native heIF2α-188, as both are able to pull some SIRT1 in the elution fraction.

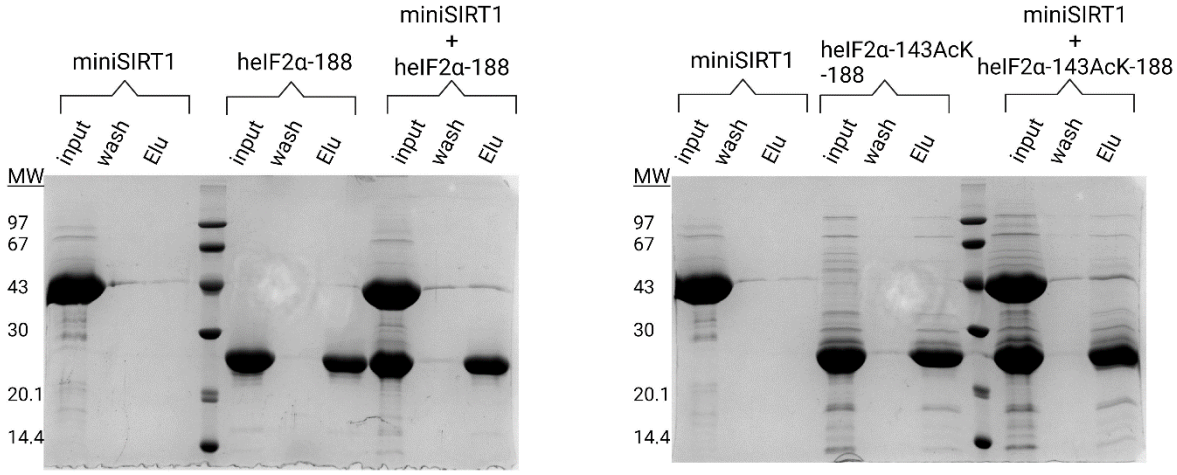

Figure 74: Pull down assays with tagged heIF2α-188 (left) or heIF2α-143AcK-188 (right) and detagged miniSIRT1. Input stands for the initial amount of protein deposited on gel, wash stands for a wash performed at 10 mM imidazole and elu stands for elution at 125 mM imidazole.

We conducted size exclusion chromatography on purified proteins to investigate the interaction between heIF2α-143AcK-188 and miniSIRT1. However, despite our efforts, no interaction was observed with this method.

4.2 Determination of SIRT1 catalytic parameters using Western blotting

A first attempt to use the coupled enzymatic assay described in previous sections was performed to determine SIRT1 catalytic parameters on heIF2α deacetylation. However, we encountered several technical problems that prevented us from using this method. For instance, the storage buffer for acetylated heIF2α and the enzymatic test buffer are not compatible, leading to precipitation of heIF2α. Another problem that arises from this test is the high quantity of heIF2α needed, which makes the test laborious and costly in terms of protein production efforts.

Therefore, to evidence the deacetylation activity of SIRT1 for acetylated heIF2α we decided to set up an assay based on the use of anti-acetyl-lysine antibodies and the Western blotting technique.

4.2.1 Specificity of anti-acetyl-lysine and anti-heIF2α antibodies

First, to validate this method, we performed several control experiments with Anti-acetyl-lysine and Anti-eIF2α antibodies. Both antibodies were used against acetylated and WT heIF2α-188. As shown in figure 75, only acetylated heIF2α was detected when the Anti-acetyl-lysine antibody was used, whereas both WT heIF2α and acetylated heIF2α were detected when the Anti- eIF2α antibody is used.

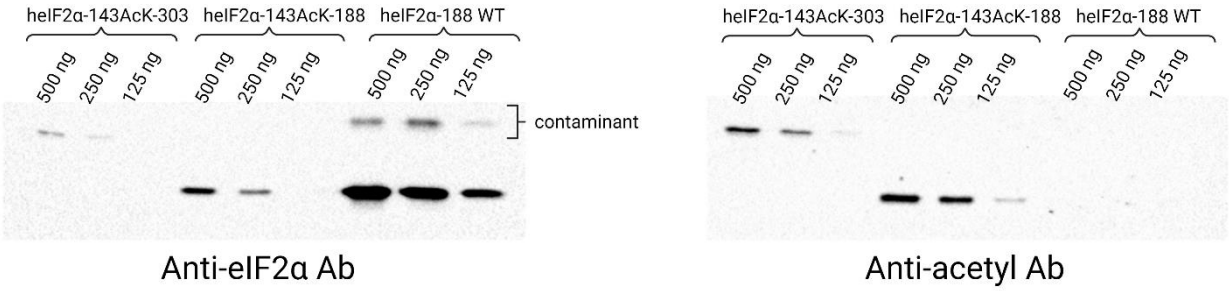

Figure 75: Western blot analyses using Anti-heIF2α antibodies (left) and anti-acetyl antibodies (right). Two different acetylated variants were used, heIF2α-143AcK-188 and heIF2α-143AcK-303. On the left panel both acetylated variants and heIF2α-188 WT were revealed during Western blot analysis. On the right, only acetylated variants were revealed, showing the specificity of the Anti-acetyl antibody. Unspecific detection of a contaminant can be seen on the left.

Once we showed the specificity of the Anti-acetyl-lysine antibodies, we performed several optimization steps to ensure a linear response of the detection. Western blotting is usually a qualitative assay, but under the appropriate conditions it can be used

as a quantitative technique. To verify linearity throughout experiments we tested different acetylated heIF2α quantities in the Western-blot analysis (figure 76).

After transfer, membranes were stained with Ponceau Red to verify transfer homogeneity. After revelation with antibodies, the signal detected was quantified with Image Lab (BioRad). According to our results we decided to use a maximum of 250 ng of acetylated heIF2α per gel lane. Moreover, to avoid any fluctuations due to antibody titer variation upon reuse, we decided to use a fresh dilution of 1/10000 of anti-acetyl lysine antibodies in each experiment (secondary antibodies were also systematically used only once at a 1/10000 dilution).

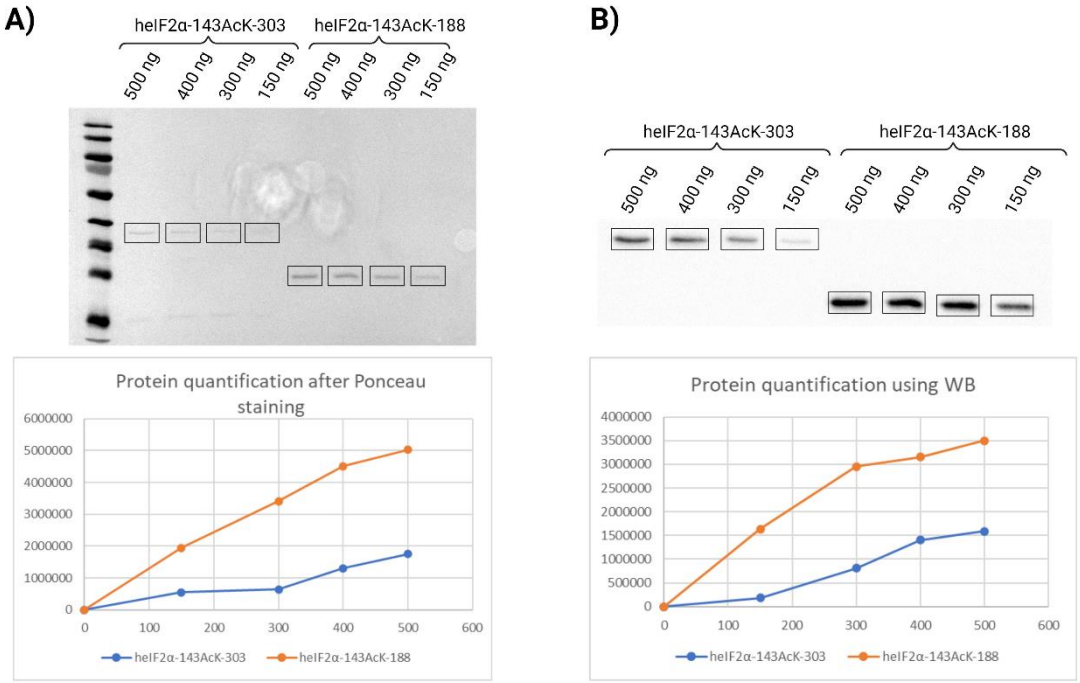

Figure 76: Protein quantification using Ponceau staining and Western blot analysis. A) Nitrocellulose membrane stained with Ponceau red, showing bands corresponding to heIF2α-143AcK-188 and heIF2α-143AcK-303 at different protein quantities. On the bottom panel, the corresponding signal after revelation against to protein quantity. In this graph we can assume linearity up to the 250 ng protein mark. B) Top panel: Western blot analysis at different acetylated protein concentration. The Anti-acetyl-lysine antibody was used. Bottom panel shows the corresponding signal to different protein quantities. In this graph we can assume linearity up top 250 ng.

4.2.2 Quantification of miniSIRT1 deacetylation reaction on acetylated heIF2α-188

We chose to study miniSIRT1 deacetylation reaction on heIF2α acetylated variants. We performed the deacetylation reaction in the presence of 1 mM NAD^+ and a concentration of substrate of 1 µM. The chosen miniSIRT1 concentration was 5 µM, as trials with a lesser concentration of enzyme failed to show any substrate consumption.

First, we used heIF2α-143AcK-188 as substrate and incubated it with miniSIRT1 for different amounts of time. The results below (figure 77-A1 and 77-A2) show a rapid decrease in the presence of the acetyl group after 10 min of about 60%, with a further decrease to around 90% deacetylation after 40 min. Once we were confident in our ability to follow the deacetylation reaction, we performed the same experiment with heIF2α-141AcK-188. Interestingly, we see that at the 10 min mark, around 60% of the protein has been deacetylated, reaching similar deacetylation levels of 90% at 40 min.

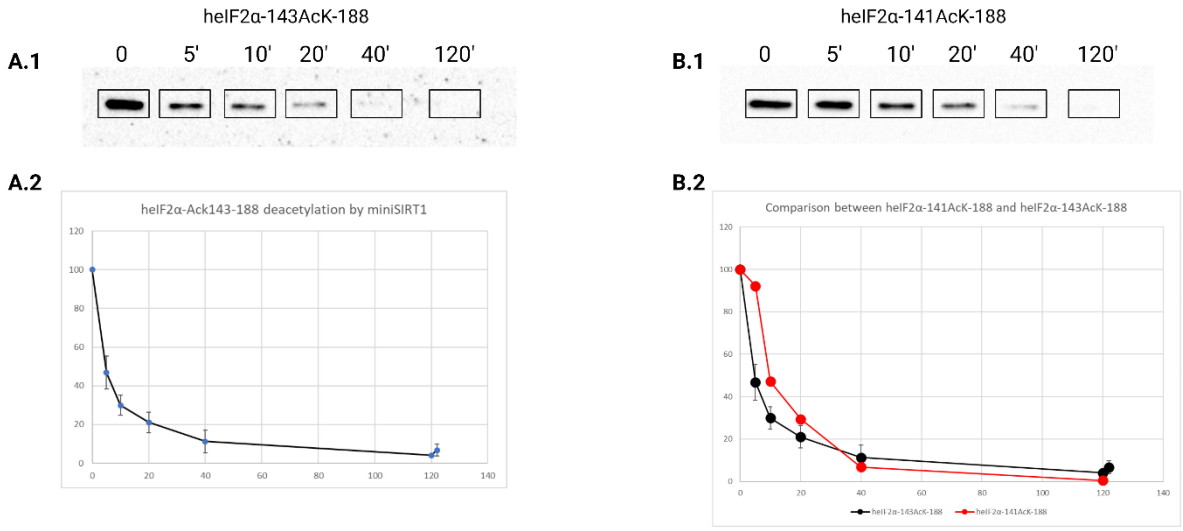

Figure 77: Deacetylation reaction by miniSIRT1 on acetylated heIF2α-188 variants. A.1 and B.1 show representative Western blot analysis of heIF2α-143AcK-188 (n=3) and heIF2α-141AcK-188 (n=1) deacetylation. On panels A.2 and B.2 the respective decrease in signal after exposure to 5 μM of miniSIRT1 during 5, 10, 20, 40 and 120 minutes, heIF2α-143AcK-188 (black) and heIF2α-141AcK-188 (red).

4.2.2.1 Determination of miniSIRT1 catalytic parameters using heIF2α-143AcK-188 as substrate

To determine miniSIRT1 catalytic parameters on heIF2α-143AcK-188 deacetylation, we used the same method as explained above, but this time several concentrations of heIF2α-143AcK-188 were used.

We performed a first experiment using 0.25 μM and 1 μM of heIF2α-143AcK-188 (figure 78), calculated the amount of product formed and plotted it against the reaction time. Assuming that the quantity of product formed varies linearly between 0 and 5 minutes, we measured a rate of deacetylation of 3.6 10^{-4} s^{-1} at 1 μM substrate and 1.33 10^{-4} s^{-1} at 0.25 μM substrate. This would indicate that the K_M value of heIF2α-143AcK-188 is close to 1 μM (or below as the rate at 0.25 μM might be underestimated).

This result will be continued by redoing the experiments with more heIF2α-143AcK-188 concentrations.

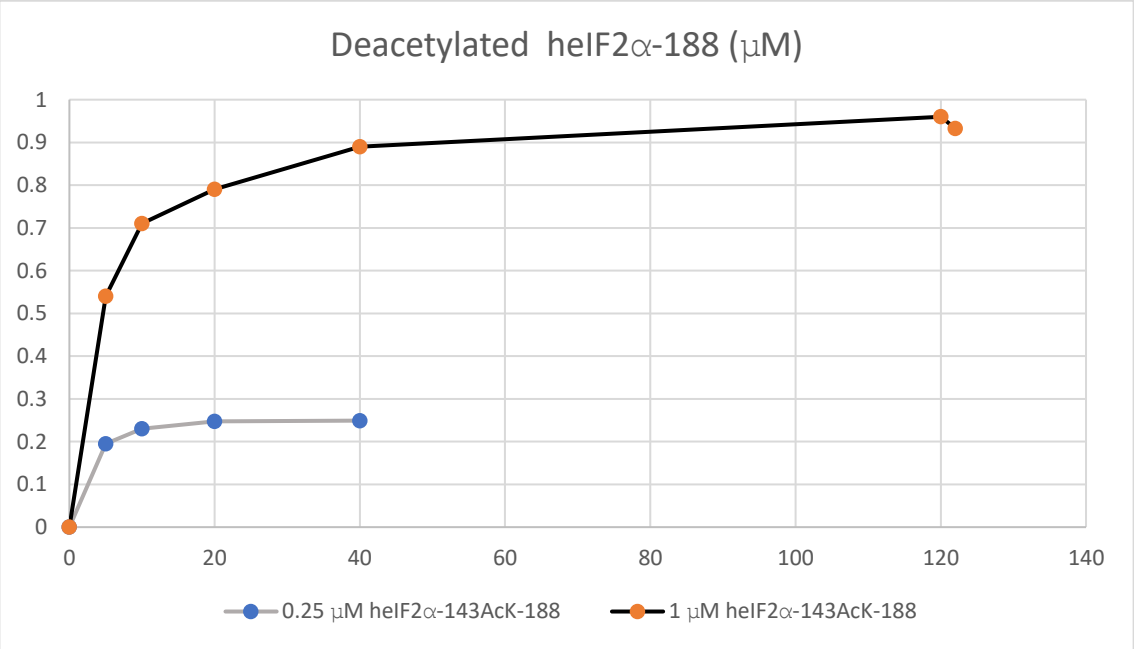

Figure 78: Product concentration against time for two concentrations of heIF2α-143AcK-188 (black 1 µM and grey 0.25 µM).

4.2.3 Comparison between miniSIRT1 and SIRT1

We compared the deacetylation reaction observed with miniSIRT1 and SIRT1. We used the same concentration of sirtuin, with the knowledge that SIRT1's concentration is underestimated due to its purity levels. Preliminary results show that no obvious increase in the deacetylation rate is observed when SIRT1 is used in place of miniSIRT1.

4.2.4 Quantification of miniSIRT1 deacetylation reaction on heIF2α-143AcK-303

We then wanted to compare the rate of miniSIRT1 deacetylation on heIF2α-143AcK-303 and heIF2α-143AcK-188, using the same protocol. As shown in figure 79, the rate of deacetylation of heIF2α-143AcK-303 is of the same order as the one measured for heIF2α-143AcK-188 ($1.8\ 10^{-4}$ as compared to $3.6\ 10^{-4}$). This shows that, as expected, the D3 of heIF2α does not strongly influence SIRT1 activity.

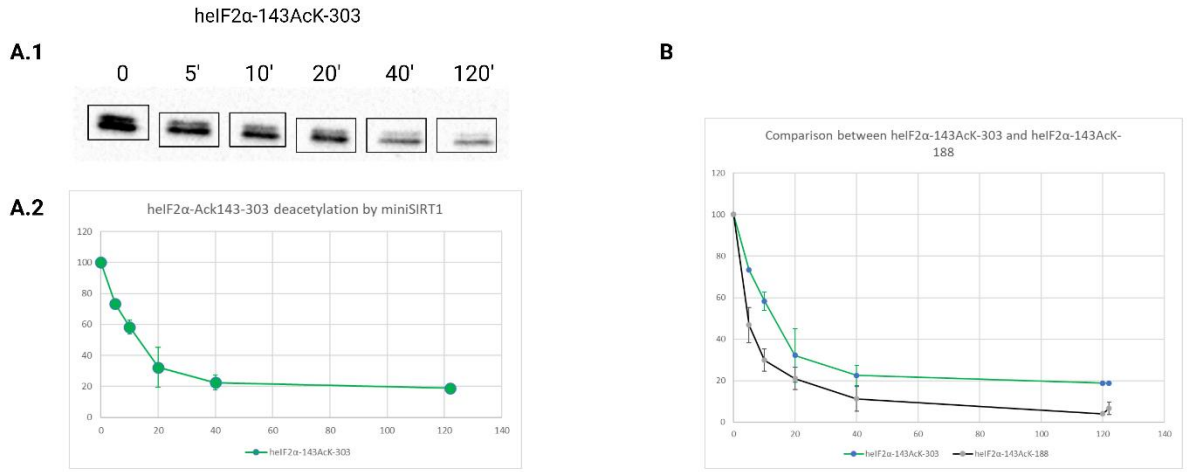

Figure 79: Deacetylation reaction by miniSIRT1 on heIF2α-143AcK-303 variants. A.1 shows a representative Western blot analysis of heIF2α-143AcK-303 deacetylation. On panels A.2 the decrease in signal after exposure to 5 μM of miniSIRT1 during 5, 10, 20, 40 and 120 minutes. B) Comparison between heIF2α-143AcK-188 (black) and heIF2α-143AcK-303 (green).

4.2.5 Quantification of miniSIRT1 deacetylation reaction on S52D acetylated variants

We aimed to study the effect of S52D substitution in deacetylation rates. To do so, heIF2α-S52D-143AcK-188 was used as substrate. As shown in figure 80, there is no visible effect of the S52D mutation on the deacetylation rates.

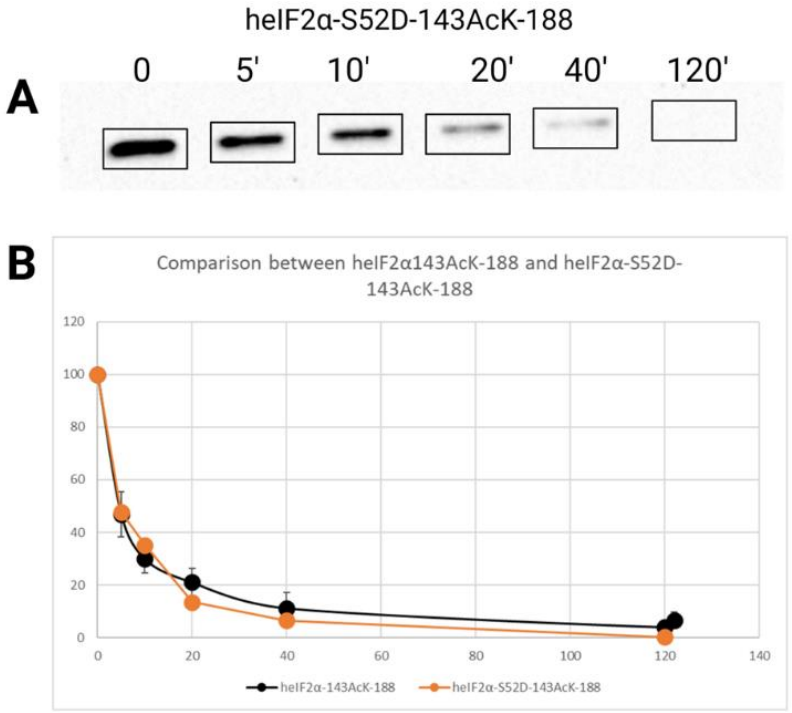

Figure 80: Deacetylation reaction by miniSIRT1 on acetylated heIF2α-S52D-188. Panel A shows a representative Western blot analysis of heIF2α-S52D-143AcK-188. B) The decrease in signal after exposure to 5 μM of miniSIRT1 during 5, 10, 20, 40 and 120 minutes, heIF2α-143AcK-188 (black) and heIF2α-S52D-143AcK-188 (orange).

4.3 Conclusion

In the first instance, we used the enzymatic coupled assay described in section 2.2 to determine the catalytic rates of SIRT1 on heIF2α deacetylation. However, we did not observe any apparent consumption of NADPH, not being able to see a deacetylation reaction in the coupled enzymatic test conditions.

Using Western blot, we are able to track SIRT1 and miniSIRT1 deacetylation reaction of a full-length substrate. These experiments prove that both heIF2α-143AcK-188 and heIF2α-141AcK-188 are a substrate of miniSIRT1/SIRT1 in vitro. As expected from structural studies, D3 of eIF2α does not influence the deacetylation rate. The rate of deacetylation is rather low (3.6 10^{-4} s^{-1} at 1 μM substrate) and seems to not be influenced by the position of the acetyl group (143 or 141). The use of phosphomimics did not show any differences in the case of the heIF2α-188 variants.

Once we had some information on the deacetylation catalytic rates, and an idea of the K_M of the deacetylation of miniSIRT1 of heIF2α-143AcK-188, we tried to use the coupled enzymatic test once again. However, the rate of deacetylation is too low to be observed using this test, as shown in figure 81. Therefore, so far, the only way we have to calculate miniSIRT1/SIRT1 catalytic rates on heIF2α deacetylation is via Western blot assay.

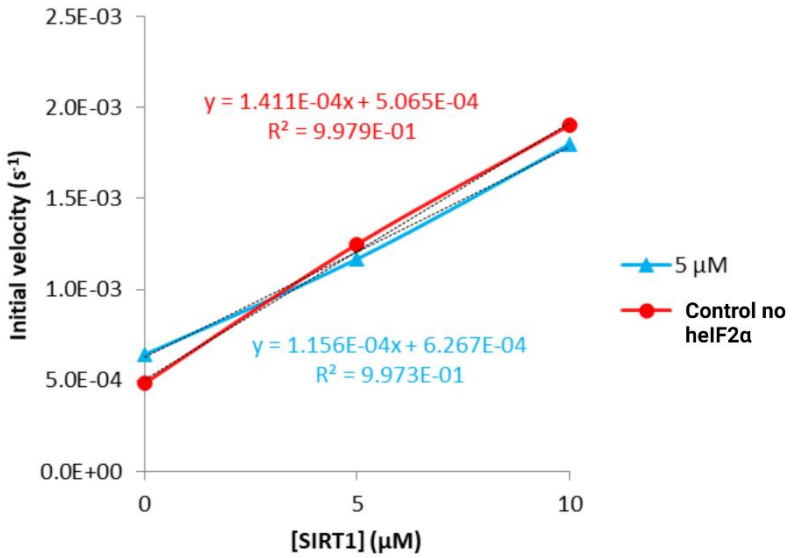

Figure 81: Coupled-enzymatic assay using heIF2∝-S52D-143AcK-188 (5 μM) and miniSIRT1 (0, 5 and 10 μM). No differences in the rates are observed using this method, 1.4 10-4 s^{-1} rate in the presence of substrate as compared to 1.16 10-4 s_1 background rate in the control.

Part 5: Interactome

Post-translational modifications may modify the interactome of a given protein. Such is the case of phosphorylation of S52 of heIF2α, which creates a stable complex with eIF2B and triggers the Integrated Stress Response (of which the ER stress response is part of). Acetylation is a novel PTM for heIF2α whose consequences in heIF2α activity and partner binding are just starting to be studied. The only known partner due to this modification, so far, is SIRT1. However, acetylation of heIF2α may implicate other interactants that are yet to be discovered and may widen heIF2α interaction network, maybe outside of the translation machinery.

To study heIF2α interactome our collaborator kindly provided us with H9c2 cell pellets. This embryonic cardiomyocyte cell line was used by our collaborator in their studies. Two types of cell pellets were provided: cells treated with tunicamycin (10 μg/mL) to induce ER stress, and untreated ones to serve as controls. To do so, we used His-tagged heIF2α-143AcK-303 as bait on metal affinity columns onto which treated and untreated cell extracts were applied. We used the heIF2α-303 version and not the heIF2α-188 one to be as close as possible to the WT version of heIF2α. For example, D3, only present in the heIF2α-303 version, is needed for the binding of heIF2α to heIF2γ. This experiment was performed four times, with independent cell cultures, to reinforce the validity of the results.

In parallel, we also used His-tagged heIF2α-S52D-143AcK-303 variant as bait in the same manner as described above. This variant carries the S52D mutation, which mimics phosphorylation and can give us an insight into the interplay between acetylation and phosphorylation, and their impact in heIF2α interaction with known partners, and hopefully, newly discovered partners.

As control we used WT heIF2α-303 to remove heIF2α interactants that are not directly related to the acetylation PTM. However, since heIF2α acetylation levels are increased during ER stress, the experiment with heIF2α-303 can possibly identify the acetylase responsible for acetylating heIF2α using this variant.

As a negative control we used the His-tagged GFP protein. Since this protein belongs to a different organism (*Aequorea victoria*) and its function is completely

unrelated to both SIRT1 and heIF2α, all interaction seen with this protein would be unspecific.

The pull down was analyzed by SDS-PAGE, loading a sample of every step performed during the assay: a supernatant sample after cell lysis; the input, the mix between the lysed cells and the bait; flow-through; the first wash, the washes with lysis buffer; the wash with 10mM imidazole, to eliminate any non-specific interactions with the resin; and the elution (figure 82).

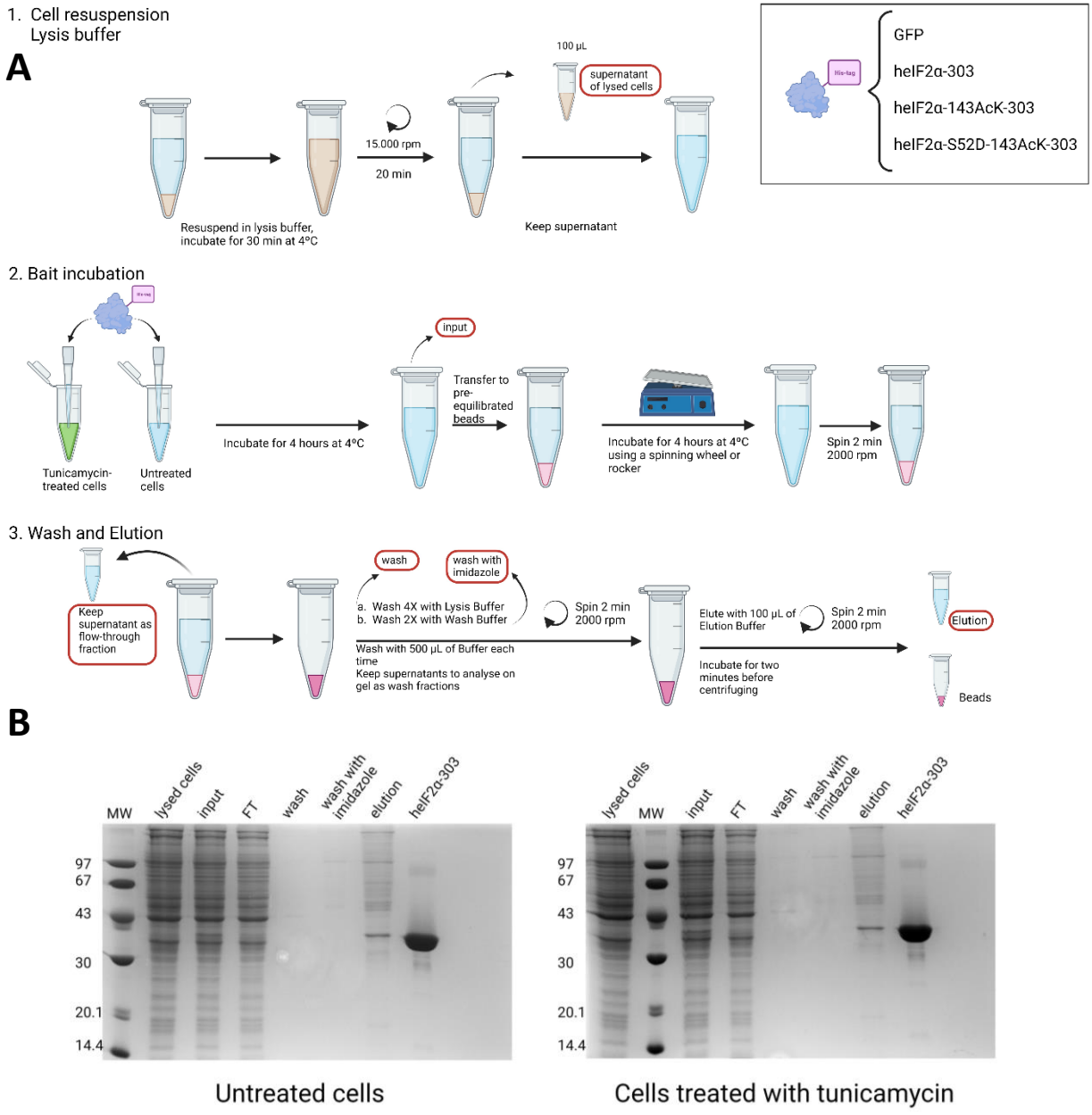

Figure 82: A) Step by step pull down protocol. Circled in red are the different fractions loaded onto the gel. B) SDS-PAGE analysis of the pull-down assays with treated and untreated cell H9c9 cell extracts with heIF2α-303 WT.

All samples were sent to the Mass-Spectrometry facility at the Pasteur Institute for analysis. Partial results were recently made available corresponding to heIF2α-143AcK-303 and heIF2α-303, which show that sample treatment and the Mass-Spectrometry initial data output are technically correct. Due to the large data set to interpret the complete set of results will be discussed during the thesis defense.

As an example, figure 83 shows a volcano plot with differential analysis between heIF2α-143AcK-303 and heIF2α-303.

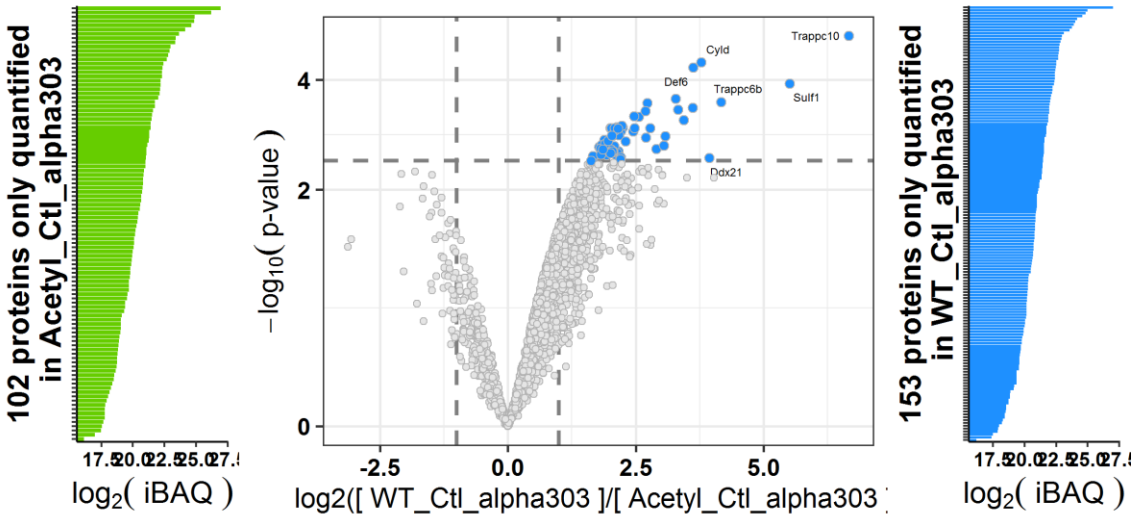

Figure 83: Volcano plot showing proteomics data from heIF2α-303 and heIF2α-143AcK-303 possible interactants. These points indicate different proteins that display both large magnitude fold-changes (x axis) and high statistical significance (-log10 of p values, y axis). Dashed horizontal line shows the p values cutoff, and the two vertical dashed lines indicate down/up regulated proteins. iBAQ: relative abundance of a protein obtained by dividing the total intensities by the number of theoretically observable peptides of a given protein.

Part 6: Cdc123 article presentation

The assembly of the eIF2 heterotrimer requires the aid of the Cdc123 protein as discovered in the Seufert lab (Perzlmaier, Richter and Seufert, 2013); (Vanselow *et al.*, 2022). Research in our lab has elucidated the structure of the yeast Cdc123 protein bound to the domain 3 of eIF2γ, showed that Cdc123 was a member of the ATP grasp family, and proposed a mechanism where Cdc123 acts as a scaffold for the interaction between eIF2γ and eIF2α. Moreover, we are now able to purify yeast eIF2 subunits using *E. coli* systems, provided that the three eIF2 subunits are co-expressed with Cdc123 (unpublished data). The study of the human eIF2 heterotrimer proves to be more difficult, as we are only capable of expressing domain 3 of eIF2γ (eIF2γ-D3) bound to Cdc123 in *E. coli* systems, suggesting that other parameters can influence expression of human eIF2.

During this thesis we were able to produce a quasi-native version of heIF2α, heIF2α-303. We wanted to test its ability to bind eIF2γ. We decided to purify yeast eIF2γ, co-expressed with Cdc123. Using this strategy, we were able to purify a fraction of eIF2γ not bound to Cdc123. Using pull-down assays, we observed that heIF2α-303 and yeast eIF2γ can interact, thereby proving that heIF2α-303 is correctly folded (figure 83).

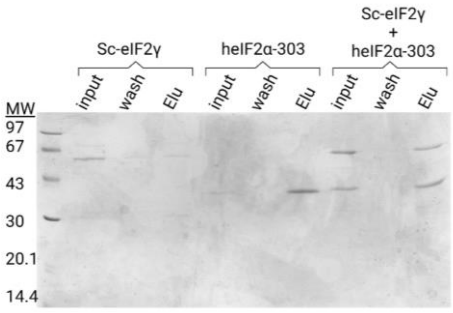

Figure 84: Pull down assays with tagged heIF2α-303 (left) non-tagged Sc-eIF2γ. Input stands for the initial amount of protein deposited on gel, wash stands for a wash performed at 10 mM imidazole and elu stands for elution at 125 mM imidazole.

Cdc123 is part of the essential genes in humans, which only includes about 10% of all genes. It is a partner that facilitates heIF2 assembly, however the mechanism remains to be fully understood.

During my thesis, I also worked on hCdc123 and its interaction with ATP and domain 3 of heIF2γ. I performed TSA assays with ATP and ADP using Cdc123 from three organisms and determined their K_D values. I also participated in the refinement of the crystallographic structure of hCdc123 bound to heIF2γ-D3.

Our work, as well as that of the Seufert lab, allowed us to propose a refined model for the mechanism of action of Cdc123 in eIF2 assembly.

Binding of human Cdc123 to eIF2γ

Cristina Cardenal Peralta[1], Paul Vandroux[1], Lea Neumann-Arnold[2], Michel Panvert[1], Jérôme Fagart[1], Wolfgang Seufert[2], Yves Mechulam[1] and Emmanuelle Schmitt[1]

[1] Laboratoire de Biologie Structurale de la Cellule, BIOC, Ecole polytechnique, CNRS, Institut Polytechnique de Paris, 91128 Palaiseau cedex, France.

[2] Department of Genetics, Regensburg Center for Biochemistry, University of Regensburg, Regensburg, Germany.

*Co-corresponding authors: emmanuelle.schmitt@polytechnique.edu and Wolfgang.Seufert@ur.de

SUMMARY

Eukaryotic initiation factor 2 (eIF2) plays a key role in protein synthesis and in its regulation. The assembly of this heterotrimeric factor is facilitated by Cdc123, a member of the ATP grasp family that binds the γ subunit of eIF2. Notably, some mutations related to MEHMO syndrome, an X-linked intellectual disability, affect Cdc123-mediated eIF2 assembly. The mechanism of action of Cdc123 is unclear and structural information for the human protein is awaited. Here, the crystallographic structure of human Cdc123 (Hs-Cdc123) bound to domain 3 of human eIF2γ (Hs-eIF2γD3) was determined. The structure shows that the domain 3 of eIF2γ is bound to domain 1 of Cdc123. Moreover, the long C-terminal region provides a link between the ATP binding site on Hs-Cdc123 and Hs-eIF2γD3. A thermal shift assay shows that ATP is tightly bound to Cdc123 whereas the affinity of ADP is much smaller. Yeast cell viability experiments, western blot analysis and two-hybrid assays show that ATP is important for the function of Hs-Cdc123 in eIF2 assembly. These data and recent findings allow us to propose a refined model to explain the mechanism of action of Cdc123 in eIF2 assembly.

The heterotrimeric initiation factor 2 (e/aIF2) has a central role in eukaryotic and archaeal translation initiation (Hinnebusch, 2014; Schmitt et al., 2020). It is composed of three subunits α, β, γ. The γ subunit forms the core of the heterotrimer and binds GTP. α and β subunits are bound to γ but do not interact with each other (Schmitt et al., 2010). In canonical eukaryotic translation initiation, eIF2:GTP specifically binds the methionyl-initiator tRNA and carries it to the small ribosomal subunit to form, in the presence of other initiation factors, a pre-initiation complex (PIC) able to scan the mRNA to search for a start codon in a correct nucleotidic context. Once the start codon has been found, eIF2 is released from the PIC in its GDP-bound form. Final steps of translation initiation allow the recruitment of the large ribosomal subunit and the formation of a ribosome competent for elongation (Kazan et al., 2023). Specific binding of the initiator tRNA to eIF2-GTP and the control of the nucleotide state of the factor are crucial for efficient translation initiation (Dubiez et al., 2015; Hinnebusch, 2014). Once eIF2-GDP is released from the PIC, the guanine nucleotide exchange factor eIF2B catalyzes recycling of eIF2-GDP to eIF2-GTP to allow additional rounds of translation initiation (Pavitt, 2018). However, stress conditions, such as amino acid deprivation, viral infection or increase of the load of unfolded proteins in the endoplasmic reticulum, trigger phosphorylation of the α subunit of eIF2 at the Serine 52 residue (S51 in yeast) by eIF2α-specific kinases (Wek, 2018). Phosphorylated eIF2α tightly binds eIF2B and prevents its recycling activity (Krishnamoorthy et al., 2001). As a consequence, the global availability of eIF2-GTP decreases leading to a global attenuation of protein synthesis. Importantly, translation of some mRNAs (most of them containing short open reading frames upstream from the main one, uORFs) coding for regulatory proteins is activated by the low levels of eIF2:GTP:Met-tRNA$_i^{Met}$ and allows the cell to respond to stress. This specific response

called ISR (integrated stress-response) is crucial to recover cellular homeostasis and deregulation of ISR are linked to a wide range of human diseases (Wek, 2018).

In eukaryotes, the assembly of the heterotrimeric protein eIF2 is facilitated by the Cdc123 protein (Perzlmaier et al., 2013). Indeed, Cdc123 interacts with eIF2γ (Bieganowski et al., 2004; Chen et al., 2023; Ho et al., 2002) and the association of eIF2γ to eIF2α and eIF2β was shown to depend on the interaction of the C-terminal domain (D3) of eIF2γ with Cdc123 in yeast and human (Panvert et al., 2015; Perzlmaier et al., 2013; Vanselow et al., 2022). Moreover, the C-terminal region of *S. cerevisiae* Cdc123 (the last 30 residues) is indispensable for its *in vivo* function (Panvert et al., 2015). In yeast, human and plants, mutations in Cdc123 lower the availability of functional eIF2 and dysregulate protein synthesis triggering ISR (Chen et al., 2023; Perzlmaier et al., 2013; Vanselow et al., 2022; Young-Baird et al., 2020). Notably, mutations related to MEHMO syndrome (Mental deficiency, Epilepsy, Hypogenitalism, Microcephaly and Obesity), an X-linked intellectual disability, were found in the gene encoding eIF2γ in mammals (*EIF2S3*) (Gregory et al., 2019; Kotzaeridou et al., 2020; Moortgat et al., 2016; Skopkova et al., 2017). One mutation (eIF2γ-I222T) impairs the binding of eIF2β to eIF2γ (Borck et al., 2012). Another impairs the binding of the initiator tRNA to eIF2 (eIF2γ-I259M) (Young-Baird et al., 2019). Some other mutations are located close to the GTP binding site in eIF2γ domain 1 (Kotzaeridou et al., 2020). The P432S mutation, located in the domain 3 of eIF2γ is additionally related to hypopituitarism and glucose dysregulation (Gregory et al., 2019). The mechanism for the pathological effect of this mutation has not been described yet. Finally, a mutation corresponds to a 4-nucleotide deletion near to the 3' end of the EIF2S3 coding region that changes the C-terminal amino acid sequence of eIF2γ from G_{462}VTIKPTVDD to G_{462}VTSQQ (Moortgat et al., 2016). This frameshift mutation (eIF2γ-I465Sfs*4 also abbreviated eIF2γ-fs) impairs the

Cdc123-assisted assembly of eIF2 (Young-Baird et al., 2020) but the mechanism remains to be described. Overall, the data suggest that Cdc123-assisted eIF2 assembly can be a new node of translation regulation from yeast to human. Notably, *CDC123* is part of the essential genes in human, which only include about 10% of all human genes (Wang et al., 2015).

The crystallographic structure of *Schizosaccharomyces pombe* Cdc123 (Sp-Cdc123) showed that the protein belongs to the ATP grasp family. Binding of ATP was indeed observed in the structure and Cdc123 variants in the ATP binding pocket suggested that ATP was important for the Cdc123 function (Chen et al., 2023; Panvert et al., 2015; Perzlmaier et al., 2013; Vanselow et al., 2022). On the other hand, the crystallographic structure of Sp-Cdc123 bound to the domain 3 of eIF2γ from S*accharomyces cerevisiae* (Sc-eIF2γD3 or simply Sc-γD3) was determined (Sp-Cdc123:Sc-eIF2γD3). This structure showed how Sc-eIF2γD3 is bound to domain I of Sp-Cdc123 in yeast. However, the C-terminal tail of Cdc123 was not visible in the structure, leaving the essential function of this region unexplained. A docking of the eIF2αγ structure onto Cdc123, combined with genetic and biochemical experiments, allowed the authors to propose a model for the role of Cdc123 in the assembly of eIF2γ to eIF2α (Panvert et al., 2015). Despite these recent findings based on the structure of a heterologous complex, the mechanism of action of Cdc123 remains unclear and structural information for the human protein is still awaited.

In the present study, we determined the crystallographic structure of human Cdc123 (Hs-Cdc123) bound to human eIF2γD3 (Hs-eIF2γD3) domain. The overall structure of the human complex is similar to that of the yeast complex. However, the present structure shows how the long C-terminal region of Hs-Cdc123 interacts with Hs-eIF2γD3 and is connected to the ATP binding site. We also used a thermal shift assay to

study the binding of ATP and ADP to Cdc123 from yeast and human. The results show that ATP is tightly bound to Cdc123 whereas the affinity of ADP is much smaller. Using yeast cell viability experiments, western blot analysis and two-hybrid assays, we show that ATP is important for the function of Hs-Cdc123 in eIF2 assembly. These data and recent findings (Chen et al., 2023; Vanselow et al., 2022) allow us to propose a refined model to explain the mechanism of action of Cdc123 in eIF2 assembly.

Materials and Methods

Production and purification of Cdc123

The coding sequence of Hs-Cdc123 was amplified by PCR using a Hs-Cdc123 cDNA plasmid (Vanselow et al., 2022) and cloned into NdeI and NotI restriction sites of pET15blpa. The resulting plasmid, pET15b-Hs-Cdc123 allows expression of an N-terminally tagged version of Hs-Cdc123. The plasmid was transformed into *E. coli* BL21 Rosetta pLacI-Rare (Merck, Novagen). 1 L cultures were in 2xTY containing 50 µg/mL of ampicillin and 34 µg/mL of chloramphenicol. Expression was induced by adding 1 mM of IPTG in an overnight 37°C culture. After induction, the cultures were continued for 5 hours at 18°C. For Hs-Cdc123, cells corresponding to 1 L of culture were disrupted by sonication in 40 mL of buffer A (10 mM HEPES pH 7.5, 500 mM NaCl, 3 mM 2-mercaptoethanol, 0.1 mM PMSF, 0.1 mM benzamidine). The crude extract was loaded onto a column (5 mL) containing Talon affinity resin (Clontech) equilibrated in buffer A. After washing the column with buffer A supplemented with 10 mM imidazole, the tagged protein was eluted with buffer A supplemented with 125 mM imidazole. The eluted protein was diluted to reach a 200 mM NaCl concentration and then loaded onto a Q-Sepharose column (10 mm x 4 cm; GE-Healthcare) equilibrated in buffer A1 (10 mM HEPES pH 7.5, 3 mM 2-mercaptoethanol, 0.1 mM PMSF, 0.1 mM benzamidine) supplemented with 200 mM NaCl. A gradient from 200 mM NaCl to 1 M NaCl was used for elution (200 mL at a flow rate of 2.5 mL/min). The recovered protein was finally loaded onto a Superdex 200 10/300 (GE-Healthcare) equilibrated in buffer A1 supplemented with 200 mM NaCl. Hs-Cdc123 was finally concentrated to 10 mg/mL using centricon 30. The same protocol was used to purify Sp-Cdc123 (Panvert et al., 2015) and Sc-Cdc123 (Supplementary Figure 1A).

Production and purification of the human Hs-Cdc123:Hs-γD3 complex

The gene coding for human eIF2γ was first PCR amplified from cDNA and cloned into the NdeI-XhoI restriction sites of the pColaDuet-1-ORF2. The resulting plasmid was then modified using standard QuikChange™ site-directed mutagenesis (Stratagene) to produce a gene fragment coding for the γD3 domain (residues 362-471) of human eIF2γ. The corresponding plasmid was named pColaDuet-1-ORF2-H-eIF2γD3. pColaDuet-1-ORF2-H-eIF2γD3 and pET15b-Hs-Cdc123 were co-transformed into *E. coli* BL21 Rosetta pLacI-Rare (Merck, Novagen) and selected onto LB plates containing 50 µg/mL of ampicillin, 34 µg/mL of chloramphenicol and 25 µg/mL kanamycin. 1 L cultures were in 2xTY containing the desired antibiotics. Expression was induced by adding 1 mM of IPTG when OD_{650} nm reached 0.8. After induction, the cultures were continued overnight at 18°C. Cells corresponding to 1 L of culture were disrupted by sonication in 40 mL of buffer A. The crude extract was loaded onto a column (5 mL) containing Talon affinity resin (Clontech) equilibrated in buffer A. After washing the column with buffer A supplemented with 10 mM imidazole, the tagged protein was eluted with buffer A supplemented with 125 mM imidazole. The eluted protein was diluted in buffer A1 to reach 200 mM NaCl concentration and then loaded onto a Q-Sepharose column (10 mm x 4 cm; GE-Healthcare) equilibrated in the same buffer. A gradient from 200 mM NaCl to 1 M NaCl was used for elution (200 mL at a flow rate of 2.5 mL/min). This step allowed us to separate the Hs-Cdc123:γD3 complex from the large excess of Hs-Cdc123 isolated after Talon affinity purification. The recovered Hs-Cdc123:γD3 complex was finally loaded onto a Superdex 200 10/300 column (GE-Healthcare) equilibrated in buffer A containing 200 mM NaCl to polish purification of the complex. Finally, Hs-Cdc123:γD3

was concentrated to 10 mg/mL using centricon 30 before crystallization (Supplementary Figure 1A).

To facilitate structure resolution, we also produced and purified Hs-Cdc123:γD3 containing selenomethionine. The selenomethionylated proteins were epressed in autoinducible medium as described (Studier, 2005). After cultivation, the selenomethionylated protein complex was purified as described for native Hs-Cdc123:γD3.

Crystallization and structure determination

Crystallization trials were performed at 4°C with or without 1 mM ATP and 5 mM $MgCl_2$. Sitting drops were made with a Mosquito robot (TTP Labtech) and standard commercial kits (Hampton Research and Qiagen) by mixing 1:1 Hs-Cdc123:γD3 w/wo 1 mM ATP and 5 mM $MgCl_2$ and the precipitating solution. Crystals for native or selenomethionylated Hs-Cdc123:γD3 were rapidly obtained in many different conditions containing PEG3350 (PEG/ION and Index Hampton Research). Before data collection, the crystals were rapidly soaked into a solution containing the precipitating agent supplemented with 25 to 30% of glycerol. Two X-ray crystallographic datasets collected at the Soleil Synchrotron (Saint Aubin France) on the Proxima-2 beamline were used in this study (Table 1). One dataset was collected from a crystal obtained with selenomethionylated Hs-Cdc123:γD3 with no added ATP-Mg^{2+} and a second dataset was collected from a crystal of Hs-Cdc123:γD3 obtained in the presence of 1 mM ATP and 5 mM Mg^{2+}. Data were processed with XDS (Kabsch, 2010), scaled with AIMLESS (Evans and Murshudov, 2013), analyzed with CCP4 programs (Winn et al., 2011) and finally processed for anisotropy in STARANISO (Tickle et al., 2016). All these steps were performed in AUTOPROC (Vonrhein et al., 2018). Crystals belong to the $P2_1$ space

group. However, there is a two-fold NCS axis yielding a strong pseudo $P2_12_12$ symmetry. The structure of Hs-Cdc123:γD3 complex was solved by molecular replacement with PHASER (McCoy et al., 2007) using two separate ensembles, one corresponding to Sp-Cdc123 and the second one to the Sc-γD3 domain (Panvert et al., 2015, PDB ID Code 4ZGQ). For each ensemble, a solution with a high Z-score value was found (Z=8.9 and Z=16.7). The molecular replacement 2mFo-DFc electron density map was of good quality and allowed us to build a first model of Hs-Cdc123:γD3. To facilitate the refinement process, we also calculated an experimental map using the automated SAD phasing procedure with a partial model in Phaser-EP (McCoy et al., 2007; Winn et al., 2011). Coordinates and associated B factors were then refined through several cycles of manual adjustments with Coot (Emsley et al., 2010) and positional refinement with PHENIX (Adams et al., 2010). A small fraction of twinning was evidenced and refined in PHENIX. Moreover, residual electron density showed that some ATP-Mg^{2+} was present in the selenomethionylated Hs-Cdc123:γD3 crystals. Therefore ATP-Mg^{2+} was positioned in the model and the occupancy of the molecule was refined. In the final models, regions 50-68, 294-299 and 311-318 of Hs-Cdc123 and regions 384-390 and 466-470 of Hs-γD3 belonging to long mobile loops could not be traced in the electron density. Statistics for data collection and refinement are given in Supplementary Table 1.

Binding of ATP to Cdc123 using fluorescence-based thermal shift assays

Experiments were done in 96-well plates using a Bio-Rad CFX-96 Real-Time PCR system. Reaction mixtures (25 µL) were assembled in buffer A (10 mM HEPES-NaOH pH 7.5, 500 mM NaCl, 2 mM $MgCl_2$, 10 mM 2-mercaptoethanol) and contained Cdc123 (0.15 mg/mL), 5x SYPRO™ orange (Invitrogen) and various concentrations of ATP-Mg^{2+} (0.1 µM to 6.4 mM). Temperature was increased by 0.5°C every 60 seconds. Fluorescence curves as a function of temperature in the 10°C-70°C range were processed

as described (Pantoliano et al., 2001; Redhead et al., 2015), by non-linear least square fitting of the following equation 1 to the experimental datapoints (Supplementary Figure 1B), using Origin (OriginLab) or Prism (GraphPad):

$$F(T) = F_u + m_u(T - T_m) + \frac{F_f - F_u + (T - T_m)(m_f - m_u)}{1 + \exp\left(-\frac{\Delta H_u}{R}\left(\frac{1}{T} - \frac{1}{T_m}\right) + \frac{\Delta Cp_u}{R}\left(\ln\left(\frac{T}{T_m}\right) + \frac{T_m}{T} - 1\right)\right)}$$

F(T) is the measured fluorescence in arbitrary units at the temperature *T*; F_u and F_f are the fluorescence at the melting temperature T_m with the protein in the unfolded and folded states, respectively; m_u and m_f are coefficients reflecting temperature dependence of the fluorescence of the dye bound to the unfolded and folded states, respectively; ΔH_u and ΔCp_u are the enthalpy and heat capacity, respectively, of protein unfolding at a reference temperature chosen as T_m in the absence of ligand and R is the gas constant. Usually, all parameters were allowed to vary in the fitting procedure. In the case of Sc-Cdc123, that had a lower melting temperature than the two other orthologues, m_f was poorly defined for curves recorded at low ATP concentrations and was therefore kept at a constant value of 0 throughout, consistent with the shape of the fluorescence curves at high ATP concentration. In the case of the *Schizosaccharomyces pombe* protein (Sp-Cdc123,) in addition to the main fluorescence transition that occurred around 52°C, a minor fluorescence increase was observed around 80°C. This suggested the existence of an additional minor denaturation step. Only the main transition was considered for T_m calculations (Supplementary Figure 1C).

The obtained T_m values were then used to estimate the dissociation constant of the studied enzyme-ligand couple as described (Cimmperman et al., 2008; Matulis et al., 2005; Pantoliano et al., 2001; Redhead et al., 2015; Zubrienė et al., 2009). Briefly, the equilibrium constant for protein unfolding at a temperature *T* can be expressed as:

$$K_u = \exp(-\frac{\Delta H_u}{R}\left(\frac{1}{T} - \frac{1}{T_r}\right) + \frac{\Delta Cp_u}{R}(\frac{T_r}{T} - 1 + \ln\left(\frac{T}{T_r}\right)))$$

where ΔH_u and ΔCp_u are the enthalpy and heat capacity, respectively, of protein unfolding at a reference temperature T_r chosen as T_m in the absence of ligands. Moreover, the binding constant of the ligand at temperature T can be expressed as:

$$K_b = \frac{1}{K_d}\exp(\frac{\Delta H_b}{R}(\frac{1}{T_o} - \frac{1}{T}) - \frac{\Delta Cp_b}{R}(-\frac{T_o}{T} + 1 + \ln\left(\frac{T_o}{T}\right)))$$

where ΔH_b and ΔCp_b are the enthalpy and heat capacity, respectively, of binding of the ligand to the protein unfolding at a reference temperature T_0 chosen as 298K here, and K_d is the dissociation constant of the protein:ligand complex at T_0. The total concentration of ligand in the assay $[L_t]$ necessary to raise the melting temperature to a temperature T can be expressed as (equation 2):

$$[L_t] = (K_u - 1)(\frac{[\mathrm{P}_t]}{2K_u} + \frac{1}{K_b})$$

where $[P_t]$ is the total protein concentration in the assay.

For estimating K_d values, curves simulating the variation of melting temperature as a function of $[L_t]$ were calculated using equation 2 for various K_d values and visually compared with the experimental curves. In this procedure, ΔH_u and ΔCp_u were set to the mean of the values obtained from the fluorescence curves obtained with the control experiments in the absence of ligands. In some cases, for better fitting the whole data, the *Tr* value was slightly adjusted. Each experiment was repeated at least twice, and the means ± sd of the melting temperatures were plotted as a function of the logarithm of ligand concentration. ΔH_b was set to -3 kcal.mol^{-1}, the value measured for ATP binding to Sp-Cdc123 using Isothermal Titration Calorimetry (Panvert et al., 2015) and ΔCp_b to -0.2 kcal.mol^{-1}.K^{-1}, an average value for protein-ligand interactions (Matulis et al., 2005).

Note that when varied in realistic ranges, the values of ΔH_b and ΔCp_b did not have a large influence on the K_d estimates (less than a factor of two).

Yeast methods

Standard protocols were followed for growth of budding yeast cells, transformation, sporulation and tetrade dissection (Ausubel et al., 2005). Yeast strains are derivatives of W303 and listed in Supplementary Table 2. Preparation of yeast cell extracts, immunoprecipitation of flag-tagged proteins and Western analysis were done as described (Panvert et al., 2015; Vanselow et al., 2022). For detection of the flag and myc epitopes mouse monoclonal antibodies were used (anti-flag M2; anti-myc 9E10). Sc-eIF2β and Sc-eIF2γ were detected by antisera raised in rabbits (Perzlmaier et al., 2013). In the yeast-two-hybrid vectors pEG202 and pJG4-5 (Ausubel et al., 2005) the human eIF2α encoding cDNA was fused to a lexA-DNA binding domain sequence (pWS4018) and the human eIF2γ encoding cDNA was fused to the B42 transcriptional activator sequence (pWS4023). The human eIF2α and eIF2γ cDNAs were obtained from the DNASU plasmid repository. In addition to the regular reporter strain W276, derivatives expressing Hs-Cdc123 wild type (W15327) or the mutant versions Hs-Cdc123-D233A (W15328) and Hs-Cdc123-D246A (W15329) were used. The mutant alleles of the Hs-Cdc123 gene were created by site-directed mutagenesis (QuickChange; Stratagene). To visualize β-galactosidase production following activation of the *lex*A-operator controlled *lac*Z gene in W276 and its derivatives, yeast colonies were overlaid with an X-Gal top agar (0.2 mg/ml X-Gal; 0.5 M sodium phosphate buffer pH 7.0; 0.1% SDS; 6% DMFA; 0.5% Bacto agar).

RESULTS

Binding of ATP or ADP to Cdc123 using thermal shift assay

In order to study the binding of ATP-Mg^{2+} to Cdc123, we used a thermal shift assay. This method is based on the general idea that ligand binding increases protein stability (Pantoliano et al., 2001). Protein denaturation caused by increasing temperature was monitored using the ThermoFluor™ method with an environmentally sensitive fluorescent dye, allowing us to determine the protein melting temperature T_m (Pinz et al., 2022). This experiment was repeated in the presence of various concentrations of ATP-Mg^{2+} (Supplementary Figure 1B). From the analysis of the variations of the melting temperatures as a function of the concentrations of the nucleotide, dissociation constants can be derived ((Cimmperman et al., 2008; Matulis et al., 2005; Pantoliano et al., 2001; Redhead et al., 2015; Zubrienė et al., 2009); see Materials and methods).

	Estimated *Kd* (µM) ATP	Estimated *Kd* (µM) ADP
Hs-Cdc123	1.6 (17°C)	120 (13°C)
Sc-Cdc123	1.2 (18°C)	18 (11°C)
Sp-Cdc123	140 (6°C)	900 (4°C)

Table 1 : *Kd* values of the ATP and ADP nucleotides for the indicated Cdc123 enzymes. Values in parentheses show the amplitudes of *Tm* variation in the range of nucleotide concentrations used in the thermal shift assay.

A K_d value of 140 µM could be estimated for the Sp-Cdc123:ATP-Mg^{2+} complex (Figure 1 and Table 1), in reasonable agreement with the value determined using Isothermal Titration Calorimetry (67 µM; (Panvert et al., 2015)). With Sc-Cdc123 and Hs-Cdc123, small concentrations of ATP-Mg^{2+} -in the micromolar range- had larger effects of the stabilities of the proteins as compared to Sp-Cdc123. Consistent with these observations, the estimated dissociation constants were 1.6 µM and 1.2 µM for Hs-

Cdc123 and Sc-Cdc123 (Table 1). As compared to ATP-Mg^{2+}, larger concentrations of ADP-Mg^{2+} were required to observe changes in the melting temperature of the three Cdc123 proteins. Accordingly, the estimated dissociation constants were systematically increased to values of 120 µM (Hs-Cdc123), 18 µM (Sc-Cdc123) and 900 µM (Sp-Cdc123) (Table1).

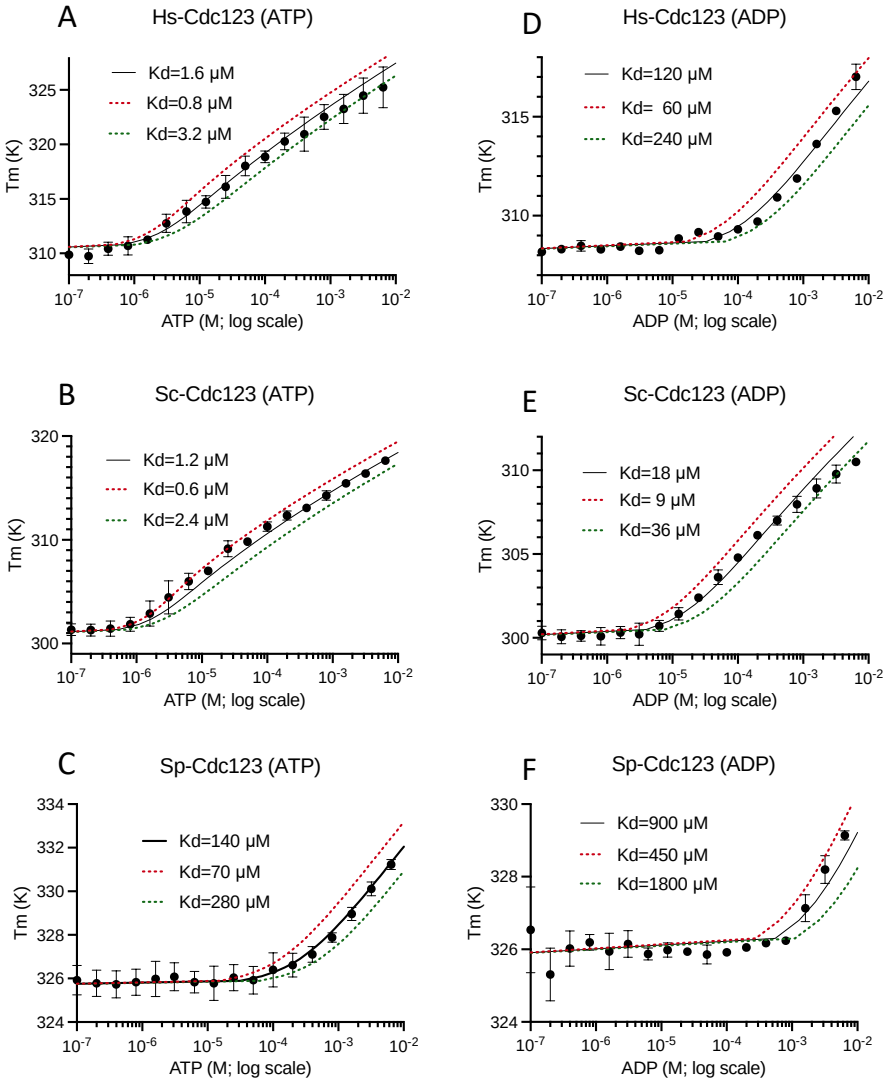

Figure 1: Estimation of *Kd* values. Each panel plots the measured *Tm* value (mean ± sd from at least two experiments) as a function of the nucleotide concentration in log scale. The best fit to a curve calculated as described in Materials and Methods (Cimmperman et al., 2008; Matulis et al., 2005; Pantoliano et al., 2001; Redhead et al., 2015; Zubrienė et al., 2009) is drawn with a solid line. The corresponding *Kd* value is shown on the panel. Curves obtained with a *Kd* value two-fold higher (green) or two-fold lower (red) are also drawn for comparison. Panels A, B, C: ATP binding to Hs-Cdc123, Sc-Cdc123 and Sp-

Cdc123, respectively. Panels D, E, F: same for ADP binding. The estimated dissociation constants are shown in Table 1.

Crystallographic structure of Hs-Cdc123:eIF2γD3 complex

The Hs-Cdc123:eIF2γD3 complex was first purified by affinity chromatography using an N-terminally tagged version of Hs-Cdc123 to trap Hs-eIF2γD3 (See Materials and Methods). Additional steps using anion exchange chromatography and molecular sieving allowed us to polish the preparation (Supplementary Figure 1A). Crystals of Hs-Cdc123:γD3 were obtained at 4°C in solutions containing 20% PEG3350 and various additives, in the presence or in the absence of ATP-Mg^{2+} (Table 1). The structure was solved by molecular replacement and experimental phasing using a selenomethionine version of the complex. Data were processed with STARANISO to deal with diffraction anisotropy. The structure of Hs-Cdc123:γD3:ATP-Mg^{2+} was refined to 2.08 Å resolution and the structure of the selenomethionylated complex was refined to 1.97 Å resolution (Supplementary Table 1). Two molecules related by a pseudo two-fold axis are present in the asymmetric unit. Because the quality of the electron density is slightly better for monomers C and D of Hs-Cdc123 and Hs-γD3, particularly for the long loops of Hs-Cdc123, these two molecules are hereafter used as references. On the other hand, comparison of the structure of the selenomethionylated complex to that of Hs-Cdc123:γD3:ATP-Mg^{2+} complex did not reveal major conformational changes (rms value of 0.267 Å for 357 C-α atoms compared). Therefore, the Hs-Cdc123:γD3:ATP-Mg^{2+} will be majorily described.

Binding of Hs-γD3 to Hs-Cdc123

Hs-Cdc123 is composed of two domains with ATP-Mg^{2+} bound at the interface, as observed in Sp-Cdc123 (Panvert et al., 2015) and in enzymes belonging to the ATP-grasp family (Fawaz et al., 2011) (Figure 2A and Supplementary Figure 2A). D3 of Hs-eIF2γ forms a β barrel highly homologous to its eukaryotic orthologs (Supplementary Figure 3A). It is mainly bound to domain I of Hs-Cdc123 (Figure 2A and 2B).

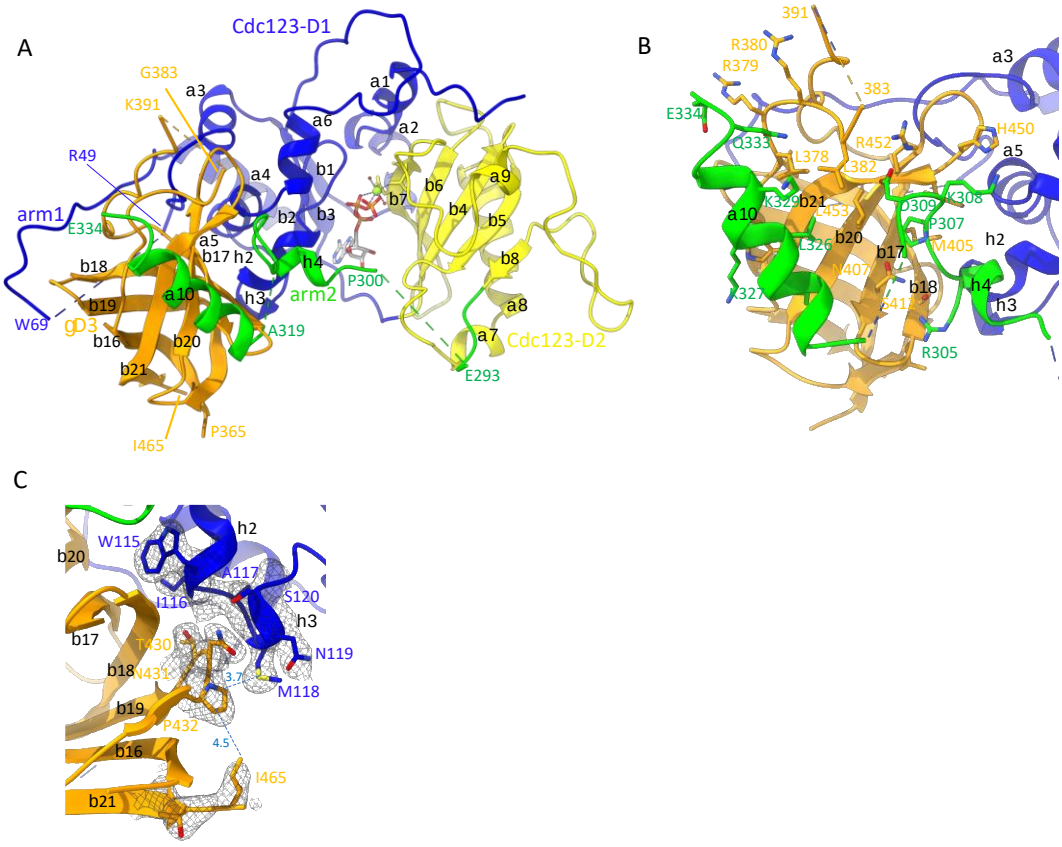

Figure 2: Crystallographic structure of Hs-Cdc123:Hs-γD3:ATP-Mg^{2+}

(A) Overall structure of Hs-Cdc123:γD3:ATP-Mg^{2+}. Hs-Cdc123 is shown in blue (residues 1-174), yellow (residues 175-289) and green (C-terminal peptide, residues 290-336). Regions 50-68, 294-299 and 311-318 of Hs-cdc123 are highly mobile and could not be traced in the electron density. ATP is shown with sticks, Mg^{2+} ion is shown as a green sphere. Hexacoordination of the Mg^{2+} ion is shown with dashed lines (see also Supplementary Figure 4). Hs-γD3 is shown in orange. Secondary structures are labeled as defined for the Sp-Cdc123 structure (Panvert et al., 2015). The figures were made with ChimeraX (Pettersen et al., 2021).

(B) Close-up view of the binding of the C-terminal region of Hs-Cdc123 to Hs-eIF2γD3. Interacting residues belonging to these regions (as listed in Supplementary Table 3) are in sticks and labeled.

(C) Close-up view showing the hydrophobic interaction of P432 with M118 and the proximity of I465 from P432. Interactions involving T430, N431 and P432 with residues from the h2-h3 helices of Cdc123 are listed in Supplementary Table 3.

The η2−η3, α6 and the 39-43 loop of Hs-Cdc123 carry residues involved in the interaction with Hs-γD3 (Supplementary Table 3). Overall, the structure of Hs-Cdc123:γD3:ATP-Mg^{2+} is similar to the previously determined structure of Sp-Cdc123:Sc-γD3 complex (Panvert et al., 2015) (rmsd between the two structures is 1.2 Å for 299 Cα atoms compared). This shows that the main regions of contact between γD3 and domain I of Cdc123 are similar in the two structures (Supplementary Figure 2A) and conserved from yeast to human. When the Cdc123 molecules of the human and yeast complexes are superimposed, a small difference in the positioning of the γD3 domain with respect to Cdc123-D1 is observed (3.06 Å translation and 9.6° rotation, Supplementary Figure 2A). This difference in the orientation of γD3 is possibly related to a small movement of Cdc123 α3 and the following loop as well as to the participation of C-terminal region of Hs-Cdc123 in the binding to γD3 (Figure 2B). Indeed, in Hs-Cdc123 domain I, the long linker containing forty-four residues located between α3 and α4 (residues 40-83, Supplementary Figure 2) is partially ordered. Residues 40-50 and 69-83 were positioned in the electron density (Supplementary Figure 4). This region surrounds γD3 and contacts it on the side of the β18-β19 hairpin. This region is hereafter named arm 1 (Figure 2). On the other hand, the C-terminal region of Hs-Cdc123 could be partially built (Figure 2 and Supplementary Figure 4 A-C). This long C-terminal tail, from residue 290 to residue 336, starts from Hs-Cdc123 domain 2 and extends to Hs-γD3 with which it interacts via its C-terminal α-helix. This region is hereafter named arm 2. These two regions contribute many interactions described in Supplementary Table 3. Arm1 and arm2 of Hs-Cdc123 act as tweezers that wrap the Hs-γD3 domain and increase

the surface of interaction between Cdc123 and γD3 to 4530 Å^2, as compared to 1307 Å^2 for the Sp-Cdc123:Sc-γD3 complex or 1742 Å^2 for the present complex where regions 69-80 and 291-336 have been deleted from the model (Supplementary Figure 2B). These two regions have B-values above the mean B-values for the model (Supplementary Figure 2C) indicative of their flexibility. Packing analysis shows that region from residue 290 to 319 of Hs-Cdc123 is not involved in packing interactions in the crystals. However, the C-terminal α10 helix of one Hs-Cdc123 also contacts a neighbor molecule. Therefore, its positioning could have been stabilized by crystal packing interactions. In the Sp-Cdc123:Sc-γD3 structure, arm 2 was mostly disordered and only the C-terminal helix could be built. However, the positioning of this C-terminal helix with respect to the main part of Cdc123 could not be established. Overall, the present data suggests that these two arms are mobile regions of Cdc123 that are involved in the binding of the γD3 domain.

ATP-Mg^{2+} binding site of Hs-Cdc123

ATP-Mg^{2+} is bound to Hs-Cdc123 at the interface between D1 and D2. Residues involved in ATP-Mg^{2+} binding were analyzed with Ligplot (Wallace et al., 1996) and shown in Figure 3A. For comparison, the Sp-Cdc123 structure bound to ATP-Mg^{2+} is shown in Figure 3B. Most residues involved in ATP binding are conserved in the two proteins (Supplementary Figure 3).

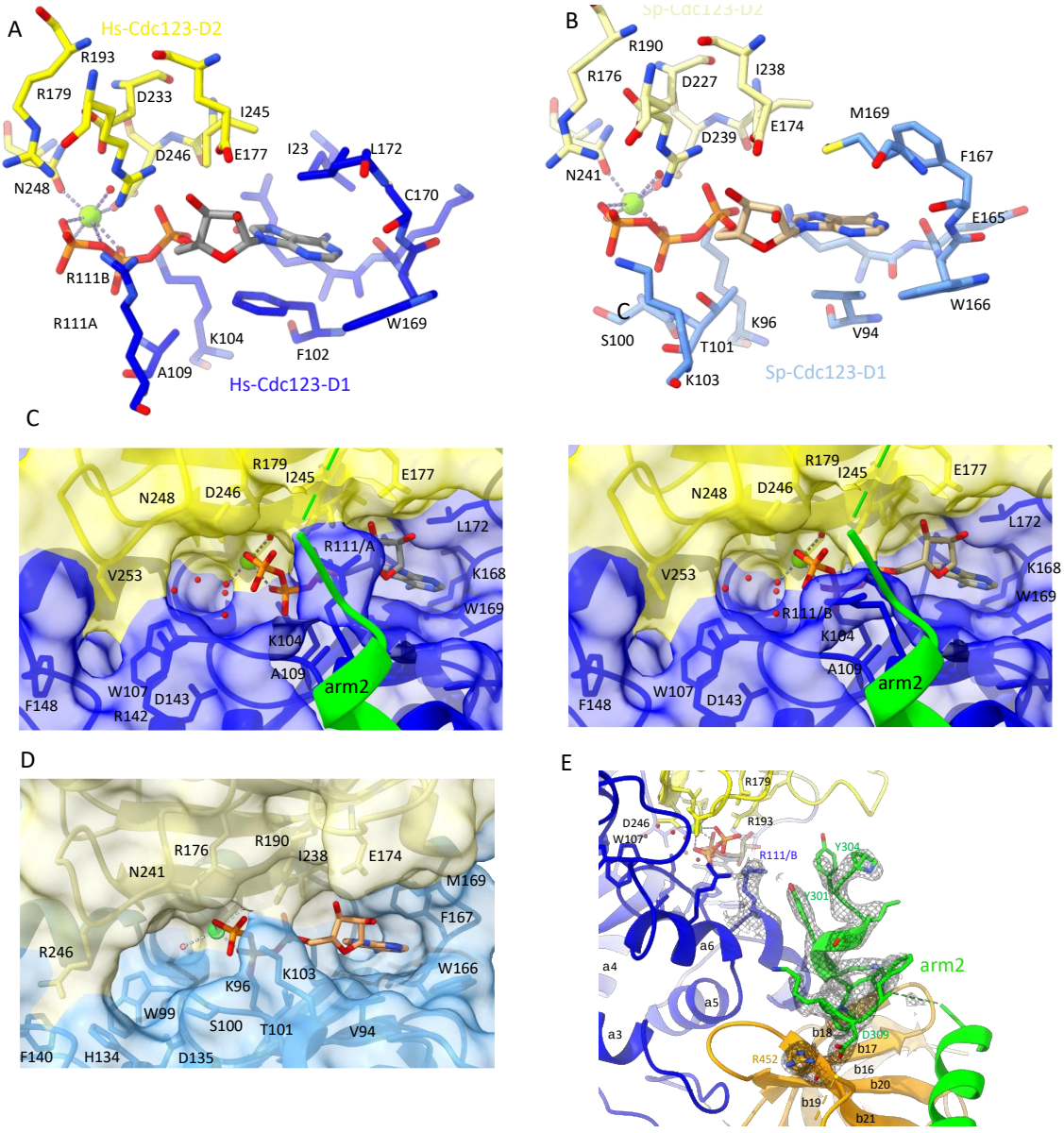

Figure 3: Binding of ATP-Mg^{2+}

(A) The Hs-Cdc123 residues involved in ATP binding are shown in sticks. D233 (D227 in Sp-Cdc123) is also represented as it tightly interacts with R179, N248, and a water molecule (see also Supplementary Figure 4D). Residues belonging to domain 1 are colored in blue and those belonging to domain II are colored in yellow. Water molecules are shown with red spheres and the magnesium ion is shown as a green sphere.

(B) Same as view A but for Sp-Cdc123 (Panvert et al., 2015).

(C) Molecular surface representation of Hs-Cdc123:Hs-γD3 :ATP-Mg^{2+}. The color code is the same as in view A. The view shows the cavity facing the ATP binding pocket with the side chain of R111 in two alternative conformations (A, right and B, left).

(D) Same as C but for Sp-Cdc123:Sc-γD3:ATP-Mg^{2+}.

(E) Close-up view showing the contacts of Hs-Cdc123 arm 2 with the ATP binding site and with γD3.

To address the relevance of ATP binding to the human Cdc123 ortholog, we generated two variants altered in the ATP-binding site and studied their properties. To this end, we replaced two conserved aspartate residues (D233 and D246 in Hs-Cdc123 corresponding to D227 and D239 in Sp-Cdc123, Panvert et al., 2015); Figure 3A and B, Supplementary Figure 3) by alanine residues through site-directed mutagenesis of the Hs-Cdc123 gene. In a first step, we tested for biological function by complementation analysis in budding yeast. For this, we expressed wild type Hs-Cdc123 and the mutant versions D233A and D246A in a diploid yeast strain heterozygote for a *CDC123* gene deletion. Western analysis confirmed that the mutant Hs-Cdc123 versions were expressed at levels comparable to the wild type protein (Figure 4A). By tetrade dissection following meiosis and sporulation, we recovered haploid progeny carrying a Hs-Cdc123 expression construct but lacking the yeast *CDC123* gene. In case of wild type Cdc123, these cells had normal growth properties as indicated by the formation of regular sized colonies (Figure 4A). Apparently, Hs-Cdc123 can take over the function of its yeast ortholog consistent with a previous systematic gene replacement study (Kachroo et al., 2015). In contrast, yeast *cdc123*-Δ cells expressing the Hs-Cdc123-D233A or -D246A mutant version formed only tiny or small colonies, respectively (Figure 4A). These data suggest that the biological function of Hs-Cdc123 depends on the integrity of its ATP binding site.

To define further the defect caused by a compromised ATP binding site, we studied the interaction of the Hs-Cdc123 mutant proteins with eIF2 subunits. For this, flag-tagged Hs-Cdc123 constructs were expressed in yeast and a strain expressing flag-tagged yeast Cdc123 served as a positive control. Flag-tagged proteins were immunoprecipitated from cell extracts and analyzed for co-precipitation of eIF2 subunits by Western analysis. Precipitates of Hs-Cdc123 contained eIF2 subunits in amounts

similar to precipitates of Sc-Cdc123 (Figure 4B). In contrast, the mutant versions of Hs-Cdc123 co-precipitated hardly any (D233A) or only very little (D246A) of the β and γ subunits of eIF2 consistent with the view that integrity of the ATP binding site of Cdc123 is essential for the interaction of Cdc123 with eIF2γ and the eIF2γ-eIF2β dimer (Panvert et al., 2015; Vanselow et al., 2022). To facilitate detection of Sc-eIF2α, the yeast strains used in this analysis carried a myc-epitope fusion of the *SUI2* gene, which encodes eIF2α in budding yeast. The myc-tagged Sc-eIF2α subunit was present in similar amounts in the precipitates of Sc-Cdc123 and both the wild type and mutant versions of Hs-Cdc123. This confirms a previously observed direct contact of Sc-Cdc123 with Sc-eIF2α (Vanselow et al., 2022) and suggests that the Cdc123-eIF2α contact does not require intactness of the ATP binding site of Cdc123.

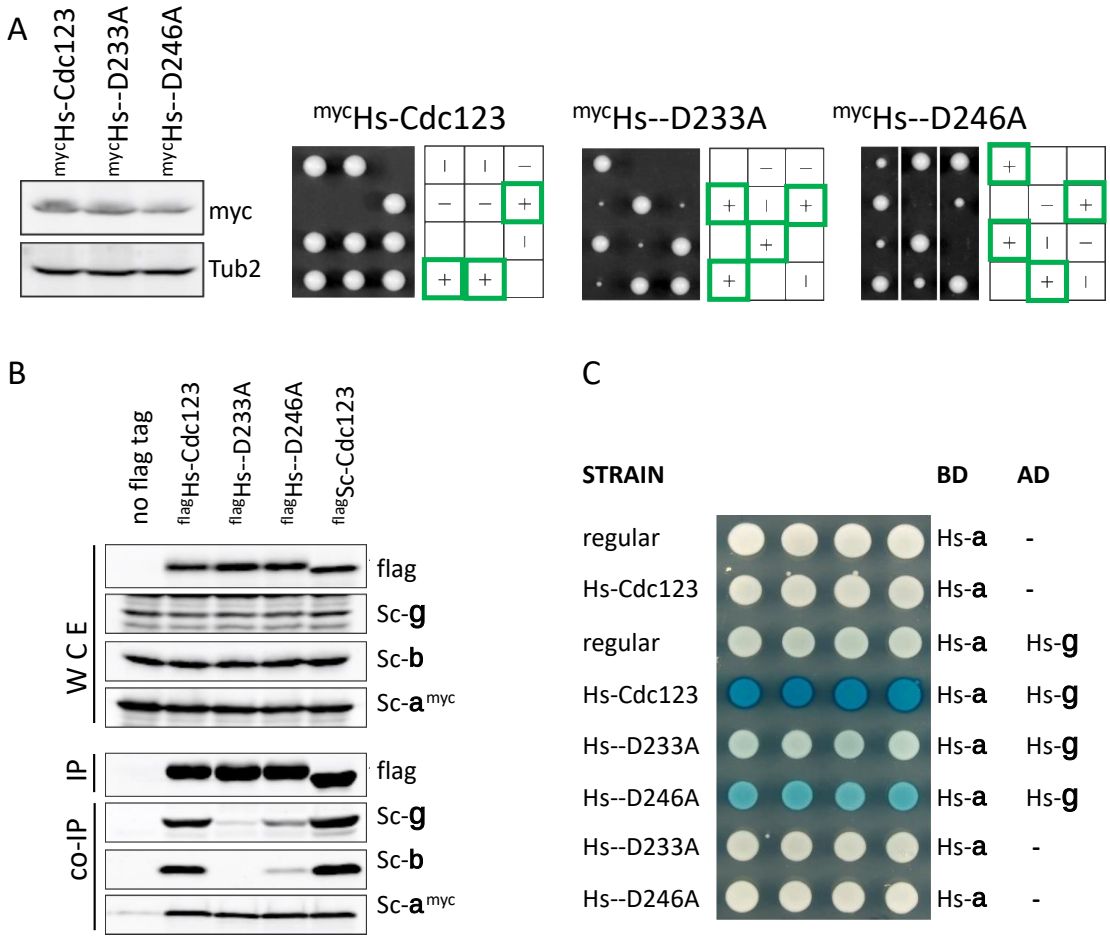

Figure 4: ATP binding site variants of Hs-Cdc123.

(A) Complementation analysis in yeast. Expression of myc-tagged wild type or mutant versions of Hs-Cdc123 in CDC123/cdc123-Δ diploid strains (Hs-Cdc123: W15001; Hs-Cdc123-D233A: W15002; Hs-Cdc123-D246A: W15003) was compared by Western analysis. Tub2 served as a protein loading control. The four haploid spores generated by a single diploid cell were recovered by tetrade dissection and placed in a vertical line on solid growth medium to monitor colony formation. Green squares indicate the positions of haploid progeny carrying both the cdc123-□ allele (horizontal line) and the Hs-Cdc123 expression construct (vertical line).

(B) Hs-Cdc123 protein interaction with Sc-eIF2 subunits. Expression of flag-tagged wild type or mutant versions of Hs-Cdc123 in a SUI2-myc strain (Hs-Cdc123: W14968; Hs-Cdc123-D233A: W14969; Hs-Cdc123-D246A: W14970) was inspected by Western analysis. Negative and positive controls were the SUI2-myc strain lacking a flag expression construct (no flag tag: W9877) or expressing flag-tagged Sc-Cdc123 (W14974), respectively. Whole cell extracts (WCE) of these strains were also probed for Sc-eIF2γ, Sc-eIF2β and Sc-eIF2α-myc. From the whole cell extracts, flag-tagged proteins were immunoprecipitated by an antibody against the flag epitope (IP). These precipitates were probed by Western analysis for the presence of flag-tagged proteins, Sc-eIF2γ, Sc-eIF2β and Sc-eIF2α-myc (co-IP).

(C) Yeast-two-hybrid analysis of Hs-eIF2γ association with Hs-eIF2α. Y2H-reporter strains that lack any Hs-Cdc123 construct (regular: W276) or express flag-tagged wild type (Hs-Cdc123: W15327) or mutant versions (Hs--D233A: W15328; Hs--D246A: W15328) of Hs-Cdc123 were used to express the lexA DNA binding domain (BD) fused human eIF2α subunit (Hs-α) either alone to test for autoactivation or in combination with a B42 transcriptional activation domain (AD) fused human eIF2γ subunit (Hs-γ) to test for association of Hs-eIF2α with Hs-eIF2γ. Yeast colonies were overlaid with a X-gal containing top agar to visualize β-galactosidase activity resulting from transcriptional activation of the lexAop-lacZ reporter gene.

As a third test, we analyzed the ability of Hs-Cdc123 to promote eIF2 assembly. For this, we used a Y2H-assay to monitor the association of Hs-eIF2α fused to a DNA-binding domain with Hs-eIF2γ fused to a transcriptional activation domain. Co-expression of the human α and γ subunits activated the *lac*Z reporter gene only weakly (Figure 4C). Interestingly, the additional expression of wild type Hs-Cdc123 in the Y2H strain increased the reporter signal substantially. This suggests that Hs-Cdc123 can promote assembly of human eIF2 subunits in yeast. In contrast, the ATP binding site mutants of Hs-Cdc123 had either marginal (D233A) or significantly reduced (D246A) activity in this assembly assay. Together the data point to a critical role of the ATP binding site for the biological function of Hs-Cdc123 and its biochemical activity in eIF2 subunit binding and assembly.

Interestingly, R111 in Hs-Cdc123 replaces K103 of Sp-Cdc123 (Figure 3A and B). R111 shows two alternative side chain conformations that make several interactions with the γ and β phosphate of ATP-Mg^{2+} (Figure 3C and D). These additional contacts could participate in the high binding affinity of Hs-Cdc123 for ATP-Mg^{2+}. An R residue is also found at this position in Sc-Cdc123 which also displays high affinity for ATP (Table 1, Supplementary Figure 3B). As already observed in Sp-Cdc123 (Panvert et al., 2015), a cavity borders the gamma phosphate group of ATP (Figure 3C and D). This cavity, filled with water molecules, may be the binding site of another substrate. The

shape of the cavity in Hs-Cdc123 is different from that of Sp-Cdc123 due to some variations in the side chains of residues that border it. Notably, the 300-306 region in the C-terminal of Hs-Cdc123 is located close to R111 and the ATP binding site (Figure 3E). In particular, Y304 contacts the side chain of R111 in its B conformation. Moreover, as mentioned above, the "300" region of Hs-Cdc123 also contacts γD3 and the α10 helix is packed onto the γD3 barrel. Therefore, the present structure shows a link between the ATP binding site and the binding of the γD3 domain (Figure 3E).

DISCUSSION

Previous results showed that the C-terminal tail of yeast eIF2γ was required for the interaction with yeast Cdc123. Removal of the last 13 amino acids of Sc-eIF2γ rendered eIF2γ unable to co-precipitate Cdc123 or α and β subunits (Perzlmaier et al., 2013). On the other hand, the C-terminal region of yeast Cdc123 is required for its function in vivo (Panvert et al., 2015). Moreover, similarly to the situation in yeast, it was shown using a yeast strain expressing Hs-eIF2 subunits, that the C-terminus of Hs-eIF2γ was also required for interaction with Hs-Cdc123 or Hs-eIF2α or Hs-eIF2β (Vanselow et al., 2022). The present structure shows for the first time the tracing for the C-terminal region of Cdc123 that goes from Cdc123 domain 2 to eIF2γD3 binding site. γD3 interacts with residues 305 to 309 and the C-terminal helix of Cdc123. These two regions contact the face β17-18-20-21 (Figure 2B) of the γD3 β-barrel which overlaps the binding site of domain I of eIF2γ. Therefore, the binding of the C-terminal domain of Cdc123 at this position is not compatible with the binding of the active conformation of eIF2γ as it is observed in the heterotrimeric eIF2 (Brito Querido et al., 2020; Llacer et al., 2015; Schmitt et al., 2012). This observation agrees well with recent conclusions obtained with the yeast proteins that Cdc123 can interrupt the intramolecular association of the G-domain (D1) of eIF2γ with domains 2 and 3 (Vanselow et al., 2022). One could imagine that in a first step, Cdc123 binds an immature form of eIF2γ that prevents its interaction with α and β subunits. This immature conformation may resemble the open form of elongation factor 1A -a protein homologous to eIF2γ (Schmitt et al., 2002)- observed in the presence of GDP (Andersen et al., 2001; Berchtold et al., 1993; Crepin et al., 2014; Kjeldgaard and Nyborg, 1992). Such an open conformation of eIF2γ would be compatible with the binding of Cdc123 as observed here. In a second step, during Cdc123-guided

maturation of eIF2γ, the C-terminal part of Cdc123 would be released from its binding site on the γD3 domain allowing eIF2γ to reach its active conformation capable of binding eIF2α and eIF2β (Figure 4). Importantly, the C-terminal part of Cdc123 contacts both the ATP binding pocket and the eIF2γD3 domain. These contacts may allow Cdc123 to couple eIF2γ binding to ATP consumption. Recent results show that effector-triggered immunity in plants is enhanced by Cdc123 through elevated ATP levels and that impairment of ATP hydrolysis disfavors Cdc123-mediated eIF2 assembly (Chen et al., 2023). This supports the idea that Cdc123 activity might be regulated by ATP concentration.

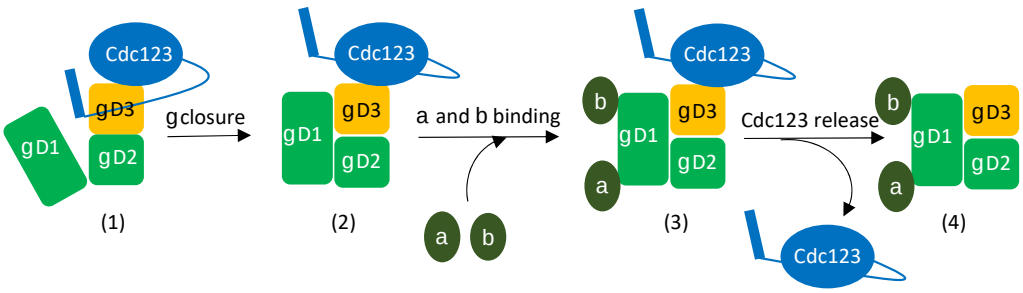

Figure 5: Model of Cdc123-assisted eIF2 assembly.

Cdc123 would bind an open conformation of eIF2γ unable to bind α and β subunits (1). In a second step, during Cdc123-guided maturation of eIF2γ, the C-terminal part of Cdc123 would be released from its binding site on γD3 allowing eIF2γ to reach its active conformation (2). eIF2γ is now capable of binding to α and β (3) triggering Cdc123 release (4). During the process, ATP hydrolysis would occur on Cdc123, which would be released in an ADP-bound form. Because of the lower affinity for ADP (Table 1), Cdc123 would be spontaneously recycled to its ATP-bound form, under the control of intracellular concentration of ATP.

The present work also gives a structural support for interpreting the effects of mutations in eIF2γ gene that are responsible for MEHMO diseases. A P432S mutation in the gene coding for eIF2γ was isolated in patients affected by X-linked hypopituitarism

and glucose dysregulation (Gregory et al., 2019). The Hs-Cdc123:γD3 structure shows hydrophobic contacts between P432 of eIF2γD3 and Hs-Cdc123 domain 1 (Figure 2C). Moreover, many interactions between the 430-432 region of eIF2γD3 and η2,η3 Cdc123 helices are observed (Supplementary Table 3). Therefore, it is possible that mutation P432S destabilizes the contacts between eIF2γ and Cdc123 and results in deficiency of Cdc123-assisted eIF2 assembly. The frameshifting mutation, known to impair Cdc123 promotion of eIF2 complex formation, changes the C-terminal sequence of eIF2γ from G_{462}VTIKPTVDD to G_{462}VTSQQ. The last residue visible in the present structure is eIF2γ-I465. Interestingly, I465 side chain is close to P432 (4.5 Å). Thus, the frameshifting mutation may affect contacts between the C-terminal extremity of eIF2γ and Cdc123. To conclude, the present study provides structural basis for the design of new molecules that could reinforce the interaction of Cdc123 with eIF2γ to compensate for the effect of MEHMO associated mutations.

Data availability

X-ray data and models have been deposited to the Protein Data Bank under the accession numbers 8PHD (Hs-Cdc123:Hs-eIF2γD3:ATP-Mg^{2+}), 8PHV (Hs-Cdc123:Hs-eIF2γD3 selenomethione).

Supplementary Data

Supplementary Data are available.

Funding

This work was supported by grants from the Centre National de la Recherche Scientifique and Ecole Polytechnique to Unité Mixte de Recherche n°7654 and by a grant from the Deutsche Forschungsgemeinschaft (SFB960 project B10) to WS. CCP was a recipient of a PhD fellowship from Institut Polytechnique de Paris.

Acknowledgements

X-ray data were collected at Soleil synchrotron. We thank Pierre Legrand (PX1), William Shepard (PX2), Martin Savko (PX2) and for their help with X-ray data collections on Proxima-1 and Proxima-2 beamlines.

REFERENCES

Adams, P.D., Afonine, P.V., Bunkóczi, G., Chen, V.B., Davis, I.W., Echols, N., Headd, J.J., Hung, L.-W., Kapral, G.J., Grosse-Kunstleve, R.W., McCoy, A.J., Moriarty, N.W., Oeffner, R., Read, R.J., Richardson, D.C., Richardson, J.S., Terwilliger, T.C., H., Z.P., 2010. PHENIX: a comprehensive Python-based system for macromolecular structure solution. Acta Cryst. D66, 213-221.

Andersen, G.R., Valente, L., Pedersen, L., Kinzy, T.G., Nyborg, J., 2001. Crystal structures of nucleotide exchange intermediates in the eEF1A- eEF1Balpha complex. Nat. Struct. Biol. 8, 531-534.

Ausubel, F.M., Brent, R., Kingston, R.E., Moore, D.D., Seidman, J.G., Smith, J.A., Struhl, K., 2005. Current Protocols in Molecular Biology John Wiley &Sons Hoboken, NJ.

Berchtold, H., Reshtnikova, L., Reiser, C.O.A., Schirmer, N.K., Sprinzl, M., Hilgenfeld, R., 1993. Crystal structure of active elongation factor Tu reveals major domain rearrangements. Nature 365, 126-132.

Bieganowski, P., Shilinski, K., Tsichlis, P.N., Brenner, C., 2004. Cdc123 and checkpoint forkhead associated with RING proteins control the cell cycle by controlling eIF2gamma abundance. J Biol Chem 279, 44656-44666.

Borck, G., Shin, B.S., Stiller, B., Mimouni-Bloch, A., Thiele, H., Kim, J.R., Thakur, M., Skinner, C., Aschenbach, L., Smirin-Yosef, P., Har-Zahav, A., Nürnberg, G., Altmüller, J., Frommolt, P., Hofmann, K., Konen, O., Nürnberg, P., Munnich, A., Schwartz, C.E., Gothelf, D., Colleaux, L., Dever, T.E., Kubisch, C., Basel-Vanagaite, L., 2012. eIF2γ mutation that disrupts eIF2 complex integrity links intellectual disability to impaired translation initiation. Mol Cell 48, 641-646.

Brito Querido, J., Sokabe, M., Kraatz, S., Gordiyenko, Y., Skehel, J.M., Fraser, C.S., Ramakrishnan, V., 2020. Structure of a human 48S translational initiation complex. Science 369, 1220-1227.

Chen, T., Xu, G., Mou, R., Greene, G.H., Liu, L., Motley, J., Dong, X., 2023. Global translational induction during NLR-mediated immunity in plants is dynamically regulated by CDC123, an ATP-sensitive protein. Cell Host Microbe 31, 334-342.e335.

Cimmperman, P., Baranauskiene, L., Jachimoviciūte, S., Jachno, J., Torresan, J., Michailoviene, V., Matuliene, J., Sereikaite, J., Bumelis, V., Matulis, D., 2008. A quantitative model of thermal stabilization and destabilization of proteins by ligands. Biophys J 95, 3222-3231.

Crepin, T., Shalak, V.F., Yaremchuk, A.D., Vlasenko, D.O., McCarthy, A., Negrutskii, B.S., Tukalo, M.A., El'skaya, A.V., 2014. Mammalian translation elongation factor eEF1A2: X-ray structure and new features of GDP/GTP exchange mechanism in higher eukaryotes. Nucleic Acids Research 42, 12939-12948.

Dubiez, E., Aleksandrov, A., Lazennec-Schurdevin, C., Mechulam, Y., Schmitt, E., 2015. Identification of a second GTP-bound magnesium ion in archaeal initiation factor 2. Nucleic Acids Res 43, 2946-2957.

Emsley, P., Lohkamp, B., Scott, W.G., Cowtan, K., 2010. Features and development of Coot. Acta Crystallogr. D66, 486-501.

Evans, P.R., Murshudov, G.N., 2013. How good are my data and what is the resolution? Acta Crystallographica Section D 69, 1204-1214.

Fawaz, M.V., Topper, M.E., Firestine, S.M., 2011. The ATP-grasp enzymes. Bioorg Chem 39, 185-191.

Gregory, L.C., Ferreira, C.B., Young-Baird, S.K., Williams, H.J., Harakalova, M., van Haaften, G., Rahman, S.A., Gaston-Massuet, C., Kelberman, D., Gosgene, Qasim, W., Camper, S.A., Dever, T.E., Shah, P., Robinson, I., Dattani, M.T., 2019. Impaired EIF2S3 function associated with a novel phenotype of X-linked hypopituitarism with glucose dysregulation. EBioMedicine 42, 470-480.

Hinnebusch, A.G., 2014. The scanning mechanism of eukaryotic translation initiation. Annu Rev Biochem 83, 779-812.

Ho, Y., Gruhler, A., Heilbut, A., Bader, G.D., Moore, L., Adams, S.L., Millar, A., Taylor, P., Bennett, K., Boutilier, K., Yang, L., Wolting, C., Donaldson, I., Schandorff, S., Shewnarane, J., Vo, M., Taggart, J., Goudreault, M., Muskat, B., Alfarano, C., Dewar, D., Lin, Z., Michalickova, K., Willems, A.R., Sassi, H., Nielsen, P.A., Rasmussen, K.J., Andersen, J.R., Johansen, L.E., Hansen, L.H., Jespersen, H., Podtelejnikov, A., Nielsen, E., Crawford, J., Poulsen, V., Sorensen, B.D., Matthiesen, J., Hendrickson, R.C., Gleeson, F., Pawson, T., Moran, M.F., Durocher, D., Mann, M., Hogue, C.W., Figeys, D., Tyers, M., 2002. Systematic identification of protein complexes in Saccharomyces cerevisiae by mass spectrometry. Nature 415, 180-183.

Kabsch, W., 2010. XDS. Acta crystallographica. Section D, Biological crystallography 66, 125-132.

Kachroo, A.H., Laurent, J.M., Yellman, C.M., Meyer, A.G., Wilke, C.O., Marcotte, E.M., 2015. Evolution. Systematic humanization of yeast genes reveals conserved functions and genetic modularity. Science 348, 921-925.

Kazan, R., Bourgeois, G., Lazennec-Schurdevin, C., Coureux, P.D., Mechulam, Y., Schmitt, E., 2023. Structural insights into the evolution of late steps of translation initiation in the three domains of life. Biochimie.

Kjeldgaard, M., Nyborg, J., 1992. Refined structure of elongation factor EF-Tu from Escherichia coli. J. Mol. Biol. 223, 721-742.

Kotzaeridou, U., Young-Baird, S.K., Suckow, V., Thornburg, A.G., Wagner, M., Harting, I., Christ, S., Strom, T., Dever, T.E., Kalscheuer, V.M., 2020. Novel pathogenic EIF2S3 missense variants causing clinically variable MEHMO syndrome with impaired eIF2γ translational function, and literature review. Clin Genet 98, 507-514.

Krishnamoorthy, T., Pavitt, G.D., Zhang, F., Dever, T.E., Hinnebusch, A.G., 2001. Tight binding of the phosphorylated alpha subunit of initiation factor 2 (eIF2alpha) to the regulatory subunits of guanine nucleotide exchange factor eIF2B is required for inhibition of translation initiation. Mol Cell Biol 21, 5018-5030.

Llacer, J.L., Hussain, T., Marler, L., Aitken, C.E., Thakur, A., Lorsch, J.R., Hinnebusch, A.G., Ramakrishnan, V., 2015. Conformational Differences between Open and Closed States of the Eukaryotic Translation Initiation Complex. Mol Cell 59, 399-412.

Matulis, D., Kranz, J.K., Salemme, F.R., Todd, M.J., 2005. Thermodynamic stability of carbonic anhydrase: measurements of binding affinity and stoichiometry using ThermoFluor. Biochemistry 44, 5258-5266.

McCoy, A.J., Grosse-Kunstleve, R.W., Adams, P.D., Winn, M.D., Storoni, L.C., Read, R.J., 2007. Phaser crystallographic software. Journal of Applied Crystallography 40, 658-674.

Moortgat, S., Desir, J., Benoit, V., Boulanger, S., Pendeville, H., Nassogne, M.C., Lederer, D., Maystadt, I., 2016. Two novel EIF2S3 mutations associated with syndromic intellectual disability with severe microcephaly, growth retardation, and epilepsy. Am J Med Genet A 170, 2927-2933.

Pantoliano, M.W., Petrella, E.C., Kwasnoski, J.D., Lobanov, V.S., Myslik, J., Graf, E., Carver, T., Asel, E., Springer, B.A., Lane, P., Salemme, F.R., 2001. High-density miniaturized thermal shift assays as a general strategy for drug discovery. J Biomol Screen 6, 429-440.

Panvert, M., Dubiez, E., Arnold, L., Perez, J., Mechulam, Y., Seufert, W., Schmitt, E., 2015. Cdc123, a Cell Cycle Regulator Needed for eIF2 Assembly, Is an ATP-Grasp Protein with Unique Features. Structure 23, 1596-1608.

Pavitt, G.D., 2018. Regulation of translation initiation factor eIF2B at the hub of the integrated stress response. WIREs RNA 9, e1491.

Perzlmaier, A.F., Richter, F., Seufert, W., 2013. Translation initiation requires cell division cycle 123 (Cdc123) to facilitate biogenesis of the eukaryotic initiation factor 2 (eIF2). J Biol Chem 288, 21537-21546.

Pettersen, E.F., Goddard, T.D., Huang, C.C., Meng, E.C., Couch, G.S., Croll, T.I., Morris, J.H., Ferrin, T.E., 2021. UCSF ChimeraX: Structure visualization for researchers, educators, and developers. Protein Sci 30, 70-82.

Pinz, S., Doskocil, E., Seufert, W., 2022. Thermofluor-Based Analysis of Protein Integrity and Ligand Interactions. Methods Mol Biol 2533, 247-257.

Redhead, M., Satchell, R., Morkūnaitė, V., Swift, D., Petrauskas, V., Golding, E., Onions, S., Matulis, D., Unitt, J., 2015. A combinatorial biophysical approach; FTSA and SPR for identifying small molecule ligands and PAINs. Anal Biochem 479, 63-73.

Schmitt, E., Blanquet, S., Mechulam, Y., 2002. The large subunit of initiation factor aIF2 is a close structural homologue of elongation factors. EMBO J. 21, 1821-1832.

Schmitt, E., Naveau, M., Mechulam, Y., 2010. Eukaryotic and archaeal translation initiation factor 2: a heterotrimeric tRNA carrier. FEBS Lett. 584, 405-412.

Schmitt, E., Coureux, P.-D., Kazan, R., Bourgeois, G., Lazennec-Schurdevin, C., Mechulam, Y., 2020. Recent advances in archaeal translation initiation. Frontiers in Microbiology.

Schmitt, E., Panvert, M., Lazennec-Schurdevin, C., Coureux, P.D., Perez, J., Thompson, A., Mechulam, Y., 2012. Structure of the ternary initiation complex aIF2-GDPNP-methionylated initiator tRNA. Nat. Struct. Mol. Biol. 19, 450-454.

Skopkova, M., Hennig, F., Shin, B.S., Turner, C.E., Stanikova, D., Brennerova, K., Stanik, J., Fischer, U., Henden, L., Muller, U., Steinberger, D., Leshinsky-Silver, E., Bottani, A., Kurdiova, T., Ukropec, J., Nyitrayova, O., Kolnikova, M., Klimes, I., Borck, G., Bahlo, M., Haas, S.A., Kim, J.R., Lotspeich-Cole, L.E., Gasperikova, D., Dever, T.E., Kalscheuer, V.M., 2017. EIF2S3 Mutations Associated with Severe X-Linked Intellectual Disability Syndrome MEHMO. Hum Mutat.

Studier, F.W., 2005. Protein production by auto-induction in high density shaking cultures. Protein Expr Purif 41, 207-234.

Tickle, I.J., Flensburg, C., Keller, P., Paciorek, W., Sharff, A., Vonrhein, C., Bricogne, G., 2016. STARANISO (http://staraniso.globalphasing.org/cgi-bin/staraniso.cgi). Cambridge, United Kingdom: Global Phasing Ltd. .

Vanselow, S., Neumann-Arnold, L., Wojciech-Moock, F., Seufert, W., 2022. Stepwise assembly of the eukaryotic translation initiation factor 2 complex. J Biol Chem 298, 101583.

Vonrhein, C., Tickle, I.J., Flensburg, C., Keller, P., Paciorek, W., Sharff, A., Bricogne, G., 2018. Advances in automated data analysis and processing within autoPROC, combined with improved characterisation, mitigation and visualisation of the anisotropy of diffraction limits using STARANISO. Acta Crystallographica Section A 74, a360.

Wallace, A.C., R.A., L., J.M., T., 1996. LIGPLOT: a program to generate schematic diagrams of protein-ligand interactions. . Protein Eng. 8, 127-134.

Wang, T., Birsoy, K., Hughes, N.W., Krupczak, K.M., Post, Y., Wei, J.J., Lander, E.S., Sabatini, D.M., 2015. Identification and characterization of essential genes in the human genome. Science 350, 1096-1101.

Wek, R.C., 2018. Role of eIF2α Kinases in Translational Control and Adaptation to Cellular Stress. Cold Spring Harb Perspect Biol 10.

Winn, M.D., Ballard, C.C., Cowtan, K.D., Dodson, E.J., Emsley, P., Evans, P.R., Keegan, R.M., Krissinel, E.B., Leslie, A.G., McCoy, A., McNicholas, S.J., Murshudov, G.N., Pannu, N.S., Potterton, E.A., Powell, H.R., Read, R.J., Vagin, A., Wilson, K.S., 2011. Overview of the CCP4 suite and current developments. Acta Crystallogr D Biol Crystallogr 67, 235-242.

Young-Baird, S.K., Shin, B.S., Dever, T.E., 2019. MEHMO syndrome mutation EIF2S3-I259M impairs initiator Met-tRNAiMet binding to eukaryotic translation initiation factor eIF2. Nucleic Acids Res 47, 855-867.

Young-Baird, S.K., Lourenço, M.B., Elder, M.K., Klann, E., Liebau, S., Dever, T.E., 2020. Suppression of MEHMO Syndrome Mutation in eIF2 by Small Molecule ISRIB. Mol Cell 77, 875-886.e877.

Zubrienė, A., Matulienė, J., Baranauskienė, L., Jachno, J., Torresan, J., Michailovienė, V., Cimmperman, P., Matulis, D., 2009. Measurement of nanomolar dissociation constants by titration calorimetry and thermal shift assay - radicicol binding to Hsp90 and ethoxzolamide binding to CAII. Int J Mol Sci 10, 2662-2680.

SUPPLEMENTARY DATA

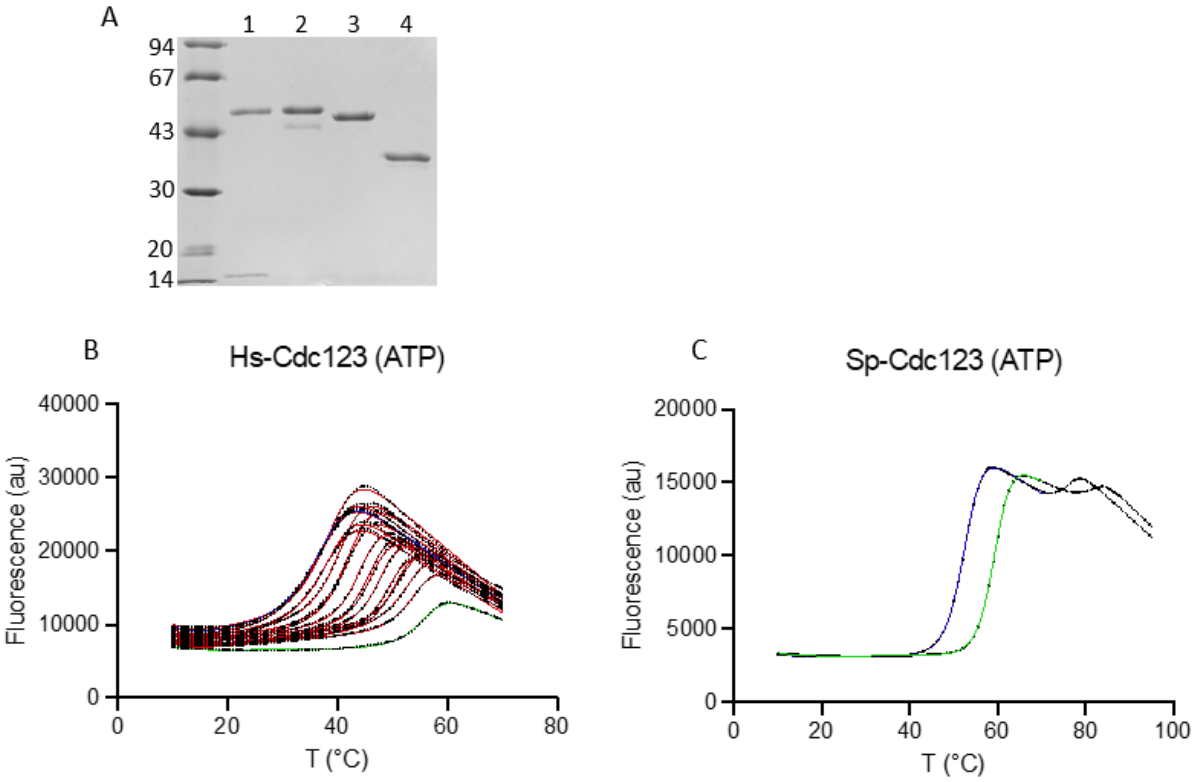

Supplementary Figure 1: Determination of Tm values.

(A) SDS-PAGE analysis of the various proteins used in this study. 1. Hs-Cdc123:Hs-γD3, 2. Hs-Cdc123, 3. Sc-Cdc123, 4. Sp-Cdc123.

(B) Raw fluorescence curves obtained in a typical Thermofluor experiment as a function of temperature (black dots). The curves fitted using equation 1, from which the Tm values were derived, are shown with red lines (or a blue line for 0 ATP-Mg^{2+} and a green line for 12.8 mM ATP-Mg^{2+}). The experiment shown corresponds to Hs-Cdc123 in the presence of increasing concentrations (0 to 12.8 mM) of ATP-Mg^{2+}.

(C) Two experiments at 0 ATP-Mg^{2+} (raw data fitted with a blue curve) and 12.8 mM ATP-Mg^{2+} (fitted with a green curve) for Sp-Cdc123. In this case, two successive denaturation peaks were observed but only the main denaturation was fitted. For this purpose, fluorescence data between 10°C and 70°C were fitted.

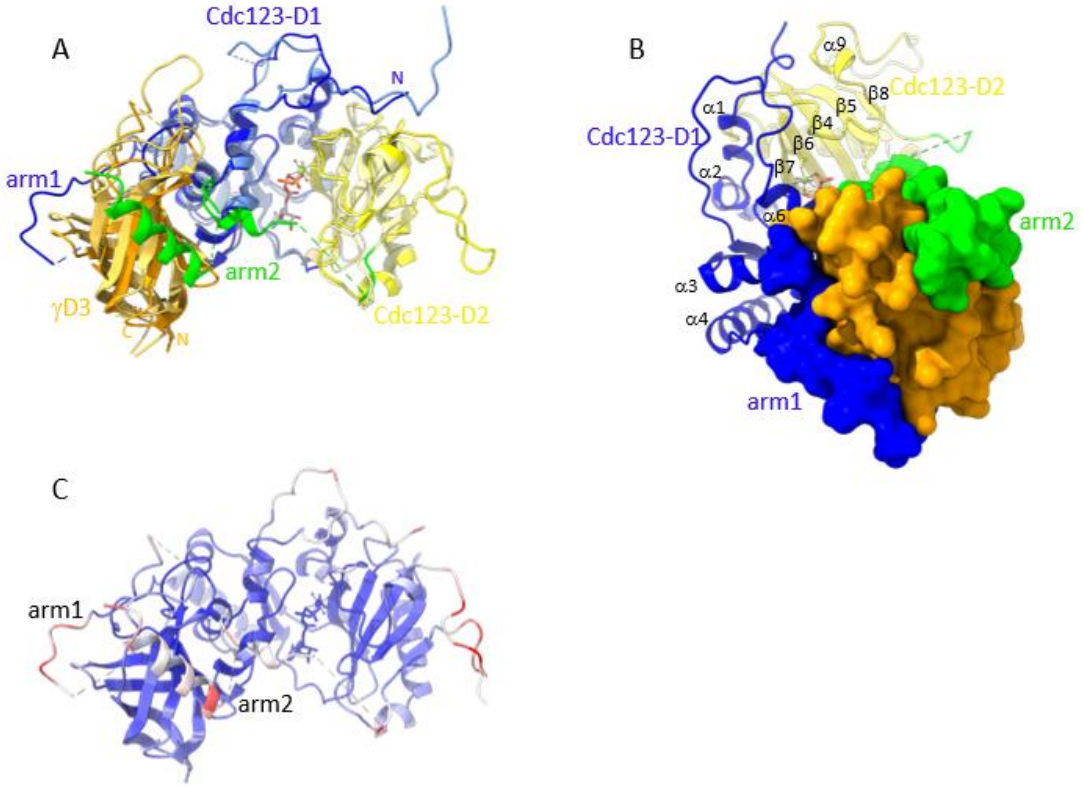

Supplementary Figure 2: Hs-Cdc123:Hs-gD3:ATP-Mg^{2+} ....

(A) Comparison of Hs-Cdc123:Hs-γD3:ATP-Mg^{2+} with Sp-Cdc123:Sc-γD3:ATP-Mg^{2+}. The color code is the same as in Figure 2 for the human Cdc123-γD3 complex. The yeast complex is in light colors. The two Cdc123 molecules were superimposed (rmsd value of 0.936 Å for 192 Cα atom). A small difference between the human and the yeast complex is observed in the positioning of the γD3 domain with respect to Cdc123-D1 (3.06 Å translation and 9.6° rotation as calculated with Pymol script https://raw.githubusercontent.com/speleo3/pymol-psico/master/psico/orientation.py).

(B) Surface representation of Cdc13 arms 1 and bound to γD3.

(C) Cartoon representation of Hs-Cdc123:γD3:ATP-Mg^{2+} colored according to the B factor values. B factors range from 16.7 Å^2 (blue) to 150 Å^2 (red). This view highlights the flexibilities of arms 1 and 2 as well as of the long loops.

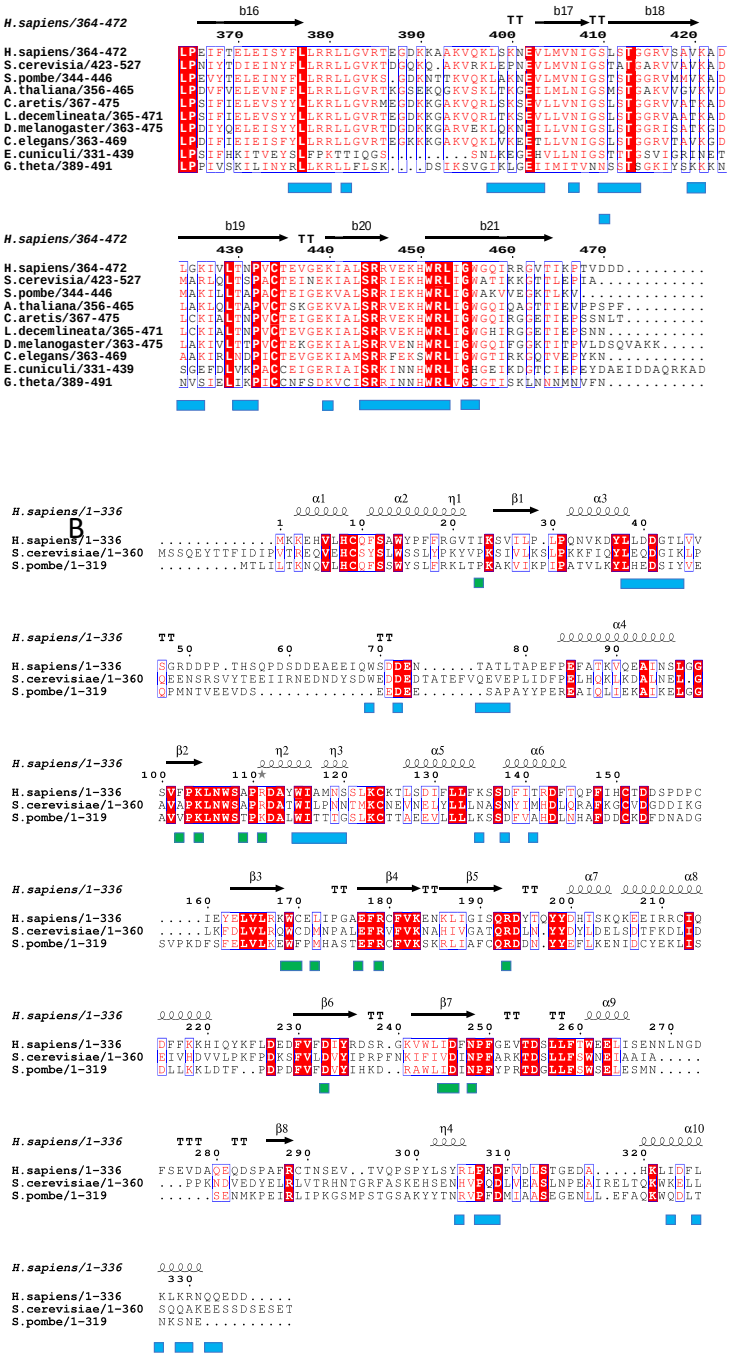

Supplementary Figure 3: Alignment of Cdc123 and gD3 sequences.

(A) Alignment of eIF2gD3 sequences.

When the percentage of identity is higher that 70%, residues are colored in red and framed in blue. In case of strict identity, residues are in white on a red background. Residues involved in the binding of Hs-gD3 domain to Hs-Cdc123 are indicated with blue bars. Secondary structures of Hs-gD3 are indicated at the top of the alignment. The figure is modified from {Panvert, 2015 #3754}.

(B) Alignment of Cdc123 sequence from human, *S. cerevisiae* and *S. pombe*. Sequences were aligned using ClustalW {Larkin, 2007 #3671} The figure was drawn with Espript {Gouet, 1999 #1495} and edited manually. Residues involved in ATP binding to Hs-Cdc123 are indicated with green bars and those in the binding to Hs-gD3 are indicated with blue bars.

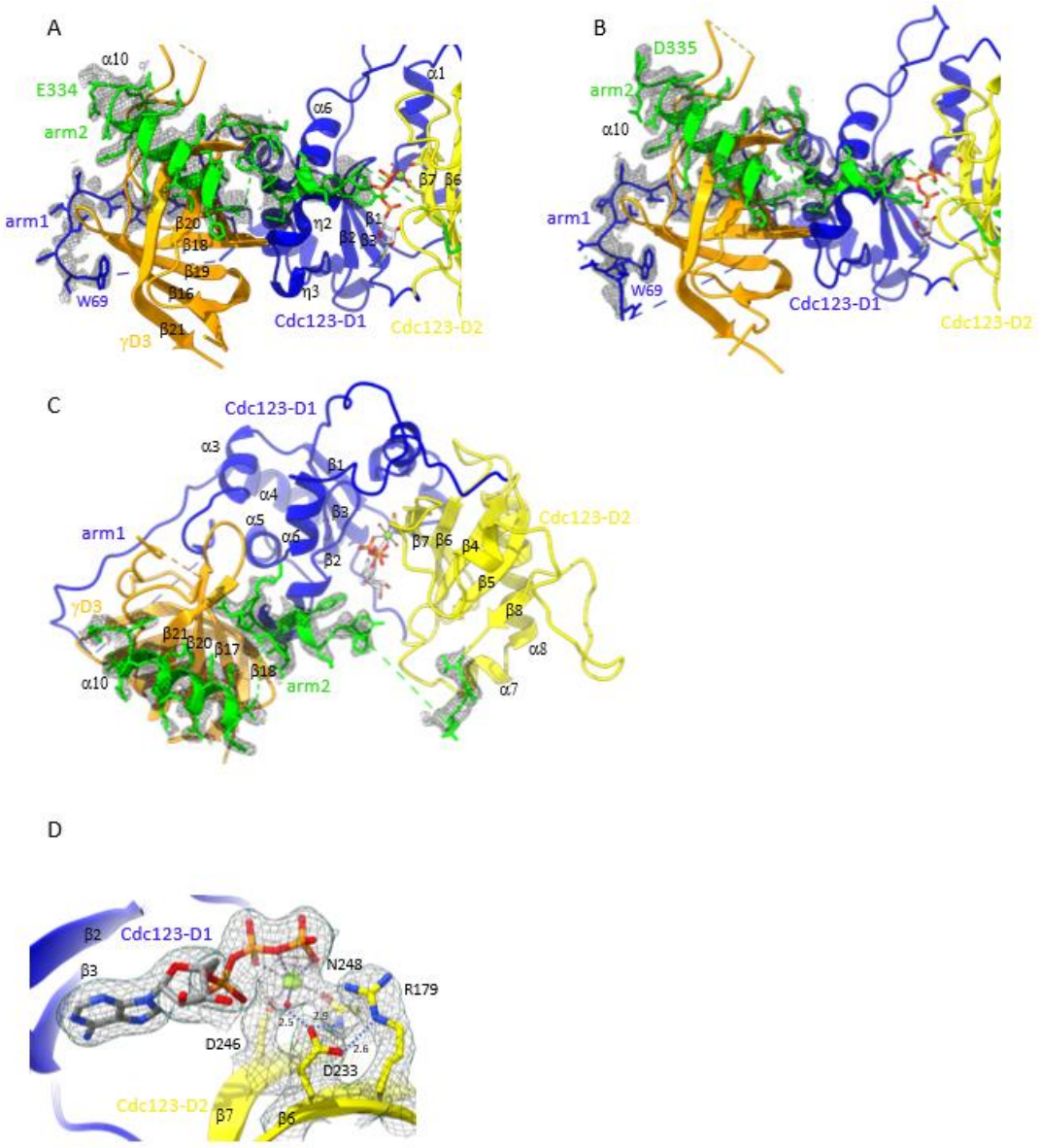

Supplementary Figure 4: views of electron density.

(A)- view of the final '2mFo-DFc' map of the Hs-Cdc123:ATP-Mg^{2+}:Hs-γD3 complex (map A) at arm 1 (loop 69-80, blue) and arm 2 (green) of Hs-Cdc123.

(B)- view of the final '2mFo-DFc' map of the Hs-Cdc123:Hs-γD3 Se-met complex (map B) at arm 1 (loop 69-80, blue) and arm 2 (green) . The quality of map B at arm 1 is better than that of map A. Therefore arm 1 was first built into map B and used as a template for model building in map A.

(C)- global view of map A around arm 2.

(D)- view of map A around the ATP-Mg^{2+} molecule and residues D233, D246, N248 and R179.

Data collection	Hs-Cdc123:γD3 Se-Met-Peak	Hs-Cdc123:γD3 Se-Met-Remote	Hs-Cdc123:γD3:ATP-Mg^{2+}
Molecule in a. u		2	2
Crystallization conditions	20%PEG3350, 8% tacsimate pH8.0	20%PEG3350, 8% tacsimate pH8.0	20%PEG3350, 0.2M lithium citrate
Space group	$P2_1$	$P2_1$	$P2_1$
Cell dimensions			
a, b, c (Å)	60.3, 125.3 74.1	60.26, 125.34, 74.08	60.5, 126.0, 74.6
α, β, γ (°)	90 90.062 90	90 90.062 90	90 90.055 90
Resolution (Å)	60.26-2.25	60.26-1.974	64.22-2.08
R_{meas}	9.4 (142.1)	7.8 (109.8)[a]	15.1 (112.8)
I/σ(I)	8.4 (0.55)	13.7 (1.5)	9.1 (1.7)
Completeness (%)	98.9 (95.8)	94.1 (63.7)*	93.0 (65.6)*
Redundancy	3.3 (2.5)	7.0 (6.9)	6.9 (6.7)
$CC_{1/2}$[b]	0.538 (0.270)	0.997 (0.648)	0.995 (0.599)
Unique reflections	101522 (15913)	58305 (2915)	39743 (1988)
SigAno	0.949 (0.625)		
Ano. Correlation (%	22 (5)		
Refinement			
R_{work}/R_{free}[c]		0.1892/0.2216	0.1762/0.2035
Twining fraction[d]		0.1	0.24
No atoms		6817	6874
Protein		801	795
Waters		195	282
Heterogen atoms			
B-factors (Å^2) prote		Chain A 50.6 Chain B 44.4 Chain C 51.1 Chain D 46.7	Chain A 45.5 Chain B 49.2 Chain C 47.6 Chain D 44.0
Nucleotide/Mg^{2+}		Chain A ATP 68.0 occ 1 Chain C ATP 47.9 occ 0.61	Chain A ATP 25.1 Mg^{2+} 25.2 occ 1 Chain C ATP 24.2 Mg^{2+} 21.8 occ 1
Waters		42.8	39.2
Bond lengths (Å)		0.02	
Bond angles (°)		0.54	

Supplementary Table 1: Crystallographic structures, data collection and refinement statistics
A single crystal was used for data collection.
[a] Values in parentheses are for highest-resolution shell.
[b] $CC_{1/2}$ is the correlation coefficient between two random half data sets (1).
[c] R_{free} is calculated with 5% of the reflections.
[d] Structure refinement in Phenix was performed with the twining law is h,-k,-l.

*ellipsoidal completenesses calculated after STARANISO processing are given.
Resolution limits & eigenvectors of ellipsoid fitted to resolution cut-off surface for Hs-Cdc123:γD3:ATP-Mg^{2+} dataset:
2.063 0.9669 0.0000 0.2550 0.951 _a_* + 0.309 _c_*
2.519 0.0000 1.0000 0.0000 _b_*
2.732 -0.2550 0.0000 0.9669 -0.209 _a_* + 0.978 _c_*

Anisotropy ratio: 0.528 [= (Emax - Emin) / Beq]
Fractional anisotropy: 0.279 [= sqrt(1.5 Sum_i (E_i - Beq)^2 / Sum_i E_i^2)]
Anisotropic S/N ratio: 8.61 [= max_h | exp(4 pi^2 s~_h delta(B) s_h) - 1 | <I_h/sd(I_h)>]

Resolution limits & eigenvectors of ellipsoid fitted to resolution cut-off surface for Hs-Cdc123:γD3 dataset:
1.939 0.9765 0.0000 -0.2154 0.965 _a_* - 0.263 _c_*
2.217 0.0000 1.0000 0.0000 _b_*
2.232 0.2154 0.0000 0.9765 0.177 _a_* + 0.984 _c_*

Anisotropy ratio: 0.333 [= (Emax - Emin) / Beq]
Fractional anisotropy: 0.185 [= sqrt(1.5 Sum_i (E_i - Beq)^2 / Sum_i E_i^2)]
Anisotropic S/N ratio: 10.55 [= max_h | exp(4 pi^2 s~_h delta(B) s_h) - 1 | <I_h/sd(I_h)>]

Name	Relevant Genotype
W15001	MATa/MATalpha CDC123/cdc123-delta::kanMX4 leu2-3,112/leu2::pTEF2-myc3-humanCDC123-tCYC1-LEU2
W15002	MATa/MATalpha CDC123/cdc123-delta::kanMX4 leu2-3,112/leu2::pTEF2-myc3-humanCDC123(D233A)-tCYC1-LEU2
W15003	MATa/MATalpha CDC123/cdc123-delta::kanMX4 leu2-3,112/leu2::pTEF2-myc3-humanCDC123(D246A)-tCYC1-LEU2
W9877	MATalpha SUI2-myc13-HIS3MX6
W14968	MATalpha SUI2-myc13-HIS3MX6 leu2::pTEF2-flag3-humanCDC123-tCYC1-LEU2
W14969	MATalpha SUI2-myc13-HIS3MX6 leu2::pTEF2-flag3-humanCDC123(D233A)-tCYC1-LEU2
W14970	MATalpha SUI2-myc13-HIS3MX6 leu2::pTEF2-flag3-humanCDC123(D246A)-tCYC1-LEU2
W14974	MATalpha SUI2-myc13-HIS3MX6 ura3::pTEF2-flag3-CDC123-tCYC1-URA3
W276	MATalpha his3-11,15, trp1-1, ura3::URA3-lexA-op-lacZ
W15327	MATalpha his3-11,15, trp1-1, ura3::URA3-lexA-op-lacZ, leu2::pTEF2-flag3-humanCDC123-tCYC1-LEU2
W15328	MATalpha his3-11,15, trp1-1, ura3::URA3-lexA-op-lacZ, leu2::pTEF2-flag3-humanCDC123(D233A)-tCYC1-LEU2
W15329	MATalpha his3-11,15, trp1-1, ura3::URA3-lexA-op-lacZ, leu2::pTEF2-flag3-humanCDC123(D246A)-tCYC1-LEU2

Supplementary Table 2: Yeast strains used in this study.

Hs-Cdc123	γD3	Type
Loop 38-83		
L39 O	K449 NZ	H-bond
D40	D449	Hydrophobic
D41 O D41 OD1	E448 N K449 NZ	H-bond
D41	K449,E448,K449,E448	Hydrophobic
G42	R446	Hydrophobic
T43	E402,R445,E402,R445,R446	Hydrophobic
T43 SC OG1	E402 SC OE1	H-bond
L44 O	V403 N	H-bond
L44	N401,V403,E402,	Hydrophobic
W69	G425,L424,K421,K426,E372,K421,K426	Hydrophobic
D72	V420,K421	Hydrophobic
T75 OG	L398 O	H-bond
T75	V420,S399,L398,V420,L398	Hydrophobic
A76	K400,S399	Hydrophobic
A76 0	K400 N	H-bond
T77	K400,N401	Hydrophobic
L78 N	K400 O	H-bond
L78 O	N401 ND2	H-bond
L78	S399,K400,N401	Hydrophobic
η2-η3		
W115	W451,M405,T413	Hydrophobic
I116	G414,T430	Hydrophobic
I116 O	T430 OG1	H-bond
A117	N431	Hydrophobic
M118	T430,P432	Hydrophobic
N119	N431	Hydrophobic
N119 N	N431 OD1	H-bond
S120 OG	N431 ND2	H-bond
α6		
K135	R446	Hydrophobic
D138 OD1 OD2	H450 ND1 R446 NH2	H-bond H-bond
D138	R446	Hydrophobic
T141	K449	Hydrophobic
Region 300		
R305 O	N407 ND1	H-bond
R305 O NH1	S412 OG S412 OG	H-bond
R305	S410,L411,S412,M405	Hydrophobic
P307	W451 O	H-bond
P307	M405,S444,W451	Hydrophobic
K308 N	W451 O	H-bond
K308	H450,W451	Hydrophobic
D309 OD1 OD2 OD2	R452 NH1 NE L453 N	H-bond
D309	L453,R452	Hydrophobic
α10		
I323	I441,K440,W456	Hydrophobic
L326	G455,W456	Hydrophobic
K327	K440,W456	Hydrophobic
K329	L382	Hydrophobic
R330 NH1	L377 O	H-bond
R330	W456,L377,L378	Hydrophobic
Q333 OE1 OE1 NE2	R379 N R380 N R380 O	H-bond
E334 OE2	R379 NE	H-bond
E334	R379	Hydrophobic
Q333	R379, L378,R380	Hydrophobic

Supplementary Table 3: Interactions between Hs-Cdc123 and the Hs-γD3 domain.

The bonded and non -bonded interactions as identified by Ligplot are listed {Wallace, 1996 #3837}

Discussion and Perspectives

1. On heIF2α expression:

The first milestone of this thesis work is the production of human eIF2α using an *E. coli* expression system. Thanks to previous work by Ito et al., 2004, and our own improvements, we are now able to produce two versions of heIF2α (heIF2α-188/303) in great quantities.

Moreover, we are now able to produce acetylated heIF2α in great amounts using the orthogonal system developed by the Chin lab. The use of full-length acetylated substrates to test SIRT1 catalytic activity is not common. During the course of this thesis we had two examples of the use of a full-length substrate: p53, partially acetylated by enzymatic means (Pacholec *et al.*, 2010), and acetylated histones H3 and H4, purified from HeLa cells (Vaquero *et al*., 2004). In comparison, the production of an evenly acetylated substrate using orthogonal systems provides us with accurate data when studying the deacetylation reaction.

2. On the catalytic characterization of miniSIRT1

MiniSIRT1 has proven to be a good substitute for WT SIRT1. Using mimic substrate peptides, we can compare the differences in K_M and k_{cat} between SIRT1 and miniSIRT1, finding very little difference between the two proteins. In fact, despite our efforts, SIRT1 was not as pure as miniSIRT1. An improvement in protein expression is expected using an optimized gene coding for SIRT1 expression in *E. coli*.

Characterizing miniSIRT1 catalytic parameters using different peptides gave us some insights into the importance of each individual acetylated lysine. We found that acetylated lysine 143 showed a lower K_M than 141, suggesting that, in the case of peptide substrates, it is the preferred substrate out of the two acetylated lysines. Interestingly, substitution of K141 for an A resulted in a slight increase in the K_M, indicating that K141 does have a role in the binding affinity of the peptide. Another important remark concerns the peptide length. A shorter peptide length is paired with higher K_M. It is 5 times higher in the case of DG-7 (143) as compared toTG-15 (143), and 4 times higher for FR-7 (141) as compared to TG-15 (141). This observation suggests that the increase in K_M could be attributed to the absence of interacting residues in shorter peptides. In addition, a slight

increase in k_{cat} is observed for both TG-15 (141) and TG-15 (143), approximately 1.4-fold and 1.6-fold, as compared to the respective shorter peptides.

Moreover, we observed a substrate inhibition phenomenon when using high concentrations of the TG-15 (143) and TG-15 (141A, 143AcK) peptides but not with the shorter ones, nor TG-15 (141). These results suggest that a second nonproductive binding site exists for longer peptides. This effect may not be visible in the tested conditions for peptides other than TG-15 (143), due to their high K_M.

These results agree with the K_D values. The K_D of acetylated 143 was lower than that of 141, which could not be measured. When using an acetylated peptide where K141 was substituted by A, no changes in the K_D were observed, suggesting that acetylation in K143 is enough to bind miniSIRT1. Also, in agreement with the K_M, shorter peptides exhibit a higher K_D.

The rate values obtained for model peptides and miniSIRT1 and SIRT1 are consistent with other SIRT1 studies (Smith, Hallows and Denu, 2009); (Cao *et al.*, 2015) ; (Dai *et al.*, 2015) ; Huynh *et al.*, 2022). In our experiments we decided to use unmodified peptides, that is without any added fluorophore or aromatic amino acid (outside of its native sequence) that could modify its innate binding affinity. Therefore, our results are robust, as what we observe is only due to the peptides' ability to be substrates of miniSIRT1/SIRT1.

One of the challenges of this thesis was to prove the *in vitro* activity of SIRT1 for a native acetylated heIF2α substrate.

In our first attempts, we could not measure a catalytic rate with miniSIRT1 and heIF2α using the coupled enzymatic test. Therefore, we used an alternative Western blotting method. Western-blotting analysis of miniSIRT1 deacetylation on heIF2α-143AcK-188 suggested that the estimated K_M is around 1 μM, lower than that obtained for the peptide, but the reaction was indeed very slow ($3.6\ 10^{-4}\ s^{-1}$). Moreover, work by Vaquero et al., showed similar rates ($5.4\ 10^{-4}\ s^{-1}$), when using SIRT1 and full-length acetylated histones (Vaquero *et al.*, 2004). Another study with SIRT6 (Chio *et al.*, 2023) characterized its catalytic rates using Western-blotting and a full length acetylated substrate (Histone H3), again obtaining similar rates.

Once we were able to measure the rate using Western blotting, we attempted to measure it again using the coupled enzymatic assay, however, considering the low rate

value and the substrate concentration, the signal was too low to deduce kinetic information.

The low K_M value for heIF2α-143AcK-188 is rather consistent with what was observed with the peptides, where a longer substrate has a lower K_M for the enzyme, with a lower catalytic rate. This could be due to necessary unfolding phenomena, by which the acetylated lysine becomes available to the enzyme. Using Western blotting, we do not see any difference in the deacetylation rate between heIF2α-143AcK-188 and heIF2α-141AcK-188. Therefore, it becomes evident that specificity studies conducted using short peptides cannot be directly extrapolated to *in cellulo* substrates. This finding strongly emphasizes the necessity to focus on developing kinetic and specificity studies that are centered around the interaction of SIRT1 with more native substrates.

Interestingly, in the case of SIRT6 researchers performed a microarray analysis with more than 6000 peptide substrates, finding that SIRT6 had a preference for uncharged residues around the acetyl-group. However, none of the three histone targets of SIRT6 satisfied this *in vitro* findings (Rauh *et al.*, 2013).

Using deacetylation mimics in cardiomyocytes subject to ER stress, our collaborator observed a slightly higher protective effect in the case of K143R as compared to K141R.

Concerning the study of the interplay between phosphorylation and acetylation, we did not observe any differences with the S52D mutants, suggesting that this substitution, and potentially phosphorylation, does not modify miniSIRT1 capacity to deacetylate heIF2α-143AcK-188. By comparing heIF2α-143AcK-188 and heIF2α-143AcK-303 we did not observe any differences due to the presence of the D3 domain.

We still don't know the cellular context the deacetylation takes place, but it could be that heterotrimeric eIF2 is necessary to ensure a correct deacetylation. To this date, it is not possible to produce human eIF2 *in vitro*. However, during this thesis we were able to produce heIF2α-303, a quasi-native version of the protein, capable of binding yeast eIF2γ. The formation of the heterotrimer eIF2 is facilitated by Cdc123 in eukaryotes. Studies will continue to try to express human eIF2 and measure the deacetylation of SIRT1 in the context of the heterotrimer. Characterization of human Cdc123 (see article included in this manuscript) will be useful in this endeavor.

Early studies showed that SIRT1 interacts with both GADD34 and heIF2α (Ghosh, Reizis and Robbins, 2011). The low catalytic rate of the reaction observed *in vitro* may be due to it taking place within a larger a macromolecular complex *in vivo*, paired with heIF2α dephosphorylation. In the future, it may be worth studying the assembly of a GADD34: PP1α: heIF2α: SIRT1 complex and the deacetylation reaction in this context (Lee *et al.*, 2018). Moreover, the context in which this deacetylation takes place is not known, and both orientation and protein: protein interaction could be crucial for SIRT1 activity. This is the case for SIRT6, whose *in vitro* activity is improved when its substrate, histones, are in the context of the nucleosome (Gil *et al.*, 2013).

2.1 On the effect of STACs

STACs, especially resveratrol, were given the status of miracle molecules by David Sinclair, the scientist that led the research on sirtuin activating compounds using AMC-tagged peptides. His research even led him to found Sirtris pharmaceuticals, a company focused on finding resveratrol derived SIRT1 activators. Published studies that contradicted Sinclair's claims put in question the efficiency of STACs (Kaeberlein *et al.*, 2005); (Pacholec *et al.*, 2010) and the use of fluorescent moieties tagged to peptides and led to the closure of the company in 2013, although initial clinical trials using STACs continued (Dai *et al.*, 2019). To this date, the use of STACs remains controversial, as their direct impact on the SIRT1 deacetylation mechanism cannot be proven (Denu, 2011).

In our research we did not observe any K_M effects due to STACs on miniSIRT1 using TG-15 (143) as a substrate. In this work we did not use STACs in our Western blot analysis as the method is probably not precise enough to detect any effect on the K_M due to STACs. However, our collaborators research points out the efficiency of some STACs *in vivo*, and it might be worth studying their effectiveness *in vitro* once we find a suitable method. Moreover, if SIRT1 activity improves in the presence of other heIF2α interactants (as explained above, if we find the macromolecular context in which the deacetylation takes place), we can consider testing STACs in an environment closer to the biological one.

3. On crystallization

The structure determination of the heIF2α-K143Q-188 variant did not show conformational changes due to the presence of glutamine in position 143. The crystals belonged to the P1 space group, which renders data collection more difficult (in terms of

completeness). Efforts will continue to improve crystal quality, and more importantly, to try to crystallize acetylated heIF2α-188. In the same manner, crystallization attempts will continue with miniSIRT1 variants, bound to acetylated heIF2α.

4. On the interactome

Certain PTMs can expand or reduce the interactome of a protein. There is still not much information on the effects of acetylation on heIF2α ability to interact with known partners, or whether there are new ones due to this new PTM.

Analyzing the results obtained from our Mass-Spectrometry experiment in detail will provide us with valuable information regarding potential interactants.

Moreover, in sight of the results obtained in the Western-blot enzymatic assay, it may be worth studying the interactome using heIF2α-141AcK-303 and heIF2α-S52D-141AcK-303, focusing on finding the acetylase or acetylases that are in charge of acetylating these two residues.

5. Perspectives

Our work proves for the first time that SIRT1 (miniSIRT1) is capable of deacetylating heIF2α-188. Until this work, the deacetylation reaction had only been performed with full-length histones, partially acetylated p53 protein, and peptide substrates.

Interestingly, SIRT1 is capable of deacetylating heIF2α independently of the position of the acetyl-lysine (141 or 143). This, paired with the low velocity observed, suggests that the deacetylation reaction *in vivo* might require more elements that are not present in the *in vitro* reaction. In fact, work in SIRT6 implied that the deacetylation reaction is dependent on the biological context it takes place in, in this case the nucleosome (Gil *et al.*, 2013).

In the initial discovery of SIRT1's association with eIF2α, it was found that SIRT1 interacted with GADD34:PP1α, responsible for dephosphorylating eIF2α. Previous research conducted by Lee et al. in 2018 suggests that during ER stress, phosphorylated eIF2α is recruited to the GADD34:PP1α complex. However, acetylation on lysines 141/143 prevents its dephosphorylation. This is why SIRT1, in its inactive phosphorylated state, would be recruited to the complex. Subsequently, SIRT1 would undergo dephosphorylation by PP1α, which would activate and enable it to deacetylate

eIF2α. This would then prompt PP1α to dephosphorylate eIF2α (Lee *et al.*, 2018), figure 85. Efforts will be made in the future to obtain information of heIF2α-188 with SIRT1 bound to GADD34: PP1α. Our lab is especially well-suited to doing so using Cryo-EM.

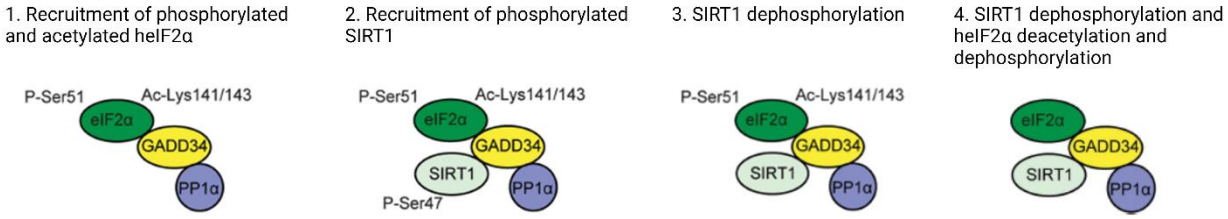

Figure 85: Deacetylation and dephosphorylation of heIF2. Proposed step by step mechanism by Lee et al., 2018.

In fact, this work did not study the effect of acetylation on dephosphorylation, but the effect of a mimic phosphorylation on deacetylation. What is observed *in cellulo* is that deacetylation is paired with increased levels of dephosphorylation. Further experiments need to be designed to study the effect of this acetylation in dephosphorylation rates by PP1. To do so, we could either use another orthogonal system that introduces a phosphoserine (Rogerson *et al.*, 2015) on position 52 of heIF2α, and introduce K141R and K143R mutations, which mimic deacetylation; or phosphorylate acetylated heIF2α-188 using one of the eIF2α specific kinases. We already performed some phosphorylation assays using PKR and acetylated heIF2α-188, proving that we could separate non-phosphorylated protein from phosphorylated. This strategy will be further developed in the future.

The role of acetylation on heIF2α-188 dephosphorylation remains to be understood, however, this work has provided significant milestones that can serve as a basis for future research in this area.

Materials

1. List of bacteria

The different bacterial strains were transformed via electroporation, using a Gene Pulser electroporator (Bio-Rad, Hercules, California). Electrocompetent bacteria are prepared in the lab as described in the protocol by Shigekawa and Dower, 1988.

Name of bacterial strain (*E.coli*)	Genotype	Source and phenotype
XL1-blue	*end*A1 *gyr*A96(nal^R) *thi*-1 *recA1 relA1 Δlac glnV44 F'[::Tn*10 *proAB$^+$ lacI^q Δ(lacZ)*M15] *hsdR17 (*r$_K^-$ m$_K^+$*)*	*HsdR* deficient bacteria, a restriction enzyme capable of recognizing non-methylated DNA
BL21 Rosetta (DE3)	F$^-$ *ompT hsdS$_B$*(r$_B^-$ m$_B^+$) *gal dcm λ*DE3 pLacI (Cam^R)	
BL21 (DE3) pG-Tf2		Bacteria expressing groES, groEL and TF chaperon proteins

Table 13: Bacterial strains

2. List of plasmids

Genes	Name	Source plasmid	Description
His Tag + SIRT1	pET15b-SIRT1-Amp^R	pECE-Flag-SIRT1	Human SIRT1
His Tag + Nter+CAT+Cter SIRT1	pET15b-miniSIRT1-Amp^R	pET15blpa (Guillon *et al.*, 2005)	Mini Human SIRT1
His Tag + Nter+CAT (H363A) + Cter SIRT1	pET15b-miniSIRT1-H363A- Amp^R	pET15blpa	Mini Human SIRT1 (H363A)
His Tag + Nter+CAT (H363L) + Cter SIRT1	pET15b-miniSIRT1-H363L- Amp^R	pET15blpa	Mini Human SIRT1 (H363L)
His Tag + CAT + Cter SIRT1	pET15b-ΔNminiSIRT1-Amp^R	pET15blpa	ΔN Human SIRT1
His Tag + EIF2S1 (STOP 188)	pET15b-heIF2α-188-Amp^R	pET15blpa	Human eIF2α domains 1 and 2
His Tag + EIF2S1 (STOP 303)	pET15b-heIF2α-303-Amp^R	pET15blpa	Human eIF2α domains 1, 2 and 3
His Tag + EIF2S1 (K141Q + STOP 188)	pET15b-heIF2α-K141Q-188- Amp^R	pET15blpa	Human eIF2α domains 1 and 2, K141Q
His Tag + EIF2S1 (K143Q + STOP 188)	pET15b-heIF2α-K143Q-188- Amp^R	pET15blpa	Human eIF2α domains 1 and 2, K143Q
His Tag + EIF2S1 (K141Q + STOP 303)	pET15b-heIF2α-K141Q-303- Amp^R	pET15blpa	Human eIF2α domains 1,2 and 3, K141Q
His Tag + EIF2S1 (K143Q + STOP 303)	pET15b-heIF2α-K143Q-303- Amp^R	pET15blpa	Human eIF2α domains 1,2 and 3, K143Q
His Tag + EIF2S1 (S52D + STOP 188)	pET15b-heIF2α-S52D-188- Amp^R	pET15blpa	Human eIF2α domains 1 and 2, S52D
His Tag + EIF2S1 (S52D + K141Q + STOP 188)	pET15b-heIF2α-S52D-K141Q -188- Amp^R	pET15blpa	Human eIF2α domains 1 and 2, S52D and K141Q
His Tag + EIF2S1 (S52D + K143Q + STOP 188)	pET15b-heIF2α-S52D-K143Q -188- Amp^R	pET15blpa	Human eIF2α domains 1 and 2, S52D and K143Q
EIF2S1 (S52D + STOP 303)	pET15b-heIF2α-S52D-303- Amp^R	pET15blpa	Human eIF2α domains 1, 2 and 3, S52D
His Tag + EIF2S1 (S52D + K141Q + STOP 303)	pET15b-heIF2α-S52D-K141Q -303- Amp^R	pET15blpa	Human eIF2α domains 1, 2 and 3, S52D and K141Q
His Tag + EIF2S1 (S52D + K143Q + STOP 303)	pET15b-heIF2α-S52D-K143Q -303- Amp^R	pET15blpa	Human eIF2α domains 1, 2 and 3, S52D and K143Q

His Tag + EIF2S1 (TAG 141 + STOP 188)	pCDF-tRNACUA-pylT-heIF2α-141AcK-188-Sm^R	pCDF-tRNACUA-pylT (Chin lab)	Human eIF2α domains 1 and 2, TAG 141 and tRNA^{CUA}
His Tag + EIF2S1 (TAG 143 + STOP 188)	pCDF-tRNACUA-pylT-heIF2α-143AcK-188-Sm^R	pCDF-tRNACUA-pylT (Chin lab)	Human eIF2α domains 1 and 2, TAG 143 and tRNA^{CUA}
His Tag + EIF2S1 (TAG 141 + STOP 303)	pCDF-tRNACUA-pylT-heIF2α-141AcK-303-Sm^R	pCDF-tRNACUA-pylT (Chin lab)	Human eIF2α domains 1, 2 and 3, TAG 141 and tRNA^{CUA}
His Tag + EIF2S1 (TAG 143 + STOP 303)	pCDF-tRNACUA-pylT-heIF2α-143AcK-303-Sm^R	pCDF-tRNACUA-pylT (Chin lab)	Human eIF2α domains 1, 2 and 3, TAG 143 and tRNA^{CUA}
His Tag + EIF2S1 (S52D + TAG 141 + STOP 188)	pCDF-tRNACUA-pylT-heIF2α-S52D-141AcK-188-Sm^R	pCDF-tRNACUA-pylT (Chin lab)	Human eIF2α domains 1 and 2, S52D, TAG 141 and tRNA^{CUA}
His Tag + EIF2S1 (S52D + TAG 143 + STOP 188)	pCDF-tRNACUA-pylT-heIF2α-S52D-143AcK-188-Sm^R	pCDF-tRNACUA-pylT (Chin lab)	Human eIF2α domains 1 and 2, S52D, TAG 143 and tRNA^{CUA}
His Tag + EIF2S1 (S52D + TAG 143 + STOP 303)	pCDF-tRNACUA-pylT-heIF2α-S52D-143AcK-303-Sm^R	pCDF-tRNACUA-pylT (Chin lab)	Human eIF2α domains 1, 2 and 3, S52D, TAG 143 and tRNA^{CUA}
	pBK-AcKRS-pylT-Kan^R	(Chin lab)	Evolved tRNA synthetase capable of aminoacylating N-ε-acetyl-lysine to tRNA^{CUA}
MBP-Ncase	pPNC2	(Escalante-Semerena lab)	MBP-Nicotinamidase
His Tag + GST + PKR	pTEM33-PKR	(This lab)	GST-PKR fusion protein
EIF2S1 (K143Q + STOP 188)	pET15b-heIF2α-K143Q-188- Amp^R	pET15blpa (This lab)	Human eIF2α domains 1 and 2, K143Q
His Tag + *gfp*	pET15b-GFP (this lab)	pET15b	GFP protein from *Aequorea victoria*, N-terminally tagged with 6x His

Table 14: Plasmids used and produced during this thesis

3. Culture media, buffers, and antibiotics

Culture media	**Composition**
Luria-Bertani (LB)	Tryptone (bacto) 10 g/L, yeast extract 5 g/L, NaCl 5 g/L
2xTY	Tryptone (bacto) 16 g/L, yeast extract 10 g/L, NaCl 5 g/L

Table 15: Culture media

Protein	Step	Name	Composition
heIF2α -303 variants and SIRT1 variants	Metal affinity chromatography	Resuspension buffer (Buffer MA)	500 mM NaCl, 10 mM HEPES, pH 7.5, 1 mM Benzamidine, 1 mM PMSF
		Elution buffer (Buffer MB)	Buffer MA + 250 mM imidazol
	Ion Exchange chromatography	Dilution buffer (Buffer D)	10 mM HEPES, pH 7.5
		Buffer QA	100 mM NaCl, 10 mM HEPES, pH 7.5
		Buffer QB	1 M NaCl, 10 mM HEPES, pH 7.5
	Size exclusion chromatography	Buffer SE	150 mM NaCl, 10 mM HEPES, pH 7.5
heIF2α-188variants*	Metal affinity chromatography	Resuspension buffer (Buffer MGA)	Buffer MA + 2% glycerol
		Elution buffer (Buffer MGB)	Buffer MB A + 2% glycerol
	Ion Exchange chromatography	Dilution buffer (Buffer DG)	Buffer D + 2% glycerol
		Buffer QGA	Buffer QA + 2% glycerol
		Buffer QGB	Buffer QB + 2% glycerol
	Dialysis	Dialysis	Buffer MA + 55% glycerol

*Table 16: Buffers used for protein purification. *For acetylated and mimic acetylated variants, a PH of 8.5 was used.*

Antibiotic	Final concentration used
Ampicillin	50 ng/µL
Kanamycin	25 ng/µL
Spectinomycin	25 ng/µL
Chloramphenicol	20 ng/µL
Tetracycline	5 ng/µL

Table 17: Antibiotics and their concentrations

Methods

1. Cloning

1.1 Subcloning of miniSIRT1 and heIF2α onto the pET15blpa plasmid

The sequence of the human EIF2S1 gene encoding human eIF2α was optimized for bacterial expression, flanked at its 5' and 3' ends by the sequence for the NdeI and KpnI restriction sites, and synthetized at the Eurofins platform. The resulting pEK-A128 plasmid was transformed into XL1-blue bacteria and left to grow overnight at 37ºC on LB-agarose plates supplemented with ampicillin. After a second clone selection the plasmid was amplified and purified by maxi prep.

The heIF2α gene was first cloned into the pET15b-lpa plasmid. The two restriction enzymes used, KpnI and NotI need different buffers, therefore a PCR clean-up was performed between digestions.

Around 5 µg of backbone (pET15b-lpa) and donor (pEX-128-heIF2a) plasmids were subsequently digested with NdeI and KpnI restriction enzymes. The remaining digestion products were loaded onto a 1% agarose gel and the desired fragments, linearized plasmid pET15b-lpa and free insert heIF2α, were cut out of the gel and cleaned using a PCR clean up kit (Macherey Nagel, ThermoFisher).

Ligation was performed using 100 ng of linearized backbone in a 1:3 ratio backbone: insert using 3 U of T4 DNA ligase (NEB, New England Biolabs) for one hour at room temperature. Then, to linearize the residual parental vectors, the T4 DNA ligase was denatured 10 min at 65°C and 1 µl of 10x smart cut buffer and 0.5 µl de BamHI and XhoI were added to the reaction mixture and kept at 37°C one hour. XL-1 blue E. coli were then transformed with the ligation product (1 µl) and left to grow overnight at 37ºC on LB-agarose plates (25 µg/mL ampicillin).

Selected clones were then cultured in 5 mL LB media with a final concentration of ampicillin of 50 µg/mL and then mini-prepped. The resulting plasmids were digested either using SphI or BlpI, both cut within the backbone and the insert, generating if the ligation has been successful a fragment of 823 or 885 bp. Once confirmed, the plasmid was sent to sequencing and, on a positive result, the plasmid was then amplified and purified via midi-prep using the midi-prep kit (Macherey Nagel, ThermoFisher).

Human miniSIRT1 (miniSIRT1) consists in the fusion of the C-terminal end of the N-terminal domain (residues 183 to 233), the catalytic domain (residues 234 to 512) and a C-terminal regulatory segment (CTR, residues 641 to 665). This sequence was optimized for bacterial expression, flanked at its 5' and 3' ends by the sequence for the NdeI and KpnI restriction sites, and synthetized at the Eurofins platform. The resulting pEK-A258-miniSIRT1 plasmid was transformed into XL1-blue bacteria and left to grow overnight at 37ºC on LB-agarose plates supplemented with ampicillin. After a second clone selection the plasmid was amplified and purified by maxi prep.

The miniSIRT1 gene was subcloned into the NdeI and KpnI restriction sites of the pET15b-lpa plasmid.

Around 5 µg of backbone (pET15blpa) and donor (pEX-258-miniSIRT1) plasmids were subsequently digested with NdeI and KpnI restriction enzymes. The remaining digestion products were loaded onto a 1% agarose gel and the desired fragments, linearized plasmid pET15b-lpa and free insert miniSIRT1, were cut out of the gel and cleaned using a PCR clean up kit (Macherey Nagel, ThermoFisher).

Ligation was performed using 100 ng of linearized backbone in a 1:3 ratio backbone: insert using 3 U of T4 DNA ligase (NEB, New England Biolabs) for one hour at room temperature. XL-1 blue *E. coli* were then transformed with the ligation product (1 µl) and left to grow overnight at 37ºC on LB-agarose plates (25 µg/mL ampicillin).

Selected clones were then cultured in 5 mL LB media with a final concentration of ampicillin of 50 µg/mL and then mini-prepped. The resulting plasmids were digested using EcoRV (two restriction sites are present in the backbone) and BamHI (restriction site present in the insert). If the ligation has been successful three fragments of 903, 1783 and 4229 bp are generated. Once confirmed, the plasmid was sent to sequencing and on a positive result the plasmid was then amplified and purified via midi-prep using the midi-prep kit (Macherey Nagel, ThermoFisher).

1.2 Subcloning of heIF2α onto the pCDF-tRNACUA-pyIT plasmid by restriction enzymes

The heIF2α gene was cloned into the pCDF-tRNACUA-pyIT plasmid to improve protein expression. We used the pCDF-tRNACUA-pyIT, which was kindly donated by the Chin lab, as the backbone plasmid, and our own pET15b-heIF2α as the donor plasmid.

Around 5 µg of backbone and donor plasmid were subsequently digested with KpnI and Not I restriction enzymes. The remaining products were placed on an agarose gel and the desired fragments, linearized plasmid and free insert, were cut out of the gel and cleaned using a PCR clean up kit (Macherey Nagel, ThermoFisher).

Ligation was performed using 100 ng of linearized backbone in a 1:3 ratio backbone: insert using 3 U of T4 DNA ligase (NEB, New England Biolabs) for one hour at room temperature. XL-1 blue *E. coli* were then transformed with the ligation product (1 µL) and left to grow overnight at 37ºC on LB-agarose plates (spectinomycin of 25 ng/µL).

Selected colonies were then cultured in 5mL LB media with a final concentration of spectinomycin of 50 ng/µL and then mini-prepped. The resulting plasmid was digested using NcoI and XhoI, which cut both backbone and within the insert, obtaining 1000 bp fragment if the ligation has been successful. Once confirmed, the plasmid was sent to sequencing and on a positive result the plasmid was then amplified and purified via midi-prep using the midi-prep kit (Macherey Nagel, ThermoFisher).

This method was used to subclone the heIF2α-188STOP and heIF2α-303STOP genes.

1.3 Subcloning of full length SIRT1 onto the pET15blpa plasmid by restriction enzymes

The pECE-Flag-SIRT1 plasmid was kindly gifted by Dr. Michael Greenberg (Addgene plasmid # 1791 ; http://n2t.net/addgene:1791 ; RRID:Addgene_1791(Brunet *et al.*, 2004)). The SIRT1 gene was amplified by PCR using the forward primer TACCCATATGGCGGACGAGGCGGCCCTC, which contains the NdeI restriction site, and the reverse primer TTAAGCGGCCGCCTATGATTTGTTTGATGGATAG, which contains the NotI restriction site.

The resulting PCR product (insert) was purified using a PCR clean up kit. The insert and the pET15blpa vector were then digested by NdeI and NotI enzymes. Both digested products were recovered by cutting the agarose gel and purified using the cleaning kit. Insert and vector were ligated with 3:1 ratio with the fast-link ligase for 30 min at room temperature, followed by a denaturation step for 15 min at 70°C. The ligation mix was treated with BamHI which cuts the parental pECE vector if still present and then used to transform XL1blue bacteria. After double selection on LB-Agar plates supplemented with ampicillin the plasmid was recovered by maxi prep.

1.4 Subcloning of PKR onto the pTEM33 vector

The sequence coding the catalytic domain (KD, residues 242 to 551) of the human interferon-induced, double-stranded RNA-activated protein kinase (hPKR) was optimized for bacterial expression, flanked at its 5' and 3' ends by the sequence for the NcoI and XhoI restriction sites, and synthetized at the Eurofins platform. The resulting pEK-A128-hPKR plasmid was transformed into XL1-blue bacteria and left to grow overnight at 37ºC on LB-agarose plates supplemented with kanamycin. After a second clone selection the plasmid was amplified and purified by maxi prep.

The hPKR gene was subcloned into the NdeI and KpnI restriction sites of the pTEM33 plasmid. Insert and vector were ligated with 3:1 ratio with T4 DNA ligase (NEB, New England Biolabs) for one hour at room temperature followed by a denaturation step for 10 min at 65°C. XL-1 blue E. coli were then transformed with the ligation product (1 µl) and left to grow overnight at 37ºC on LB-agarose plates (25 µg/mL kanamycin).

Selected clones were then cultured in 5 mL LB media with a final concentration of kanamycin of 25 µg/mL and then mini-prepped. The resulting plasmids were digested by NcoI and XhoI to confirm the presence of the insert. Once confirmed, the plasmid was sent to sequencing and, on a positive result, the plasmid was then amplified and purified via midi-prep using the midi-prep kit (Macherey Nagel, ThermoFisher).

2. PCR

2.1 Site-directed mutagenesis

heIF2α acetylated variants were generated using the QuickChangeTM Site directed Mutagenesis (Stratagene), using a protocol with 12 amplification cycles at 68ºC.

After the reaction and DpnI digestion, the resulting product was transformed into *XL1-blue* electrocompetent bacteria and plated on LB-agar with the antibiotic of choice. Selected clones were then cultured in 5 mL LB media with the desired antibiotic, mini-prepped and sent to sequencing.

2.2 Deletion mutagenesis

The N-terminal coding region of miniSIRT1 and the His-tag coding region were removed from their respective plasmids to generate ΔNminiSIRT1 and untagged heIF2α-

K143Q-188. We used QuickChangeTM Site directed Mutagenesis (Stratagene), using a protocol with 18 amplification cycles at 68ºC.

3. Protein expressions and purifications

3.1 Expression and purification of mini-hSIRT1:

Human recombinant miniSIRT1 was expressed as a His-tagged protein in the BL21 derivative Rosetta (DE3) pLacI strain of *Escherichia coli* (Stratagene) using a pET15blpa vector (Novagen). This version of SIRT1 contains the STAC-binding N-terminal domain, the catalytic domain, and the CTR domain. The design of this minimally functional protein was done by (Dai et al., 2015), and shows similar catalytic rates as those of SIRT1, making it a good surrogate for enzymatic and crystallographic studies.

Bacteria were transformed with the pET15b-mini-hSIRT1 and incubated at 37ºC overnight in LB plates supplemented with ampicillin and chloramphenicol. Colonies were then recovered in a small volume of 2xTY expression media and inoculated into 1 L bottles of 2xTY media supplemented with ampicillin, chloramphenicol, and tetracycline at 37ºC until the A_{600} reached 0.8-1, upon which 1 mL of IPTG 1M was added to induce protein expression. The cultures were then incubated at 18 ºC, 180 r.p.m overnight. Cells were collected by centrifugation, washed with phosphate Buffer Saline (PBS) pH 7.5, centrifuged and stored at -20 ºC.

Pellets were resuspended in buffer MA (see table 16) and sonicated. The extract was clarified by centrifugation and loaded onto a TALON® Metal Affinity Resin column (TAKARA) pre-equilibrated with buffer MA. The column was washed with five volumes of buffer MA and proteins were recovered using two elution steps, one with 10 mM imidazole, to eliminate any unspecific binding, and another one containing 125 mM imidazole (buffer MB), to elute the tagged protein. The fractions containing miniSIRT1 were pooled, five-fold diluted with DA buffer and loaded onto an anion exchange column (Q-Sepharose High Performance, Merck), pre-equilibrated in buffer QA. After a washing step with buffer QA, proteins were eluted using a 0-100% buffer QB gradient. Fractions containing miniSIRT1 were pooled, concentrated in a 30 kDa cutoff centricon to a 500 µL final volume and loaded onto a Superdex 200 10/300 size-exclusion chromatography column (Sigma Aldrich) equilibrated in buffer SE. Finally, the eluted protein was concentrated to 20 mg/mL and stored at -80 ºC.

3.2 Expression and purification of ΔNminiSIRT1:

The expression and purification of ΔNminiSIRT1was done in an identical manner to that of the miniSIRT1up to the second step. After this step, the protein was concentrated and stored at -80 ºC.

3.3 Expression and purification of hSIRT1:

SIRT1 expression and purification were identical to those described for miniSIRT1.

3.4 Expression and purification of heIF2α and its variants:

Human eIF2α and its variants were expressed in BL21 (DE3) pG-Tf2 strain of *E. coli.* This plasmid contains the groEL-groES and TF (Trigger Factor) chaperone system, which is necessary for the expression of eIF2α variants in *E. coli* expression systems. Bacteria transformed with the pET15b-heIF2α plasmids listed in table 14, were incubated overnight at 37 ºC on LB plates supplemented with ampicillin and chloramphenicol. Colonies were then recovered in a small volume of 2xTY expression media and inoculated into 1 L bottles of 2xTY media supplemented with ampicillin, chloramphenicol, and tetracycline at 37 ºC until the A_{600} reached 1-1.2, upon which 1 mL of IPTG 1 M was added. The cultures were then transferred to 18 ºC, 180 r.p.m overnight. Cells were collected by centrifugation, washed with phosphate Buffer Saline (PBS) pH 7.5, centrifuged and stored at -20 ºC.

The purification of heIF2α-303 and of its mimic variants follows the same three-step protocol as SIRT1 variants with the exception that the anion-exchange chromatography was replaced by a cation-exchange chromatography. For heIF2α-188 and its mimic variants only the two first purification steps were performed. Due to pI differences, all heIF2α-188/303 variants need a Q-Sepharose as a second purification step, whereas WT heIF2α-188 needs an S-Sepharose.

3.5 Expression and purification of eIF2α (acetylated versions):

Virtually, the purifications steps for the acetylated versions of either heIF2α-188 and heIF2α-303 are identical to that one of their non-acetylated counterparts, except for acetylated heIF2α-188, where the ion exchange chromatography is performed using a Q-Sepharose instead of an S-Sepharose.

The BL21 (DE3) pG-Tf2 strain of *E. coli* was transformed with two different plasmids: pCDF-tRNACUA-pyIT-heIF2α-143AcK-188STOP and pBK-AcKRS-pylT. The former plasmid contains an heIF2α version in which the amino acid acetyl-lysine can be included using an Amber STOP codon, as well as the $tRNA^{CUA}$ that recognizes the Amber STOP codon; the later plasmid contains the aminoacyl tRNA synthetase capable of aminoacylating N-ε-acetyl-lysine to $tRNA^{CUA}$. After the transformation, bacteria were incubated at 37 ºC overnight in LB plates containing spectinomycin kanamycin and chloramphenicol, respective resistances for the pCDF-tRNACUA-pyIT-heIF2α-143AcK-188STOP vector, the pBK-AcKRS-pylT vector and the pG-Tf2 vector. Colonies were then recuperated in a small volume of 2xTY expression media and inoculated at an OD_{600} of 0.01-0.02 into 1 L bottles of 2xTY media containing the above-mentioned antibiotics, as well as tetracycline. Once the optical density reached a value of 0.25-0.3, 0.1 mM N-ε-acetyl-lysine and 0.2 mM nicotinamide (NCD, the Sirtuin inhibitor) were added (final concentrations). Bacteria were left to grow until they reached an OD_{600} of 1.2, upon which IPTG was added at a final concentration of 1 mM. The cultures were then incubated at 18 ºC, 180 r.p.m overnight.

The protocol described in this section was developed by the Chin lab (Neumann, Peak-Chew and Chin, 2008) and has been modified to our needs to obtain the highest amount of protein. The original method included a pre-culture step, in which one clone was grown overnight and then inoculated into a 1L 2xTY bottle. We also varied the addition of N-ε-acetyl-lysine and NCD. Some prefer to add these two compounds at the same time as IPTG, whereas others add it sooner in the expression. Different proteins might need to be optimized differently, and this method should be taken as a general guideline to be optimized for specific proteins, and modify it as needed.

3.6 Expression and purification of MBP-Nicotinamidase fusion protein:

S. enterica nicotinamidase (Ncase) was expressed and purified as an MBP-His6 fusion protein using the pPNC2 expression vector kindly provided by Dr. Jorge C. Escalante-Semerena (Garrity *et al.*, 2007). The plasmid was transformed by electroporation into BL21 derivative Rosetta (DE3) pLacI strain of *Escherichia coli* (Stratagene) and incubated at 37ºC overnight in LB plates supplemented with ampicillin and chloramphenicol. Colonies were then recovered in a small volume of 2xTY expression media and incubated at 37 ºC until the OD_{600} reached 0.8-1, upon which 1 mL

of IPTG was added to a final concentration of 1 mM. The cultures were then incubated at 18 ^{o}C and stirred overnight at 180 rpm. Cells were collected by centrifugation and the pellet washed in PBS and stored at -20°C.

Pellets were resuspended in buffer MA and lysed by sonication. The supernatant was recovered by centrifugating twice at 12000 g for 10 minutes at 4 ^{o}C and loaded onto a TALON® Metal Affinity Resin column (TAKARA) pre-equilibrated in buffer MA. The column was then washed with five volumes of buffer MA and proteins eluted with buffer MB. The elution was done in two steps (4 and 50% buffer B). The MBP-Ncase was eluted within the 4% buffer B step, concentrated to 12 mg/mL and stored at -80 ^{o}C.

3.7 expression and purification of the GST-PKR fusion protein:

The hPKR catalytic domain was expressed and purified as an His6-GST fusion protein using the pTEM33-PKR plasmid. The plasmid was transformed by electroporation into BL21 derivative Rosetta (DE3) pLacI strain of *Escherichia coli* (Stratagene) and incubated at 37^{o}C overnight in LB plates supplemented with kanamycin and chloramphenicol. Colonies were then recovered in a small volume of 2xTY expression media and incubated at 37 ^{o}C until the OD_{600} reached 0.8-1, upon which 1 mL of IPTG was added to a final concentration of 1 mM. The cultures were then incubated at 18 ^{o}C and stirred overnight at 180 rpm. Cells were collected by centrifugation and the pellet washed in PBS and stored at -20°C.

Pellets were resuspended in buffer SE and lysed by sonication. The supernatant was recovered by centrifugating twice at 12000 g for 15 minutes at 4 ^{o}C and loaded onto a Glutathione-Sepharose Affinity column pre-equilibrated in buffer SE. The column was then washed with five volumes of buffer SE and proteins eluted with buffer SE supplemented with 15 mM Glutathione. The fractions containing the fusion protein were pooled and loaded onto a Superdex 200 Hiload 16/60 column preequilibrated in SE buffer. The fractions containing the fusion protein were pooled concentrated and dialyzed over WE against SE buffer containing 55% glycerol.

3.8 His-tag removal via thrombin digestion:

Some experiments required the removal of the His-tag. Regardless of the protein, the removal was performed in the same manner. Lyophilized thrombin (500 U, Cytiva) was dissolved in 500 µL buffer MA. For long time storage, this solution is mixed with 550 µL glycerol and stored at -20°C. The His-tagged protein was diluted in the buffer

used for the Metal Affinity exchange to a final concentration of 1 mg/mL, placed in a dialysis membrane and one unit of thrombin was added per mg of protein and the mixture left to dialyse overnight. The resulting products were then recovered and loaded onto a metal affinity column. His-tag free protein was recovered in the flow-through whereas the residual non detagged protein was eluted with 125 mM imidazole.

3.9 Purification of untagged heIF2α-K143Q-188 for crystallization:

Untagged heIF2α-K143Q-188 was expressed as described for the other heIF2α variants and transformed bacteria collected by centrifugation, washed with phosphate Buffer Saline (PBS) pH 7.5, centrifuged and stored at -20 ºC.

After being resuspended in MA buffer, the protein was loaded onto an anion exchange column (Q-Sepharose High Performance, Merck), pre-equilibrated in buffer MA. The protein is expected to appear in the flow through which was collected, and 5-fold diluted. The protein was then applied again onto an anion exchange column (Q-Sepharose High Performance, Merck), pre-equilibrated in buffer QA. After a washing step with buffer QA, the protein was eluted using a 0-100% buffer QB gradient. The protein was then washed in a 10 kDa cutoff centricon with MA buffer and concentrated till 10 mg/mL.

3.10 Purification of His-tagged GFP:

The GFP protein from *Aequorea victoria* was expressed as a His-tagged protein in the BL21 derivative Rosetta (DE3) pLacI strain of *Escherichia coli* (Stratagene) using a pET15b vector (Novagen).

Bacteria were transformed with the pET15b-GFP plasmid and incubated at 37ºC overnight in LB plates supplemented with ampicillin and chloramphenicol. Colonies were then recovered in a small volume of 2xTY expression media and inoculated into 1 L bottles of 2xTY media supplemented with ampicillin, chloramphenicol, and tetracycline at 37ºC until the A_{600} reached 0.8-1, upon which 1 mL of IPTG 1M was added to induce protein expression. The cultures were then incubated at 18 ºC, 180 r.p.m overnight. Cells were collected by centrifugation, washed with phosphate Buffer Saline (PBS) pH 7.5, centrifuged and stored at -20 ºC.

Pellets were resuspended in buffer MA and sonicated. The extract was clarified by centrifugation and loaded onto a TALON® Metal Affinity Resin column (TAKARA)

pre-equilibrated with buffer MA. The column was washed with five volumes of buffer MA and proteins were recovered using two elution steps, one with 10 mM imidazole, to eliminate any unspecific binding, and another one containing 125 mM imidazole (buffer MB), to elute the tagged protein. The fractions containing GFP were pooled, five-fold diluted with DA buffer and loaded onto an anion exchange column (Q-Sepharose High Performance, Merck), pre-equilibrated in buffer QA. After a washing step with buffer QA, proteins were eluted using a 0-100% buffer QB gradient. Fractions containing GFP were pooled, concentrated in a 10 kDa cutoff centricon to 10 mg/mL and stored at -80 ^{o}C.

4. SIRT1 enzymatic coupled assay:

4.1 Chemicals and reagents:

The acetyl-lysine peptides were based on the sequence surrounding lysines 141 and 143 of the eIF2α sequence. All peptides were synthesised by ProteoGenix (ProteoGenix SAS), at a final purity of >96.80%.

Peptide Name	Sequence	Molecular Weight	Description
TG-15	TAWVFDDKYKRPGYG	1802.98 g/mol	Original sequence with no changes
TG-15 (141)	TAWVFDD(AcK)YKRPGYG	1845.02 g/mol	Acetylation on lysine 141
TG-15 (143)	TAWVFDDKY(AcK)RPGYG	1845.02 g/mol	Acetylation on lysine 143
FR-7 (141)	FDD (AcK)YKR	1013.10 g/mol	Acetylation on lysine 141
DG-7	DKY(AcK)RPG	905.00 g/mol	Acetylation on lysine 143
TG-15 (141A, 143AcK)	TAWVFDDAY(AcK)RPGYG	1787.93 g/mol	Acetylation on lysine 143, K141A
DG-7 (K143Q, K141A)	DAYQRPG	805.83 g/mol	K143Q, K141A

Table 18: List of peptides used for enzymatic tests or ITC

Name of substance	Molecular Weight	Stock concentration	Final concentration
Nicotinamide adenine dinucleotide hydrate (NAD^+)	663.43 g/mol	3.3 mM	1 mM
Reduced nicotinamide adenine dinucleotide phosphate (NADPH)	744.413 g/mol	4 mM	0.2 mM
α-ketoglutarate disodium salt hydrate	226.09 g/mol	66 mM	3.3 mM
Phosphate buffer		100 mM pH 8.0	20 mM

Table 19: Reagents used during the enzymatic test

4.2 Enzymes

SIRT1 variants were purified as described in section 3.1 of methods, whereas Glutamate dehydrogenase from *Proteus sp.* was purchased from Sigma-Aldrich. MBP-H_6-PncA (maltose binding protein fused to nicotinamidase from *Salmonella enterica*) was purified as described in section 3.6.

Name of enzyme	Molecular Weight	Final concentration
miniSIRT1	47 KDa	0.25 or 0.5 µM
ΔNminiSIRT1	36.7 KDa	0.25 or 0.5 µM
SIRT1	83.7	0.25 or 0.5 µM
Glutamate Dehydrogenase *S.proteus* (GDH)	318 KDa	2 U
MBP-Nicotinamidase	67.5 KDa	1.96 µM

Table 20: enzymes used during the enzymatic test.

4.3 General sirtuin enzyme coupled assay:

To characterize the catalytic activity of SIRT1 regarding mimic peptides, we used a three-step coupled enzymatic assay (Smith, Hallows and Denu, 2009). The first step generates nicotinamide, which is converted to nicotinic acid and ammonia in the second step by the nicotinamidase enzyme. In the third one, the glutamate dehydrogenase condenses ammonia and α-ketoglutarate to form glutamate upon consumption of one NADPH molecule. Therefore, the deacetylation of the substrate by SIRT1 can be followed, in real time, by measuring the reduction in the absorbance of NADPH at 340 nm.

Typical assay mixture (200 µL) contained 7.8-500 µM of acetylated peptide, 1 mM of NAD^+, 0.2 mM NADPH, 3.3 mM α-ketoglutarate, 1.96 µM MBP-PncA, 2 units of glutamate dehydrogenase from *S. proteus* and 0-0.5 µM of mini-SIRT1/ΔNminiSIRT1/SIRT1, in a final volume of 200 µL. All components were resuspended in 20 mM phosphate buffer, pH 8.0.

To determine the enzymatic parameters for a given substrate a MASTER-MIX enough for 30 reactions is prepared. It contains: 600 µL of NAD^+, 300 µL α-Ketoglutarate, 81.6 µL (1/10e dilution of the stock solution at 7.35 u/µL) of GDH and 20.4 µL of phosphate buffer.

For a given peptide, a stock solution at 2 or 4 mM is prepared in phosphate buffer. From this stock solution a range of 320 µL aliquots is prepared (1 mM / 500 µM/ 250 / 125 / 62.5 / 31.25 / 15.625 / 7.8125 µM). These aliquots are prepared at a concentration that is two-fold the final assay concentration.

The measure is performed in two steps. First, three quartz cuvettes (Hellma® High performance Quartz Glass, spectral range 200-2,500 nm, pathlength 10 nm, chamber volume 160 µL) are filled with 10 µL NADPH, 40 µL MASTER MIX and 100 µL substrate and the solution is well homogenized by up-down pipetting. The three cuvettes are placed in the spectrophotometer thermostated at 25°C and the absorbance at 340 nm is recorded simultaneously for each of them. When the absorbance is stabilized, the recording is paused. 50 µL of buffer or of 0.25 µM or 0.5 µM SIRT1 solution is added, well homogenized by up-down pipetting and recording of the evolution of absorption is resumed.

When STACs compounds or the inhibitor EX527 are tested, the reaction mixture consists in 10 µL of NADPH, 40 µL of MASTER MIX, 50 µL of compound (80 µM) or phosphate buffer, 50 µL of peptide at a 4X concentration instead of 2.

5. Crystallization and data collection

5.1 Preparation of heIF2α-K143Q-188 crystals

heIF2α-K143Q-188 crystallization was performed using the PEG II Suite screen. heIF2α-188 crystallizes in several conditions containing PEG 4000, however, the best crystals were obtained in the following condition:100 mM HEPES pH 7.5, 10% PEG 4000, 0.1M $MgCl_2$. Crystals were obtained in sitting drops and the growing time was around a week, with crystals appearing after two to three incubation days. For transport and X-ray exposure, crystals were transferred into a solution containing their crystallization solution and 15% glycerol before being flash frozen in liquid nitrogen.

5.2 Principles of X-ray crystallography

When electromagnetic waves interact with matter, two phenomena occur: absorption and scattering. In the case of X-rays, scattering occurs mainly as a result of interactions with electrons. Crystals, which have a regular arrangement, exhibit a phenomenon known as diffraction. During diffraction, scattered waves interact with the crystal lattice, causing X-rays to bend and diffract in specific directions. This diffraction only occurs for certain sets of lattice planes (represented by hkl, where h, k and l are specific indices) that follow Bragg's law: $2d \sin\theta = \lambda n$. Here, d represents the distance between two lattice planes, λ is the wavelength of the X-ray, θ is the angle between the incident radiation and the lattice plane, and n is a positive integer. Each reticular plane

corresponds to a point in diffraction space, forming a reciprocal grating. The structure factor characterizes the wave diffracted in amplitude and phase by the reticular planes (hkl).

$$F_{hkl} = \iiint_{v} \rho(xyz) e^{2i\pi(hx+ky+lz)} dxdydz$$

With v being the cell volume and ρ the electron density. In the case of molecular crystals, this structure factor can be written as follows:

$$F_{hkl} = \sum_{j} f_j e^{2i\pi(hx_j+ky_j+lz_j)}$$

The diffracted intensity Ihkl is proportional to the square of the modulus of Fhkl and can be obtained directly from the diffraction pattern. Phases, on the other hand, cannot be measured. The electronic density at each point of the crystal is then obtained by inverse Fourier transform, a function that takes the following form:

$$\rho(xyz) = \frac{1}{V} \sum_{hkl} F_{hkl} e^{-2i\pi(hx+ky+lz)}$$

5.3 Acquisition and treatment of crystallographic data

The electron density of a crystal is the Fourier-transformed image of the F_{hkl} structure factors that characterize reciprocal space. It is therefore necessary to map the entire reciprocal space to reconstruct the electron density in real space. The method most used in x-ray crystallography is the so-called crystal rotation method, which involves rotating the crystal and taking a diffraction image every 0.1°. A complete set of data is obtained by rotating the crystal through a symmetry-dependent total angle. Modern detectors allow very rapid data collection and usually a data set corresponding to 360º rotation are collected.

Once a complete data set has been collected, it is processed to convert the diffraction patterns into integrated intensities. This is done in three stages: 1) Cell

parameters, mosaicity and crystal orientation are determined based on a diffraction pattern. These parameters, together with those relating to data acquisition, are then refined based on all the diffraction images. 2) Based on these parameters, the position of the reflections is then predicted. This prediction is used to measure the intensity of each spot. This method improves measurement quality, especially where reflections are of low intensity. 3) The intensity of each independent reflection is calculated from the measurements of all the equivalent reflections recorded on all the images. Scale factors are calculated for each frame to homogenize the data.

The quality of the data set is given by various statistical values, including the R_{sym} factor:

$$R_{sym} = \frac{\sum_{hkl} \sum_i \left| \langle I_{hkl} \rangle - I^i_{hkl} \right|}{\sum_{hkl} \sum_i I_{i,hkl}}$$

Ihkl being the ith measurement of the hkl reflection and <Ihkl> the mean value of the N common reflections. We also used the correlation coefficient calculated between reflections belonging to two random halves of the data set (CC1/2).

5.4 Structure resolution

Structure resolution was performed using the molecular replacement method, which assumes that the structure of a similar molecule is known.

The water-free structure of domains 1 and 2 of heIF2α was used as a model (PDB 1kl9, Nonato et al., 2004) for molecular replacement. Solutions with very good z and LLG values were obtained readily using PHASER (McCoy *et al.*, 2007). The coordinates of these solutions were used to calculate an electron density map in which the model could be easily constructed.

Finally, coordinates and B-factors were refined by several cycles of manual adjustment using the COOT program (Emsley et al., 2010) and minimization with PHENIX software (Adams et al., 2010).

6. Analysis of miniSIRT1 deacetylation reaction by Western blotting

6.1 Enzymes and substrates

	Final concentration	Buffer
miniSIRT1	5 µM	20 mM K-phosphate pH 8.0
heIF2α-188 acetylated variants	1 µM, 2 µM, 4 µM	10 mM Hepes pH 8.5, 500 mM NaCl, 10 mM $MgCl_2$, 2% Glycerol
heIF2α-303 acetylated variants	1 µM	10 mM Hepes pH 7.5, 300 mM NaCl

Table 21: Enzymes and substrates used for Western blot.

6.2 Buffers and stains

	Composition
Transfer buffer	25 mM Tris, 192 mM glycine, 20% ethanol
Ponceau S Red staining	0.2% Ponceau S, 20% ethanol, 10% acetic acid
TBS	10 mM Tris pH 8.0, 150 mM NaCl
TBS with 5% milk	TBS with 5% milk
TBS-T	TBS + 0.2% Triton

Table 22: Buffers and stains used for Western blot.

6.2 Western Blotting

Typical assay volumes are 10 µL per time point and include: 1 µL of NAD^+ (from a 10 mM stock), 5 µL of heIF2α (to a final concentration of 1 µM) and 2 µL of 20 mM K-phosphate pH 8.0. The reaction starts by adding 2 µL of miniSIRT1. Samples were incubated for 0, 5, 10, 20, 40, and 120 minutes at 37ºC. The reaction was stopped by the addition of Coomassie blue SDS-PAGE loading dye. Samples were denatured for 5 min at 95ºC.

After denaturation samples were loaded on an SDS-PAGE 12% acrylamide gel and migrated for 40 minutes at 210 V. Proteins were then transferred to a nitrocellulose membrane (Amersham Protran 0.45 µm ref GE: 10600041) for one hour at 100 V. The membrane was colored using Ponceau red staining to check for the quality of the transfer.

The membrane was thoroughly rinsed with water until the dye was completely removed and saturated with TBS with 5 % milk for 30 minutes. After saturation the

membrane was incubated with the Anti-acetyl primary antibody (acetylated-lysine antibody, Cell Signaling, reference: 9441S) diluted 1/10000 in TBS-T with 5% milk for 30 minutes. Alternatively, the primary antibody incubation was done with the anti-eIF2α antibody (cell signaling, reference: 2103S). The membrane was then washed three times for 5 minutes with TBS-T, and then incubated for 30 minutes with the secondary antibody diluted 1/10000 in TBS-T. Depending on the primary antibody, the antirabbit (Acetyl) or antimouse (heIF2α) antibody was used. Both secondary antibodies are tagged with an HRP enzyme. The membrane was then washed three times for 5 minutes with TBS-T. The membrane was dried between two whatman filter paper sheets.

As a substrate of the HRP enzyme tagged to our secondary antibodies, the ECL mix was added onto the membrane for 5 minutes (400 µL of each solution contained in the commercial kit, ThermoFischer). After 5 minutes the membrane was revealed using the ChemiDoc MP Imaging System (Bio-Rad) and exposed for 10 s under the Chemi Hi Sensitivity program.

The band integration value at the 0 point was considered as 100% acetylated. The percentage of deacetylated protein was calculated with this value as reference and plotted against time. The plot obtained showed the decrease in signal due to removal of the acetyl group according to time.

7. Thermal Shift Assay

	Stock concentration	Final concentration (25 µL final volume)
SYPRO™	25x	5x
miniSIRT1	0.5 mg/mL	0.15 mg/mL
TG-15 (143)	0.2 µM to 1 mM	0.1 µM to 0.5 mM

Table 23: Reagents used for TSA.

A typical reaction mix (25 µL) contained 7.5 µL of (0.5 mg/mL miniSIRT1), 5 µL of 25x SYPRO™ orange (Invitrogen) and 12.5 µL of various TG-15 (143) peptide concentrations, ranging from 0.1 µM to 0.5 mM. All reaction components were prepared in phosphate buffer. The mix was directly prepared in a 96-well plate and placed in a Bio-Rad CFX-96 Real-Time PCR system. Temperature was increased by 0.5°C every 60 seconds. Fluorescence curves as a function of temperature were processed as described in the article presented in this manuscript.

7.1 Determination of buffer conditions for miniSIRT1's used in ITC

The storage buffer was tested, as well as a buffer with high salt concentration (500 mM NaCl, like heIF2α-188 storage buffer), and phosphate buffer (used for the coupled enzymatic test). We also performed the test in the presence or absence of NAD^+ or NAD^+ derivatives, as well as acetylated peptides and STACs. Results are shown in figure 86 for the TSA experiment performed in phosphate buffer, which was finally chosen as the ITC working buffer.

Results for conditions with 150 mM (storage buffer) and 500 mM NaCl are shown in appendix. These curves show a global decrease in Tm of around two to three degrees in the presence of 500 mM NaCl, which is less than ideal considering that heIF2α-188 needs high salt concentrations to prevent precipitation. In the case of the buffer containing 150 mM NaCl, the Tm are one to two degrees lower than the Tms obtained in the presence of phosphate buffer (see appendix).

A)

		1	2	3	4	5	6	7
		10 mM of compound	60 µM of compound	10 mM of compound +143pepeptide	60 µM of compound + 143 peptide			
A	NAD+	46	46	46.5	46.5		SIRT1 alone 46	SIRT1+peptide 47.5
B	NAM	46	46	47.5	47		SIRT1 alone 45.5	SIRT1+peptide 47.5
C	AADPR	46	46	47.5	47.5		SIRT1 alone 45.5	SIRT1+peptide 47.5
D	AMP	46	46	47.5	47.5		peptide alone	
E	STAC-3	46	46	47.5	47.5		peptide alone	
F	RESV	43.5	45.5	45	47.5		peptide alone	
G	Tyr	46	46	47.5	47.5			
H	AcF	45.5	46	47	47.5			

B)

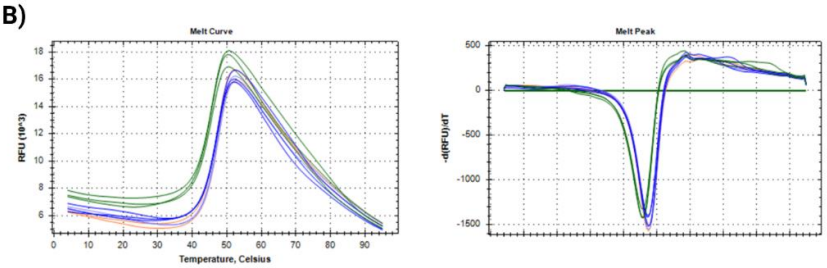

Figure 86: Thermal Shift Assays using miniSIRT1 in 20 mM phosphate buffer. A) Indicated from A to H the rows of a 96-well plate and from 1-7 the columns. The column on the left of column 1 indicates the type of compound tested: NAD^+, NAM, ADDPR, AMP, STAC-3, resveratrol (RESV), tyrosol (Tyr), and ferulic acid (AcF). In columns 1 and 2 only miniSIRT1 and the corresponding compound were added. Column 1 10 mM of compound and column 2 60 µM of compound. Columns 3 and 4 are akin to columns 1 and 2, experiments were performed in the presence of 60 µM TG-15(143) peptide. Column 6 control with only miniSIRT1 and peptide alone. Column 7, controls with miniSIRT1 and the acetylated peptide but without any compounds. B) TSA curves. The color code is shown in table A. The shift with and without compound is akin to that due to the addition of the peptide.

8. Phosphorylation of heIF2α by PKR

		Stock	Final
heIF2α-143AcK-188/ heIF2α-K143Q-188	15 µl	202 µM	4 µM
PKR	10 µl	74.4 µM	1 µM
ATP	75 µl	20 mM	2 mM
Phosphorylation buffer QSP 750 µl	650 µl		
	Buffer composition		
Phosphorylation buffer QSP	20 mM HEPES pH 7.5, 10 mM $MgCl_2$, 200 mM NaCl, 0.01 % Tween 20		
Wash buffer	10 mM HEPES pH 7.5, 100 mM NaCl, 2% glycerol		

Table 24: reactants used to phosphorylate heIF2α.

heIF2α-188 variants were phosphorylated with the PKR kinase, which specifically phosphorylates heIF2α in serine 52. A typical reaction mix contained a final concentration of 4 µM heIF2α-143AcK-188, 1 µM PKR and 2 mM of ATP, in phosphorylation buffer. The mix was incubated for one hour and 30 minutes at 37 ºC. The mix was then washed on a 10 kDa cutoff centricon with 4 mL of wash buffer.

The mix was then deposited on a native gel alongside a non-phosphorylated control, observing a different migration pattern (figure 87).

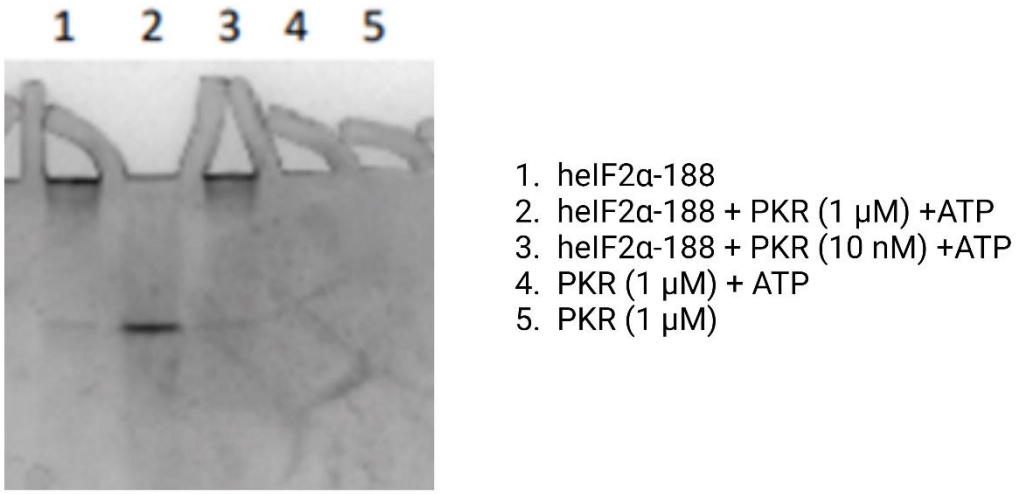

Figure 87: Native PAGE gel electrophoresis. Lane 1 was loaded with wild-type heIF2α-188, lane 2 with phosphorylated heIF2α-188 (treated with 1 µM of PKR), lane 3 with heIF2α-188 (treated with 10 nM of PKR), lane 4 with PKR and ATP, and lane 5 with PKR. Only lane 2 shows a band, presumably phosphorylated heIF2α (the pI change from 7.16 to 6.8)

9. Pull down assays with H9c2 cell extracts

Buffers	**Composition**
Lysis XB 1% NP40: 10 mL	• 50 mM HEPES pH7.7 • NP-40 1% • 150mM KCl • Protease inhibitors (Labs own, homemade) 1x • Nicotinamide (2 mM)
Wash XB: 10 mL	• 50 mM HEPES pH7.7 • 150mM KCl • Protease inhibitors (Labs own, homemade)1x • 10 mM imidazole • Nicotinamide (2 mM)
Elute XB: 10 mL	• 50 mM HEPES pH7.7 • 150mM KCl • Protease inhibitors (Complete, Sigma), 50x • 125 mM imidazole • Nicotinamide (2 mM)

Table 25: Buffers used during pull-down assays with H9c2 cell pellets

Cell pellets were resuspended in 1 mL of lysis buffer and incubated for 30 min on ice. In parallel, 50 µl of cobalt-bead slurry for each condition were equilibrated by rinsing 3 times with 1 mL of Lysis buffer and centrifuged each time at 2000 rpm on a table-top centrifuge for two minutes.

Lysed cells were spinned at max speed on a table-top centrifuge for 20 min, supernatants collected and 100 µL of each kept aside as an input. The remaining supernatant was incubated with 1 µM of bait (being 1 µM the final concentration of bait in 900 µL of remaining supernatant). Incubation lasted for 4 hours at 4ºC.The supernatant was transferred to the pre-equilibrated cobalt beads and incubated for 4 hours at 4ºC.

The mix was then centrifuged at 2000 rpm on a tabletop centrifuge, the supernatant was kept aside. The beads were washed four times with lysis buffer (500 µL) and twice with wash buffer (500 µL). An aliquot of each step was kept for further SDS-PAGE analysis. The bait and expected partners were eluted using 100 µL of elution buffer, with a sample kept to analyze on SDS-PAGE gel.

References

‘(Avalos et al., 2002) Structure of a Sir2 enzyme bound to an acetylated p53 peptide’ (no date).

Abouelfetouh, A. *et al.* (2015) ‘The E. coli sirtuin CobB shows no preference for enzymatic and nonenzymatic lysine acetylation substrate sites’, *MicrobiologyOpen*, 4(1), pp. 66–83. doi: 10.1002/mbo3.223.

Adélaïde, J. *et al.* (2007) ‘Integrated profiling of basal and luminal breast cancers’, *Cancer Research*, 67(24), pp. 11565–11575. doi: 10.1158/0008-5472.CAN-07-2536.

Alcendor, R. R. *et al.* (2007) ‘Sirt1 regulates aging and resistance to oxidative stress in the heart’, *Circulation Research*, 100(10), pp. 1512–1521. doi: 10.1161/01.RES.0000267723.65696.4a.

Van Anken, E. and Braakman, I. (2005) ‘Versatility of the endoplasmic reticulum protein folding factory’, *Critical Reviews in Biochemistry and Molecular Biology*, pp. 191–228. doi: 10.1080/10409230591008161.

Avalos, J. L., Boeke, J. D. and Wolberger, C. (2004) *Structural Basis for the Mechanism and Regulation of Sir2 Enzymes, Molecular Cell*.

Back, S. H. *et al.* (2009) ‘Translation Attenuation through eIF2α Phosphorylation Prevents Oxidative Stress and Maintains the Differentiated State in β Cells’, *Cell Metabolism*, 10(1), pp. 13–26. doi: 10.1016/j.cmet.2009.06.002.

Bagchi, M. K., Ghosh-dastidars, P. and Gupta, N. K. (1982) ‘Protein Synthesis in Rabbit Reticulocytes’, (3), pp. 1282–1288. doi: 10.1016/S0021-9258(19)68188-3.

Berger, F. *et al.* (2005) ‘Subcellular compartmentation and differential catalytic properties of the three human nicotinamide mononucleotide adenylyltransferase isoforms’, *Journal of Biological Chemistry*, 280(43), pp. 36334–36341. doi: 10.1074/jbc.M508660200.

Berlanga, J. J. and Santoyo, J. (1999) ‘Characterization of a mammalian homolog of the GCN2 eukaryotic initiation factor 2 a kinase’, 762, pp. 754–762.

Bernales, S., Papa, F. R. and Walter, P. (2006) ‘Intracellular signaling by the unfolded protein response’, *Annual Review of Cell and Developmental Biology*, 22, pp. 487–508. doi: 10.1146/annurev.cellbio.21.122303.120200.

Bevilacqua, P. C. and Cech, T. R. (1996) ‘Minor-Groove Recognition of Double-Stranded RNA by the Double-Stranded RNA-Binding Domain from the RNA-Activated Protein Kinase PKR †’, 2960(96), pp. 9983–9994.

Bhattarai, K. R. *et al.* (2021) ‘The aftermath of the interplay between the endoplasmic reticulum stress response and redox signaling’, *Experimental and Molecular Medicine*, 53(2), pp. 151–167. doi: 10.1038/s12276-021-00560-8.

Bitterman, K. J. *et al.* (2002) ‘Inhibition of silencing and accelerated aging by nicotinamide, a putative negative regulator of yeast Sir2 and human SIRT1’, *Journal of Biological Chemistry*, 277(47), pp. 45099–45107. doi: 10.1074/jbc.M205670200.

Borra, M. T. *et al.* (2004) ‘Substrate specificity and kinetic mechanism of the Sir2 family of NAD +-dependent histone/protein deacetylases’, *Biochemistry*, 43(30), pp. 9877–9887. doi: 10.1021/bi049592e.

Bousette, N. *et al.* (2010) ‘Constitutively active calcineurin induces cardiac endoplasmic reticulum stress and protects against apoptosis that is mediated by α-crystallin-B’, *Proceedings of the National Academy of Sciences of the United States of America*, 107(43), pp. 18481–18486. doi: 10.1073/pnas.1013555107.

Brown-Elliott, B. A. *et al.* (2006) ‘Clinical and laboratory features of the Nocardia spp. based on current molecular taxonomy’, *Clinical Microbiology Reviews*, 19(2), pp. 259–282. doi: 10.1128/CMR.19.2.259-282.2006.

Brunet, A. *et al.* (2004) *Stress-Dependent Regulation of FOXO Transcription Factors by the SIRT1 Deacetylase Downloaded from*, *SCIENCE*. Available at: www.sciencemag.orghttp://science.sciencemag.org/.

Calfon, M. *et al.* (2002) ‘2002 Nature Ron Calfon XBP-1’, *Nature*, 415(January), pp. 1–6.

Cao, D. *et al.* (2015) ‘Structural basis for allosteric, substrate-dependent stimulation of SIRT1 activity by resveratrol’. doi: 10.1101/gad.265462.

Castilho, B. A. *et al.* (2014) ‘Keeping the eIF2 alpha kinase Gcn2 in check’, *Biochimica et Biophysica Acta - Molecular Cell Research*, 1843(9), pp. 1948–1968. doi: 10.1016/j.bbamcr.2014.04.006.

Chio, U. S. *et al.* (2023) ‘Cryo-EM structure of the human Sirtuin 6-nucleosome complex’, *bioRxiv*, 7586(April), p. 2023.03.17.533206. doi: 10.1126/sciadv.adf7586.

Chipurupalli, S., Samavedam, U. and Robinson, N. (2021) 'Crosstalk Between ER Stress , Autophagy and Inflammation', 8(November), pp. 1–9. doi: 10.3389/fmed.2021.758311.

Clemens, M. J. and Elia, A. (1997) 'The Double-Stranded RNA-Dependent Protein Kinase PKR : Structure and Function', 524, pp. 503–524.

Cosgrove, M. S. *et al.* (2006) 'The structural basis of sirtuin substrate affinity', *Biochemistry*, 45(24), pp. 7511–7521. doi: 10.1021/bi0526332.

Coureux, P. D. *et al.* (2020) 'Cryo-EM study of an archaeal 30S initiation complex gives insights into evolution of translation initiation', *Communications Biology*, 3(1). doi: 10.1038/s42003-020-0780-0.

Cullough, K. D. M. C. *et al.* (2001) 'Gadd153 Sensitizes Cells to Endoplasmic Reticulum Stress by Down-Regulating Bcl2 and Perturbing the Cellular Redox State', 21(4), pp. 1249–1259. doi: 10.1128/MCB.21.4.1249.

Curry, A. M. *et al.* (2021) 'Human Sirtuin Regulators: The "Success" Stories', *Frontiers in Physiology*, 12(October), pp. 1–16. doi: 10.3389/fphys.2021.752117.

D'Onofrio, N. *et al.* (2015) 'Sirtuins in vascular diseases: Emerging roles and therapeutic potential', *Biochimica et Biophysica Acta - Molecular Basis of Disease*. Elsevier, pp. 1311–1322. doi: 10.1016/j.bbadis.2015.03.001.

Dai, H. *et al.* (2010) 'SIRT1 activation by small molecules: Kinetic and biophysical evidence for direct interaction of enzyme and activator', *Journal of Biological Chemistry*, 285(43), pp. 32695–32703. doi: 10.1074/jbc.M110.133892.

Dai, H. *et al.* (2015) 'Crystallographic structure of a small molecule SIRT1 activator-enzyme complex', *Nature Communications*, 6. doi: 10.1038/ncomms8645.

Dai, H. *et al.* (2019) 'challenges', pp. 140–154. doi: 10.1016/j.pharmthera.2018.03.004.Sirtuin.

Davenport, A. M., Huber, F. M. and Hoelz, A. (2014) 'Structural and functional analysis of human SIRT1', *Journal of Molecular Biology*, 426(3), pp. 526–541. doi: 10.1016/j.jmb.2013.10.009.

David L. Bentley (2014) 'Coupling mRNA processing with transcription in time and space', *Nature Reviews Genetics*. doi: 10.1038/nrg3662.

Denu, J. M. (2011) ‘Catalysis and mechanistic insights on sirtuin activation NIH Public Access’, *Chembiochem*. doi: 10.1002/cbic.201000434.Catalysis.

Dever,’, T. E. *et al.* (1992) *Phosphorylation of Initiation Factor 2a by Protein Kinase GCN2 Mediates Gene-Specific Translational Control of GCN4 in Yeast, Cell*.

Dever, T. E. and Green, R. (2012) ‘The elongation, termination, and recycling phases of translation in eukaryotes’, *Cold Spring Harbor Perspectives in Biology*, 4(7), pp. 1–16. doi: 10.1101/cshperspect.a013706.

Dever, T. E., Kinzy, T. G. and Pavitt, G. D. (2016) ‘Mechanism and regulation of protein synthesis in Saccharomyces cerevisiae’, *Genetics*. Genetics Society of America, pp. 65–107. doi: 10.1534/genetics.115.186221.

Dey, M. *et al.* (2007) ‘Conserved intermolecular salt bridge required for activation of protein kinases PKR, GCN2, and PERK’, *Journal of Biological Chemistry*, 282(9), pp. 6653–6660. doi: 10.1074/jbc.M607897200.

Dhaliwal, S. and Hoffman, D. W. (2003) ‘The crystal structure of the N-terminal region of the alpha subunit of translation initiation factor 2 (eIF2α) from Saccharomyces cerevisiae provides a view of the loop containing serine 51, the target of the eIF2α-specific kinases’, *Journal of Molecular Biology*, 334(2), pp. 187–195. doi: 10.1016/j.jmb.2003.09.045.

Ding, Y. *et al.* (2014) ‘The endoplasmic reticulum-based acetyltransferases, ATase1 and ATase2, associate with the oligosaccharyltransferase to acetylate correctly folded polypeptides’, *Journal of Biological Chemistry*, 289(46), pp. 32044–32055. doi: 10.1074/jbc.M114.585547.

Donnelly, N. *et al.* (2013) ‘The eIF2α kinases: Their structures and functions’, *Cellular and Molecular Life Sciences*, pp. 3493–3511. doi: 10.1007/s00018-012-1252-6.

Donnelly, N. and Gorman, A. M. (2013) ‘The eIF2 α kinases : their structures and functions’, pp. 3493–3511. doi: 10.1007/s00018-012-1252-6.

Doolittle, W. F. (2000) ‘The nature of the universal ancestor and the evolution of the proteome’, *Current Opinion in Structural Biology*, 10(3), pp. 355–358. doi: 10.1016/S0959-440X(00)00096-8.

Doroudgar, S. and Glembotski, C. C. (2013) ‘New concepts of endoplasmic reticulum function in the heart: Programmed to conserve’, *Journal of Molecular and*

Cellular Cardiology, pp. 85–91. doi: 10.1016/j.yjmcc.2012.10.006.

Dubiez, E. *et al.* (2015) 'Identification of a second GTP-bound magnesium ion in archaeal initiation factor 2', 43(5), pp. 2946–2957. doi: 10.1093/nar/gkv053.

Escalante-Semerena, J. R. (1997) *CobB, a New Member of the SIR2 Family of Eucaryotic Regulatory Proteins, Is Required to Compensate for the Lack of Nicotinate Mononucleotide:5,6-Dimethylbenzimidazole Phosphoribosyltransferase Activity in cobT Mutants during Cobalamin Biosynthesis in Salm*, *J. Biol. Chem.* Available at: http://www.jbc.org/.

Eva, E. (2022) 'A systems biological analysis of the ATF4-GADD34-CHOP regulatory triangle upon endoplasmic reticulum stress', 12, pp. 2065–2082. doi: 10.1002/2211-5463.13484.

Flynn, A., Oldfield, S. and Proud, C. G. (1993) 'The role of the / 3-subunit of initiation factor eIF-2 in initiation complex formation', 1174, pp. 117–121.

Fournier, G. P. and Poole, A. M. (2018) 'A briefly argued case that Asgard Archaea are part of the eukaryote tree', *Frontiers in Microbiology*, 9(AUG), pp. 1–9. doi: 10.3389/fmicb.2018.01896.

Frye, R. A. (1999) 'Characterization of five human cDNAs with homology to the yeast SIR2 gene: Sir2-like proteins (Sirtuins) metabolize NAD and may have protein ADP-ribosyltransferase activity', *Biochemical and Biophysical Research Communications*, 260(1), pp. 273–279. doi: 10.1006/bbrc.1999.0897.

Frye, R. A. (2000) 'Phylogenetic classification of prokaryotic and eukaryotic Sir2-like proteins', *Biochemical and Biophysical Research Communications*, 273(2), pp. 793–798. doi: 10.1006/bbrc.2000.3000.

Fu, H. Y. *et al.* (2010) 'Ablation of C/EBP homologous protein attenuates endoplasmic reticulum-mediated apoptosis and cardiac dysfunction induced by pressure overload', *Circulation*, 122(4), pp. 361–369. doi: 10.1161/CIRCULATIONAHA.109.917914.

Garrity, J. *et al.* (2007) 'N-lysine propionylation controls the activity of propionyl-CoA synthetase', *Journal of Biological Chemistry*, 282(41), pp. 30239–30245. doi: 10.1074/jbc.M704409200.

Gavin, A. C. *et al.* (2006) 'Proteome survey reveals modularity of the yeast cell

machinery', *Nature*, 440(7084), pp. 631–636. doi: 10.1038/nature04532.

Gemmer, M. *et al.* (2023) 'Visualization of translation and protein biogenesis at the ER membrane', 614(January 2022). doi: 10.1038/s41586-022-05638-5.

Ghosh, H. S., Reizis, B. and Robbins, P. D. (2011) 'SIRT1 associates with eIF2-alpha and regulates the cellular stress response', *Scientific Reports*, 1. doi: 10.1038/srep00150.

Gil, R. *et al.* (2013) 'SIRT6 exhibits nucleosome-dependent deacetylase activity', *Nucleic Acids Research*, 41(18), pp. 8537–8545. doi: 10.1093/nar/gkt642.

Goyal, A. *et al.* (2015) 'Directional transition from initiation to elongation in bacterial translation', *Nucleic Acids Research*, 43(22), pp. 10700–10712. doi: 10.1093/nar/gkv869.

Gualerzi, C. O. and Pon, C. L. (2015) 'Initiation of mRNA translation in bacteria: Structural and dynamic aspects', *Cellular and Molecular Life Sciences*, 72(22), pp. 4341–4367. doi: 10.1007/s00018-015-2010-3.

Guillon, L. *et al.* (2005) 'Initiator tRNA binding by e/aIF5B, the eukaryotic/archaeal homologue of bacterial initiation factor IF2', *Biochemistry*, 44(47), pp. 15594–15601. doi: 10.1021/bi051514j.

Haigis, M. C. and Guarente, L. P. (2006) 'Mammalian sirtuins - Emerging roles in physiology, aging, and calorie restriction', *Genes and Development*, pp. 2913–2921. doi: 10.1101/gad.1467506.

Haigis, M. C. and Sinclair, D. A. (2010) 'Mammalian sirtuins: Biological insights and disease relevance', *Annual Review of Pathology: Mechanisms of Disease*, pp. 253–295. doi: 10.1146/annurev.pathol.4.110807.092250.

Han, A. P. *et al.* (2001) 'Heme-regulated eIF2α kinase (HRI) is required for translational regulation and survival of erythroid precursors in iron deficiency', *EMBO Journal*, 20(23), pp. 6909–6918. doi: 10.1093/emboj/20.23.6909.

Harding, H. P. *et al.* (1999) 'Protein translation and folding are coupled by an resident kinase letters to nature Protein translation and folding are coupled by an resident kinase', 398(March).

Haze, K. *et al.* (1999) 'Mammalian transcription factor ATF6 is synthesized as a

transmembrane protein and activated by proteolysis in response to endoplasmic reticulum stress', *Molecular Biology of the Cell*, 10(11), pp. 3787–3799. doi: 10.1091/mbc.10.11.3787.

Hetz, C. (2012) 'The unfolded protein response: Controlling cell fate decisions under ER stress and beyond', *Nature Reviews Molecular Cell Biology*, 13(2), pp. 89–102. doi: 10.1038/nrm3270.

Hinnebusch, A. G. (2011) 'Molecular Mechanism of Scanning and Start Codon Selection in Eukaryotes', 75(3), pp. 434–467. doi: 10.1128/MMBR.00008-11.

Hinnebusch, A. G. (2014) 'The scanning mechanism of eukaryotic translation initiation', *Annual Review of Biochemistry*. Annual Reviews Inc., pp. 779–812. doi: 10.1146/annurev-biochem-060713-035802.

Hinnebusch, A. G. and Lorsch, J. R. (2023) 'The Mechanism of Eukaryotic Translation Initiation : New Insights and Challenges'.

Hoff, K. G. *et al.* (2006) 'Insights into the Sirtuin Mechanism from Ternary Complexes Containing NAD+ and Acetylated Peptide', *Structure*, 14(8), pp. 1231–1240. doi: 10.1016/j.str.2006.06.006.

Howitz, K. T. and Sinclair, D. A. (2003) 'Small molecule activator of sirtuins extend S.cerevisiae lifespan', *Nature*, pp. 188–191. doi: 10.1038/nature01965.

Hubbard, B. P. *et al.* (2013) 'Evidence for a common mechanism of SIRT1 regulation by allosteric activators', *Science*, 339(6124), pp. 1216–1219. doi: 10.1126/science.1231097.

Hubbard, B. P. and Sinclair, D. A. (2013) 'Measurement of sirtuin enzyme activity using a substrate-agnostic fluorometric nicotinamide assay', *Methods in Molecular Biology*, 1077, pp. 167–177. doi: 10.1007/978-1-62703-637-5_11.

Hughes, J. P. *et al.* (2011) 'Principles of early drug discovery.', *British journal of pharmacology*, 162(6), pp. 1239–1249. doi: 10.1111/j.1476-5381.2010.01127.x.

Huynh, A. T. *et al.* (2022) 'Prediction and confirmation of a switch-like region within the N-terminal domain of hSIRT1', *Biochemistry and Biophysics Reports*, 30(January), p. 101275. doi: 10.1016/j.bbrep.2022.101275.

Ito, T. and Wagner, G. (2004) *Using codon optimization, chaperone co-*

expression, and rational mutagenesis for production and NMR assignments of human eIF2α, Journal of Biomolecular NMR. KLUWER/ESCOM.

Jennings, M. D. *et al.* (2013) 'eIF2B promotes eIF5 dissociation from eIF2 • GDP to facilitate guanine nucleotide exchange for translation initiation', pp. 2696–2707. doi: 10.1101/gad.231514.113.Freely.

Jennings, M. D. *et al.* (2017) 'Fail-safe control of translation initiation by dissociation of eIF2a phosphorylated ternary complexes'. doi: 10.7554/eLife.24542.001.

Jin, L. *et al.* (2009) 'Crystal structures of human SIRT3 displaying substrate-induced conformational changes.', *The Journal of biological chemistry*, 284(36), pp. 24394–24405. doi: 10.1074/jbc.M109.014928.

Jousse, C. *et al.* (2003) 'of stressed cells', 163(4), pp. 767–775. doi: 10.1083/jcb.200308075.

Julián, P. *et al.* (2011) 'The cryo-EM structure of a complete 30S translation initiation complex from Escherichia coli', *PLoS Biology*, 9(7), pp. 1–11. doi: 10.1371/journal.pbio.1001095.

Kabsch, W. (2010) 'XDS.', *Acta crystallographica. Section D, Biological crystallography*, 66(Pt 2), pp. 125–132. doi: 10.1107/S0907444909047337.

Kaeberlein, M. *et al.* (2005) 'Substrate-specific activation of sirtuins by resveratrol', *Journal of Biological Chemistry*, 280(17), pp. 17038–17045. doi: 10.1074/jbc.M500655200.

Kang, H. *et al.* (2012) 'NIH Public Access', 44(2), pp. 203–213. doi: 10.1016/j.molcel.2011.07.038.Peptide.

Kapp, L. D. and Lorsch, J. R. (2004) 'GTP-dependent Recognition of the Methionine Moiety on Initiator tRNA by Translation Factor eIF2', *Journal of Molecular Biology*, 335(4), pp. 923–936. doi: 10.1016/j.jmb.2003.11.025.

Kazan, R. *et al.* (2022) 'Role of aIF5B in archaeal translation initiation', 50(11), pp. 6532–6548.

Kazan, R. *et al.* (2023) 'Biochimie Structural insights into the evolution of late steps of translation initiation in the three domains of life', *Biochimie*, (xxxx). doi: 10.1016/j.biochi.2023.02.002.

Kebache, S. *et al.* (2002) 'Modulation of protein translation by Nck-1', *Proceedings of the National Academy of Sciences of the United States of America*, 99(8), pp. 5406–5411. doi: 10.1073/pnas.082483399.

Kim, J., Chen, J. and Lou, Z. (2008) 'DBC1 is a negative regulator of SIRT1', 451(January). doi: 10.1038/nature06500.

Klar', A. J. S., Fogel, S. and Macleod, K. (1979) *MARl-A REGULATOR OF THE HMa AND HMa LOCI IN SACCHAROMYCES CEREVISIAE*.

Klein, M. A. and Denu, J. M. (2020) 'Biological and catalytic functions of sirtuin 6 as targets for small-molecule modulators', *Journal of Biological Chemistry*, 295(32), pp. 11021–11041. doi: 10.1074/jbc.REV120.011438.

Kojima, E. *et al.* (2003) 'The function of GADD34 is a recovery from a shutoff of protein synthesis induced by ER stress—elucidation by GADD34-deficient mice'.

Kopp, M. C. *et al.* (2020) 'Europe PMC Funders Group Europe PMC Funders Author Manuscripts UPR proteins IRE1 and PERK switch BiP from chaperone to ER stress sensor', 26(11), pp. 1053–1062. doi: 10.1038/s41594-019-0324-9.UPR.

Kouroku, Y. *et al.* (2007) 'ER stress (PERK/eIF2α phosphorylation) mediates the polyglutamine-induced LC3 conversion, an essential step for autophagy formation', *Cell Death and Differentiation*, 14(2), pp. 230–239. doi: 10.1038/sj.cdd.4401984.

Kouzarides, T. *et al.* (2004) 'Davenport et al', *Journal of Biological Chemistry*. Seventh Ed, 10(2), pp. 1249–1256. doi: 10.1074/jbc.M414080200.

Kozak, M. (1986) 'Point mutations define a sequence flanking the AUG initiator codon that modulates translation by eukaryotic ribosomes', *Cell*, 44(2), pp. 283–292. doi: 10.1016/0092-8674(86)90762-2.

Kyrpides, N. C. and Woese, C. R. (1998) *Archaeal translation initiation revisited: The initiation factor 2 and eukaryotic initiation factor 2B-subunit families*. Available at: http://www.ncbi.nlm.nih.gov/cgi-bin/.

Landry, J. *et al.* (2000) *The silencing protein SIR2 and its homologs are NAD-dependent protein deacetylases*. Available at: www.pnas.orgcgidoi10.1073pnas.110148297.

Langland, J. O. *et al.* (2006) 'Inhibition of PKR by RNA and DNA viruses', 119,

pp. 100–110. doi: 10.1016/j.virusres.2005.10.014.

Lavoie, H. *et al.* (2014) 'Dimerization-induced allostery in protein kinase regulation', *Trends in Biochemical Sciences*. Elsevier Ltd, pp. 475–486. doi: 10.1016/j.tibs.2014.08.004.

Leber, J. H., Bernales, S. and Walter, P. (2004) 'IRE1-independent gain control of the unfolded protein response', *PLoS Biology*, 2(8). doi: 10.1371/journal.pbio.0020235.

Lee, E. S. *et al.* (2007) 'The double-strand RNA-dependent protein kinase PKR plays a significant role in a sustained ER stress-induced apoptosis', *FEBS Letters*, 581(22), pp. 4325–4332. doi: 10.1016/j.febslet.2007.08.001.

Lee, I. C. *et al.* (2018) 'Oxidative stress promotes SIRT1 recruitment to the GADD34/PP1α complex to activate its deacetylase function', *Cell Death and Differentiation*, 25(2), pp. 255–267. doi: 10.1038/cdd.2017.152.

Lemaire, P. *et al.* (2008) 'Mechanism of PKR activation by dsRNA', *Bone*, 23(1), pp. 1–7. doi: 10.1016/j.jmb.2008.05.056.Mechanism.

Li, R. J. *et al.* (2015) 'Salubrinal protects cardiomyocytes against apoptosis in a rat myocardial infarction model via suppressing the dephosphorylation of eukaryotic translation initiation factor 2α', *Molecular Medicine Reports*, 12(1), pp. 1043–1049. doi: 10.3892/mmr.2015.3508.

Li, S. Y. *et al.* (2009) 'Aldehyde dehydrogenase-2 (ALDH2) ameliorates chronic alcohol ingestion-induced myocardial insulin resistance and endoplasmic reticulum stress', *Journal of Molecular and Cellular Cardiology*, 47(2), pp. 247–255. doi: 10.1016/j.yjmcc.2009.03.017.

Liou, G. G. *et al.* (2005) 'Assembly of the SIR complex and its regulation by O-acetyl-ADP-ribose, a product of NAD-dependent histone deacetylation', *Cell*, 121(4), pp. 515–527. doi: 10.1016/j.cell.2005.03.035.

Liu, L. *et al.* (2015) 'GADD34 Facilitates Cell Death Resulting from Proteasome Inhibition', 5324, pp. 5317–5324.

Liu, X. *et al.* (2015) 'ER stress sensor PERK protects against pressure overload induced heart failure and lung remodeling', 64(4), pp. 738–744. doi: 10.1161/HYPERTENSIONAHA.114.03811.Endoplasmic.

Llorens, F. *et al.* (2005) 'Cross talk between protein kinase CK2 and eukaryotic translation initiation factor eIF2β subunit', *Molecular and Cellular Biochemistry*, 274(1–2), pp. 53–61. doi: 10.1007/s11010-005-3081-5.

Lu, P. D., Harding, H. P. and Ron, D. (2004) 'Translation reinitiation at alternative open reading frames regulates gene expression in an integrated stress response', *Journal of Cell Biology*, 167(1), pp. 27–33. doi: 10.1083/jcb.200408003.

Luna, R. E. *et al.* (2012) 'NIH Public Access', 1(6), pp. 689–702. doi: 10.1016/j.celrep.2012.04.007.C-terminal.

Ma, Y. and Hendershot, L. M. (2004) 'ER chaperone functions during normal and stress conditions', *Journal of Chemical Neuroanatomy*, pp. 51–65. doi: 10.1016/j.jchemneu.2003.08.007.

Marciniak, S. J. *et al.* (2004) 'CHOP induces death by promoting protein synthesis and oxidation in the stressed endoplasmic reticulum', pp. 3066–3077. doi: 10.1101/gad.1250704.vealed.

Martindale, J. J. *et al.* (2006) 'Endoplasmic reticulum stress gene induction and protection from ischemia/reperfusion injury in the hearts of transgenic mice with a tamoxifen-regulated form of ATF6', *Circulation Research*, 98(9), pp. 1186–1193. doi: 10.1161/01.RES.0000220643.65941.8d.

McCoy, A. J. *et al.* (2007) 'Phaser crystallographic software.', *Journal of applied crystallography*, 40(Pt 4), pp. 658–674. doi: 10.1107/S0021889807021206.

McEwen, E. *et al.* (2005) 'Heme-regulated inhibitor kinase-mediated phosphorylation of eukaryotic translation initiation factor 2 inhibits translation, induces stress granule formation, and mediates survival upon arsenite exposure.', *The Journal of biological chemistry*, 280(17), pp. 16925–16933. doi: 10.1074/jbc.M412882200.

Mehanna, R. A. *et al.* (2022) *Cardiac stem cells: Current knowledge and future prospects*, *World Journal of Stem Cells*. doi: 10.4252/WJSC.V14.I1.1.

Merrick, W. C. and Pavitt, G. D. (2018) 'Protein synthesis initiation in eukaryotic cells', *Cold Spring Harbor Perspectives in Biology*, 10(12). doi: 10.1101/cshperspect.a033092.

Meurs, E. *et al.* (1990) *Molecular Cloning and Characterization of the Human Double-Stranded RNA-Activated Protein Kinase Induced by Interferon*, *Cell*.

Meurs, E. F. and Esteban, M. (2007) 'The dsRNA protein kinase PKR : Virus and cell control *', 89. doi: 10.1016/j.biochi.2007.03.001.

Mhatre V. Ho, Ji-Ann Lee, and K. C. M. and Dien et al., 2013 (2008) '基因的改变NIH Public Access', *Bone*, 23(1), pp. 1–7. Available at: https://www.ncbi.nlm.nih.gov/pmc/articles/PMC3624763/pdf/nihms412728.pdf.

Michan, S. and Sinclair, D. (2009) 'Sirtuins in mammals : insights into their biological function', 404(1), pp. 1–13. doi: 10.1042/BJ20070140.Sirtuins.

Milne, J. C. *et al.* (2007) 'Small molecule activators of SIRT1 as therapeutics for the treatment of type 2 diabetes', *Nature*, 450(7170), pp. 712–716. doi: 10.1038/nature06261.

Min, J., Landry, J. and Sternglanz, R. (2001) *Crystal Structure of a SIR2 Homolog-NAD Complex al., 1997). A different SIR2-containing protein complex strongly sug-gesting that the enzymatic activity is key to the function of the SIR2 family of proteins. The enzymatic mechanism ‡ To whom correspondenc, Cell*.

Minamino, T. and Kitakaze, M. (2010) 'ER stress in cardiovascular disease', *Journal of Molecular and Cellular Cardiology*, pp. 1105–1110. doi: 10.1016/j.yjmcc.2009.10.026.

Monceaux, K. *et al.* (2022) 'Ferulic Acid, Pterostilbene, and Tyrosol Protect the Heart from ER-Stress-Induced Injury by Activating SIRT1-Dependent Deacetylation of eIF2α', *International Journal of Molecular Sciences*, 23(12). doi: 10.3390/ijms23126628.

Moraes, D. S. *et al.* (2020) 'Sirtuins, brain and cognition: A review of resveratrol effects.', *IBRO reports*, 9, pp. 46–51. doi: 10.1016/j.ibror.2020.06.004.

Mouat, M. F. and Manchester, K. (1998) 'An α subunit-deficient form of eukaryotic protein synthesis initiation factor eIF-2 from rabbit reticulocyte lysate and its activity in ternary complex formation', pp. 69–78.

Nakahata, Y. *et al.* (2009) 'Circadian Control of the NAD+ Salvage Pathway by CLOCK-SIRT1', *Science*, 324(5927), pp. 654–657. doi: 10.1126/science.1170803.

Nakamura, T. *et al.* (2021) 'Effects of NAD + Synthesis Levels on Sirtuin 1 Deacetylase Activity in Mammalian Cells', 38, pp. 59–66.

Naveau, M. *et al.* (2013) 'Roles of yeast eIF2 a and eIF2 b subunits in the binding of the initiator methionyl-tRNA', 41(2), pp. 1047–1057. doi: 10.1093/nar/gks1180.

Neumann, H., Peak-Chew, S. Y. and Chin, J. W. (2008) 'Genetically encoding Nε-acetyllysine in recombinant proteins', *Nature Chemical Biology*, 4(4), pp. 232–234. doi: 10.1038/nchembio.73.

Nonato, M. C., Widom, J. and Clardy, J. (2002) 'Crystal structure of the N-terminal segment of human eukaryotic translation initiation factor 2α', *Journal of Biological Chemistry*, 277(19), pp. 17057–17061. doi: 10.1074/jbc.M111804200.

North, B. J. *et al.* (2003) *The Human Sir2 Ortholog, SIRT2, Is an NAD-Dependent Tubulin Deacetylase mouse Sir2 deacetylate the transcription factor protein p53 and suppress p53-dependent apoptosis in re, Molecular Cell*.

Novoa, I. *et al.* (2003) 'Stress-induced gene expression requires programmed recovery from translational repression', 22(5).

Oakes, S. A. and Papa, F. R. (2015) 'The role of endoplasmic reticulum stress in human pathology', *Annual Review of Pathology: Mechanisms of Disease*, 10, pp. 173–194. doi: 10.1146/annurev-pathol-012513-104649.

Ohno, K. *et al.* (1984) 'Genetic analysis of control of proliferation in fibroblastic cells in culture. I. Isolation and characterization of mutants temperature-sensitive for proliferation or survival of untransformed diploid rat cell line 3Y1', *Somatic Cell and Molecular Genetics*, 10(1), pp. 17–28. doi: 10.1007/BF01534469.

Okada, K. I. *et al.* (2004) 'Prolonged endoplasmic reticulum stress in hypertrophic and failing heart after aortic constriction: Possible contribution of endoplasmic reticulum stress to cardiac myocyte apoptosis', *Circulation*, 110(6), pp. 705–712. doi: 10.1161/01.CIR.0000137836.95625.D4.

Okuda, A. and Kimura, G. (1996) 'An amino acid change in novel protein D123 is responsible for temperature-sensitive G1-phase arrest in a mutant of rat fibroblast line 3Y1', *Experimental Cell Research*, 223(2), pp. 242–249. doi: 10.1006/excr.1996.0078.

Pacholec, M. *et al.* (2010) 'SRT1720, SRT2183, SRT1460, and resveratrol are not direct activators of SIRT1', *Journal of Biological Chemistry*, 285(11), pp. 8340–8351. doi: 10.1074/jbc.M109.088682.

Pakos-Zebrucka, K. *et al.* (2016) 'The integrated stress response', *EMBO reports*,

17(10), pp. 1374–1395. doi: 10.15252/embr.201642195.

Pang, Y. L. J., Poruri, K. and Martinis, S. A. (2013) ‘tRNA sytherase: tRAN Aminoacylation and beyond’, 18(9), pp. 1199–1216. doi: 10.1002/wrna.1224.tRNA.

Panvert, M. *et al.* (2015) ‘Cdc123, a Cell Cycle Regulator Needed for eIF2 Assembly, Is an ATP-Grasp Protein with Unique Features’, *Structure*, 23(9), pp. 1596–1608. doi: 10.1016/j.str.2015.06.014.

Penev, A. P. I. *et al.* (2020) ‘Eukaryotic-like ribosomal RNA in Asgard archaea Affiliations ’:, pp. 1–34.

Perzlmaier, A. F., Richter, F. and Seufert, W. (2013) ‘Translation initiation requires cell division cycle 123 (Cdc123) to facilitate biogenesis of the eukaryotic initiation factor 2 (eIF2)’, *Journal of Biological Chemistry*, 288(30), pp. 21537–21546. doi: 10.1074/jbc.M113.472290.

Pires Da Silva, J. *et al.* (2020) ‘SIRT1 Protects the Heart from ER Stress-Induced Injury by Promoting eEF2K/eEF2-Dependent Autophagy’, *Cells*, 9(2). doi: 10.3390/cells9020426.

Planavila, A. *et al.* (2011) ‘Sirt1 acts in association with PPARα to protect the heart from hypertrophy, metabolic dysregulation, and inflammation’, *Cardiovascular Research*, 90(2), pp. 276–284. doi: 10.1093/cvr/cvq376.

Prola, A. *et al.* (2017) ‘SIRT1 protects the heart from ER stress-induced cell death through eIF2α deacetylation’, *Cell Death and Differentiation*, 24(2), pp. 343–356. doi: 10.1038/cdd.2016.138.

Prola, A. *et al.* (2019) ‘Endoplasmic reticulum stress induces cardiac dysfunction through architectural modifications and alteration of mitochondrial function in cardiomyocytes’, *Cardiovascular Research*, 115(2), pp. 328–342. doi: 10.1093/cvr/cvy197.

Rafie-Kolpin, M., Han, A.-P. and Chen, J.-J. (2003) ‘Autophosphorylation of threonine 485 in the activation loop is essential for attaining eIF2alpha kinase activity of HRI.’, *Biochemistry*, 42(21), pp. 6536–6544. doi: 10.1021/bi034005v.

Ramirez, M., Wek, R. C. and Hinnebusch, A. G. (1991) *Ribosome Association of GCN2 Protein Kinase, a Translational Activator of the GCN4 Gene of Saccharomyces cerevisiae*, *MOLECULAR AND CELLULAR BIOLOGY*. Available at:

http://mcb.asm.org/.

Ramos-Fernández, E. *et al.* (2016) 'Glutamatergic stimulation induces GluN2B translation by the nitric oxide-Heme-Regulated eIF2α kinase in cortical neurons.', *Oncotarget*, 7(37), pp. 58876–58892. doi: 10.18632/oncotarget.11417.

Rauh, D. *et al.* (2013) 'An acetylome peptide microarray reveals specificities and deacetylation substrates for all human sirtuin isoforms.', *Nature communications*, 4, p. 2327. doi: 10.1038/ncomms3327.

Ree, R., Varland, S. and Arnesen, T. (2018) 'Spotlight on protein N-terminal acetylation', *Experimental and Molecular Medicine*, 50(7). doi: 10.1038/s12276-018-0116-z.

Revollo, J. R., Grimm, A. A. and Imai, S. I. (2004) 'The NAD biosynthesis pathway mediated by nicotinamide phosphoribosyltransferase regulates Sir2 activity in mammalian cells', *Journal of Biological Chemistry*, 279(49), pp. 50754–50763. doi: 10.1074/jbc.M408388200.

Rodnina, M. V. (2018) 'Translation in prokaryotes', *Cold Spring Harbor Perspectives in Biology*. Cold Spring Harbor Laboratory Press. doi: 10.1101/cshperspect.a032664.

Rogerson, D. T. *et al.* (2015) 'Efficient genetic encoding of phosphoserine and its nonhydrolyzable analog.', *Nature chemical biology*, 11(7), pp. 496–503. doi: 10.1038/nchembio.1823.

Rogina, B. and Helfand, S. L. (2004) 'Sir2 mediates longevity in the fly through a pathway related to calorie restriction', *Proceedings of the National Academy of Sciences of the United States of America*, 101(45), pp. 15998–16003. doi: 10.1073/pnas.0404184101.

Rojas, M., Gingras, A. and Dever, T. E. (2014) 'Protein phosphatase PP1 / GLC7 interaction domain in yeast eIF2 γ bypasses targeting subunit requirement for eIF2 α dephosphorylation'. doi: 10.1073/pnas.1400129111.

Rojas, M., Vasconcelos, G. and Dever, T. E. (2015) 'An eIF2α-binding motif in protein phosphatase 1 subunit GADD34 and its viral orthologs is required to promote dephosphorylation of eIF2α', *Proceedings of the National Academy of Sciences of the United States of America*, 112(27), pp. E3466–E3475. doi: 10.1073/pnas.1501557112.

Ron, D. and Walter, P. (2007) ‘Signal integration in the endoplasmic reticulum unfolded protein response’, *Nature Reviews Molecular Cell Biology*, pp. 519–529. doi: 10.1038/nrm2199.

Ronneberger, O. *et al.* (2021) ‘Highly accurate protein structure prediction with AlphaFold’, *Nature*, 596(August). doi: 10.1038/s41586-021-03819-2.

Ru, U. *et al.* (2001) ‘Block of HAC1 mRNA translation’, *October*, 107, pp. 103–114.

Rutkowski, D. T. *et al.* (2006) ‘Adaptation to ER Stress Is Mediated by Differential Stabilities of Pro-Survival and Pro-Apoptotic mRNAs and Proteins’, 4(11). doi: 10.1371/journal.pbio.0040374.

Sauve, A. A. and Schramm, V. L. (2003) ‘Sir2 regulation by nicotinamide results from switching between base exchange and deacetylation chemistry’, *Biochemistry*, 42(31), pp. 9249–9256. doi: 10.1021/bi034959l.

Scheuner, D. *et al.* (2001) *Translational Control Is Required for the Unfolded Protein Response and In Vivo Glucose Homeostasis GTP exchange reaction and thereby blocks further initia-tion events. Although the biochemical mechanism of translational inhibition mediated by eIF2 phosph*, *Molecular Cell*. Kaufman.

Schmitt, E. *et al.* (2012) ‘Structure of the ternary initiation complex aIF2-GDPNP-methionylated initiator tRNA’, *Nature Structural and Molecular Biology*, 19(4), pp. 450–454. doi: 10.1038/nsmb.2259.

Schmitt, E. *et al.* (2020) ‘Recent Advances in Archaeal Translation Initiation’, *Frontiers in Microbiology*, 11(5). doi: 10.3389/fmicb.2020.584152.

Schmitt, E., Blanquet, S. and Mechulam, Y. (2002) ‘The large subunit of initiation factor aIF2 is a close structural homologue of elongation factors’, 21(7), pp. 1821–1832.

Schmitt, E., Naveau, M. and Mechulam, Y. (2010) ‘Eukaryotic and archaeal translation initiation factor 2: A heterotrimeric tRNA carrier’, *FEBS Letters*, pp. 405–412. doi: 10.1016/j.febslet.2009.11.002.

Schröder, M. and Kaufman, R. J. (2005) ‘The mammalian unfolded protein response’, *Annual Review of Biochemistry*, 74, pp. 739–789. doi: 10.1146/annurev.biochem.73.011303.074134.

Schwarz, D. S. and Blower, M. D. (2016) 'The endoplasmic reticulum: Structure, function and response to cellular signaling', *Cellular and Molecular Life Sciences*, 73(1), pp. 79–94. doi: 10.1007/s00018-015-2052-6.

Shamu, C. E. and Walter, P. (1996) 'Oligomerization phosphorylation of the Ire1p kinase during intracellular signaling from the endoplasmic reticulum to the nucleus', *EMBO Journal*, 15(12), pp. 3028–3039. doi: 10.1002/j.1460-2075.1996.tb00666.x.

Shine, J. and Dalgarno, L. (1975) '254034a0', 254, pp. 34–38.

Sidrauski, C., Cox, J. S. and Walter, P. (1996) 'tRNA ligase is required for regulated mRNA splicing in the unfolded protein response', *Cell*, 87(3), pp. 405–413. doi: 10.1016/S0092-8674(00)81361-6.

Sinclair, D. A. (2005) 'Toward a unified theory of caloric restriction and longevity regulation', *Mechanisms of Ageing and Development*, 126(9 SPEC. ISS.), pp. 987–1002. doi: 10.1016/j.mad.2005.03.019.

Sinclair, D. A. and Guarente, L. (1997) *Extrachromosomal rDNA Circles-A Cause of Aging in Yeast*, *Cell*.

Sivanand (2019) '乳鼠心肌提取 HHS Public Access', *Physiology & behavior*, 176(3), pp. 139–148. doi: 10.1016/j.gde.2017.11.003.Cross-talk.

Smith, B. C., Hallows, W. C. and Denu, J. M. (2009) 'A continuous microplate assay for sirtuins and nicotinamide-producing enzymes', *Analytical Biochemistry*, 394(1), pp. 101–109. doi: 10.1016/j.ab.2009.07.019.

Sobie, E. and Lederer, W. . (2013) 'NIH Public Access', 52(2), pp. 304–311. doi: 10.1016/j.yjmcc.2011.06.024.Dynamic.

Sokabe, M. *et al.* (2006) 'Structure of archaeal translational initiation factor 2 βγ-GDP reveals significant conformational change of the β-subunit and switch 1 region', *Proceedings of the National Academy of Sciences of the United States of America*, 103(35), pp. 13016–13021. doi: 10.1073/pnas.0604165103.

Sokabe, M., Fraser, C. S. and Hershey, J. W. B. (2012) 'The human translation initiation multi-factor complex promotes methionyl-tRNA i binding to the 40S ribosomal subunit', *Nucleic Acids Research*, 40(2), pp. 905–913. doi: 10.1093/nar/gkr772.

Srinivasan, G., James, C. M. and Krzycki, J. A. (2002) 'Pyrrolysine encoded by

UAG in Archaea: charging of a UAG-decoding specialized tRNA.', *Science (New York, N.Y.)*, 296(5572), pp. 1459–1462. doi: 10.1126/science.1069588.

Standart, N. and Weil, D. (2018) 'P-Bodies: Cytosolic Droplets for Coordinated mRNA Storage', *Trends in Genetics*, 34(8), pp. 612–626. doi: 10.1016/j.tig.2018.05.005.

Stolboushkina, E. *et al.* (2008) 'Crystal Structure of the Intact Archaeal Translation Initiation Factor 2 Demonstrates Very High Conformational Flexibility in the α - and β -Subunits', pp. 680–691. doi: 10.1016/j.jmb.2008.07.039.

Suragani, R. N. V. S. *et al.* (2006) 'Expression and purification of the subunits of human translational initiation factor 2 (eIF2): Phosphorylation of eIF2α and β', *Protein Expression and Purification*, 47(1), pp. 225–233. doi: 10.1016/j.pep.2005.10.003.

Suragani, R. N. V. S. *et al.* (2012) 'Heme-regulated eIF2α kinase activated Atf4 signaling pathway in oxidative stress and erythropoiesis.', *Blood*, 119(22), pp. 5276–5284. doi: 10.1182/blood-2011-10-388132.

Tabas, I. and Ron, D. (2011) 'Integrating the mechanisms of apoptosis induced by endoplasmic reticulum stress', *Nature Cell Biology*, pp. 184–190. doi: 10.1038/ncb0311-184.

Tanner, K. G. *et al.* (1999) *Silent information regulator 2 family of NAD-dependent histoneprotein deacetylases generates a unique product, 1-O-acetyl-ADP-ribose*, *PNAS*. Available at: www.pnas.org.

Tanno, M. *et al.* (2007) 'Nucleocytoplasmic shuttling of the NAD+-dependent histone deacetylase SIRT1', *Journal of Biological Chemistry*, 282(9), pp. 6823–6832. doi: 10.1074/jbc.M609554200.

Thuerauf, D. J. *et al.* (2006) 'Activation of the unfolded protein response in infarcted mouse heart and hypoxic cultured cardiac myocytes', *Circulation Research*, 99(3), pp. 275–282. doi: 10.1161/01.RES.0000233317.70421.03.

Tissenbaum, H. A. and Guarente, L. (2001) 'Increased dosage of a sir-2 gene extends lifespan in Caenorhabditis elegans', *Nature*, 410(6825), pp. 227–230. doi: 10.1038/35065638.

Vaquero, A. *et al.* (2004) 'Human SirT1 Interacts with Histone H1 and Promotes Formation of Facultative Heterochromatin', 16, pp. 93–105.

Vattem, K. M. and Wek, R. C. (2004) ‘Reinitiation involving upstream ORFs regulates ATF4 mRNA translation in mammalian cells’, *Proceedings of the National Academy of Sciences of the United States of America*, 101(31), pp. 11269–11274. doi: 10.1073/pnas.0400541101.

Vazquez de Aldana, C. R. *et al.* (1994) ‘Multicopy tRNA genes functionally suppress mutations in yeast eIF-2 alpha kinase GCN2: evidence for separate pathways coupling GCN4 expression to unchanged tRNA’, *Molecular and Cellular Biology*, 14(12), pp. 7920–7932. doi: 10.1128/mcb.14.12.7920-7932.1994.

Voeltz, G. K., Rolls, M. M. and Rapoport, T. A. (2002) *Structural organization of the endoplasmic reticulum*, *EMBO reports*.

Wakula, P. *et al.* (2006) ‘The translation initiation factor eIF2β is an interactor of protein phosphatase-1’, *Biochemical Journal*, 400(2), pp. 377–383. doi: 10.1042/BJ20060758.

Wang, F. M., Chen, Y. J. and Ouyang, H. J. (2011) ‘Regulation of unfolded protein response modulator XBP1s by acetylation and deacetylation’, *Biochemical Journal*, 433(1), pp. 245–252. doi: 10.1042/BJ20101293.

Wang, M. and Kaufman, R. J. (2016) ‘Protein misfolding in the endoplasmic reticulum as a conduit to human disease’, *Nature*, 529(7586), pp. 326–335. doi: 10.1038/nature17041.

Watroba, M. and Szukiewicz, D. (2021) ‘Sirtuins at the Service of Healthy Longevity’, 12(November), pp. 1–14. doi: 10.3389/fphys.2021.724506.

Wek, R. C., Jiang, H.-Y. and Anthony, T. G. (2006) *Coping with stress: eIF2 kinases and translational control The family of eIF2 (eukaryotic initiation factor 2) kinases regulate translation during different stress conditions*.

White, R. H., Keberlein, M. and Jackson, V. (2012) ‘A mutational mimic analysis of histone H3 post-translational modifications: specific sites influence the conformational state of H3/H4, causing either positive or negative supercoiling of DNA.’, *Biochemistry*, 51(41), pp. 8173–8188. doi: 10.1021/bi300872t.

Winn, M. D. *et al.* (2011) ‘Overview of the CCP4 suite and current developments.’, *Acta crystallographica. Section D, Biological crystallography*, 67(Pt 4), pp. 235–242. doi: 10.1107/S0907444910045749.

Woese, C. R. (1987) ‘Bacterial evolution’, *Microbiological Reviews*, 51(2), pp. 221–271. doi: 10.1128/mmbr.51.2.221-271.1987.

Woese, C. R. and Fox, G. E. (1977) ‘Phylogenetic structure of the prokaryotic domain: The primary kingdoms (archaebacteria/eubacteria/urkaryote/16S ribosomal RNA/molecular phylogeny)’, *Proceedings of the National Academy of Sciences of the United States of America*, 74(11), pp. 5088–5090.

Woese, C. R., Kandler, O. and Wheelis, M. L. (1990) ‘Towards a natural system of organisms: Proposal for the domains Archaea, Bacteria, and Eucarya’, *Proceedings of the National Academy of Sciences of the United States of America*, 87(12), pp. 4576–4579. doi: 10.1073/pnas.87.12.4576.

Xin Wang, C. *et al.* (2017) ‘Endoplasmic reticulum stress in the heart: insights into mechanisms and drug targets’. doi: 10.1111/bph.v175.8/issuetoc.

Xu, C., Bailly-Maitre, B. and Reed, J. C. (2005) ‘Endoplasmic reticulum stress: Cell life and death decisions’, *Journal of Clinical Investigation*, 115(10), pp. 2656–2664. doi: 10.1172/JCI26373.

Yatime, L. *et al.* (2004) ‘Functional Molecular Mapping of Archaeal Translation Initiation Factor 2’, *Journal of Biological Chemistry*, 279(16), pp. 15984–15993. doi: 10.1074/jbc.M311561200.

Yatime, L. *et al.* (2007) ‘Structure of an archaeal heterotrimeric initiation factor 2 reveals a nucleotide state between the GTP and the GDP states’, 104(47).

Yatime, L., Mechulam, Y. and Blanquet, S. (2006) ‘Structural Switch of the g Subunit in an Archaeal aIF2 ag Heterodimer’, (January), pp. 119–128. doi: 10.1016/j.str.2005.09.020.

Ye, J. *et al.* (2000) ‘ER stress induces cleavage of membrane-bound ATF6 by the same proteases that process SREBPs’, *Molecular Cell*, 6(6), pp. 1355–1364. doi: 10.1016/S1097-2765(00)00133-7.

Ye, J. *et al.* (2010) ‘The GCN2-ATF4 pathway is critical for tumour cell survival and proliferation in response to nutrient deprivation’, *EMBO Journal*, 29(12), pp. 2082–2096. doi: 10.1038/emboj.2010.81.

Yoshida, H. *et al.* (1998) ‘Identification of the cis -Acting Endoplasmic Reticulum Stress Response Element Responsible for Transcriptional Induction of Mammalian

Glucose-regulated Proteins', *Journal of Biological Chemistry*, 273(50), pp. 33741–33749. doi: 10.1074/jbc.273.50.33741.

Yoshida, H. *et al.* (2001) 'XBP1 mRNA Is Induced by ATF6 and Spliced by IRE1 in Response to ER Stress to Produce a Highly Active Transcription Factor phorylation, the activated Ire1p specifically cleaves HAC1 precursor mRNA to remove an intron of 252 nucle-otides. The cleaved 5 and ', *Cell*, 107, pp. 881–891.

Yoshida, H. *et al.* (2006) 'pXBP1(U) encoded in XBP1 pre-mRNA negatively regulates unfolded protein response activator pXBP1(S) in mammalian ER stress response', *Journal of Cell Biology*, 172(4), pp. 565–575. doi: 10.1083/jcb.200508145.

Young, S. K. and Wek, R. C. (2016) 'Upstream Open Reading Frames Differentially Regulate Gene- specific Translation in the Integrated Stress Response *', 291(33), pp. 16927–16935. doi: 10.1074/jbc.R116.733899.

Zaborske, J. M. *et al.* (2009) 'Genome-wide Analysis of tRNA Charging and Activation of', *Journal of Biological Chemistry*, 284(37), pp. 25254–25267. doi: 10.1074/jbc.M109.000877.

Zhang, K. *et al.* (2006) 'Endoplasmic reticulum stress activates cleavage of CREBH to induce a systemic inflammatory response', *Cell*, 124(3), pp. 587–599. doi: 10.1016/j.cell.2005.11.040.

Zhang, T. *et al.* (2009) 'Enzymes in the NAD+ salvage pathway regulate SIRT1 activity at target gene promoters', *Journal of Biological Chemistry*, 284(30), pp. 20408–20417. doi: 10.1074/jbc.M109.016469.

Zhao, K., Chai, X. and Marmorstein, R. (2003) 'Structure of the yeast Hst2 protein deacetylase in ternary complex with 2′-O-acetyl ADP ribose and histone peptide', *Structure*, 11(11), pp. 1403–1411. doi: 10.1016/j.str.2003.09.016.

Zhao, K., Chai, X. and Marmorstein, R. (2004) 'Structure and Substrate Binding Properties of cobB, a Sir2 Homolog Protein Deacetylase from Escherichia coli', *Journal of Molecular Biology*, 337(3), pp. 731–741. doi: 10.1016/j.jmb.2004.01.060.

Zhao, X. *et al.* (2013) 'The 2.5 Å crystal structure of the SIRT1 catalytic domain bound to nicotinamide adenine dinucleotide (NAD +) and an indole (EX527 analogue) reveals a novel mechanism of histone deacetylase inhibition', *Journal of Medicinal Chemistry*, 56(3), pp. 963–969. doi: 10.1021/jm301431y.

Zhou, J. *et al.* (2006) 'The crystal structure of human IRE1 luminal domain reveals a conserved dimerization interface required for activation of the unfolded protein response', *Proceedings of the National Academy of Sciences of the United States of America*, 103(39), pp. 14343–14348. doi: 10.1073/pnas.0606480103.

Appendix

1. ITC optimization: miniSIRT1

A)

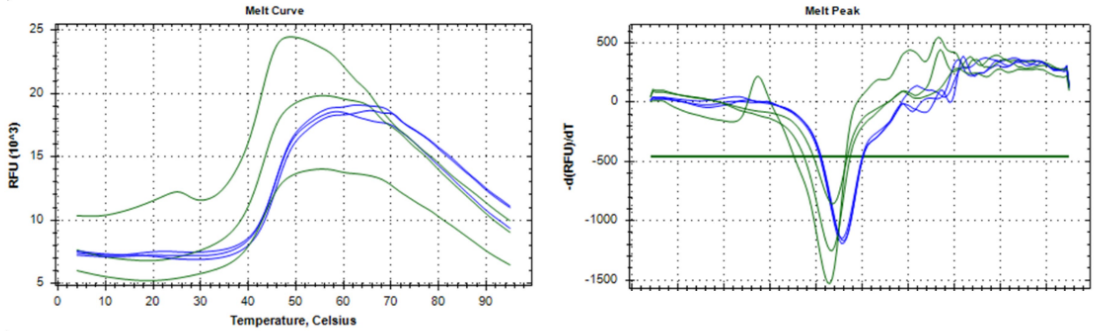

B)

		1	2	3	4	5	6	7
		10 mM of compound	60 µM of compound	10 mM of compound +143pepeptide	60 µM of compound + 143 peptide			
A	NAD+	-	-	-	-		SIRT1 alone 43.5	SIRT1+peptide 46
B	NAM	43.5	43.5	43.5	43.5		SIRT1 alone 43	SIRT1+peptide 45.5
C	AADPR	43.5	44	43.5	43.5		SIRT1 alone 43.5	SIRT1+peptide 45.5
D	AMP	43.5	43.5	43.5	43.5		peptide alone	
E	STAC-3	43.5	43.5	43.5	43.5		peptide alone	
F	RESV	-	-	-	-		peptide alone	
G	Tyr	44	44	43.5	43.5			
H	AcF	-	-	-	-			

Figure 88: Thermal Shift Assays using miniSIRT1 in 500 mM NaCl buffer. A) Indicated from A to H the rows of a 96-well plate and from 1-7 the columns. The column on the left of column 1 indicates the type of compound tested: NAD^+, NAM, ADDPR, AMP, STAC-3, resveratrol (RESV), tyrosol (Tyr), and ferulic acid (AcF). In columns 1 and 2 only miniSIRT1 and the corresponding compound were added. Column 1 10 mM of compound and column 2 60 µM of compound. Columns 3 and 4 are akin to columns 1 and 2, experiments were performed in the presence of 60 µM TG-15(143) peptide. Column 6 control with only miniSIRT1 and peptide alone. Column 7, controls with miniSIRT1 and the acetylated peptide but without any compounds. B) TSA curves. The color code is shown in table A.

A)

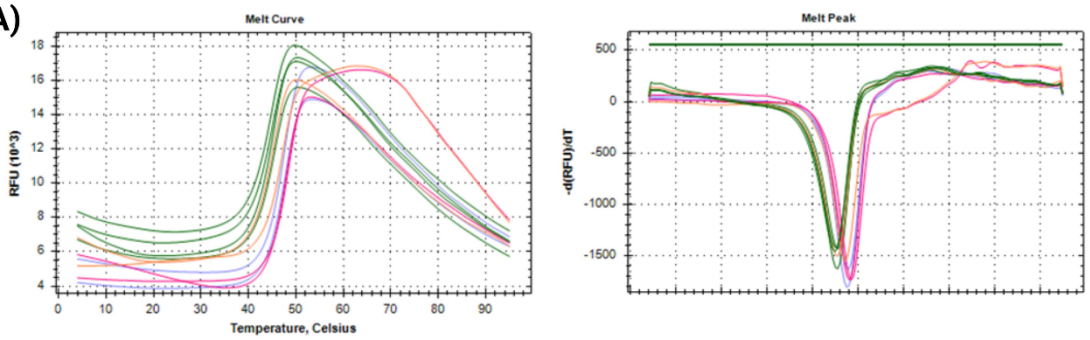

B)

		1	2	3	4	5	6
		10 mM of compound	60 µM of compound	10 mM of compound +143pepeptide	60 µM of compound + 143 peptide		
A	NAD+	-	45.5	-	46		SIRT1 alone 45.5
B	NAM	45.5	45.5	47.5	47.5		SIRT1 alone 45
C	AADPR	41	45.5	40	48		SIRT1 alone 45
D	AMP	47	45.5	48.5	48		peptide alone
E	STAC-3	45.5	45.5	48	47.5		peptide alone
F	RESV	-	45	-	47		peptide alone
G	Tyr	43	45.5	44.5	47.5		
H	AcF	-	45.5	-	47.5		

Figure 89: Thermal Shift Assays using miniSIRT1 in 150 mM NaCl buffer. A) Indicated from A to H the rows of a 96-well plate and from 1-7 the columns. The column on the left of column 1 indicates the type of compound tested: NAD^+, NAM, ADDPR, AMP, STAC-3, resveratrol (RESV), tyrosol (Tyr), and ferulic acid (AcF). In columns 1 and 2 only miniSIRT1 and the corresponding compound were added. Column 1 10 mM of compound and column 2 60 µM of compound. Columns 3 and 4 are akin to columns 1 and 2, experiments were performed in the presence of 60 µM TG-15(143) peptide. Column 6 control with only miniSIRT1 and peptide alone. Column 7, controls with miniSIRT1 and the acetylated peptide but without any compounds. B) TSA curves. The color code is shown in table A.

2. Proteins

	heIF2α- 188	**heIF2α-K143Q-188**	**heIF2α-K141Q-188**	**heIF2α-S52D-188**	**heIF2α-S52D-K141Q-188**	**heIF2α-S52D-K143Q-188**	**heIF2α-143AcK-188**	**heIF2α-141AcK-188**	**heIF2α-S52D-143AcK-188**
Number of amino acids	208	208	208	208	208	208	208	208	208
Molecular weight (Dalton)	24130.56	24130.51	24130.51	24158.57	24158.52	24158.52	24130.51	24130.51	24158.52
Theoretical pI	7.78	7.16	7.16	7.16	6.80	6.80	7.16	7.16	6.80
Extinction coefficient	19035 M-1 cm-1	19035 M-1 cm-1	19035 M-1 cm-1	19035 M-1 cm-1	19035 M-1 cm-1	19035 M-1 cm-1	19035 M-1 cm-1	19035 M-1 cm-1	19035 M-1 cm-1
Type of plasmid	pET15blpa	pET15blpa	pET15blpa	pET15blpa	pET15blpa	pET15blpa	pCF-tRNACUA-pylT	pCF-tRNACUA-pylT	pCF-tRNACUA-pylT
Tag	His-Tag	His-Tag	His-Tag	His-Tag	His-Tag	His-Tag	His-Tag	His-Tag	His-Tag

	heIF2α-303	**heIF2α-K143Q-303**	**heIF2α-S52D-K143Q-303**	**heIF2α-143AcK-303**	**heIF2α-S52D-143AcK-303**
Number of amino acids	336	336	336	336	336
Molecular weight (Dalton)	38406.68	38406.63	38246.40	38406.63	38246.40
Theoretical pI	5.45	5.37	5.31	5.37	5.31
Extinction coefficient	23630 M-1 cm-1	23630 M-1 cm-1	23630 M-1 cm-1	23630 M-1 cm-1	23630 M-1 cm-1
Type of plasmid	pET15blpa	pET15blpa	pET15blpa	pET15blpa	pET15blpa
Tag	His-Tag	His-Tag	His-Tag	His-Tag	His-Tag

	mini-hSIRT1	**hSIRT1**	**ΔN-mini-hSIRT1**
Number of amino acids	416	767	318
Molecular weight (Dalton)	47071.90	83844.33	35795.13
Theoretical pI	5.63	4.67	5.82
Extinction coefficient	28015 M-1 cm-1	46965 M-1 cm-1	15400 M-1 cm-1
Type of plasmid	pET15blpa	pET15blpa	pET15blpa
Tag	His-Tag	His-Tag	His-Tag

Résumé en français

Le stress du RE (réticulum endoplasmique) est provoqué par une dysrégulation du repliement des protéines. En réponse immédiate (réponse au stress du RE), la traduction est régulée à la baisse par la phosphorylation de l'eIF2α. La régulation de cette phosphorylation est essentielle pour restaurer l'homéostasie. Plus récemment, le stress du RE a été impliqué dans les maladies cardiovasculaires, notamment l'infarctus du myocarde, l'ischémie, la cardiomyopathie dilatée et l'insuffisance cardiaque. Une induction modérée de la réponse au stress du RE peut être protectrice, tandis que des temps de réponse prolongés entraînent l'apoptose.

Notre collaborateur Christophe Lemaire a récemment étudié le rôle de SIRT1 dans la modulation de la réponse au stress du RE cardiaque. En utilisant des souris adultes à induction de SIRT1, ils ont montré que l'inhibition de SIRT1 augmente les lésions cardiaques induites par le stress du RE, tandis que l'activation de SIRT1 est protectrice. Ils ont rapporté que SIRT1 protège les cardiomyocytes contre l'apoptose induite par le stress du RE en modulant la voie PERK/eIF2α de la réponse UPR par la désacétylation de l'eIF2α sur les résidus lysine 141 et 143. Ces résultats indiquent que la désacétylation de l'eIF2α par SIRT1 pourrait favoriser la déphosphorylation de l'eIF2α, déclenchant ainsi la fin de la réponse au stress du RE et la restauration de l'homéostasie cellulaire. L'étude de l'influence de la désacétylation de l'eIF2α sur sa déphosphorylation revêt une grande importance, car SIRT1 pourrait devenir une cible pharmacologique pour moduler le stress du RE.

Mon travail de thèse vise à compléter les résultats obtenus in vivo par le groupe de C. Lemaire avec des approches in vitro qui prouveront et caractériseront l'activité de SIRT1 sur l'eIF2α acétylé. L'expertise de notre laboratoire dans les études biochimiques et structurales nous rend particulièrement aptes à décrire l'activité catalytique de SIRT1 sur l'eIF2α acétylé et ses dérivés. Pour ce faire, le premier objectif important de mon travail de thèse était de produire une version acétylée de l'eIF2α en utilisant des systèmes de traduction orthogonaux, ainsi que des dérivés de SIRT1.

Il n'existe aucune information sur l'effet de l'acétylation sur la structure de l'eIF2α, nous visons donc également à obtenir des informations structurales sur l'eIF2α acétylé. Un autre objectif de ma thèse de doctorat est d'étudier l'interaction entre la

phosphorylation de l'eIF2α et son acétylation. En effet, le groupe de C. Lemaire a montré que l'inhibition de SIRT1 pendant les lésions cardiaques induites par le stress du RE conduisait à des niveaux accrus d'acétylation et de phosphorylation. Cela suggère fortement que la désacétylation favorise la déphosphorylation. Pour étudier l'interaction entre ces deux modifications post-traductionnelles, nous avons d'abord voulu produire des mimétiques de phosphorylation de l'eIF2α (S52D) et déterminer l'activité catalytique de SIRT1 pour caractériser l'effet des mimétiques de phosphorylation sur la désacétylation.

Enfin, l'acétylation est une modification post-traductionnelle nouvelle pour l'eIF2α, donc nous visons également à identifier un éventuel réseau d'interactions en utilisant l'eIF2α acétylé comme appât. Ce résultat vise à élargir le réseau d'interactions connues de l'eIF2α qui dépend de son état de modification post-traductionnelle.

Au cours de cette thèse, j'ai réussi à purifier une version acétylée de l'eIF2α en utilisant un système orthogonal dérivé de la pyrrolysyl tRNA-synthétase archéenne. Ce processus introduit de l'acétyl-lysine à la place d'un codon STOP. Après une optimisation approfondie, j'ai pu utiliser cette protéine pour tester l'activité catalytique de SIRT1 par Western blot. J'ai également produit une version acétylée de la protéine portant une mutation S52D, mimant la phosphorylation, et j'ai également pu mesurer une vitesse de désacétylation en utilisant cette version de la protéine. D'autre part, j'ai caractérisé l'activité catalytique de SIRT1 en utilisant des peptides dérivés des régions acétylées de l'eIF2α. J'ai également déterminé la structure cristallographique d'une variante de l'eIF2α avec un résidu de glutamine à la place de la lysine 143. Je montre que le mimétique d'acétylation Q143 n'influence pas la structure de la protéine. Enfin, j'ai utilisé l'eIF2α acétylé pour étudier son interactome en utilisant des expériences de pull-down et une analyse par spectrométrie de masse.

ECOLE DOCTORALE

Titre : Implication de eIF2 dans la réponse des cardiomyocytes au stress du réticulum endoplasmique

Mots clés : de 3 à 6 mots clefs

Au cours de la dernière décennie, le stress du réticulum endoplasmique (RE) est apparu comme un mécanisme important dans le développement des maladies cardiaques. Le stress du RE déclenche la réponse aux protéines non repliées (UPR) initiée par la phosphorylation de la sous-unité alpha du facteur d'initiation de la traduction eucaryotique 2 (eIF2). On considère qu'une induction légère à modérée du stress RE déclenche une réponse restauratrice basée sur l'autophagie alors qu'un stress RE sévère ou chronique favorise une réponse apoptotique qui contribue au développement de la maladie cardiaque. Nos collaborateurs de l'INSERM ont montré que la sirtuine 1 (SIRT1) protégeait les cardiomyocytes de l'apoptose induite par le stress du RE en atténuant spécifiquement l'activation de la voie de phosphorylation eIF2α et en favorisant l'autophagie. Ils ont également identifié l'acétylation de deux lysines d'eIF2α, K141 et K143, et ont démontré que SIRT1 désacétylait ces lysines pour protéger le cœur d'un stress ER sévère. Aucune information n'est disponible sur les conséquences de l'acétylation d'eIF2α sur son organisation structurale et sa fonction.

L'objectif de ce doctorat est de comprendre les bases moléculaires et structurales de l'interaction SIRT1 : eIF2α. Au cours de cette thèse, nous avons réussi à purifier une version acétylée d'eIF2α en utilisant un système de traduction orthogonal dérivé de la pyrrolysyl-ARNt synthétase d'archée. Ce système permet d'introduire une acétyl-lysine en réponse à un codon STOP. Après une optimisation poussée, nous avons pu utiliser cette protéine pour tester l'activité catalytique de SIRT1 par Western blotting. Nous avons également produit une version acétylée de la protéine qui portait une mutation S52D, imitant la phosphorylation, et nous avons obtenu des mesures de vitesse en utilisant cette version de la protéine. D'autre part, nous avons caractérisé l'activité catalytique de la SIRT1 en utilisant des peptides dérivés des régions acétylées d'eIF2α. Nous avons aussi déterminé la structure cristallographique d'un variant d'eIF2α possédant un résidu glutamine à la place de la lysine 143. Nous montrons que le mime d'acétylation Q143 n'influence pas la structure de la protéine. Finalement, nous avons profité de la disponibilité d'eIF2α acétylé pour mettre en évidence son interactome en utilisant des expériences de Pull-down couplées à la spectrométrie de masse.

Title : Involvement of eIF2 in cardiomyocytes response to endoplasmic reticulum stress

Keywords : eIF2, ER stress, acetylation, cardiomyocytes, SIRT1

Over the past decade, endoplasmic reticulum (ER) stress has emerged as an important mechanism in the development of heart disease. ER stress triggers the unfolded protein response (UPR) initiated by phosphorylation of the alpha subunit of eukaryotic initiation factor 2 (eIF2). Mild to moderate induction of ER stress is thought to trigger a restorative autophagy-based response, whereas severe or chronic ER stress promotes an apoptotic response that contributes to the development of heart disease. Our INSERM collaborators have shown that sirtuin 1 (SIRT1) protects cardiomyocytes from ER stress-induced apoptosis by specifically attenuating activation of the eIF2α phosphorylation pathway and promoting autophagy. They also identified acetylation of two eIF2α lysines, K141 and K143, and demonstrated that SIRT1 deacetylates these lysines to protect the heart from severe ER stress. No information is available on the consequences of eIF2α acetylation on its structural organization and function.

The aim of this PhD is to decipher the molecular and structural basis of the SIRT1: eIF2α interaction. During this thesis, we succeeded in purifying an acetylated version of eIF2α using an orthogonal system derived from the archaeal pyrrolysyl tRNA-synthetase. This process introduces acetyl-lysine in place of a STOP codon. After extensive optimization, we were able to use this protein to test the catalytic activity of SIRT1 by Western blotting. We also produced an acetylated version of the protein that carried an S52D mutation, mimicking phosphorylation, and we were also able to measure a deacetylation velocity using this version of the protein. On the other hand, we characterized the catalytic activity of SIRT1 using peptides derived from the acetylated regions of eIF2α. We have also determined the crystallographic structure of an eIF2α variant with a glutamine residue in place of the lysine 143. We show that the Q143 acetylation mimic does not influence the structure of the protein. Finally, we used acetylated eIF2α to study its interactome using pull-down experiments and mass spectrometry analysis.